UNIVERSITY OF CALIFORNIA
SANTA CRUZ

THE DESTRUCTIVE BIRTH OF MASSIVE STARS & MASSIVE STAR CLUSTERS

A dissertation submitted in partial satisfaction of the
requirements for the degree of

Doctor of Philosophy

in

ASTRONOMY & ASTROPHYSICS

by

Anna L. Rosen

June 2017

The Dissertation of Anna L. Rosen
is approved:

Professor Mark Krumholz, Chair

Professor Enrico Ramirez-Ruiz

Professor Ryan Foley

Dean Tyrus Miller
Vice Provost and Dean of Graduate Studies

Table of Contents

List of Figures

List of Tables

Abstract

The Destructive Birth of Massive Stars & Massive Star Clusters

by

Anna L. Rosen

The injection of energy and momentum into the interstellar medium by young massive stars' intense radiation fields and their fast, radiatively driven winds can have a profound influence on their formation and environment. Massive star forming regions are rare and highly obscured, making the early moments of their formation difficult to observe. Instead, we must turn to theory to elucidate the physics involved in the formation of massive stars and massive star clusters (MSCs), which can host thousands of massive stars. In my thesis, I developed analytical and numerical techniques to study the formation of massive stars and how stellar wind feedback affects the dynamics of gas that surrounds MSCs. To estimate the initial rotation rates of massive stars at birth, I developed a protostellar angular momentum evolution model for accreting protostars to determine if magnetic torques can spin down massive stars during their formation. I found that magnetic torques are insufficient to spin down massive stars due to their short formation times and high accretion rates. Radiation pressure is likely the dominate feedback mechanism regulating massive star formation. Therefore detailed simulation of the formation of massive stars requires an accurate treatment of radiation. For this purpose, I developed a new, highly accurate radiation algorithm that properly treats the absorption of the direct radiation field from stars and the re-emission and processing by

interstellar dust. With this new tool, I performed a suite of three-dimensional adaptive mesh refinement radiation-hydrodynamic simulations of the formation of massive stars from collapsing massive pre-stellar cores. I found that mass is channeled to the massive star via dense infalling filaments that are uninhibited by radiation pressure and gravitational and Rayleigh-Taylor instabilities. To determine the importance of stellar wind feedback in young MSCs, I used observations to constrain a range of kinetic energy loss channels for the hot gas produced by the shock-heating of stellar winds to explain the low X-ray luminosities observed in H II regions. I demonstrated that the energy injected by stellar winds is not a significant contributor to stellar feedback in young MSCs.

To my Grandpa,

Liston Scott Newsome,

because he “always knew I was smart.”

Acknowledgments

First, I would like to thank my PhD advisors, Mark Krumholz and Enrico Ramirez-Ruiz, for their continuous support throughout my graduate career. I greatly benefitted from their knowledge, expertise, advice, and patience throughout this arduous process. I look forward to our future collaborations. I would also like to thank my committee member Ryan Foley for not only providing me with valuable career advice, but also taking the time to read my thesis and provide comments that improved the quality of this work.

The work presented in this thesis also greatly benefitted from my collaborators, Richard Klein, Aaron Lee, Laura Lopez, Christopher McKee, and Jeffrey Oishi, for providing me with valuable scientific and numerical discussions. I would also like to thank the numerous anonymous referees for reviewing the publications that went into this thesis. Their comments and feedback greatly improved each chapter.

I am also very grateful to the numerous sources of funding I obtained during the course of my graduate career. Funding during my graduate career was provided by a National Science Foundation Graduate Fellowship, an American Association of University Women (AAUW) Dissertation Year Fellowship, and an ARCS Foundation Fellowship. Additional support for this work was provided by NASA through a Hubble Archival Research grant (award number HST-AR-13265.02-A) issued by the Space Telescope Science Institute and a Chandra Theory Grant (award number GO213003A) issued by the Chandra X-ray Observatory Center located at the Smithsonian Astro-

physical Observatory.

I could not have gotten this far without the support of my family. First, I would like to thank my mom, Sandra Decker, for being an invaluable role model and showing me that if you work hard enough anything is possible. I would also like to thank my siblings Elyssa Rosen, Jessica Rosen, and Jeffrey Rosen for their humorous (and sometimes bullying) support throughout my graduate career. Even though my grandparents, Liston and Maxine Newsome, were not able to see me obtain my PhD, I would like to thank them for their support throughout my childhood and early adult years. I know they would be very proud of my accomplishments.

My friends kept me sane and entertained throughout this challenging process. I was very fortunate to make lots of good friends outside and inside academia. I would like to thank them for their constant support, kind ears for listening to me complain about job season and grad school, and providing me with lots of entertainment throughout my time in Santa Cruz. Additional much needed entertainment was provided by my cat Nova and my family's dogs Molly, Lily, and Wilfred.

Finally, I would like to thank all of my invaluable female mentors throughout my graduate career. I was very fortunate to have many female astronomers provide advice and guidance to me throughout my PhD program. These women include Blakesley Burkhart, Cara Battersby, Rebecca Bernstein, Judy Cheng, Janet Colucci, Laura Lopez, Ruth Murray-Clay, Jill Naiman, Connie Rockosi, and Jess Werk. Not only are many of them good friends but their kind words, advice, and support kept me motivated to complete my PhD.

Chapter 1

Introduction

Massive stars, those with initial masses $\gtrsim 8\,M_{\odot}$, play an essential role in the Universe. Their explosive deaths produce most of the heavy elements, enriching the interstellar medium (ISM) and future generations of stars. They are rare, yet the energy and momentum they inject into the ISM dwarfs the contribution by their vastly more numerous low-mass cousins. This stellar feedback sets an upper limit on stars' masses, thereby affecting elemental abundances. It also destroys their natal environments, and may lead to the disruption of young star clusters. In galaxies, the integrated effect of stellar feedback makes star formation an inefficient process and may also be responsible for the launching of galactic scale outflows. All of these effects profoundly influence how galaxies form and evolve. Therefore, it is crucial to understand how massive stars form on both the individual and cluster scale.

1.1 Introduction to Star Formation

Most stars form in clusters (Lada and Lada, 2003). These clusters, including massive star clusters (MSCs; $M_\star \gtrsim 10^3 M_\odot$, which are large enough to sample the stellar initial mass function) form from the gravitational collapse of cold, dense, and magnetized giant molecular clouds (GMCs). These clouds are supersonically turbulent and this property imposes a log-normal distribution of densities within the GMCs, creating a spectrum of gas condensations over a wide range of spatial scales and masses. The densest and coldest condensations, which populate larger clumps within the GMC, act as the seeds (pre-stellar cores) that collapse under their own gravity to form stars (McKee and Ostriker, 2007).

For simplicity, and to illustrate the initial conditions for star formation at the order of magnitude level, we focus on the effect that gas pressure has on the star-formation process since it is perhaps the most basic force in opposing gravity during collapse. For the purpose of this exercise we neglect contributions from magnetic fields and turbulence, which can act as additional support against collapse and slow down the star-formation process.

Consider an isolated, isothermal core with radius $R_{\rm c}$, mass $M_{\rm c}$, and temperature $T_{\rm c}$ with corresponding sound speed $c_{\rm s} \propto \sqrt{T_{\rm c}}$. We can evaluate the condition for gravitational collapse of a pre-stellar core by comparing its gravitational potential energy

$$E_{GR} = -a\frac{GM_{\rm c}^2}{R_{\rm c}} \tag{1.1}$$

where a is a factor of order unity that depends on the internal density structure of the core, to the core's kinetic energy, which we assume is dominated by gas pressure,

$$E_{\rm KE} = \frac{3}{2} M_{\rm c} c_s^2. \tag{1.2}$$

Collapse will proceed if $|E_{\rm GR}| > E_{\rm KE}$. This condition implies that a core with mean density $\rho \sim M_{\rm c}/R_{\rm c}^3$ will undergo collapse if its size is $\gtrsim R_{\rm J}$, where

$$R_{\rm J} \sim \frac{c_s}{\sqrt{G\rho}} \tag{1.3}$$

where we have neglected factors of order unity and the subscript J denotes that this critical length is the *Jeans* length first introduced by Jeans (1902). For a typical massive core composed primarily of molecular gas $c_s \sim 0.2$ km s^{-1} and $\rho \sim 10^{-18}$ g cm^{-3}, $R_{\rm J} \approx 0.01$ pc.

This simplified argument demonstrates that the densest and coldest regions in GMCs undergo gravitational collapse to form stars. It is also trivial to estimate the characteristic time scale for a core with radius $R_{\rm J}$ and density ρ to undergo pressure-less collapse. The gravitational acceleration of the core is $g \sim GM_{\rm c}/R_{\rm J}^2$ and the distance it will collapse for a time t is $d = \frac{1}{2} g t^2$. Setting $d = R_{\rm J}$ and solving for t yields

$$t_{\rm ff} \sim \sqrt{\frac{1}{G\rho}} \tag{1.4}$$

where we have neglected factors of order unity for simplicity. This time scale represents

the minimum amount of time it would take for a pre-stellar core with mean density ρ to collapse to a star and is commonly referred to as the free-fall timescale. We note that including pressure support by sub-dominant magnetic fields and turbulence will only act to slow-down gravitational collapse. For typical massive pre-stellar cores, with $M_{\rm c} \sim 100\,M_{\odot}$ and $R_{\rm c} \sim 0.1$ pc yielding $\rho \sim 10^{-18}\,{\rm g\,cm^{-3}}$, the corresponding free-fall time is $\sim 10^5$ yr.

The simplified arguments presented thus far apply to both low-mass and massive star formation. However, once a massive protostar begins to form in the collapsing core the picture for massive star formation drastically changes from low-mass star formation because the internal evolution of an accreting massive protostar is quite rapid. This is because the timescale that governs its thermal evolution, and hence its contraction to the main-sequence (i.e., the Kelvin-Helmholtz timescale given by $t_{\rm KH} = GM_{\star}^2/(R_{\star}L_{\star})$), is much shorter for massive stars than low-mass stars due to their high luminosities. For example, the time required for a 50 $M_{\odot}$ protostar to reach the zero age main-sequence (ZAMS; i.e., the onset of core hydrogen burning) is $t_{\rm KH} \approx 20$ kyr where we assumed $R_{\rm ZAMS} = 10.7\,R_{\odot}$ and $L_{\rm ZAMS} = 3.6 \times 10^5\,{\rm L}_{\odot}$ following the ZAMS fitting formulae by Tout *et al.* (1996). For comparison, a Sun-like star has a contraction time scale of ~ 50 Myr and will therefore reach the main-sequnce long after the star-formation process is complete. Hence, massive stars will reach the main-sequence and attain their main-sequence luminosities while they are actively accreting. Their high luminosities lead to a variety of stellar feedback processes that inject energy and momentum into the infalling gas and surrounding ISM, potentially limiting accretion onto the star. We summarize

these processes next.

1.2 Introduction to Stellar Feedback

As mentioned above, massive stars contract to the main sequence very quickly during their formation and as a result they attain their high effective temperatures and main sequence luminosities while they are actively accreting (Shu *et al.*, 1987; Behrend and Maeder, 2001; Hosokawa and Omukai, 2009). This effect leads to a variety of feedback processes that can limit accretion onto the star as we discuss below. In addition, rapid contraction to the main sequence, along with accretion of material with a high specific angular momentum content from the collapsing pre-stellar core, likely causes massive stars to be born as fast rotators as we show in Chapter 2 (Goodman *et al.*, 1993; Bodenheimer, 1995). This, in turn, affects their stellar evolution by increasing their luminosities and mass-loss rates (Nieuwenhuijzen and de Jager, 1990; Ekström *et al.*, 2012).

1.2.1 Winds

The first feedback mechanism we consider is the fast, nearly isotropic mass-loss from the stellar surface known as stellar winds. These winds are launched from the stellar surface via line scattering of the star's continuum radiation field (Puls *et al.*, 2008). Wind launching becomes efficient once stars' surface temperatures exceed $\approx 2.5 \times 10^4$ K. Due to their rapid contraction, massive protostars will cross this threshold while still undergoing active accretion. The resulting mass-loss rates are of order $\dot{M}_{\rm w} \sim$

10^{-6} $M_\odot$ yr^{-1} (Vink *et al.*, 2001; Repolust *et al.*, 2004) and the mass escapes the stellar surface at velocities of $v_w \sim 1000$ km s^{-1} (i.e., at about the free-fall velocity of the star; Leitherer *et al.* (1992)). In comparison, the accretion flow onto the star has a mass flux of $\sim 10^{-4} - 10^{-3}\,M_\odot\,yr^{-1}$ (McKee and Tan, 2003) and also arrives at approximately the free-fall velocity at the stellar surface (i.e., $v_{acc} \approx v_{ff} \approx v_w$). Hence, the ram pressure of the accretion flow is typically a factor of $\sim 10^2 - 10^3$ larger than the ram pressure of the wind and therefore should be uninhibited by stellar winds.

In young MSCs winds may be more effective at limiting star formation. Stellar winds that are no longer confined will shock with winds of nearby stars and the ISM, producing hot shock-heated gas with temperatures of $\sim 10^7$ K (Castor *et al.*, 1975; Weaver *et al.*, 1977; Cantó *et al.*, 2000). The hot gas will then adiabatically expand and push on the surrounding cold ISM if it is highly coupled to the surrounding gas.

1.2.2 Ionization

A second feedback mechanism inherent to massive star and MSC formation is ionizing radiation. Since massive stars attain their main-sequence effective temperatures while they are actively accreting they can put out a significant fraction of their luminosities above the Lyman limit, and this can ionize hydrogen in the envelope around them. The absorption of ionizing radiation will heat up gas to $\sim 10^4$ K, corresponding to $c_s \sim 10\,km\,s^{-1}$, and therefore gas that is ionized may be able to escape from the massive core. Walmsley (1995) shows that, in spherical symmetry, the accretion flow will be halted by photoionization if it falls below a critical accretion rate given by

$$\dot{M}_{\rm crit} = \sqrt{\frac{m_{\rm H}^2 G M_\star S}{\alpha_{\rm H}}} \tag{1.5}$$

where S is the ionizing luminosity of the star, $M_\star$ is its mass, and $\alpha_{\rm B}$ is the case B hydrogen recombination coefficient. For a $20\,{\rm M}_\odot$ star the ionizing photon flux is $S \sim 10^{49}$ photons $\rm s^{-1}$ (Krumholz and Matzner, 2009), corresponding to $\dot{M}_{\rm crit} \sim 10^{-5}\,{\rm M}_\odot\,{\rm yr}^{-1}$. This value is much lower than the inferred accretion rates for massive stars and therefore the warm gas will be confined to a small region near the star throughout the majority of the accretion phase. Hence, photoionization should not be sufficient to shut off accretion.

In star clusters photoionization can play a more important role once star formation has ceased or if other feedback processes have removed most of the gas near the young stars. In this later phase, once accretion is no longer able to confine the photo-ionized regions around massive stars, the warm gas will expand and sweep up ISM material as the cluster evolves. Furthermore, the ionizing radiation can escape to greater distances and ionize ISM material further out. This effect can inhibit star formation near the cluster and remove gas that can otherwise form stars.

1.2.3 Radiation Pressure

As we summarized above, feedback from winds and the photo-ionizing flux from massive stars is unable to halt the accretion flow of material during massive stars early formation. However, if the radiation field is large enough, then the resulting

radiation pressure can halt accretion because the dusty envelopes around these stars are highly opaque to the strong UV flux (Weingartner and Draine, 2001). Therefore, the direct starlight will be absorbed by the dust that is immersed and coupled to the gas, transferring energy and momentum to the infalling material. The associated direct radiation pressure can oppose gravity and halt accretion onto the star (Yorke, 1979).

We can illustrate this process by comparing the direct radiation pressure (i.e., the momentum deposition rate per unit area by radiation) and the ram pressure of the infalling material at the location r at which all of the direct starlight is absorbed by dust. At this location, a slab of accreting material with column density Σ will experience radiation pressure associated with the direct starlight, $P_{\rm rad}(r) = L_\star/(4\pi r^2 c)$. The corresponding rate per unit area that gravity deposits momentum into the accretion column is $P_{\rm grav}(r) = GM_\star\Sigma/r^2$, where we have assumed isotropic accretion for simplicity. Accretion will be halted in regions where $P_{\rm rad} > P_{\rm grav}$. For isotropic accretion, this will occur when

$$\frac{L_\star}{M_\star} \gtrsim 1.3 \times 10^3 \left(\frac{\Sigma}{1\ {\rm g\,cm^{-2}}}\right) \frac{\rm L_\odot}{\rm M_\odot}. \tag{1.6}$$

This limit can be reached when the star reaches a mass of $\sim 20\,{\rm M_\odot}$, where we have assumed $\Sigma \sim 1\ {\rm g\,cm^{-2}}$.

Additionally, the absorbing dust will heat up and re-emit in the infrared. The associated dust-reprocessed radiation field diffuses throughout the envelope and enhances the total radiation pressure. This effect can also aid in impeding the accretion flow at farther radii in the collapsing core, thereby lowering the column density of the

accreting material (Kahn, 1974). This result suggests that the combination of radiation pressure from the direct and dust-reprocessed radiation fields may be large enough to halt accretion onto the star. As we discuss in Section 1.4.1, massive star formation is not a spherically symmetric problem but this analysis demonstrates that radiation pressure is potentially an important feedback mechanism that can regulate massive star formation.

1.3 Observational Challenges of Massive Star Formation

Observational studies of massive star forming regions have increased our understanding of how massive stars form and how their associated stellar feedback – the injection of energy and momentum by stars into their surroundings – may limit star formation in star clusters and galaxies (Smith and Brooks, 2007; Lopez *et al.*, 2011, 2013a; Doran *et al.*, 2013). While it is accepted that massive stars form in magnetized high-density turbulent gas clumps (Crutcher *et al.*, 2010) that are characterized by short core-collapse times and high time-averaged accretion rates (McKee and Tan, 2003; Banerjee and Pudritz, 2007), direct observation of massive star formation remains difficult for a variety of reasons.

First, massive stars are rare, representing only $\sim 1\%$ of stars by number in a newborn stellar population (Kroupa (2001), e.g., see Figure 1.1). Regions of massive star formation are far less common and typically more distant than sites of low-mass star formation. Luckily, the high luminosities associated with massive stars, also shown in

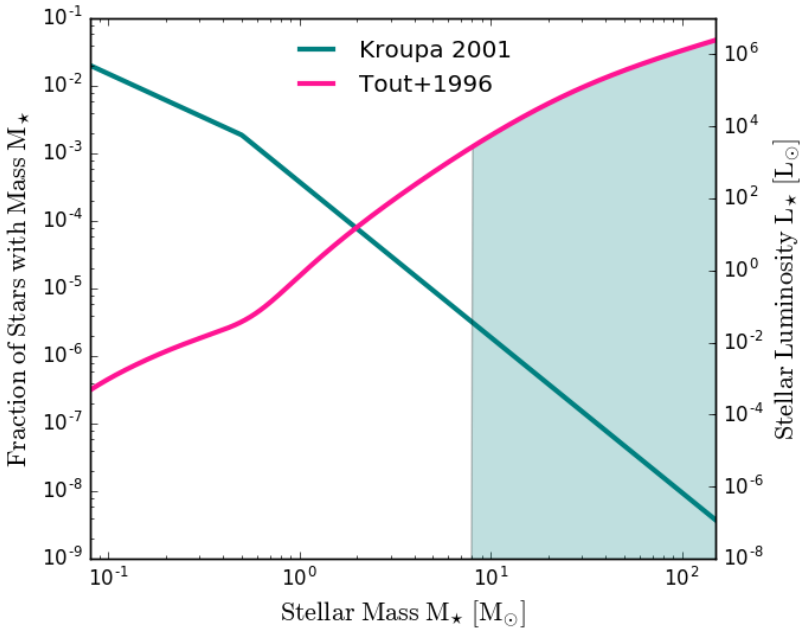

Figure 1.1 The stellar initial mass function (IMF) for $0.08 - 150\ M_{\odot}$ stars (teal line, left y-axis) following Kroupa (2001) and their associated ZAMS luminosities (pink line, right y-axis) from the fitting formula of Tout *et al.* (1996). The shaded region denotes massive stars. Integrating over the number of stars and stellar luminosities as a function of mass we find that $\sim 1\%$ of stars by number are massive ($M_{\rm star} > 8\,M_{\odot}$) and that these stars produce $\sim 98\%$ of the total radiation energy for a newly formed population of stars.

Figure 1.1 (Tout *et al.*, 1996), makes observing them over large distances feasible. However, massive stars typically form in crowded, clustered environments characterized by larger stellar densities than low-mass star-forming regions (Zinnecker and Yorke, 2007). This effect makes observing individual massive stars particularly challenging because the observations require high spatial resolution to avoid confusion by the numerous low-mass stars that accompany each massive star.

A second problem inherent to observing massive star formation is that mas-

sive stars form in regions of high obscuration, with typical gas surface densities of ~ 1 g cm^{-2}, corresponding to a visual extinction of $A_{\rm v} \approx 200$ (McKee and Tan, 2003). As a result, massive star forming regions are highly opaque at both optical and near-infrared (NIR) wavelengths. Consequently, most visible and NIR observations can only probe massive star forming regions after the majority of the formation process has completed (i.e., when most of the natal gas has been converted into stars or ejected by stellar feedback). In spite of these challenges, longer-wavelength sub-millimeter and radio observations of massive star-less clumps with size scales of 0.1-1 pc, such as those performed by ALMA, have probed the early, embedded phases of massive star formation (Tan *et al.*, 2013, 2016; Kong *et al.*, 2017). However, the fact that massive star forming regions are far away, rare, and highly-clustered makes longer-wavelength observations of massive stars challenging since these observations tend to have poorer resolution than at shorter wavelengths.

A third problem regarding the interpretation of observations of massive star and MSC formation, that has received significant attention only within the last decade, is determining what role stellar feedback plays in massive star formation. As summarized above, feedback from massive stars' intense luminosities can oppose gravity and halt accretion onto the stars. While on larger scales, the combined feedback effects from the light and radiatively-driven winds produced by the numerous massive stars in MSCs may produce effects much more impressive than the simple addition of the individual stars' energy and momentum budgets would suggest. As a result, feedback in MSCs shapes the surrounding ISM and may be able to eject the great majority of the molecular

Figure 1.2 *Hubble* image of the giant nebula NGC 3603 – one of the most massive young star clusters in the Milky Way. This image shows thousands of stars surrounded by a vast region of dust and gas that was likely ejected by stellar feedback during the star-formation process. Image Credit: NASA, ESA, and the Hubble Heritage.

gas that would otherwise form stars (e.g., see Figure 1.2). This efficient gas ejection may also be responsible for the galactic winds observed in star-forming galaxies that have extreme star formation rates (Bolatto *et al.*, 2013; Geach *et al.*, 2014).

Previous studies find that star formation in GMCs is a slow and inefficient process where only $\sim 1\%$ of the gas in a GMC will form stars per free-fall time across several orders of magnitude (Krumholz and Tan, 2007). Over a GMC's lifetime, only $\sim 5-10\%$ of the gas mass is converted to stars before it is disrupted by stellar feedback

(Williams and McKee, 1997).

Within the last decade, multi-wavelength studies have probed how different modes of feedback affect the dynamics of the gas that surround young star clusters. By exploiting radio, infrared, optical, ultraviolet, and X-ray data Lopez *et al.* (2011) studied how the radiation pressure, warm photo-ionized gas pressure, and hot gas pressure produced by feedback from the massive stars affects the dynamics of the gas that surrounds 30 Doradus (30 Dor) in the Large Magellenic Cloud (LMC), which is the most massive and largest H II region in the Local Group. Figure 1.3 shows a composite infrared, optical, and X-ray image of 30 Dor illustrating the damaging effects stellar feedback can have on the surrounding, turbulent gas. Lopez *et al.* (2011) concluded that the direct radiation pressure likely controlled the early expansion of 30 Dor and that the warm ionized gas pressure controlled the expansion once the H II region shell reached a radius of ~ 75 pc. They also concluded that the hot gas pressure, associated with stellar wind feedback, was dynamically sub-dominant and that the hot gas was only partially-confined by the H II region. In contrast, Pellegrini *et al.* (2011), using the same X-ray data, derive a hot gas pressure two orders of magnitude larger, and conclude that the hot gas pressure dominated bubbles contained within 30 Dor control the H II region dynamics. Although 30 Dor is only one prototypical example H II region in which the role of stellar feedback has been studied extensively, the discrepancy in the interpretation of observational results remains debated in the literature.

The low-number statistics of massive stars and challenges inherent to observing the early phases of massive star formation makes understanding their early formation

Figure 1.3 Composite *Hubble*, *Chandra*, and *Spitzer* image of 30 Dor. *Hubble* data, shown in green, traces the light from the massive stars (i.e., the direct radiation field from stars). Infrared emission from *Spitzer*, shown in red, traces the thermal emission from the cool dust (i.e., the dust-reprocessed radiation field). The *Chandra* data, shown in blue, detects gas that has been shock heated to $\sim 10^7$ K generated by colliding stellar winds and therefore traces the effect of feedback from stellar winds. This image demonstrates that stellar feedback shapes the ISM that surrounds young star clusters. Image credit: X-ray: NASA/CXC/PSU/L.Townsley et al.; Optical: NASA/STScI; Infrared: NASA/JPL/PSU/L.Townsley et al.

elusive. Several questions persist: how does stellar feedback affect mass delivery to the star? How does stellar feedback in MSCs limit the conversion of gas into stars and affect the dynamics of gas that surround them? What physical processes are responsible for setting the properties of massive stars at birth? In light of these challenges, further progress requires theoretical modeling as we discuss next.

1.4 Theoretical Challenges of Massive Star Formation

The theoretical challenges associated with modeling massive star formation and with determining how stellar feedback affects the formation of individual stars and the early evolution of MSCs, which are the focus of this thesis, are also quite numerous. Modeling massive star and MSC formation is a multi-dimensional and multi-physics problem. Furthermore, star formation occurs from the ∼pc size scales of GMCs to the $\sim 10^{11}$ cm size scales of stars. Therefore the dynamic range can cover seven orders of magnitude, making star formation a difficult problem to study computationally. Luckily, the advancement of analytical and numerical techniques and the vast increase in computational power over the last several decades have provided significant progress in our understanding of massive star formation.

1.4.1 Individual Massive Star Formation

As Section 1.2.3 suggests, radiation pressure is likely the dominant feedback mechanism that regulates massive star formation. Early theoretical investigations of massive star formation, which considered spherically symmetric models and one-dimensional numerical simulations, found that radiation pressure can limit the maximum masses of stars that can form, yielding a typical maximum mass of ≈ 25 $M_\odot$ (Kahn, 1974; Yorke, 1977, 1979), much smaller than observations suggest (Crowther *et al.*, 2010, 2016).

Multi-dimensional (axisymmetric and three-dimensional) radiation-

hydrodynamic (RHD) simulations of the gravitational collapse of massive laminar pre-stellar cores have demonstrated that this radiation pressure barrier can be circumvented by accretion from an optically thick accretion disk (Yorke and Sonnhalter, 2002; Krumholz *et al.*, 2009; Kuiper *et al.*, 2011, 2012). With this anisotropy, the radiative flux easily escapes along the polar directions of the star, launching radiation pressure dominated bubbles above and below the star, an effect commonly referred to as the "flashlight effect" (Yorke and Sonnhalter, 2002; Kuiper *et al.*, 2011). In agreement with this scenario, observations confirm that disks are present around massive (proto)stars (Chini *et al.*, 2006; Cesaroni *et al.*, 2007; Chini *et al.*, 2011; Johnston *et al.*, 2015).

Krumholz *et al.* (2009) performed the first three-dimensional adaptive mesh refinement (AMR) simulation of the formation of a massive stellar system and found that, in addition to disk accretion, the radiation pressure dominated-bubble shells that expand away from the star become Rayleigh-Taylor (RT) unstable, thereby leading to the growth of dense RT fingers that can penetrate the radiation-pressure dominated bubbles and deliver material to the star. One limitation of this work was that they only included the dust-reprocessed radiation pressure and deposited the stellar radiation near the star, which then diffused through the bubbles. This treatment of the radiation pressure underestimates the true radiation pressure felt by the expanding bubble shells that are opaque to the direct radiation field.

Kuiper *et al.* (2011, 2012) performed a series of three-dimensional spherically symmetric simulations that modeled both the direct and dust-reprocessed radiation fields and found that the radiation-pressure dominated bubble shells remain stable and

are eventually ejected from the core by radiation pressure. They argued that the development of RT instabilities in the radiation pressure-dominated bubble shells is likely an artifact of the underestimated radiation pressure used in Krumholz *et al.* (2009) and that the direct radiation pressure is sufficient to inhibit accretion at late times. However, in their numerical setup the star was held fixed at the center of the computational domain because they were limited to spherical symmetry. This requirement, and lack of adaptivity in regions where instabilities may develop, may have suppressed the growth of instabilities that could form.

In contrast to the idealized laminar cores modeled by the previous work discussed, McKee and Tan (2003) developed a spherically symmetric model of massive star formation in which they assume that massive stars form from cores that are primarily supported by supersonic turbulence, in agreement with observations of massive star-forming regions. They argue that marginally unstable cores that are seeded with supersonic turbulence leads to high accretion rates that carry a ram pressure sufficient to overcome radiation pressure. In this scenario, an optically thick accretion disk is not required for massive star formation as long as the ram pressure of the accreting material can overcome the radiation pressure. However, this analytical model has not been tested with multi-dimensional RHD simulations of the collapse of a massive turbulent pre-stellar core.

While significant progress in our understanding of how massive stars form has been made with the use of multi-dimensional RHD simulations there is still much debate on how radiation pressure affects mass delivery to stars (Krumholz *et al.*, 2009;

Kuiper *et al.*, 2011, 2012). As discussed above, previous three-dimensional simulations of the formation of massive stars were either limited by the radiation pressure treatment or geometry and set-up adopted. Furthermore, these simulations only considered the collapse of initially smooth cores while observations find that massive star forming cores are turbulent. In light of these limitations, we present a new hybrid radiation transfer algorithm that models the direct radiation fields from stars and the subsequent dust-reprocessed radiation field in AMR simulations in Chapter 3. We use this new method to perform RHD AMR simulations of the collapse of initially smooth and turbulent massive pre-stellar cores into massive stellar systems, which we present in Chapter 4.

1.4.2 Formation and Early Evolution of Massive Star Clusters

In MSCs, feedback from the numerous massive stars may eject gas over very large scales, leading to low star formation efficiencies in molecular clouds. Efficient gas expulsion by feedback may also lead to the disruption of young MSCs (Hills, 1980; Fall *et al.*, 2010). In young star clusters, massive stars inject energy and momentum into the ISM via photoionization flows, direct radiation pressure, dust-reprocessed radiation pressure, magnetically-launched collimated outflows, and the hot gas from shocked stellar winds and supernovae.

Analytic calculations suggest that radiation pressure is the dominant feedback mechanism in dense, MSCs (i.e., those with $M_{\rm star} \gtrsim 10^4\,{\rm M}_\odot$ and $\Sigma = 1\,{\rm g\,cm^{-2}}$; Krumholz and Matzner (2009); Fall *et al.* (2010)). SNe begin only after the $\gtrsim 3.6$ Myr lifetime of massive stars, much longer than the crossing time of MSCs. If this were

the dominant feedback mechanism, then stars would form rapidly and consume its ISM within 1-2 crossing times, long before SNe begin to explode. Collimated protostellar outflows are only effective at removing interstellar material from clusters when the escape speed is $\lesssim 7\,\mathrm{km\,s^{-1}}$ (Matzner and McKee, 2000), much less than the escape speed of dense MSCs ($v_{\rm esc} \gtrsim 10\,\mathrm{km\,s^{-1}}$). Likewise, the sound speed of photoionized gas is $\lesssim$ the escape speed of dense MSCs, making them unable to disrupt dense MSCs (Dale *et al.*, 2013).

However, the dynamical effect of the hot gas produced by shock-heating of stellar winds remain uncertain. The integrated kinetic energy carried by these winds is comparable to that delivered by supernova explosions, suggesting that at early times winds could be an important form of feedback. Yet the interaction of these winds with the surrounding clumpy, turbulent, cold gas is complex and poorly understood. Several studies have concluded that the hot gas produced by the shock-heating of stellar winds is dynamically unimportant because rather than being confined, it tends to leak out of MSCs (Harper-Clark and Murray, 2009; Lopez *et al.*, 2011; Yeh and Matzner, 2012). The question of leakage is intimately tied to the importance of stellar feedback in MSC formation. In Chapter 5, we focus on the dynamical importance of wind feedback in young MSCs.

1.5 Outline of the Remainder of this Thesis

In this thesis we explore the early phases of individual massive star formation and stellar feedback in young MSCs through the use of analytical in computational techniques. In Chapter 2 we present a protostellar rotational evolution model for accreting massive protostars to determine what physical processes set their initial rotation rates at birth. In Chapter 3 we describe a new hybrid radiation transfer algorithm developed for three-dimensional RHD simulations that models both the direct radiation fields from stars and the subsequent dust-reprocessed radiation field from dust and gas. We use this new tool to model the formation of massive stellar systems that form from the collapse of pre-stellar cores in Chapter 4. Next we focus on understanding the importance of stellar wind feedback in MSCs. Chapter 5 explores how the wind energy injected by the numerous massive stars in MSCs, which shock heat and generate hot X-ray emitting gas, can be lost through a variety of energy transfer mechanisms to explain the observed low X-ray luminosities of H II regions that surround MSCs. Finally, we conclude in Chapter 6.

Chapter 2

What Sets the Initial Rotation Rates of Massive Stars?

A version of this chapter has been published as "What Sets the Initial Rotation Rates of Massive Stars?," Rosen, A. L., Krumholz, Ramirez-Ruiz. E., 2012, *The Astrophysical Journal*, 748, 97.[1]

2.1 Introduction

While there has been significant theoretical attention to understanding the initial rotation rates of Sun-like stars, far less work has been done on more massive stars. Since the stellar evolutionary path depends on the rate of mass loss and internal mixing, both of which are enhanced by rotation (Bjorkman and Cassinelli, 1993; Maeder and Meynet, 2010), our inability to predict initial rotation rates is a limiting factor in

[1]

stellar evolution theory. Observations of young, massive stars provide evidence that they form in a similar fashion to their low-mass counterparts: via gravitational collapse of a molecular cloud core (McKee and Tan, 2003; Zapata *et al.*, 2008; Davies *et al.*, 2011). These cloud cores are slowly rotating but have very large radii, and thus have high initial angular momenta. This has led to the "angular momentum problem" in which the initial angular momentum of a cloud core is at least three orders of magnitude greater than the resulting star (Goodman *et al.*, 1993; Bodenheimer, 1995; Larson, 2010) and must be redistributed or removed during collapse.

Massive stars form in magnetized high-density turbulent gas clumps (Crutcher, 1999) that are characterized by short core collapse times and high time-averaged accretion rates (McKee and Tan, 2003). Due to the high angular momentum content of the diffuse gas, material is unable to be directly deposited on to the central object and is instead circularized at a distance far from the star, resulting in a disk (Krumholz *et al.*, 2007a, 2009). Observations, although rare, confirm that disks form around massive protostars during cloud collapse (Cesaroni *et al.*, 2006, 2007; Chini *et al.*, 2011) and the accretion onto these disks is regulated at least in part by the magnetic field (Vlemmings *et al.*, 2010). Furthermore, these disks might evolve like those located around young, low-mass stars (Chini *et al.*, 2006). The disk transfers mass and angular momentum to the central protostar, which acts to spin it up. This transfer of angular momentum, along with contraction of the protostar towards the main sequence, suggests that young stars should be rotating at or near their break up speed, the rotational speed at which the centripetal force at the equator balances gravity.

Lin *et al.* (2011) found that gravitational torques prohibit a star from rotating above $\sim 50\%$ of its break up speed during formation. However, the observed projected rotation rates of young low mass and some massive stars suggest that they rotate at a much lower fraction. Observations of low-mass PMS stars suggest that their rotation periods span a factor of ~ 30 and approximately half are slow rotators, rotating at about 10% of their break up speed (Hartmann and Stauffer, 1989; Herbst *et al.*, 2007). The observed rotational velocities of massive stars suggest that they are spinning significantly faster than their low-mass counterparts. Wolff *et al.* (2006) studied a sample of young massive stars ($M_\star > 25$ $M_\odot$) and found that their median rotation rate was 20% of their break up speed. Huang *et al.* (2010) observed the projected rotational velocity distribution of 220 young B stars and found that approximately 53.3% are rapid rotators, rotating with a velocity that is at least 40% of their break up speed. How these initial rotation rates are achieved and their dependence on stellar mass is still an unanswered question.

The physical mechanism responsible for causing young low-mass stars to be slow rotators has received considerable attention over the last three decades. One popular theory is that during the T Tauri phase (experienced by PMS stars with masses less than ~ 3 $M_\odot$), when the accretion rate is low, $\dot{M}_a \lesssim 10^{-7}$ $M_\odot$ yr^{-1} (Hartmann *et al.*, 2006), the magnetic connection between the star and its accretion disk can transport substantial angular momentum away from the star, resulting in spin rates well below break up in agreement with observations (Koenigl, 1991; Armitage and Clarke, 1996). The fact that T Tauri stars have strong magnetic fields, typically, several hundred G

to several kG (Johns-Krull, 2007), long contraction timescales after their main assembly, and long accretion disk lifetimes support this spin down scenario (Bouvier, 2007). However, Matt and Pudritz (2005) and Matt *et al.* (2010) found that when the stellar magnetic field lines open due to the differential twisting between the star and disk the resulting rotation rates, while still below break up, are higher than those of the slowest rotators.

Magnetic fields have been detected in a small sample of young and evolved OB stars. These fields are between a few hundred G to several kG and typically have a bipolar topology (Donati *et al.*, 2006; Wade *et al.*, 2006; Hubrig *et al.*, 2008; Grunhut *et al.*, 2009; Martins *et al.*, 2010). The origin of these fields is poorly understood, since the envelopes of such stars are radiative rather than convective, excluding the possibility of a Solar-type dynamo effect (Moss, 2001). The favored hypothesis for the presence of magnetic fields in massive stars is that they are fossil fields that were either accumulated or generated during star formation (Walder *et al.*, 2012). Alecian *et al.* (2008) discovered two very young B stars with strong surface magnetic fields. They found that the younger of the two is a rapid rotator and situated in the first half of the PMS phase, whereas the older star, which might already be on the main sequence, is a slow rotator most likely spun down via magnetic torques.

This implies that massive stars likely have strong magnetic fields present during their formation and that these fields, due to coupling with the accretion disk, may be able to remove a substantial amount of angular momentum from the star, producing spin rates on the zero-age main sequence (ZAMS) well below break up in a similar

fashion to their low-mass counterparts. However, massive stars reach the ZAMS very quickly since they have short thermal equilibrium timescales. They also have higher accretion rates during their formation and their magnetic fields are weaker relative to their stellar binding energy as compared to low mass stars. They likely have shorter disk lifetimes than contracting low mass stars, since their disks are likely to be quickly photo-disintegrated due to their high luminosities (Cesaroni *et al.*, 2007). All of these factors make magnetic spin-down more difficult. In this chapter we explore whether the initial spins of massive stars are regulated by the interaction of their accretion disk with the stellar magnetic field. To study this issue we model the angular momentum evolution for both low-mass and massive protostars by considering both magnetic and gravitational torques. We apply the star-disk interaction model developed by Matt and Pudritz (2005) (hereafter MP05) where the stellar magnetic field is connected to a finite region of the accretion disk, and the twisting of the magnetic field lines due to the differential rotation between the star and disk leads to a spin-down torque on the star.

This chapter is organized as follows. In the following section (Section 2.2), we give a brief introduction to how the presence of surface magnetic fields during the protostellar phase can extract angular momentum from the star. We describe our stellar angular momentum evolution model, which include a prescription for protostellar evolution and the star-disk interaction, in Section 2.3 . We state our results in Section 2.4. Lastly, we discuss our results in Section 2.5.

2.2 Magnetic Torques: Theory & Background

Protostars embedded in circumstellar disks accrete material from an angular momentum-rich mass reservoir. If the disk is Keplerian the specific angular momentum content of the circulating material, $j = \sqrt{GM_\star r}$, increases outward and the angular velocity increases inwards. The presence of a stellar magnetic field is able to disrupt the disk outside the stellar radius and channel the disk material along field lines. Spin-down torques will be conveyed to the star due to the differential twisting of the field lines threading the accretion disk at radii where the disk rotates at a lower rate than the star. In this section we give simple scaling arguments to demonstrate how spin evolution varies with stellar mass, before proceeding to a more detailed numerical model in Section 2.3. The derivation that follows is an oversimplification and ensures maximum spin down via magnetic braking. We include this section for the reader who is unfamiliar with the literature.

The radial extent of the accretion disk can be altered if the protostar has a magnetic field. The magnetic field is able to truncate the disk at the Alfvèn radius (denoted $R_{\rm A}$) where the magnetic pressure, $B^2/8\pi$, balances the ram pressure, ρv^2, of the infalling material. Assuming the stellar magnetic field is dipolar and the magnetic field axis is aligned with the rotation axis of the star, the z component of the field in the equatorial plane at a distance r from the star is given by

$$B_{\rm z} = B_\star \left(\frac{r}{R_\star}\right)^{-3} \tag{2.1}$$

where $B_\star$ is the magnetic field strength at the stellar surface. The location at which the magnetic pressure is able to truncate the disk, assuming spherical free-fall accretion, is

$$\frac{R_{\rm A}}{R_\star} = 2.26 \left(\frac{B_\star}{2\,{\rm kG}}\right)^{4/7} \left(\frac{\dot{M}_{\rm a}}{10^{-7} M_\odot\ {\rm yr}^{-1}}\right)^{-2/7} \left(\frac{M_\star}{M_\odot}\right)^{-1/7} \left(\frac{R_\star}{R_\odot}\right)^{5/7} \tag{2.2}$$

where $\dot{M}_{\rm a}$ is the accretion rate. In the case of disk accretion, the truncation radius is in general smaller than the value given in Equation (2.2) by a factor of order unity. For simplicity and for the purpose of this section we neglect this factor in the following discussion.

If the stellar magnetic field lines are connected to the disk the differential rotation between the two will cause the field lines to twist in the azimuthal direction inducing torques on the star. The disk co-rotates with the star at the location $R_{\rm co} \equiv (GM_\star)^{1/3}\,\Omega_\star^{-2/3}$ where $\Omega_\star$ is the angular velocity of the star. The stellar field lines that connect to the disk outside $R_{\rm co}$ spin up the disk and spin down the star. If the field lines connect to a significant portion of the disk outside of $R_{\rm co}$ the star can be spun down to a velocity well below its break up speed.

The stellar magnetic field lines threading an annulus of the accretion disk with width dr will exert a torque:

$$d\tau_{\rm m} = B_\phi B_{\rm z} r^2 dr \tag{2.3}$$

where B_ϕ is the azimuthal component of the field generated by the twisting of the field

lines relative to the star and is given by

$$B_\phi = B_z \frac{\Omega(r) - \Omega_\star}{\Omega(r)} \tag{2.4}$$

where Ω is the angular velocity of the Keplerian accretion disk. Integrating Equation (2.3) from $R_{\rm A}$ to infinity the total torque on the star due to the stellar magnetic field lines connected to the disk is

$$\tau_{\rm m} = \frac{B_\star^2 R_\star^6}{3} \left(R_{\rm A}^{-3} - 2 R_{\rm co}^{-3/2} R_{\rm A}^{-3/2} \right). \tag{2.5}$$

The accretion of disk material at $R_{\rm A}$ adds angular momentum to the star at a rate

$$\tau_{\rm a} = \dot{M}_{\rm a} \sqrt{G M_\star R_{\rm A}}. \tag{2.6}$$

Notice that Equation (2.5) contains both spin-up and spin-down torques acting on the star due to field lines connected to the disk within and outside of $R_{\rm co}$, respectively. In order for the net magnetic torque to transport angular momentum away from the star (i.e., $\tau_{\rm m} < 0$) $R_{\rm A}$ must be greater than

$$R_{\rm A,\,min} \approx 0.63 R_{\rm co}. \tag{2.7}$$

In a system where the stellar parameters ($M_\star$, $R_\star$, $B_\star$, $\dot{M}_{\rm a}$) are relatively

constant there exists an equilibrium state, called the "disk-locked" state (Koenigl, 1991; Armitage and Clarke, 1996; Matt and Pudritz, 2005), in which the stellar spin rate will adjust to its equilibrium value (i.e., when $\tau_a + \tau_m = 0$). Setting $\tau_{\rm a} = -\tau_{\rm m}$ the equilibrium spin rate, as a fraction of the break-up speed ($\Omega_{\rm bu} = \sqrt{GM_\star/R_\star^3}$), is

$$\frac{\Omega_{\star,\rm eq}}{\Omega_{\rm bu}} = \frac{1}{2}\left(\frac{R_{\rm A}}{R_\star}\right)^{-3/2} \times \left[0.014\left(\frac{M_\star}{M_\odot}\right)^{1/2}\left(\frac{\dot{M}_{\rm a}}{10^{-7}M_\odot\,{\rm yr}^{-1}}\right)\left(\frac{B_\star}{2\,{\rm kG}}\right)^{-2}\left(\frac{R_{\rm A}}{R_\star}\right)^{7/2} + 1\right]. \quad (2.8)$$

Assuming that the moment of inertia of the star stays constant, the characteristic timescale to reach equilibrium is:

$$t_{\star,\rm eq} = k^2 M_\star R_\star^2 \left(\frac{\Omega_{\star,\rm eq} - \Omega_\star}{\tau_{\rm a} + \tau_{\rm m}}\right) \quad (2.9)$$

where k is the dimensionless radius of gyration whose value depends on the stellar structure. Equation (2.7) only holds when $R_{\rm A} > R_\star$, which is true if the star has a surface magnetic field strength above a minimum value:

$$B_\star > 400\left(\frac{\dot{M}_a}{10^{-7}\ {\rm M}_\odot\ {\rm yr}^{-1}}\right)^{1/2}\left(\frac{M_\star}{M_\odot}\right)^{1/4}\left(\frac{R_\star}{R_\odot}\right)^{-5/4} G. \quad (2.10)$$

Figure 2.1 shows the equilibrium spin rate as a fraction of the star's break up speed and the corresponding time scales required for a 1 $M_\odot$ star and a 30 $M_\odot$ star to reach equilibrium starting from rotation at break up, both as a function of the

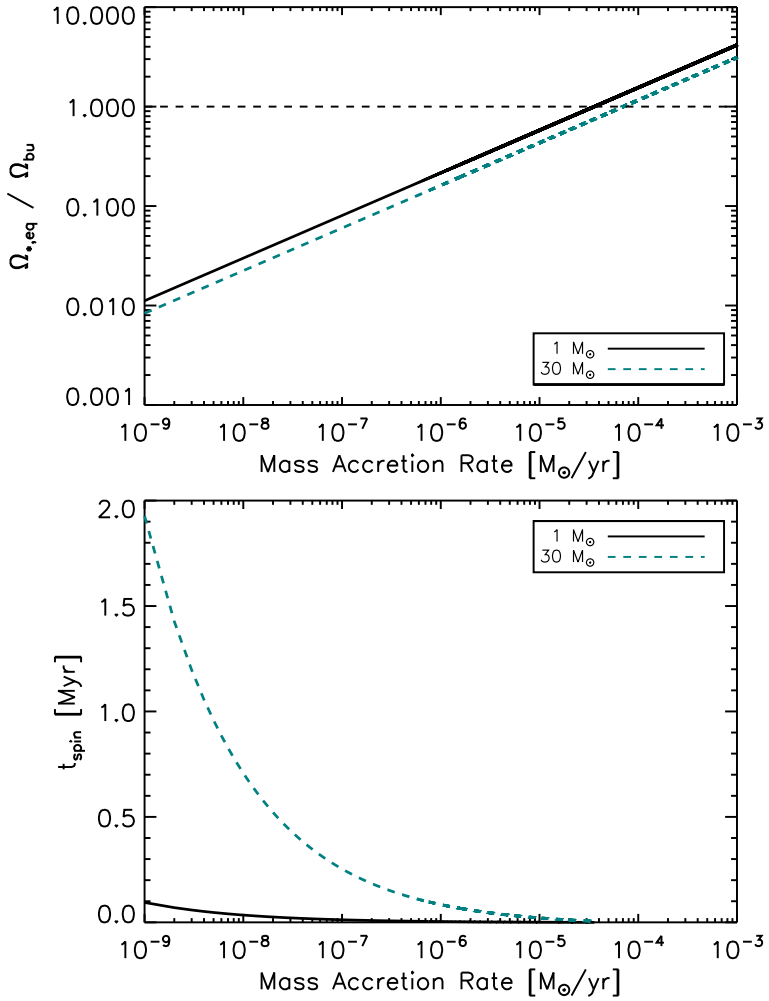

Figure 2.1 The equilibrium spin rate of a star as a fraction of its break up spin rate (top panel), and the corresponding spin down time scale (bottom panel) for 1 $M_\odot$ (black solid line) and 30 $M_\odot$ (teal dashed line) stars to reach equilibrium. Both stars have a surface magnetic field strength of 2 kG with a dipolar topology and are initially rotating at break up. The horizontal line in the top panel shows where the equilibrium spin rate is equal to the break up rate.

accretion rate. We adopt surface magnetic field strengths of 2 kG similar to observations (Wade *et al.*, 2006; Johns-Krull, 2007; Grunhut *et al.*, 2009) and assume $k = 0.27$ for a radiative star (e.g., n=3 polytrope). We adopt radii of 3 $R_\odot$ for the 1 $M_\odot$ star (the

typical radius of a T Tauri star of this mass) and 7.76 $R_\odot$ for the 30 $M_\odot$ star (ZAMS value). We consider only accretion rates where the equilibrium spin rate is below the break up rate. As the accretion rate increases, the equilibrium spin rate approaches the break up rate and the equilibrium timescale quickly decreases. We find that magnetic torques produce equilibrium spin rates below break up only for accretion rates below $\dot{M}_a \lesssim 5 \times 10^{-5}$ $M_\odot$ yr^{-1}, regardless of the stellar mass. In this regard, low- and high-mass stars are similar. The typical mass accretion rates during the main accretion phase, where the majority of the stellar mass is accreted, for low- and high-mass star formation are 5×10^{-6} $M_\odot$ yr^{-1} (Shu, 1977) and 5×10^{-4} $M_\odot$ yr^{-1} (McKee and Tan, 2003), respectively. For our adopted field strength, R_A for the 30 $M_\odot$ star is within the stellar surface at this accretion rate. In contrast, the disk is truncated very close to the stellar surface for the 1 $M_\odot$ star, leading to an equilibrium spin rate close to break up. We conclude that disk truncation does not occur for massive stars and is unimportant for low-mass stars during the main accretion phase. At the lower accretion rates that are likely to occur after the main accretion phase ends, we find that low- and high-mass stars differ in that the latter have much longer equilibration timescales than the former due to their larger inertia. For example, the equilibration timescale for the 30 $M_\odot$ star for very low accretion rates is a significant fraction of its stellar lifetime, $t_{ms} = 5.9$ Myr (Parravano *et al.*, 2003). Furthermore, at high accretion rates this timescale is comparable to the star's formation timescale (McKee and Tan, 2003) suggesting that massive stars are unable to reach spin equilibrium. To further explore the consequences of this analysis we follow the angular momentum evolution of massive protostars to

determine the physical conditions that are required to spin them down by magnetic torques.

2.3 Stellar Angular Momentum Evolution Model

The goal of this work is to determine if the initial rotation rates of massive stars can be regulated by magnetic torques due to the interaction of the stellar magnetic field and surrounding accretion disk during formation. To this end, we construct a simple model to track the mass, radius, and angular momentum content of accreting protostars subjected to gravitational and magnetic torques. We describe the elements of this model in the following subsections.

2.3.1 Protostellar Model

We monitor the spin and angular momentum evolution by following the protostellar radius and internal structure evolution during its formation with the use of the one-zone model of McKee and Tan (2003) (hereafter MT03) as updated by Offner *et al.* (2009). By treating the protostar as an accreting polytrope and requiring conservation of energy, the evolution of the protostellar radius is given by:

$$\frac{dR_\star}{dt} = \frac{2\dot{M}_{\rm a} R_\star}{M_\star}\left(1 - \frac{1-f_{\rm k}}{a_{\rm g}\beta_{\rm P}} + \frac{1}{2}\frac{d\log\beta_{\rm P}}{d\log M_\star}\right) - 2\left(\frac{R_\star^2}{GM_\star^2}\right)(L_{\rm int} + L_{\rm I} - L_{\rm D}) \qquad (2.11)$$

where $\dot{M}_{\rm a}$ is the accretion rate onto the protostar, $f_{\rm k}$ is the fraction of kinetic energy of the infalling material that is radiated away, $\beta_{\rm P}$ is the ratio of radiation pressure to

the total pressure, $a_{\rm g} = 3/(5-n)$ is the coefficient describing the binding energy of a polytrope, $L_{\rm int}$ is the internal stellar luminosity, $L_{\rm I}$ is the rate of energy required to dissociate and ionize the infalling material, and $L_{\rm D}$ is the rate at which energy is supplied from burning deuterium (Nakano *et al.*, 2000). The model also includes a few discontinuous changes in polytropic index and radius to represent events such as the onset and cessation of core deuterium burning and the formation of a radiative core. We use the model parameters recommended by Offner *et al.* (2009), which are based on the detailed stellar evolution calculations by Hosokawa and Omukai (2009). We refer the reader to MT03 and Appendix B of Offner *et al.* (2009) for a detailed description of the model and protostellar evolutionary states.

We treat the protostar as a solid body to follow its angular momentum content ($J_\star = I_\star \Omega_\star$). We evolve the stellar angular momentum content by computing the net torque on the star due to the coupling of the stellar magnetic field with the surrounding accretion disk described in Section 2.3.3.

2.3.2 Accretion History

The accretion history of our protostars is divided into two distinct accretion phases. The first is the main accretion phase given by the turbulent core model from MT03, which describes an accelerating accretion rate, where the majority of the stellar mass is accreted. This model assumes that the star-forming core is marginally unstable, massive, and supported by turbulent motions. Next, we follow the disk clearing phase in which the accretion disk is no longer being fed by the core envelope. These accretion

phases are described in Section 2.3.2.1 and Section 2.3.2.2.

2.3.2.1 Primary Accretion Phase: Core Collapse

We model the mass accretion using the two-component core model of MT03, which assumes the central region of a molecular cloud core is dominated by thermal motions and the core envelope is dominated by non-thermal motions (Myers and Fuller, 1992). This leads to a density distribution that is equivalent to the sum of a singular polytropic sphere and a singular isothermal sphere:

$$\rho = \rho_{\rm s}\left(\frac{R_{\rm core}}{r}\right)^{k_\rho} + \frac{c_{\rm th}^2}{2\pi G r^2} \tag{2.12}$$

where $\rho_{\rm s}$ is the density at the surface of the core, $R_{\rm core}$ is the core radius, and $c_{\rm th}$ is the thermal sound speed within the core and is assumed to be constant. We adopt the fiducial value of $k_\rho = 1.5$ from MT03 in agreement with observations describing the turbulence-supported density profile of massive star forming cores (Caselli and Myers, 1995; van der Tak *et al.*, 2000; Beuther *et al.*, 2002).

The accretion rate onto the disk, which is supplied by the background core, is:

$$\dot{M}_{\rm a} \simeq \frac{\phi_\star M_{\star,{\rm f}}}{t_{\star,{\rm ff}}}\left[\left(\frac{M_\star}{M_{\star,{\rm f}}}\right)^{2{\rm j}} + \left(\frac{\phi_{\star,{\rm th}}}{\phi_{\star,{\rm nth}}}\right)^2\left(\frac{\epsilon_{\rm core}M_{\rm th}}{M_{\star,{\rm f}}}\right)^{2{\rm j}}\right] \tag{2.13}$$

where $t_{\star,{\rm ff}} = \left(3\pi/32G\rho\right)^{1/2}$ is the free fall time evaluated at $R_{\rm core}$, $M_\star$ is the current

stellar mass, $M_{\star,\mathrm{f}}$ is the final stellar mass, and

$$j = \frac{3\big(2 - k_\rho\big)}{2\big(3 - k_\rho\big)}. \tag{2.14}$$

The dimensionless constants ϕ, $\phi_{\star,\mathrm{th}}$, and $\phi_{\star,\mathrm{nth}}$ are of order unity and depend on k_ρ and the magnetic field strength. The efficiency factor, ϵ_{core}, describes how much of the core mass will end up in the star rather than being ejected by protostellar outflows and we adopt the value of 0.5 from MT03, which is typical of both low-mass (Matzner and McKee, 2000) and high-mass star formation (Cunningham *et al.*, 2011). The parameter M_{th} describes the mass below which the thermal density distribution dominates. For a core with surface density $\Sigma = M_{\star,\mathrm{f}}\epsilon_{\mathrm{core}}^{-1}/\pi R_{\mathrm{core}}^2$, M_{th} is defined as:

$$M_{\mathrm{th}} = 1.23 \times 10^{-3} \left(\frac{T}{20\ K}\right)^3 \left(\frac{30\epsilon_{\mathrm{core}} M_\odot}{M_{\star,f}}\right)^{1/2} \Sigma_0^{3/2} M_\odot \tag{2.15}$$

where $\Sigma_0 = \Sigma/\big(1\ \mathrm{g\ cm^{-2}}\big)$. We further assume that the accretion rate onto the disk is the same as that onto the star and use this value for our protostellar accretion rate.

2.3.2.2 Secondary Accretion Phase: Disk Clearing

Late in the formation the core envelope will exhaust its reservoir of mass and no longer feed the accretion disk. We assume that we are left with a thin, Keplerian accretion disk that continues to transfer mass and angular momentum to the central protostar. For simplicity and because observations of disks located around massive stars

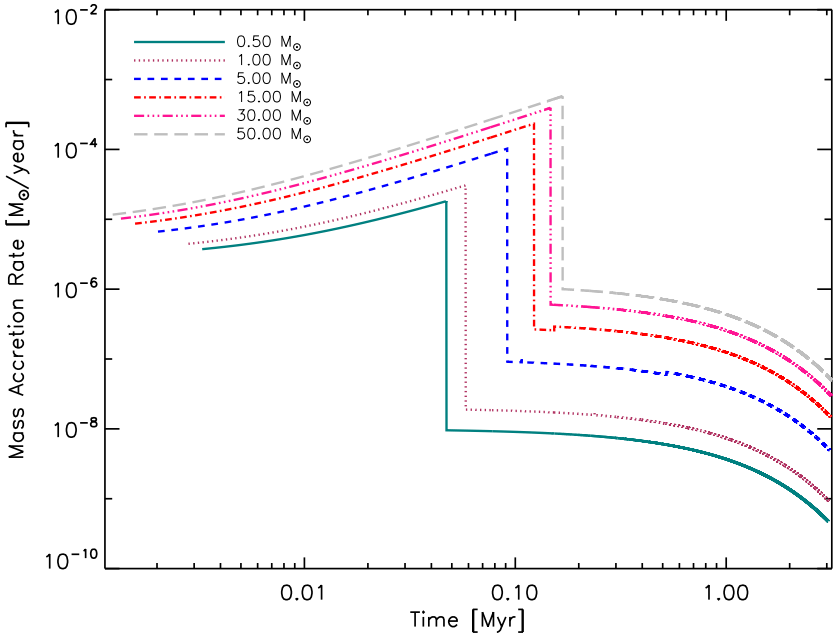

Figure 2.2 Accretion history of protostars with final masses of 0.5 - 50 $M_\odot$, following Equations (2.13) and (2.16), for our fiducial parameters given in Table 2.1 in Section 2.4.

are rare, we assume that this results in a decreasing accretion rate as a function of time which we model as a decaying exponential (Collier Cameron and Campbell, 1993; Yi, 1994, 1995; Matt *et al.*, 2010):

$$\dot{M}_{\rm a} = \frac{M_{\rm D}}{t_{\rm a}} e^{-t/t_{\rm a}} \tag{2.16}$$

where $M_{\rm D}$ is the remaining mass in the accretion disk (i.e., the total amount of mass that would accrete from $t = 0 \rightarrow \infty$) and $t_{\rm a}$ is the decay timescale. Since $M_{\rm D}$ and $t_{\rm a}$ are highly unconstrained, we experiment with different values in Section 2.4. Figure 2.2 shows the accretion history, including both the core collapse and disk clearing accretion phases, for stars with final masses of 0.5-50 $M_\odot$.

2.3.3 Star-Disk Interaction Model

In Section 2.2 we showed how the presence of a stellar magnetic field can remove angular momentum from the star as it accretes matter from an accretion disk. This description assumed that the stellar field lines were connected at all radii of the disk larger than $R_{\rm A}$. However, the differential rotation between the star and disk will twist the connected field lines. This twisting will cause the magnetic field to undergo a rapid inflation leading to an opening of the field lines, effectively decreasing the size of the disk region that is connected to the stellar magnetic field (Lovelace *et al.*, 1995; Uzdensky *et al.*, 2002; Matt and Pudritz, 2005). We now include this effect when calculating the net magnetic torque on the star with the use of the model developed by MP05, which is an extension to the disk-locking model first developed by Ghosh and Lamb (1978) for accreting neutron stars and extended by Koenigl (1991) to describe the star-disk coupling for magnetized T Tauri stars.

2.3.3.1 Magnetic Coupling to the Disk and the Connection State

The effect of the opening of the magnetic field lines depends on the strength of the magnetic coupling to the disk and how strongly the field lines can be twisted until they are severed. The variable $\gamma(r) = B_{\phi}/B_{\rm z}$ describes the twisting of the magnetic field between the star and disk. This twisting occurs rapidly so a steady state configuration depends on how well the field couples to the disk (i.e., the balance between the differential rotation and the tendency for the magnetic field to untwist). Uzdensky *et al.* (2002) describe this coupling by a dimensionless magnetic diffusivity parameter,

$$\beta \equiv \frac{\eta_{\rm t}}{H v_{\rm k}} \tag{2.17}$$

where η_t is the effective magnetic diffusivity and is of the order of magnitude of the disk's effective viscosity (Lovelace *et al.*, 1995), H is the scale height of the disk, and v_k is the Keplerian rotation velocity. MP05 assume β is constant throughout the disk. The field is strongly coupled to the disk for values of $\beta < 1$ and weakly coupled for $\beta > 1$. Uzdensky *et al.* (2002) find that when γ exceeds a value of order unity (defined by the critical twist parameter γ_c) the magnetic field will be severed because the magnetic pressure force associated with B_ϕ will push outward and cause the dipole field loops to open. The magnetic field is connected to the disk only in the location where $|\gamma| \leq \gamma_c$. MP05 use the values $\beta = 0.01$ and $\gamma_c = 1$ in their models, and we adopt the same fiducial values in this work. They suggest that $\beta = 0.01$ is the most probable value for a T Tauri accretion disk with the use of an α model prescription; however it is uncertain that disks surrounding massive stars will have this same value. For example, massive stars emit more ionizing radiation which will yield a higher ionization fraction on the disk surface, causing β to decrease, but these disks are also more massive than those surrounding low-mass PMS stars and are therefore thicker, causing β to increase. To account for our uncertainty in this parameter we experiment with different values in the following section.

MP05 show that the magnetic connection between the star and disk changes

at a threshold value of the stellar spin rate. Specifically, the stellar magnetic field will only be connected to a small region of the disk within $R_{\rm co}$ if the stellar rotation rate as a fraction of break up,

$$f = \frac{\Omega_\star}{\Omega_{\rm bu}} = \Omega_\star \sqrt{\frac{R_\star^3}{GM_\star}}, \tag{2.18}$$

falls below:

$$f < \big(1 - \beta\gamma_c\big)\big(\gamma_{\rm c}\psi\big), \tag{2.19}$$

where

$$\psi \equiv \frac{2B_\star^2 R_\star^{5/2}}{\dot{M}_{\rm a}\sqrt{GM_\star}} \tag{2.20}$$

is a dimensionless parameter that relates the strength of the magnetic field to the accretion rate. This connection state, which MP05 denote as state 1, will result in no spin-down torques transferred to the star. If f exceeds this value then the system is in state 2 which is characterized by a magnetic connection on either side of $R_{\rm co}$ resulting in both spin-up and spin-down torques acting on the star.

2.3.3.2 Magnetic and Accretion Torques

The twisting of the magnetic field by the differential rotation between the star and disk causes torques to be conveyed between the two. The twisting of the magnetic field within $R_{\rm co}$ leads to spin-up torques whereas the field lines connected to the disk outside of $R_{\rm co}$ act to spin down the star. If the magnetic field is strong enough then the disk will be disrupted by the stellar magnetosphere where the magnetic stress is able to maintain the accretion rate within the disk. At this location, denoted by $R_{\rm t}$, the magnetic stress is large enough to remove the excess angular momentum and funnel the disk material along the magnetic field lines. This material and its angular momentum is transferred to the star. If $R_{\rm t} > R_{\rm co}$ the magnetic stress hinders the accretion rate.

The location of $R_{\rm t}$ depends on the connection state of the system. In state 1 the truncation radius is

$$R_{\rm t} = (\gamma_{\rm c}\psi)^{2/7} R_{\star}. \tag{2.21}$$

In state 2 the truncation radius is given by

$$\left(\frac{R_{\rm t}}{R_{\rm co}}\right)^{-7/2} \left[1 - \left(\frac{R_{\rm t}}{R_{\rm co}}\right)^{3/2}\right] = \frac{\beta}{\psi f^{7/3}}. \tag{2.22}$$

We assume the accreted disk material is quickly integrated into the structure of the star and adds angular momentum to the star at a rate given by Equation (2.6) where $R_{\rm A}$ is

replaced by $R_{\rm t}$. This material acts to spin up the star.

The magnetic connection over a range in radii in the disk can extract angular momentum from the star and transfer it to the disk. If the system is in state 2 then the magnetic field is connected to the disk from $R_{\rm t}$ to $R_{\rm out} = (1+\beta\gamma_{\rm c})^{2/3} R_{\rm co}$ which yields a net magnetic torque on the star:

$$\tau_{\rm m} = \frac{B_\star^2 R_\star^6}{3\beta R_{\rm co}^3}\left[2\left(1+\beta\gamma_{\rm c}\right)^{-1} - \left(1+\beta\gamma_{\rm c}\right)^{-2} - 2\left(R_{\rm co}/R_{\rm t}\right)^{3/2} + \left(R_{\rm co}/R_{\rm t}\right)^3\right]. \quad (2.23)$$

If the system is in state 1 then the magnetic field is connected to only a small portion of the disk which leads to a negligible torque on the star, so we set $\tau_{\rm m} = 0$ following Matt *et al.* (2010). Note that Equation (2.23) reduces to Equation (2.5) for the limiting case of no field opening ($\gamma_{\rm c} \to \infty$), marginal coupling ($\beta = 1$), and a disk that is truncated at the Alfvén radius ($R_{\rm A}$) and extends to infinity.

2.4 Results

The initial star-forming core properties are determined by the core mass ($M_{\rm core}$), core density profile (k_ρ), and core surface density (Σ). These parameters control the accretion rate for the primary accretion phase as described in Section 2.3.2.1. We initially create a "pre-collapse" object with a mass less than 0.01 $M_\odot$ which grows in mass with the accretion rate given by Equation (2.13). When the object reaches a mass of 0.01 $M_\odot$ we initialize our protostellar and angular momentum evolution model and assume the protostar is initially rotating at 1% of its break up speed. When the protostar is

initialized, it is immediately spun up since the accretion rate is large, so our chosen value for the initial rotation speed is unimportant. We solve Equation (2.11) with the fourth-order Runge-Kutta scheme of Press *et al.* (2002) and update the angular momentum of the star by computing the net torque on the star arising from the accretion and magnetic torques described in Section 2.3.3.2. We use this result to update $\Omega_\star$. We cap the stellar rotation rate at 50% of breakup, a limit imposed by gravitational torques (Lin *et al.*, 2011). The fiducial values used for our model parameters are given in Table 2.1.

Parameter	Fiducial Value
Σ	1 g cm^{-2}
$M_{\rm D}$	0.02 $M_{\star,{\rm f}}$
$t_{\rm a}$	10^6 yr
$B_\star$	2 kG
β	0.01
$\gamma_{\rm c}$	1

Table 2.1 Table of fiducial values used for our model parameters.

2.4.1 Effect of the Star-Disk Magnetic Interaction

Figure 2.3 shows the radial and rotational evolution for stars ranging in final stellar mass from 0.5 - 50 $M_\odot$. These models were simulated with the fiducial parameters given in Table 2.1. The disk-clearing accretion phase is assumed to last 3 Myr, although as discussed in Section 2.1, this assumption is almost certainly not correct for high mass stars. As we show below, using a shorter disk clearing timescale for the massive stars would only strengthen our results. We choose to run the disk clearing phase for 3 decay

time scales because accretion disks around low-mass stars survive for several million years (Herbst *et al.*, 2007), with an accretion rate that likely decreases with time. The swelling in radius by a factor of three, shown in the upper plots of Figure 2.3, is a result of the star transitioning from a convective to radiative core (Hosokawa and Omukai, 2009), which redistributes entropy within the star. For the stars presented in Figure 2.3 this occurs in the primary accretion phase for the most massive stars ($M_{\star,\mathrm{f}} \geq 15$ M$_\odot$) and during the disk clearing accretion phase for the 0.5, 1, and 5 M$_\odot$ stars. If the jump in radius occurs during the main accretion phase, it causes the star to immediately slow down, but the star is almost instantly spun back up because of the high accretion rate. In the case of the 5 M$_\odot$ star, this jump in radius also significantly decreases the spin rate of the star, but since it occurs when the accretion rate is much lower the star only gradually spins up as it contracts and accretes material. In contrast, for the 0.5 and 1 M$_\odot$ stars magnetic torques are able to continue to spin down the star after the jump in radius occurs. We note that Matt *et al.* (2010) produced Sun-like stars with faster rotation rates ($\sim 20 - 40\%$ of break up) performing a similar analysis. We report a lower rotation rate for our 1 M$_\odot$ protostar because it has a different radial history than the stars produced by Matt *et al.* (2010). Our 1 M$_\odot$ protostar contracts more slowly than the 1 M$_\odot$ protostar model used by Matt *et al.* (2010). After 3 Myr, our model gives a radius of 3.8 R$_\odot$ as compared to Matt *et al.* (2010)'s ~ 3 R$_\odot$. At times <1 Myr, the model radii can differ by factors of ∼2. The larger radii in our model produces more spin-down. The differences in predicted radii likely arise because our model accounts for the extra entropy provided both by deuterium burning and by ongoing accretion,

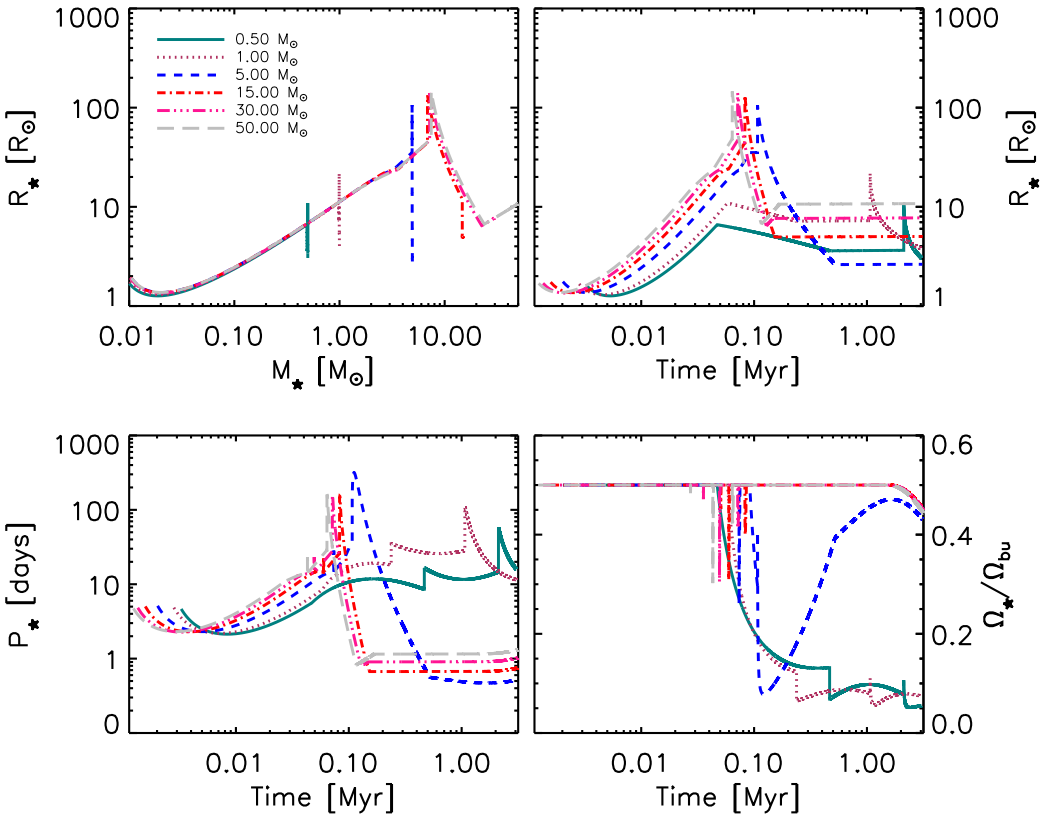

Figure 2.3 The top left panel shows the stellar radius as a function of stellar mass for stars with masses 0.5 - 50 $M_{\odot}$. The other panels show the stellar radius (top right), stellar period (bottom left), and stellar spin rate as a fraction of break up (bottom right) as a function of time for stars with masses 0.5 - 50 $M_{\odot}$. Figure 2.2 shows the accretion histories.

while Matt *et al.* (2010)'s does not. We do warn, however, that there are significant uncertainties in how much of the accretion entropy is actually absorbed by the star, and differing assumptions on this point can produce significant differences in radial evolution (Hosokawa *et al.*, 2011).

We find that the torques that arise from the star-disk magnetic interaction are unable to spin down both low-mass and massive protostars during the main accretion phase, but are important during the disk clearing phase, especially for low-mass stars.

Low-mass stars begin to spin down the instant the disk clearing accretion phase begins whereas it takes approximately 2 Myr to begin to spin down massive stars for our chosen fiducial values. This suggests that massive stars are difficult to spin down due to their larger inertia and because their magnetic fields are weaker relative to their stellar binding energy as compared to low mass stars.

Figure 2.4 shows snapshots of the stellar radius, disk truncation radius, stellar period, and stellar rotation rate as a fraction of break up as a function of stellar mass taken at different times during the disk clearing phase. First consider the upper left panel, showing radius versus mass at different times. The $R-M$ relation toward which the models converge at high mass is the ZAMS; by 3 Myr all stars above ~ 2 $M_\odot$ have reached it. At smaller masses, the maximum radius occurs at a mass that corresponds to stars that have just made the convective-radiative core transition at a given time. This value shifts to progressively smaller masses at later times.

An interesting feature of Figure 2.4 is that the stellar rotation rates as a fraction of break up show a bimodal distribution: stars with $M_{\star,f} \lesssim 1$ $M_\odot$ rotate at $\sim$10% of their break up speed whereas stars with $M_{\star,f} \gtrsim 6$ $M_\odot$ are rapid rotators. In between these plateaus (i.e., the "transition region") the rotation rates as a fraction of break up increases with stellar mass. Furthermore, as time increases we find that the ratio of rotation speed to break up speed decreases on both plateaus, but that this decrease is more noticeable for the fast rotator plateau. This is because the stars located on the fast rotator plateau have already reached the ZAMS and are no longer contracting whereas those located on the slow rotator plateau are easy to spin down because of

their low inertia, even though they are still contracting towards the ZAMS. In contrast, we find that the rotation rates as a fraction of break up of the stars in the transition region increases with time. This suggests that the magnetic torques conveyed by the star-disk interaction are unable to counteract the increase in the stellar spin rate due to contraction for stars in the transition region. However, once these stars have reached the ZAMS magnetic torques do become important. The points located in the bottom right panel of Figure 2.4 represents the minimum mass of stars rotating at $\gtrsim$20% of their break up speed. We use this as an indicator of the transition between slow and fast rotators, which we discuss further in Section 2.4.3.

2.4.2 Sensitivity to Model Parameters

In the previous subsection we found that massive stars are much more difficult to spin down than low-mass stars. This causes low-mass stars to become slow rotators and massive stars to be rapid rotators, yielding a bimodal distribution in stellar rotation speeds as a fraction of the break up speed. To explore if this qualitative result is sensitive to our chosen model parameters, we vary certain parameters while holding the other parameters fixed. In the figures that follow we see that by varying certain parameters we do not lose this feature, but only alter it.

2.4.2.1 Varying Σ

Figure 2.5 shows the final stellar radius, disk truncation radius, stellar period, and rotation rate as a fraction of break up as a function of final stellar mass for different

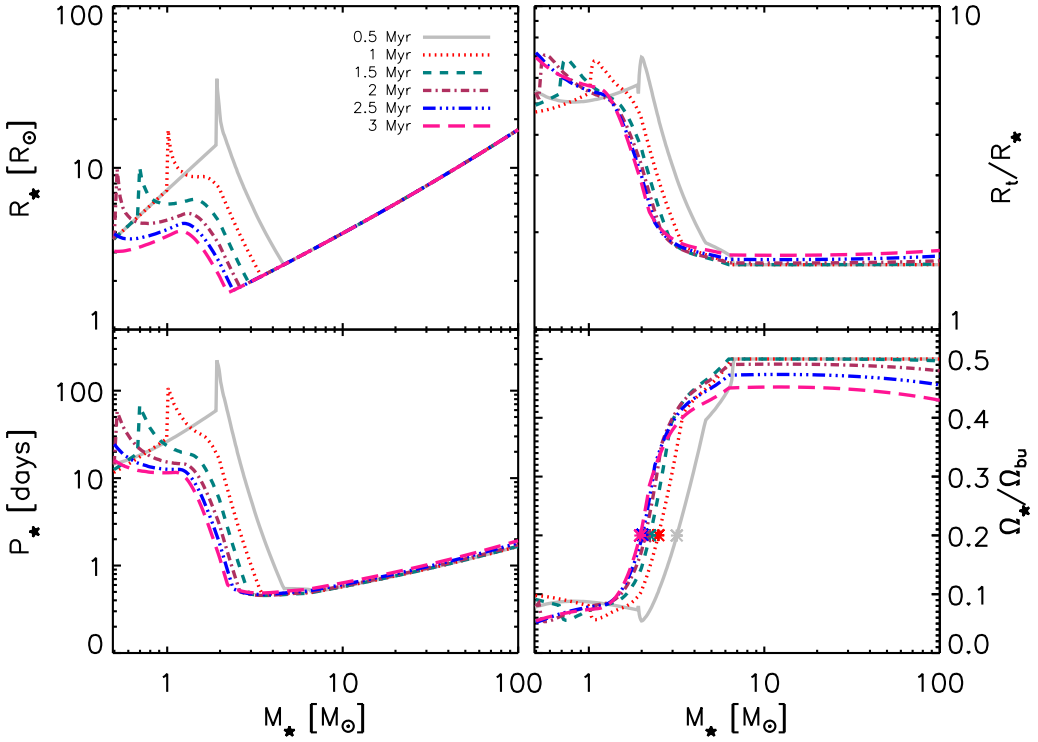

Figure 2.4 Snapshots of the stellar radius (upper left), disk truncation radius (upper right), stellar period (lower left), and rotation rate as a fraction of break up (lower right) as a function of stellar mass taken at different times during the disk clearing phase for our fiducial case. The times in the legend represent the time that has elapsed since the disk clearing phase began. The points located in the bottom right panel represents the minimum mass of stars rotating at $\gtrsim$ 20% of its break up speed. We use this as an indicator of the transition between slow and fast rotators.

values of the initial core surface density, Σ. The accretion rate during the main accretion phase increases for higher Σ, so varying this value affects the accretion history only during this phase. We find that this parameter has little to no effect on the final spin rate of the stars because the magnetic torques are unimportant during this accretion phase. The very minor differences that do appear arise because the value of Σ affects the time at which a star of a given final mass reaches the swelling phase: the swelling phase

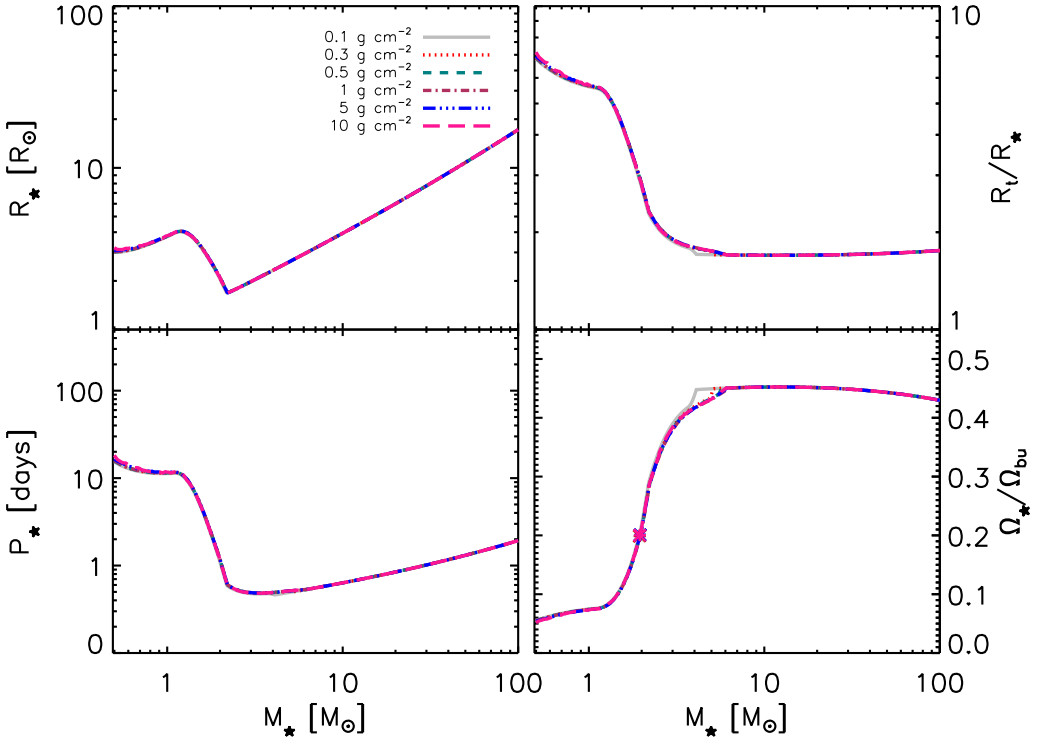

Figure 2.5 Same as Figure 2.4 but all quantities are shown at a time of 3 Myr, and we vary Σ as indicated in the legend.

of the star occurs earlier in time at lower Σ. For each value of Σ used in our models there is a slight kink in between $M_{\star,f} \approx 3-6 M_\odot$ and the location of this kink decreases in mass for smaller values of Σ. Stars to the right of this kink experience the jump in radius, discussed in Section 2.4.1, before the end of the main accretion phase whereas those to the left experience the swelling during the disk-clearing accretion phase. However, the net effect on the stellar rotation rate is obviously minor.

2.4.2.2 Varying $M_{\rm D}$

Figure 2.6 shows the final stellar radius, disk truncation radius, stellar period, and rotation rate as a fraction of break up as a function of final stellar mass for different values of the initial disk mass, $M_{\rm D}$, used for the disk clearing accretion phase. Increasing $M_{\rm D}$ increases the accretion rate during the disk clearing phase, thus increasing the accretion torque. A larger accretion rate also causes the disk to be truncated closer to the star, effectively reducing the net spin down magnetic torque. This is because the stellar magnetic field lines will connect to a greater portion of the disk within $R_{\rm co}$ yielding greater spin up magnetic torques on the star while the magnetic spin down torques remain unchanged. We find that altering $M_{\rm D}$ changes the location and shape of the transition between the slow and fast rotation plateaus, but the qualitative result that rotation rates are bimodal, with slow rotation at low mass and rapid rotation at high mass, remains unchanged. Also note that the models converge in the limit $M_{\rm D} \rightarrow 0$.

2.4.2.3 Varying $t_{\rm a}$

Figure 2.7 shows the final stellar radius, disk truncation radius, stellar period, and rotation rate as a fraction of break up as a function of final stellar mass for different values of the disk decay time scale, $t_{\rm a}$, used for Equation 2.16. Smaller values of $t_{\rm a}$, as compared to our fiducial value of 1 Myr, correspond to a higher initial accretion rate that declines more rapidly for the disk clearing accretion phase. This yields lower final spin rates at the end of 3 Myr. However, the overall shape of the distribution of final spin rates as a function of stellar mass does not change.

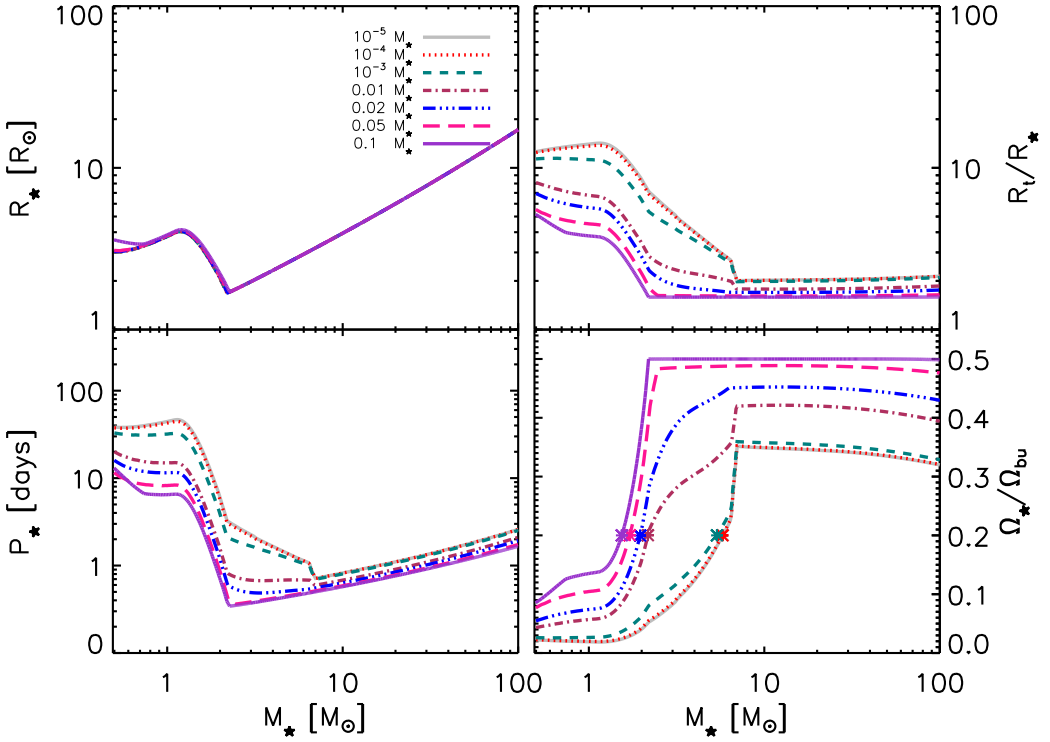

Figure 2.6 Same as Figure 2.4 but all quantities are shown at a time of 3 Myr, and we vary $M_{\rm D}$ as indicated in the legend.

2.4.2.4 Varying $B_\star$

Figure 2.8 shows the final stellar radius, disk truncation radius, stellar period, and rotation rate as a fraction of break up as a function of final stellar mass for different values of the stellar magnetic field strength. Clearly, a larger magnetic field strength provides a greater spin down torque on the star, yielding smaller final spin rates as a function of mass. As can be seen in this figure, stars above $\rm M_{\star,f} \gtrsim 2\,M_\odot$ require surface fields greater than 1 kG to experience any significant spin down torques and do not become slow rotators, $\Omega_\star/\Omega_{\rm bu} \lesssim 0.1$, unless the field reaches ∼10 kG. Magnetic

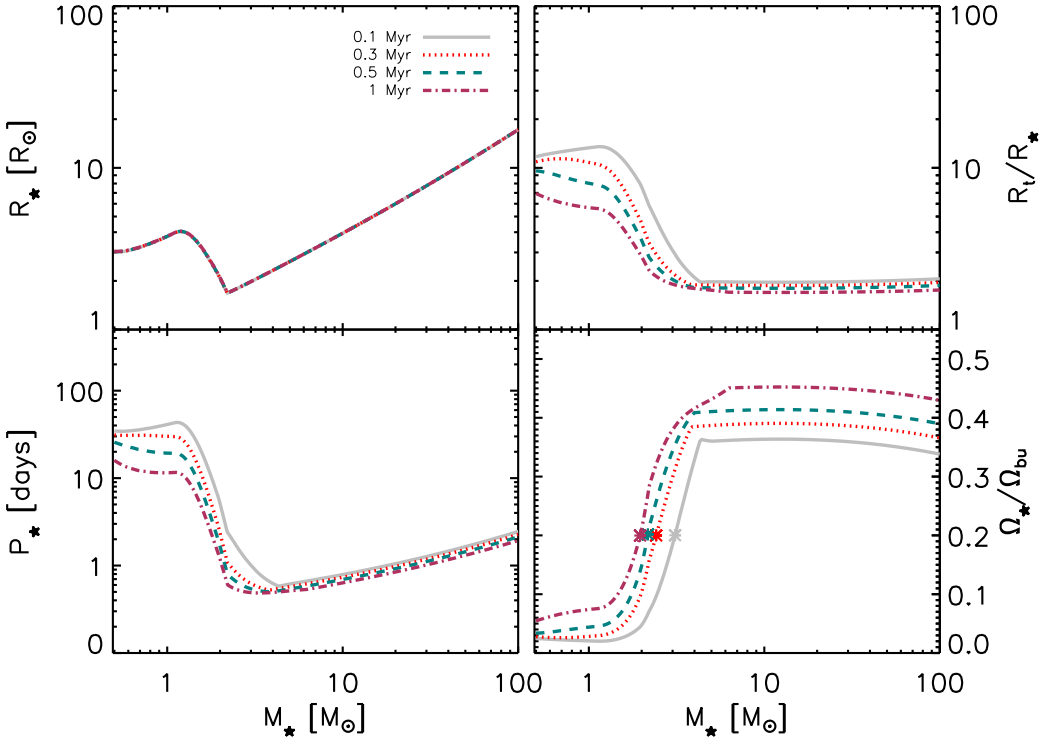

Figure 2.7 Same as Figure 2.4 but all quantities are shown at a time of 3 Myr, and we vary $t_{\rm a}$ as indicated in the legend.

fields this large have only been detected in the chemically peculiar (e.g., helium strong) Ap/Bp stars (Borra and Landstreet, 1979; Oksala *et al.*, 2010). Generally, as the field strength increases the final spin rates decrease, but the qualitative division between slow and fast rotators remains. We also find that this same trend in rotation rates as a fraction of break up occurs as the field lines become weakly coupled to the accretion disk, while holding the magnetic field strength fixed, as discussed next.

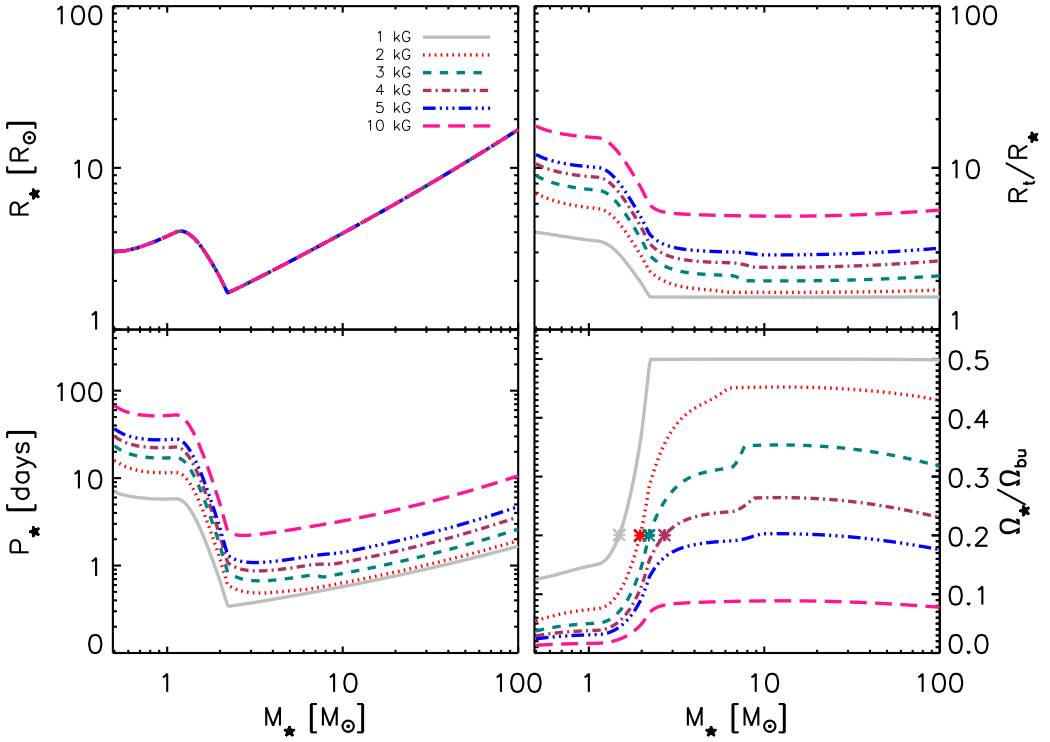

Figure 2.8 Same as Figure 2.4 but all quantities are shown at a time of 3 Myr, and we vary $B_\star$ as indicated in the legend.

2.4.2.5 Varying β and γ_c

Figure 2.9 shows the final stellar radius, disk truncation radius, stellar period, and rotation rate as a fraction of break up as a function of final stellar mass for different values of β and γ_c. These parameters describe the coupling and connection of the stellar magnetic field lines to the accretion disk (i.e., the location where the field lines open and disconnect from the disk). A larger β for a given γ_c increases the extent of the connected disk region. This is because the coupling of the stellar field lines to the disk acts to resist the twisting of these lines due to the differential rotation between the star

and disk. Thus, weaker field coupling will lead to a greater spin-down torque acting on the star leading to lower rotation rates as depicted in Figure 2.9. Likewise, a greater γ_c for a given β will allow the field lines to experience a greater twist before opening, also increasing the size of the connected disk region. For the case where $\gamma_c \to \infty$ (i.e., field lines are allowed to twist to large values without opening), the field lines will connect to the whole disk outside R_t. This will lead to a greater spin down torque. The case where $\beta = 1$ and $\gamma_c = \infty$ reduces to the case described in Section 2.2. Figure 2.9 shows that as β increases for $\gamma_c = 1$, all stars have lower rotation rates. However the two plateaus still remain.

2.4.3 The Characteristic Mass for the Slow to Fast Rotator Transition

In this work we have found a robust division between slow and fast rotators. Specifically, we find that low-mass stars (e.g., stars with $M_\star \lesssim 1$ M$_\odot$) are slow rotators, easily spun down via magnetic torques that arise from the star-disk interaction, and rotate at $\sim 10\%$ of their break up speed, whereas massive stars (e.g., $M_\star \gtrsim 6$ M$_\odot$) are preferentially fast rotators. This is because massive stars are difficult to spin down due to their larger inertia and because their magnetic fields are weaker relative to their stellar binding energy as compared to low mass stars. Furthermore, this division is also dependent on the R-M relationship. The stars located on the fast rotator plateau have reached the ZAMS by the end of the main accretion phase or early on during the disk clearing phase; whereas, the stars located on the slow rotator plateau are shrinking towards the ZAMS for the entirety of the disk clearing phase. Likewise, the stars located

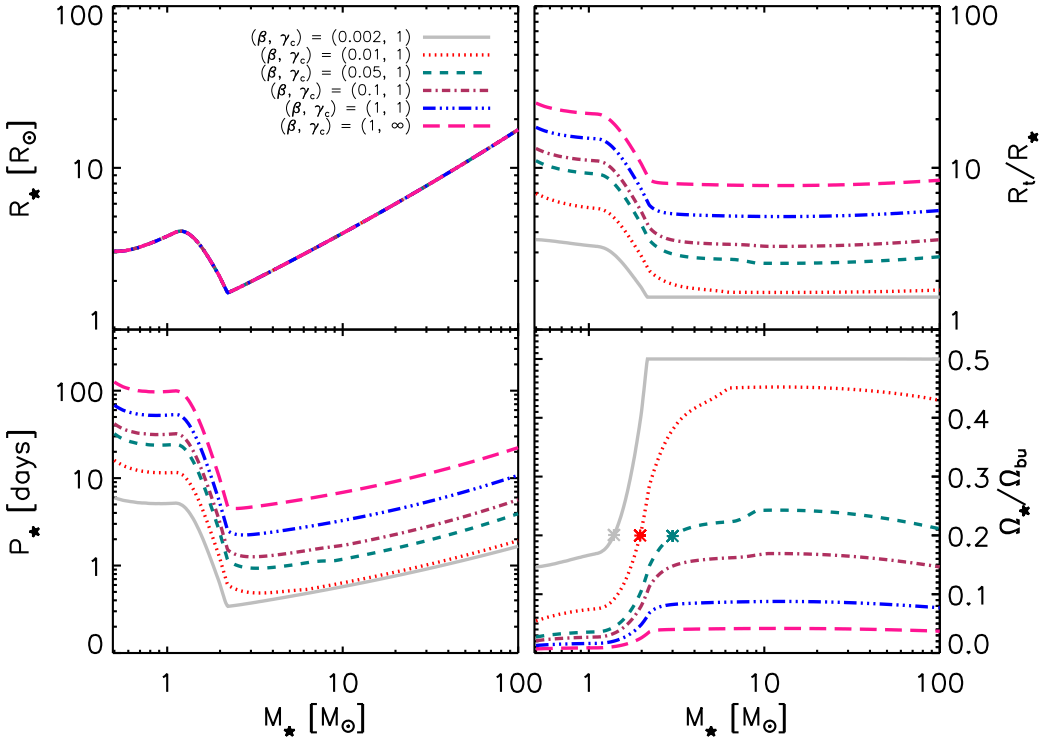

Figure 2.9 Same as Figure 2.4 but all quantities are shown at a time of 3 Myr, and we vary β and γ_c as indicated in the legend.

in the transition region are contracting towards the ZAMS for a significant portion of the disk clearing phase but are contracting much faster than the low-mass slow rotators, leading to the sudden rise in rotation rates as a fraction of break up.

To further illustrate the division between slow and fast rotators for each of our model parameters, in Figure 2.10 we plot the minimum stellar mass at which the star ends accretion rotating at 20% of its break up speed, which we call M_{20}. Each panel shows how M_{20} depends on the individual parameters in our model (while setting the other parameters to their fiducial values). The top panels show that M_{20} decreases

by only a small amount as the disk lifetime (i.e., the amount of time the disk survives and supplies mass to the star during the disk clearing phase) or disk decay time scale increases. We also see that this characteristic mass, as a function of the initial core surface density, is relatively constant as indicated by the nearly horizontal line on the middle right panel of Figure 2.10. In contrast, M_{20} spans a larger mass range as we vary the initial disk mass used for the secondary accretion phase as shown in the middle left panel. This is because the accretion rate, and therefore the accretion torque, is proportional to the disk mass used in our model. We find that as $M_{\rm D} \rightarrow 0$ the values of M_{20} become constant but we notice that M_{20} decreases most as the disk mass increases from $\sim 10^{-3} - 10^{-2}$ $M_\star$. The division between slow and fast rotators slowly decreases in stellar mass for initial disk masses above $\sim 10^{-2}$ $M_\star$. Even though varying this parameter leads to larger variations in M_{20} as compared to the top panels, it does not change the qualitative division between slow and fast rotators.

The bottom panels of Figure 2.10 show how the slow-fast rotator division is affected by the stellar magnetic field strength and the coupling of the stellar magnetic field lines to the disk, which are the parameters that are responsible for the removal of angular momentum from the star. The black solid lines in these panels show that the division between the slow and fast rotators (i.e., M_{20}) diverges for large magnetic field strengths ($B_\star \gtrsim 4.5$ kG) or weak field coupling ($\beta \gtrsim 0.05$) for a disk clearing accretion phase that lasts for 3 Myr. This is because no stars will be rotating at or above 20% of their break up speed at the end of 3 Myr for such high values of $B_\star$ or β. For comparison, and also because we expect disks to have shorter lifetimes around massive

stars, we also include the values of M_{20} at 0.5 Myr after the disk clearing phase began (teal dotted lines). We find that M_{20} is larger at shorter times because these stars are still contracting towards the ZAMS. At 0.5 Myr stars with masses greater than ~ 5 $M_{\odot}$ have reached the ZAMS, as indicated by the kink and faster increase of M_{20} in these plots for the 0.5 Myr case.

2.5 Discussion

We have shown that massive stars are fast rotators at birth and that their initial rotation rates are unlikely to be regulated by the star-disk magnetic interaction. We have found that magnetic torques can only effectively spin down massive stars that have low accretion rates, long disk lifetimes, weak magnetic coupling with the disk, and/or surface magnetic fields that are significantly larger than what current observational estimates suggest. We thus conclude that their initial rotation rates are likely regulated by gravitational torques. Since massive stars arrive on the main sequence as fast rotators, their variation in rotation rates as a fraction of their break-up rate is likely a result of evolutionary spin down, due to stellar expansion and/or angular momentum loss via stellar winds while on the main sequence.

2.5.1 Observational Implications

A topic of current debate is whether the distribution of the projected rotational velocities of massive stars depend on birth environment or if this property is only affected by evolutionary spin down (Strom *et al.*, 2005; Dufton *et al.*, 2006; Huang and Gies, 2006;

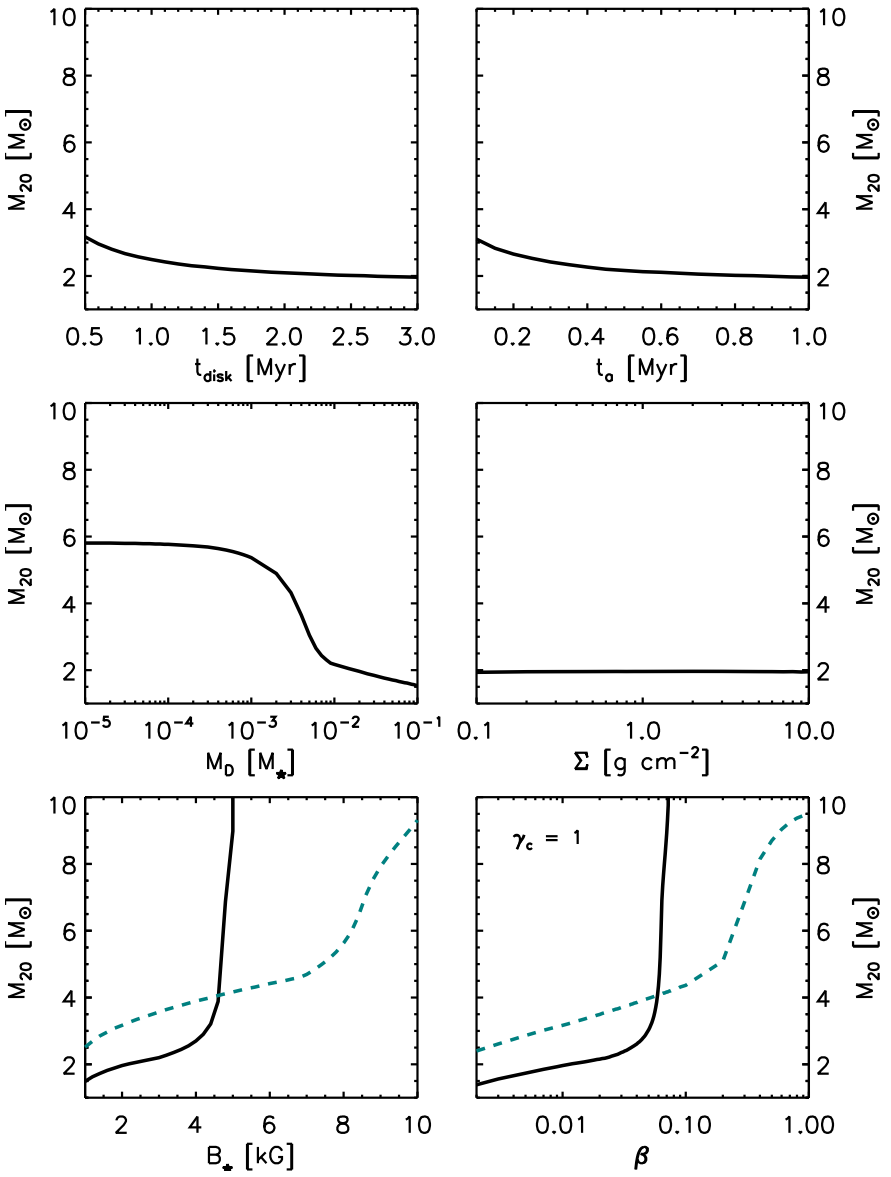

Figure 2.10 This figure illustrates the sensitivity of the model parameters. The y-axes show the minimum stellar mass where $f \geq 0.2$, denoted as M_{20}, for different parameters as indicated on the x-axes. Except for the top left plot, the black solid lines indicate that these values were taken for a disk lifetime of 3 Myrs. In the bottom panels, the teal dashed lines show the value of M_{20} 0.5 Myrs after the beginning of the disk clearing phase for comparison.

Wolff *et al.*, 2006, 2008; Huang *et al.*, 2010). Strom *et al.* (2005) observed the rotational velocities of B stars located in high stellar density clusters and compared them to field stars of similar age (∼12-15 Myr). They found that, on average, the cluster stars had larger rotational velocities than the field stars in their sample and that only the most evolved cluster stars had similar rotational velocities as their field star counterparts. Likewise, Wolff *et al.* (2006, 2008) observed that massive stars (e.g., $M_\star \gtrsim 6$ $M_\odot$) found in clusters characterized by a high stellar density are faster rotators than their similar mass counterparts located in lower density clusters. These studies concluded that the initial spin rates of these stars depend on the initial star-forming environment since these stellar ensembles, which have survived as bound clusters, likely form in molecular clouds characterized by high surface densities. Furthermore, Wolff *et al.* (2006) compared the distribution of the rotational velocities of B stars in both young and older high density and low density environments and did not detect a significant evolutionary change.

In agreement, Huang *et al.* (2010) compared the rotation rates of cluster and field B stars and found that, on average, cluster stars tend to rotate faster than field stars. However, by grouping the stars by surface gravity, an age proxy, they found there is little difference between the average rotational velocities for the field and cluster stars as a function of age, and that they exhibit a similar spin-down with advanced evolution. They also found that field stars are in general more evolved than cluster stars. These results suggest that the observed trend in the rotational velocities of B stars are due to evolutionary spin down rather than to the initial conditions of the environment in

which they formed. They argue that the discrepancy between the average rotation rate of the field stars and cluster stars in their sample is that the field stars have undergone evolutionary spin down since the field star sample contained more evolved stars.

For a fixed surface magnetic field strength, we find here that the initial rotation rates of massive stars, due to disk locking, have no dependence on the environmental density. As described in Section 2.3.2.1, the accretion rate during the main accretion phase does depend on the star forming environment, with larger surface density yielding a greater time-averaged accretion rate. Wolff *et al.* (2006) proposed that the higher rotation rates they report for stars in dense clusters are the result of disk-locking plus a systematically higher accretion rate in dense clusters. However, we find that magnetic torques are insignificant during the main accretion phase regardless of environment density because of the high accretion rates. These torques only become important during the disk clearing phase, and there is no obvious reason that the properties or behavior of the disk during this phase should depend on the environment. However, this does not rule out other factors that may depend on the environment. In this work we assumed that all stars had the same surface magnetic field strength. If the strength of the magnetic fields present during the star-formation process depends on environment, either because the star-forming cloud has a different magnetic mass to flux ratio and/or because the ambipolar diffusion process depends on density, then this could provide a viable explanation for the difference in rotational velocities of young stars in environments of varying density. Another possibility for the difference in rotational velocities of stars born in different environments may be related to the lifetimes of disks

in such environments. We have found that the rotation rates of these stars depend crucially on the lifetime of the accretion disk. Thus, if disks have shorter lifetimes in higher stellar density environments, possibly due to tidal dissipation from interactions with neighbors or rapid photoevaporation due to radiation from nearby massive stars, then the initial rotation rates of these stars will only increase as they contract towards the ZAMS (Wolff *et al.*, 2006).

2.5.2 Future Work and Caveats

In this work, we have omitted two potentially important effects: that magnetic fields might be stronger early in stars' lives, and that stars can be spun down by winds on the main sequence. As mentioned in Section 2.1, magnetic fields in massive stars are likely to be the decaying remnants of magnetic flux swept up during the star-formation process. Therefore, it is plausible that accreting massive stars have stronger magnetic fields than those we observe as main sequence O and B stars. If this is the case, then massive stars will likely be spun-down via magnetic torques. If the decay process is the same for all stars then we expect that the strongest magnetic fields should be observed in the slowest rotators. However, we also discovered that the spin rates of these stars depend heavily on how well the stellar magnetic field lines couple to the accretion disk. As described in Section 2.3.3.1 the true value of β is highly uncertain because it depends on the microphysics of the accretion disk. Since observations of disks around massive stars are rare we are unable to provide a confident estimate for β. However, by exploring a range of values for β we have determined that if the field lines are weakly coupled to

the disk then magnetic torques can sufficiently spin down massive stars. Also, measuring the rotation rates of young, massive stars can provide a better estimate for β. If the slowest rotators prove to have weak magnetic fields, then it may be likely that the field lines were weakly coupled to the disk, resulting in a larger β, thus producing these slower rotators.

Stars on the main sequence also shed mass and angular momentum via stellar winds, which we have neglected in this work. In the presence of a stellar magnetic field, these winds will couple with the field lines causing the star to lose a significant amount of angular momentum as it evolves (Weber and Davis, 1967). Since the mass loss rates of stars increases with stellar mass (Nieuwenhuijzen and de Jager, 1990) more massive stars will lose angular momentum at a greater rate. If the spin rates of massive stars are regulated by gravitational torques rather than magnetic torques produced by the star-disk magnetic interaction then we expect that all massive stars should be rotating at $\sim$50% of their break up speed once they are deposited on the ZAMS, assuming that their disks survive long enough. Spin down will occur as they evolve and shed angular momentum via stellar winds. This is consistent with the results of Huang *et al.* (2010) who found that young stars with masses greater than $\sim 2\ M_{\odot}$ are preferentially fast rotators and that the average rotation speed as a fraction of the break up speed, for each mass bin, decreases for increasing stellar mass.

Chapter 3

Numerical Methodology: Hybrid Radiative Transfer for Adaptive Mesh Refinement Simulations

A version of this chapter has been published as "Hybrid Adaptive Ray-Moment Method (*HARM*^{2}): A Highly Parallel Method for Radiation Hydrodynamics on Adaptive Grids," Rosen, A. L., Krumholz, M. R., Oishi, J. S., Lee, A. T., Klein, R. I. 2017, *Journal of Computational Physics*, 330, 924.[1]

3.1 Introduction

Radiation-hydrodynamics (RHD) is a challenging numerical problem, but it is a crucial component in modeling several physical phenomena in the fields of astrophysics,

[1]

laser physics, and plasma physics. Accurate solution of the radiative transfer (RT) equation, which governs the evolution of radiation interacting with matter, is difficult because of its high dimensionality. This equation depends on six independent variables: three spatial, two angles describing the direction of the propagation of photons, and one frequency dimension. For time-dependent RHD calculations, this solution must be obtained at every time step, and then coupled to the hydrodynamics. Even on parallel supercomputers direct solution of the RT equation at each time step of a time-dependent calculation is prohibitively expensive, because of this most numerical RHD codes use approximations to treat the evolution of the radiation field and its interaction with matter.

One common approach to solving the RHD equations is to reduce the dimensionality of the problem. This class of approximations are known as moment methods because they take the moments of the radiative transfer equation in direct analogy to the Chapman-Enskog procedure used to derive the hydrodynamic equations from the kinetic theory of gases (Krumholz, 2011; Teyssier, 2015). This method averages over the angular dependence, and thus is a good approximation for smooth, diffuse radiation fields such as those present in optically thick media when the radiation is tightly coupled to the matter. The accuracy with which moment methods recover the angular dependence of the true solution depends on the order at which the moments are closed, and on the closure relation adopted. Common approximations include flux-limited diffusion (FLD; closure at first moment) (Levermore and Pomraning, 1981; Krumholz *et al.*, 2007b; Commerçon *et al.*, 2011), the M1 method (closure at the 2nd moment using

a minimum entropy closure) (González and Audit, 2005; Rosdahl and Teyssier, 2015), and Variable Eddington Tensor (VET; closure at the 2nd moment using an approximate solution to the full transfer equation) (Dykema *et al.*, 1996; Jiang *et al.*, 2012; Davis *et al.*, 2012). Regardless of the order and closure relation, the computational cost of these methods usually scales as N or $N \log N$, where N is the number of cells, and the technique is highly parallelizable (Krumholz, 2011).

An alternative technique used to solve the RT equation numerically is characteristics-based ray tracing, which solves this equation directly along specific rays. With this method, the directionality of the radiative flux is highly accurate, but the accuracy depends on the sampling of rays. Two widely used schemes for ray tracing in grid-based codes are *long* and *hybrid* characteristics. Long characteristics traces rays on a cell by cell basis, and provides maximum possible accuracy. Hybrid characteristics is a combination of long characteristics within individual grids and short characteristics between grids (i.e., in which only neighboring grid cells are used to interpolate incoming intensities) (Rijkhorst *et al.*, 2006; Buntemeyer *et al.*, 2016). The method of short characteristics is faster but more diffusive compared to long characteristics methods. The computational cost for both methods scales linearly with the number of sources, rays traced, and grid cells with which the rays interact, making these methods prohibitively expensive for treating diffuse radiation fields where every computational cell is a source. Instead, they are ideal for treating the radial radiation fields of point sources. Even for this application, however, one major drawback of ray tracing methods, especially long characteristics, is that they are difficult to parallelize in a code where the hydrodynamics

is parallelized by domain decomposition. In such a configuration, each ray will usually cross multiple processor domains, creating significant communications overheads and serial bottlenecks.

In summary, moment methods are better at approximating the diffuse radiation field from a fluid but are poor at modeling the propagation of radiation from point sources where the direction of the field is important. Characteristics methods, in contrast, are good at approximating the direction-dependent radiation fields from point sources but are too computationally expensive for practical use in simulating a diffuse radiating fluid. When both point and diffuse radiation sources are present, therefore, a natural approach is to combine both techniques by using long characteristics to model the propagation of radiation from a point source and its subsequent interaction (e.g., absorption) with the fluid and then use a moment method to follow the subsequent diffuse re-emission.

This technique has been developed in several numerical codes in the past 20 years, but these codes typically have been limited to cases where a geometric symmetry simplifies the long characteristics solution. Wolfire and Cassinelli (1986, 1987) introduced a formal decomposition between the direct and dust-reprocessed radiation fields for a calculation in 1D spherical geometry. The first published 2D simulation using such a method is Murray *et al.* (1994), who coupled long characteristics to FLD to model the direct (ray tracer) and scattered (FLD) radiation field in accretion disk coronae. Kuiper *et al.* (2010) incorporated a similar hybrid approach in the 3D grid based code Pluto, but again limiting the problem to a special geometry: in this case a single point source

at the origin of a spherical computational grid. Most recently, Klassen *et al.* (2014) developed a hybrid scheme in the FLASH adaptive mesh refinement (AMR) code but uses FLD plus hybrid characteristics which, although faster, is less accurate than long characteristic methods.

The reason that many authors have resorted to special geometries or abandoned long characteristics is the difficulty in parallelizing long characteristics in a general geometry, particularly in the case of adaptive grids. The problem is difficult because it is unknown *a priori* how far rays will travel and what grids they will interact with in an adaptive grid framework. In a distributed memory paradigm where different grids may be stored in memory on different processors, this can easily result in a complex communication pattern with numerous serial bottlenecks. Indeed, all implementations of long characteristics on adaptive grids published to date use synchronous communication algorithms in which processors must wait for other processors to receive ray information (Wise and Abel, 2011), leading to exactly this problem.

In this chapter we present our Hybrid Adaptive Ray-Moment Method ($HARM^2$) which uses long characteristics to treat radiation from point sources coupled to a moment method to handle the diffuse radiation field from the fluid. $HARM^2$ works on adaptive grids with asynchronous time stepping. We have greatly improved the parallelism of the long characteristics solve in a distributed memory framework through a new, completely asynchronous, non-blocking communication method. The rest of this chapter is organized as follows. We begin with a formal derivation of our method for decomposing the radiation field into two components in Section 3.2. Section 3.3 describes

our numerical implementation of our hybrid radiation scheme in the astrophysical AMR code ORION. Next we confirm the robustness of our method by providing validation and performance tests in Sections 3.4 and 3.5, respectively. Finally, we summarize our methods and results in Section 3.6.

3.2 Decomposition of the Radiation-Hydrodynamics Problem

Here we describe a formal method to separate the radiation field into two components – (1) the diffuse radiation from the fluid and (2) the direct radiation field from point sources (Norman *et al.*, 1998). Formally, we consider a system consisting of a volume-filling radiating fluid plus point sources of radiation, and we wish to decompose the radiation fields produced by the fluid and the point sources. An example where such a decomposition is valuable is in the problem of simulating stars embedded in an optically thick, dusty medium such as is present during the early formation of a star cluster while the stars are actively accreting. The radiative flux from the stars will be absorbed by nearby dust and the dust will re-emit thermal radiation in the infrared. This radiation will be highly coupled to the interstellar medium and diffuse through the dense gas.

We begin with the equations of radiation-hydrodynamics (RHD) written in

the lab-frame (Mihalas and Klein, 1982; Mihalas and Auer, 2001):

$$\frac{\partial \rho}{\partial t} + \nabla \cdot (\rho \mathbf{v}) = 0 \tag{3.1}$$

$$\frac{\partial}{\partial t}(\rho \mathbf{v}) + \nabla \cdot (\rho \mathbf{v}\mathbf{v}) = -\nabla P + \mathbf{G} \tag{3.2}$$

$$\frac{\partial}{\partial t}(\rho E) + \nabla \cdot [(\rho E + P)\mathbf{v})] = cG^0 \tag{3.3}$$

where ρ, $\mathbf{v}$, E, and P are the density, velocity, specific energy (thermal plus kinetic), and thermal pressure of the fluid, respectively; and $\left(G^0, \mathbf{G}\right)$ is the radiation four-force density which is the negative of the radiation energy stress tensor and is given by

$$cG^0 = \int_0^\infty d\nu \int d\Omega \left[\kappa(\mathbf{n}, \nu) I(\mathbf{n}, \nu) - \eta(\mathbf{n}, \nu)\right] \tag{3.4}$$

$$c\mathbf{G} = \int_0^\infty d\nu \int d\Omega \left[\kappa(\mathbf{n}, \nu) I(\mathbf{n}, \nu) - \eta(\mathbf{n}, \nu)\right] \mathbf{n} \tag{3.5}$$

where $I(\mathbf{n}, \nu)$ is the intensity of the radiation field at frequency ν in direction $\mathbf{n}$. We note that the physical quantities given in Equations (3.1)-(3.3) depend on spatial position and time. The time-like and space-like components of $\left(G^0, \mathbf{G}\right)$ represent the rate of energy and momentum transfer from the radiation to the fluid, respectively. The intensity is governed by the time-independent radiative transfer equation

$$\mathbf{n} \nabla I(\nu, \mathbf{n}) = -\kappa(\mathbf{n}, \nu) I(\mathbf{n}, \nu) + \eta(\mathbf{n}, \nu) \tag{3.6}$$

where $\kappa(\mathbf{n}, \nu)$ and $\eta(\mathbf{n}, \nu)$ are the direction and frequency dependent absorption and

emission coefficients in the lab-frame, respectively. For simplicity, we have neglected the effects of scattering because we expect to solve the equations of RHD in astrophysical problems where absorption is the dominant transfer mechanism. However, it would be straightforward to extend the method to include scattering in the diffuse component, as we point out below. We also ignore the time-dependence of the radiative transfer equation because our primary target application is systems where the light travel time is orders of magnitude smaller than the system dynamical time, and thus the radiation intensity is always in instantaneous equilibrium.

We now separate $I(\mathbf{n},\nu)$ into two components

$$I(\mathbf{n},\nu) = I_{\rm dir}(\mathbf{n},\nu) + I_{\rm diff}(\mathbf{n},\nu) \tag{3.7}$$

to describe the direct radiation fields from point sources ($I_{\rm dir}$) and the diffuse radiation field ($I_{\rm diff}$) emitted by the fluid. Since the sources that contribute to the direct radiation field are point sources we can represent their intensity as a sum of $\delta-$functions

$$I_{\rm dir}(\mathbf{n},\nu) = \sum_{i=1}^{N} I_{{\rm src},i}(\nu)\delta\left(\mathbf{n}-\mathbf{n}_{{\rm src},i}\right), \tag{3.8}$$

where $\mathbf{n}_{{\rm src},i} = (\mathbf{x}-\mathbf{x}_i)/|\mathbf{x}-\mathbf{x}_i|$ for any position $\mathbf{x}$ in the computational domain, $\mathbf{x}_i$ and $I_{{\rm src},i}$ are the position and intensity of the ith point source, and we assume that the sources are isotropic emitters, so $I_{{\rm src},i}$ is independent of $\mathbf{n}$.[2] With this formulation $I_{\rm dir}$ is

[2]Note that this limits our method to non-relativistic problems, where we can neglect the effects of relativistic beaming of the source radiation fields.

non-zero only at special values of $\mathbf{n}$, i.e., those that point from the position of a source $\mathbf{x}_i$ to the position in question $\mathbf{x}$, and zero for all others; while $I_{\rm diff}$ will be non-zero everywhere. However, because the four-force vector $(G^0, \mathbf{G})$ depends on integrals over $\mathbf{n}$, the δ-function contributions from $I_{\rm dir}$ may dominate at some positions, while the contribution from $I_{\rm diff}$ dominates elsewhere. This makes solution with a pure moment method difficult, and motivates us to treat the radiation fields of the point sources and fluid separately so that we can properly take into account the direction of the radiation fields from point sources. With this decomposition Equations (3.4)-(3.5) become

$$\begin{aligned} cG^0 &= \int_0^\infty d\nu \int d\Omega \left[\kappa(\mathbf{n},\nu) I_{\rm dir}(\mathbf{n},\nu) - \eta_{\rm dir}(\mathbf{n},\nu)\right] \\ &\quad + \int_0^\infty d\nu \int d\Omega \left[\kappa(\mathbf{n},\nu) I_{\rm diff}(\mathbf{n},\nu) - \eta_{\rm diff}(\mathbf{n},\nu)\right] \qquad (3.9) \\ c\mathbf{G} &= \int_0^\infty d\nu \int d\Omega \left[\kappa(\mathbf{n},\nu) I_{\rm dir}(\mathbf{n},\nu) - \eta_{\rm dir}(\mathbf{n},\nu)\right] \mathbf{n} \\ &\quad + \int_0^\infty d\nu \int d\Omega \left[\kappa(\mathbf{n},\nu) I_{\rm diff}(\mathbf{n},\nu) - \eta_{\rm diff}(\mathbf{n},\nu)\right] \mathbf{n} \qquad (3.10) \end{aligned}$$

where $\eta_{\rm dir}(\mathbf{n},\nu)$ and $\eta_{\rm diff}(\mathbf{n},\nu)$ describes the emission due to point sources and the fluid, respectively.

This decomposition allows the following general approach to a hybrid scheme: (1) use a long characteristics method to solve for $I_{\rm dir}$, (2) use a moment method to solve for $I_{\rm diff}$, (3) add the two components to obtain the radiation four-force density $(G^0, \mathbf{G})$, (4) update the hydrodynamic state using the radiation four-force density. As a further benefit to this approach, we note that there is no requirement that steps (1) and (2) use the same frequency resolution, since $(G^0, \mathbf{G})$ depends only on an integral over frequency.

It is relatively straightforward to bin the intensity from the point sources by frequency with a ray tracer since each ray can be approximated by an array of intensities, while using a lower frequency resolution in the (generally more expensive) moment method. This is ideal for point sources such as stars which have color temperatures much higher than the absorbing medium.

3.3 The *HARM*^{2} Algorithm

In this section we describe the *HARM*^{2} algorithm. We have implemented this algorithm in the ORION astrophysical adaptive mesh refinement (AMR) code (Klein, 1999; Fisher, 2002; Krumholz *et al.*, 2007b; Li *et al.*, 2012) and we use this implementation for all the algorithm tests described below. ORION uses grid-based adaptivity (Berger and Oliger, 1984; Berger and Colella, 1989) with individual time steps for each level, and the *HARM*^{2} algorithm can be applied to any AMR code following this design. Variable definitions from this section are defined in table 3.1. ORION uses the FLD approximation for its moment method (Krumholz *et al.*, 2007b), and we will use this for all tests below, but *HARM*^{2} is equally compatible with any other moment method.

3.3.1 Update Cycle

Consider an adaptive mesh covering some computational domain of interest. The mesh consists of levels with different cell sizes, with $l = 0$ denoting the coarsest level and $l = l_{\max}$ the finest. Each level, in turn, is made up of a union of rectangular grids,

each with the same cell size. In a distributed-memory parallel computation, different grids may be stored in memory on different processors or nodes. The grids on a given level need not be contiguous, but they are required to be non-overlapping, and the grids are properly nested such that a cell of a level l grid may have as its neighbor the domain edge, another level l cell, or a cell of level $l-1$ or $l+1$, but not a cell of any other level. Point sources are only placed at locations covered by a grid of level $l_{\max}$. Each level advances on a time step dt_l, ordered such that $dt_l \geq dt_{l+1}$, and so that, after some number of time steps on level $l+1$, the simulation time t_{l+1} on that level will be equal to the time t_l on the next coarsest level. That is, we require that, a level $l+1$ syncs up in time with the next coarsest level l. In all the tests we perform with ORION the time steps obey $dt_{l+1} = dt_l/2$, and synchronization occurs every 2 fine time steps, but this is not required by *HARM*^{2}.

Given this setup, our algorithm is as follows:

1. Operator split the direct and diffuse components of the radiation field:
   (a) if l equals 0 **or** $t_{\mathrm{start},l}$ is greater than $t_{\mathrm{start},l-1}$, where $t_{\mathrm{start},i}$ is the current time on level i, then
      i. Loop over point sources and inject rays onto grids that belong to level $l_{\max}$ where they are located.
      ii. Advance rays across grids on level $l_{\max}$ and all coarser grids that the rays interact with, store the rates at which radiative energy and momentum,

dE/dt and $d\mathbf{p}/dt$, are absorbed by the gas (Section 3.3.2).

iii. Restrict dE/dt and $d\mathbf{p}/dt$ from finer level grids down to level l.

(b) Add $(dE/dt)\,dt_l$ and $(d\mathbf{p}/dt)\,dt_l$ to the gas energy and momenta, respectively.

(c) Update the diffuse radiation field with a moment method.

2. Apply the hydrodynamics update to all cells on level l.

3. Update point sources if $l = l_{\max}$.

For the pattern of time steps used by ORION, whereby there are 2 fine time steps per coarse time step, this method results in $2^{l_{\max}}$ ray trace updates per update on the coarsest level. Note that, because we only perform a ray trace if $t_{\text{start},l} > t_{\text{start},l-1}$, we do not perform any redundant ray tracing steps. In other words, we perform the ray trace at a given time only if we have not already performed it at that time.

3.3.2 Direct Radiation Field: Adaptive Ray Trace

We now describe the adaptive ray tracing procedure that forms step 1a(ii) of the algorithm above. Consider a single point source with a specific luminosity given by L_ν and luminosity given by $L_\star = \int_0^\infty L_\nu\,d\nu$. The generalization to multiple point sources is trivial. We discretize the point source spectrum in frequency into N_ν frequency bins, with the ith bin covering a range in frequency $(\nu_{i-1/2}, \nu_{i+1/2})$. Let $L_i = \int_{\nu_{i-1/2}}^{\nu_{i+1/2}} L_\nu\,d\nu$ be the luminosity of the point source integrated over the ith frequency such that $\sum L_i = L_\star$. We generally expect that L_i will be the energy radiated per unit time in a given frequency

bin, but the algorithm is identical if we instead take L_i to be a photon luminosity, measured in photons per unit time.

We wish to solve the transfer equation along rays that end at this source. Along a ray characterized by a direction $\mathbf{n}$ and a solid angle $\Omega_{\rm ray}$ that it subtends, the propagation of the radiation is described by the time-independent transfer equation (i.e., Equation (4.16)), with the emission term η set to zero because we are taking the direct radiation field to have zero emissivity except at the point sources. Multiplying both sides of this equation by $4\pi r^2/\Omega_{\rm ray}$, we obtain an integrated form of the transfer equation

$$\frac{\partial L_{{\rm ray},i}}{\partial r} = -\kappa_i L_{{\rm ray},i}, \tag{3.11}$$

where $L_{{\rm ray},i}(r)$ is the luminosity along the ray at a distance r from the point source and κ_i is the total absorption opacity for the ith frequency bin in units of cm^{-1}. This equation is subject to the boundary condition $L_{{\rm ray},i}(0) = L_i/N_{\rm pix}$, where $N_{\rm pix} = 4\pi/\Omega_{\rm ray}$. We solve this equation by discretizing it along the line segments defined by the intersection of the ray with the cells of the computational mesh. Specifically, when a ray with luminosity $L_{{\rm ray},i}$ passes through a cell along a segment of length dl, the optical depth of the segment is $\tau_i = \kappa_i\, dl$, and the luminosity of the ray decreases by an amount

$$dL_{{\rm ray},i} = L_{{\rm ray},i}\left(1 - e^{-\tau_i}\right). \tag{3.12}$$

In the process, the cell absorbs an amount of energy and momentum at a rate

$$\frac{dE}{dt} = \sum_{i=1}^{N_\nu} dL_{\mathrm{ray},i} \tag{3.13}$$

$$\frac{d\mathbf{p}}{dt} = \sum_{i=1}^{N_\nu} \frac{dL_{\mathrm{ray},i}}{c}\mathbf{n}. \tag{3.14}$$

The total absorption rate for each cell is simply the sum of dE/dt and $d\mathbf{p}/dt$ over all rays from all point sources that pass through it. When computing the line segments dl, we only consider grids that are not masked by any finer grid. That is, when solving Equation (4.17), we only ever consider the most highly spatially resolved data at any given position.

We choose the directions $\mathbf{n}$ and solid angles Ω_{ray} using the angular discretization introduced by Abel and Wandelt (2002) and Wise and Abel (2011). In this approach, $\mathbf{n}$ and Ω_{ray} are chosen using the Hierarchical Equal Area isoLatitude Pixelization of the sphere (HEALPix) scheme (Górski *et al.*, 2005), which divides the surface area of a sphere into equal area pixels that can be further subdivided into four equal-area sub-pixels. There are $N_{\mathrm{pix}}(0) = 12$ pixels at the coarsest HEALPix level, and there are $N_{\mathrm{pix}}(j) = 12 \times 4^j$ pixels on HEALPix level j; note that the HEALPix level j and the AMR grid level l are distinct and in general are not the same. The scheme is adaptive in that, as we trace rays away from point sources, we subdivide them as needed to ensure that cells are adequately resolved. Specifically, we divide a ray into 4 sub-rays if

it satisfies the condition

$$\frac{\Omega_{\rm cell}}{\Omega_{\rm ray}} = \frac{N_{\rm pix}(j)}{4\pi}\left(\frac{\Delta x}{r}\right)^2 < \Phi_{\rm c}, \tag{3.15}$$

where $\Omega_{\rm cell} = (\Delta x/r)^2$ is the solid angle subtended by a cell of linear size Δx at a distance r from the point source. The quantity $\Phi_{\rm c}$ is the minimum number of rays required to go through each cell, which we usually set to 4 following the resolution tests of Krumholz *et al.* (2007c) and Wise and Abel (2011) but, in general, the exact value for $\Phi_{\rm c}$ is problem-dependent. The initial luminosity per ray for frequency bin i is $L_{{\rm ray},i,j_0} = L_i/N_{\rm pix}(j_0)$ where j_0 is the initial healpix level. When a ray splits, we solve the transfer equation along the sub-rays using the boundary condition $L_{{\rm ray},i,j+1}(R) = L_{{\rm ray},i,j}(R)/4$, where $L_{{\rm ray},i,j}(R)$ is the luminosity of the ray at frequency bin i on HEALPix level j. As proposed by Krumholz *et al.* (2007c), we randomly rotate the orientation of the rays every time they are cast to minimize errors due to discretization in angle. Finally, we terminate the ray trace when either a ray exits the computational domain, or when $L_{{\rm ray},j}(r) < 0.001 L_{{\rm ray},j}(0)$ where $L_{{\rm ray},j}(0) = \sum_i L_i/\left(12\times 4^{j-j_0}\right)$, i.e., when 99.9% of the energy originally assigned to that ray on ray level j has been absorbed.

3.3.3 Parallelization

Thus far the algorithm we have described is substantially identical to that of Wise and Abel (2011). However, we adopt a very different, and much more efficient strategy to parallelize this procedure. The primary challenge to parallelizing this algo-

rithm is avoiding serial bottlenecks. The grids through which the rays must be traced may be distributed across any number of processors, and solution of Equation (4.17) is an intrinsically serial process because the rate of change of the energy and momentum in any cell due to radiation arriving along a particular ray depends upon the properties of all cells that lie between the point source and the cell in question. Since the numbers and positions of point sources and computational grids in the AMR structure, and their distribution in memory, are not known *a priori*, minimizing bottlenecks requires an opportunistic approach: rays should be able to be processed in arbitrary order, with each processor performing ray tracing given the data available to it, and waiting for other processors only when no useful work can be done. To this end, communication must be non-blocking and asynchronous. At the same time, each process must be able to determine when the entire ray trace has been completed, so that it can proceed to the remainder of the update cycle (the moment method, hydrodynamics, etc.), and this determination must be robust against race conditions.

Recall that we consider the tracing of a particular ray done when it either exits the computational domain or when 99.9% of its energy has been absorbed. To handle the problem of determining when the algorithm should terminate without relying on blocking communication, we *pretend* we know how many rays *could* be created by computing a maximum number of rays to be used as a counter:

$$N_{\rm max} = N_{\rm src} \times 12 \times 4^{j_{\rm max}} \tag{3.16}$$

where $N_{\rm src}$ is the number of sources and $j_{\rm max}$ is the maximum HEALPix level we allow; we set this to 20 in all of our tests. Our algorithm involves accounting for "all rays" that are destroyed on each processor by computing

$$N_{{\rm destroyed},k} = \sum_{N_{{\rm ray},k}} 4^{j_{\rm max}-j} \tag{3.17}$$

where k is the processor number, j is the HEALPix level of the ray that is deleted due to absorption or leaving the computational domain, and $N_{{\rm ray},k}$ is the total number of rays that have been deleted on processor k. This information is communicated to all other processors. Once the total destroyed,

$$N_{\rm destroyed} = \sum_{N_{\rm CPU}} N_{{\rm destroyed},k}, \tag{3.18}$$

on each processor equals $N_{\rm max}$ the ray trace is complete.

With this bookkeeping method understood, we present our message passing scheme as Algorithm 1. Note that this algorithm requires version 3.0 or later of the Message Passing Interface (MPI) standard, because only that version supports some of the non-blocking communications we require (e.g., **MPI_Iprobe** see Algorithm 1). A detailed description of our parallelization strategy follows. Every processor has 4 flags that can change: (i) ALLDONE which is initially set to **false** and will be set to **true** once all rays have been destroyed, (ii) WORKREMAINS which is set to **true** if rays exist on this processor and **false** otherwise, (iii) DATARECV which is set to **true** when the

processor can receive rays from other processor(s), and (iv) COUNTRECV which is set to **true** when the processor can receive $N_{\text{destroyed},k}$, the number of rays destroyed from other processor(s). Every processor also has a counter, LOOPITER, which tracks the number of times the parallelization algorithm is iterated over.

For each processor, our algorithm is as follows:

1. Inject rays from point sources to grids.
2. Compute $N_{\max}$ (Equation (3.16)).
3. Set ALLDONE to **false**, set LOOPITER = 0, and enter outer **while**(not ALLDONE) loop.
   (a) Set WORKREMAINS to **true** if rays exist on grids that belong to this processor, otherwise set WORKREMAINS to **false**.
   (b) If WORKREMAINS is **true** enter **while**(WORKREMAINS) loop.
      i. Loop over all grids that belong to this processor and **for each** grid advance all rays that belong to that grid until they (i) leave the grid and need to be moved to another grid, (ii) become extinct, or (iii) leave the domain. Every time (ii) or (iii) occurs for a ray we delete the ray and increase the value of $N_{\text{destroyed},k}$ on this processor per Equation (3.17). If (i) occurs we determine the new grid and processor for that ray.
      ii. Set WORKREMAINS to **false**.

iii. Loop over rays that must be transferred to other grids and check if they belong to a grid on this processor or another processor. If the former is true place the ray on the correct grid and set WORKREMAINS to **true**, otherwise the ray must be transferred to another processor so we place the ray in a linked list, **outgoing_ray_list**, to be communicated to the other processors.

iv. **Repeat** until all rays have been either destroyed and/or placed into **outgoing_ray_list**.

(c) Loop over rays in **outgoing_ray_list**. Place rays from **outgoing_ray_list** into a contiguous array for MPI communication (one array per receiving processor) and perform a non-blocking **MPI_Isend** for each array to send it to the appropriate processor.

(d) Set DATARECV to **true** and if (LOOPITER **modulo** $N_{\mathrm{CPU}} == 0$)[3] then enter the **while**(DATARECV) loop to begin receiving rays from other processors.

i. Probe other processors with the non-blocking **MPI_Iprobe** function to see if rays need to be received, if this is true set DATARECV to **true** otherwise set it to **false**.

ii. If DATARECV is **true** then receive rays on this processor with **MPI_Recv**. Place the incoming rays onto the new grids they belong to.

iii. **Repeat** until **MPI_Iprobe** returns false.

[3]This requirement reduces the time spent on performing MPI_Iprobes which becomes more expensive as N_{procs} increases.

(e) If this processor sent rays to another processor then perform non-blocking **MPI_Testsome** to test for some given ray send requests to complete.

(f) If WORKREMAINS is false then perform non-blocking **MPI_Testsome** to test for some of the $N_{\text{destroyed, k}}$ send requests to complete.

(g) Set COUNTRECV to **true** and if (LOOPITER **modulo** $N_{\text{CPU}} == 0$) then enter the **while**(COUNTRECV) loop to begin receiving rays from other processors.

i. Probe other processors with the non-blocking **MPI_Iprobe** function to see if the value of $N_{\text{destroyed},k}$ on those processors needs to be received. If this is true set COUNTRECV to **true**, otherwise set it to **false**.

ii. Receive $N_{\text{destroyed},k}$ from processor k on this processor with **MPI_Recv** if COUNTRECV is **true** and assign to the kth element of an array **rayDestProc** containing N_{CPU} elements.

iii. **Repeat** until **MPI_Iprobe** returns false.

(h) If $N_{\text{destroyed},k}$ on this processor has increased in the outer loop iteration then send this number with a non-blocking **MPI_Isend** to all other processors.

(i) Compute sum of **rayDestProc**. If this value equals N_{max} terminate the outer loop, else repeat outer loop and increment LOOPITER by 1.

3.4 Validation Tests

In this section we demonstrate the accuracy of our adaptive ray tracing algorithm, the absorption of the direct radiation field from point sources supplied by our

```
Data: Rays and destroyed ray counts
compute maxRays;
all_done = False;
do
    do
        foreach grid that belongs to this processor do
            advance all rays, return number "destroyed" and add to
             destroyedCount;
        end
        check grids to see if work_remains;
    while work_remains;
    Non-blocking MPI_Isend rays to other processors;
    do
        Non-blocking MPI_Iprobe other processors for rays;
        if MPI_Iprobe returns true then
            Blocking MPI_Recv(rays);
        end
    while MPI_Iprobe for rays returns true;
    Non-blocking MPI_Testsome rays MPI_Isend requests;
    Non-blocking MPI_Testsome destroyed counts MPI_Isend requests;
    do
        Non-blocking MPI_Iprobe other processors for destroyed counts;
        if MPI_Iprobe returns true then
            Blocking MPI_Recv(processor destroyed counts);
        end
    while MPI_Iprobe for destroyed counts returns true;
    if destroyedCount greater than previous destroyedCount then
        Non-blocking MPI_Isend(destroyedCount to all processors);
    end
    if no work_Remains and Ray Send Requests == 0 and Destroyed
     Count Send Requests == 0 and sum(destroyedCount) == maxRays
     then
        all_done = True;
    end
while not all_done;
```

Algorithm 1: Asynchronous parallelization algorithm developed for the communication of rays to other processors.

Table 3.1 Variable definitions used in Section 3.3.

Variable	Description
dl	Path length of ray across cell
dE/dt	Energy absorbed by fluid in cell from direct radiation
$d\mathbf{p}/dt$	Momenta absorbed by fluid in cell from direct radiation
$dL_{\mathrm{ray},i}$	Absorbed luminosity from ray for the ith frequency bin
dt_i	Time step on level i
j	HEALPix ray level
j_0	Initial HEALPix ray level
$j_{\max}$	"Maximum" ray level for adaptive ray trace
κ_i	total absorption opacity for the ith frequency bin
l	AMR Level
$l_{\max}$	Maximum AMR level
L_ν	Specific luminosity of point source
L_i	Luminosity of point source integrated over ith frequency bin
$L_{ray,i}$	Luminosity in ith frequency bin along ray
$\mathbf{n}$	Normal direction of ray
N_{CPU}	Number of processors
$N_{\mathrm{destroyed},k}$	Number of rays "destroyed" on processor k
$N_{\mathrm{destroyed}}$	Number of rays "destroyed" on all processors
$N_{\max}$	Maximum number of rays used as a counter
N_ν	Number of frequency bins used for adaptive ray trace
$N_{\mathrm{pix}}(j)$	Number of HEALPix pixels on level j
$N_{\mathrm{ray},k}$	Number of rays deleted on processor k
N_{src}	Number of point sources
Δx	linear size of cell
Φ_{c}	Angular resolution of ray trace [rays/cell]
Ω_{cell}	Solid Angle subtended by a cell
Ω_{ray}	Solid angle associated with ray
τ	Optical depth of cell

adaptive ray tracing scheme, and our hybrid radiative transfer algorithm by performing four tests. In the first test, we turn off absorption of the radiation field to trace the radiative flux from a point source located at the center to demonstrate that our method recovers the correct r^{-2} fall-off of the flux. The second test focuses on the coupling of the hydrodynamics with the adaptive ray trace. We also demonstrate that *HARM*^{2} can

handle multiple sources with the third and fourth tests. Our third test demonstrates that our hybrid radiative transfer method can properly cast shadows and transfer radiative energy to the gas by illuminating a dense clump in a low-density medium with two point sources when the hydrodynamics is neglected. Finally, our fourth test follows a similar setup as the third test but demonstrates how the hydrodynamics are coupled to *HARM*^{2}. We set $\Phi_{\rm c} = 4$ for all validation tests in this section, and we use only a single frequency bin. For the first two tests we disable the moment method part of *HARM*^{2}, so that we can focus on the ray-tracing part of the algorithm. Further validation tests for the moment method have been presented in Krumholz *et al.* (2007b).

3.4.1 Flux Test

To demonstrate the accuracy of our adaptive ray trace and its ability to maintain spherical symmetry, we place a point source of luminosity $L_\star$ at the origin of a cubical domain extending from -1 to $+1$ pc in all directions. We set the opacity in all cells to zero and take $L_\star = 10^6\ L_\odot$ where $L_\odot = 3.84 \times 10^{33}$erg s^{-1} is the luminosity of the Sun. We use a base resolution of 128^3 and two levels of refinement. We refine cells that are located within 16 cells from the star.

In this setup, the total energy contained in the region that is a distance $< r$ from the origin should be exactly $E_{\rm exact}(< r) = L_\star r/c$, where the quantity r/c is simply the light-crossing time of the distance r. We can compare this to the total energy in this region returned by our code, which we can compute by noting that the radiation

energy density of a given cell that is traversed by a series of rays is

$$U_{\rm rad} = \sum_i \frac{L_{{\rm ray},i}}{dV}\frac{dl_i}{c} \tag{3.19}$$

where $L_{{\rm ray},i}$ is the luminosity for ray i, dV is the cell volume, and dl_i is the path length of the ray through the cell. The total energy contained within cells whose distance r_j from the origin is $< r$ is then

$$E_{\rm num}(< r) = \sum_{{\rm cells},\, r_j < r} U_{{\rm rad},j}\, dV \tag{3.20}$$

where $U_{{\rm rad},j}$ is the total radiation energy density summed over all cells with distance $< r$ from the origin. Perfect agreement would consist of $E_{\rm num}(< r) = E_{\rm exact}(< r)$.

Our results are shown in Figure 3.1. The left panel shows the line-of-sight projected radiation energy density of the point source radiation field (i.e., Equation (3.19)) integrated over the line of sight, which drops off as r^{-2} as expected. The two right panels compare $E_{\rm num}(< r)$ and $E_{\rm exact}(< r)$. We find that the difference between the numerical and exact results is always $< 5\%$, with the maximum error occurring close to the source where the resolution is poor. This error is expected because of the fact that we are using Cartesian rather than spherical grids.

3.4.2 Radiation-Pressure-Dominated HII Region

Next we perform a test to illustrate the coupling of the radiative transfer from the adaptive ray trace with the hydrodynamics, based on a similarity solution obtained

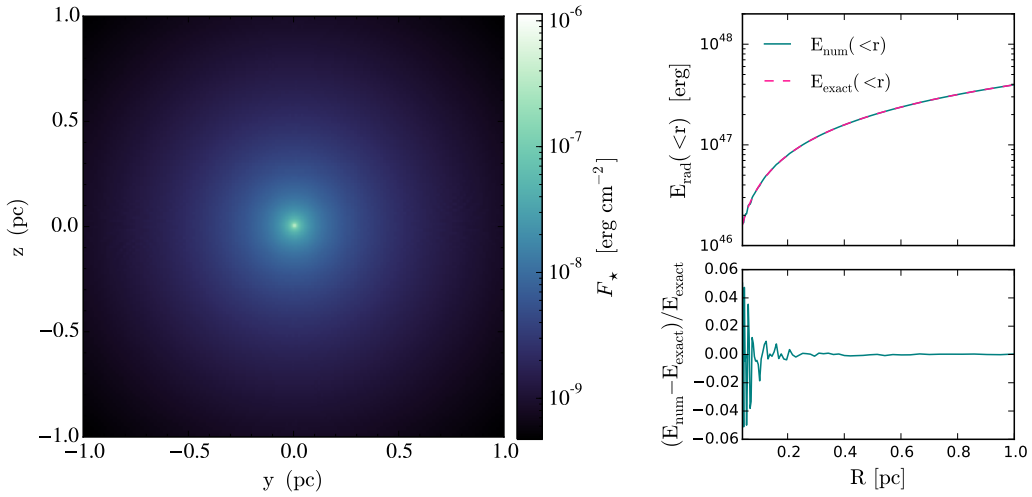

Figure 3.1 Performance test for the adaptive ray trace. Left panel: Projection plot of the stellar radiation density for a source with luminosity $10^6\ L_\odot$. The source flux falls off as $F(r) \propto r^{-2}$ as expected. Right panels: Comparison of the numerical and analytical results of the energy enclosed within radius r (i.e, $E_{\rm num}(< r)$) for the same source. Top panel: The pink dashed line shows the exact analytical solution and the teal solid line is the numerical result from the adaptive ray trace. The bottom panel shows the residuals from the exact and numerical solutions.

by Krumholz and Matzner (2009). We consider an initially-uniform, cold gas with an isothermal equation of state. At time $t = 0$ a point source of radiation with luminosity $L_\star$ turns on and begins depositing momentum in the gas. We consider material that has a very high opacity to photons coming directly from the point source, but a very low opacity to any re-emitted photons. A real-world example of this would be interstellar dust absorbing ultraviolet photons from a star, and then re-emitting them as infrared light, to which the dust is essentially transparent.

Because the opacity is high, all of the radiation from the point source is absorbed in an extremely thin layer, but then escapes immediately. Thus the point source deposits radial momentum into the gas at a rate $dp/dt = L_\star/c$. After a short time the

material around the point source will have been swept into a thin shell of radius $r_{\rm sh}$ and mass $M_{\rm sh} = 4\pi r_{\rm sh}^3 \rho_0/3$, where ρ_0 is the initial density. The shell obeys an equation of motion

$$\frac{d}{dt}\left(M_{\rm sh}\dot{r}_{\rm sh}\right) = \frac{L_\star}{c}. \tag{3.21}$$

This equation admits a similarly solution given by

$$r_{\rm sh}(t) = 1.15\left(\frac{n_0}{10^5\,{\rm cm}^{-3}}\right)^{-1/4}\left(\frac{L_\star}{10^6\,L_\odot}\right)^{1/4}\left(\frac{t}{\rm Myr}\right)^{1/2}\,{\rm pc} \tag{3.22}$$

where $n_0 = \rho_0/\mu m_{\rm p}$ is the number density, μ is the mean molecular weight which we set to 2.33 for molecular hydrogen and helium mixed in the usual cosmic ratio, and $m_{\rm p}$ is the proton mass.

To test the ability of our code to reproduce this solution, we consider a domain with a width of 1 pc, a uniform number density of $n_0 = 10^5$ cm^{-3} ($\rho_0 = 3.89 \times 10^{-19}$ g cm^{-3}), and a point source of luminosity $L_\star = 10^6 L_\odot$ at the origin. We set the specific opacity to $\kappa/\rho = 10^6$ cm^2 g^{-1}. We perform 3 tests on non-adaptive grids with varying resolution (64^3, 128^3, and 256^3) to explore how the accuracy of the adaptive ray trace depends on resolution.

Figure 3.2 shows a snapshot of the simulation results at $t = 0.1$ Myr. The top panels show the density slices and the bottom panels show the deposition rate of the stellar radiation energy density. We run the simulations to $t = 0.35$ Myr, but at later times we develop the carbuncle instability which distorts the shape of shock waves that move along grid directions (Pandolfi and D'Ambrosio, 2001; Stone *et al.*, 2008). One

can eliminate this instability by implementing extra dissipation in grid-aligned flows (Stone *et al.*, 2008), but since real applications are never perfectly grid-aligned, we have not done so here.

In Figure 3.3 we show how the radius of the shell in our simulation compares to the analytic similarity solution. We define the radius of the shell to be the density weighted average distance from the origin for cells where the density exceeds 1.5 ρ_0:

$$R_{\rm sh} = \frac{\sum_{\rm cells,\, \rho_j > 1.5\rho_0} \rho_j r_j}{\sum_{\rm cells,\, \rho_j > 1.5\rho_0} \rho_j}. \tag{3.23}$$

The top panel shows the shell radius as a function of time for each resolution and for the analytic solution, while the bottom panel shows the residuals. As in Figure 3.1, the residuals are largest at early times when the shell is poorly resolved, but the agreement becomes excellent at later times. The accuracy of the solution also improves with increasing resolution, as expected.

3.4.3 Hybrid Radiation Tests with Multiple Sources

To demonstrate that our hybrid radiation algorithm can properly cast shadows we perform two validation tests in which we have two point sources irradiate a dense clump of material. These tests are similar to the tests presented in Rijkhorst *et al.* (2006), Jiang *et al.* (2012), and Klassen *et al.* (2014). In our setup, we have a dense clump of material with radius 267 AU at the center of a (2000 AU)^3 computational domain. We take the clump density to be $\rho_{\rm c} = 3.89 \times 10^{-17}$ g cm^{-3} with uniform temperature of

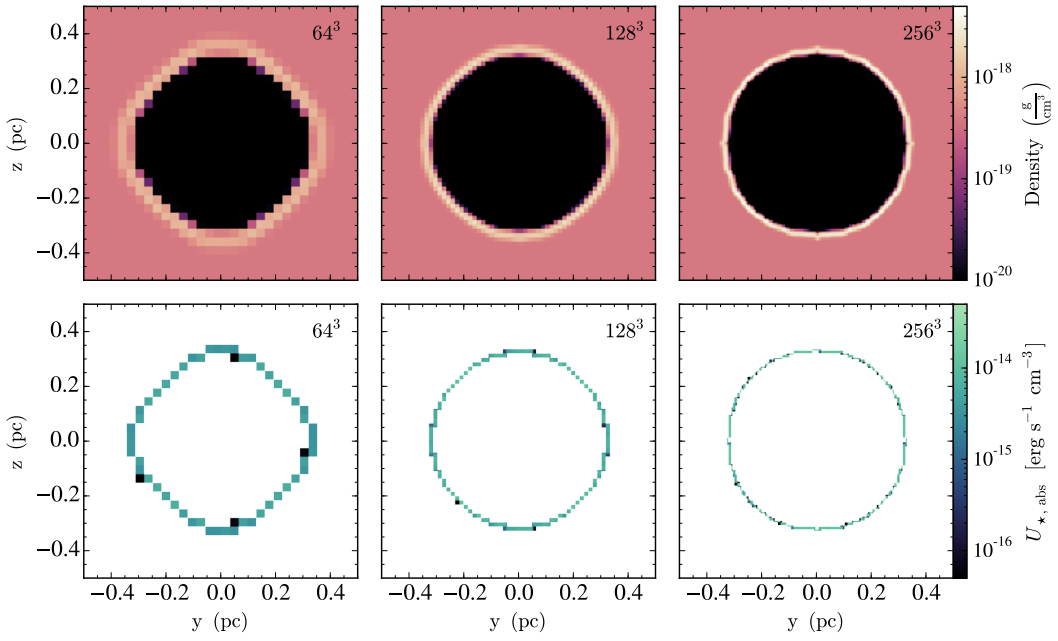

Figure 3.2 Results from the radiation-pressure-dominated H II region test to demonstrate the performance of the adaptive ray trace coupled to the hydrodynamics. Top (bottom) panels show slice plots of the gas density (rate of absorbed radiation energy density per unit time) for our radiation dominated sphere test at three different uni-grid resolutions (64^3, 128^3, and 256^3) taken at $t = 0.1$ Myr. As the bottom panels show, the direct radiation is absorbed only by the dense shell due to the high specific opacity, $\kappa = 10^6$ cm^2/g, used.

20 K. It is surrounded by a low density medium with density $\rho_a = 3.89 \times 10^{-20}$ g cm^{-3}. The clump is irradiated by two point sources, each with luminosity $L = 1\ L_\odot$. The two point sources are both located 368 AU from the edge of the spherical clump, and they are placed 90° apart from one another, so that they irradiate the clump from two angles.

We perform two tests to show that our new hybrid radiative transfer method can properly cast shadows and affect the hydrodynamics. The first test, presented in Section 3.4.3.1, assumes that the ambient medium is at the same temperature as the

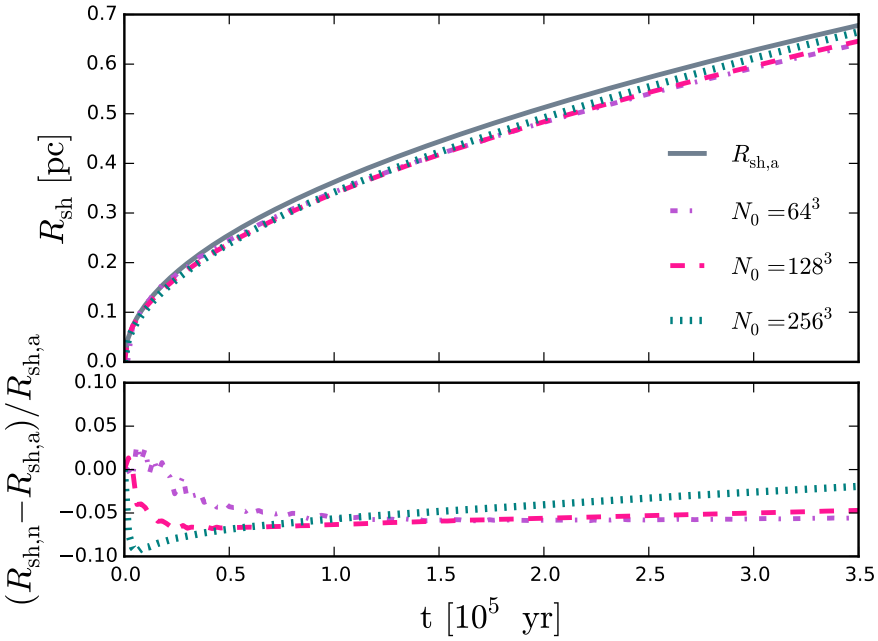

Figure 3.3 Shell position (top panel) and residuals (bottom panel) as compared to the analytical solution (i.e., eqn 3.22) for our radiation dominated sphere test at three different uni-grid resolutions (64^3, 128^3, and 256^3). The largest deviations from the analytical solution occur at early times when the shell is located close to the source but the numerical result follows the analytical solution better as the shell expands.

clump (20 K) so that we can follow the radiative heating of the gas. For this test we disable the hydrodynamics. In the second test, we set the temperature of the ambient medium to be 20×10^3 K so that the clump is initially in pressure balance with the low-density medium. In this test we enable the hydrodynamics. For both tests we use one frequency bin for the absorption of the direct radiation field and assume that the gas opacity is $\kappa = 64$ cm^2/g following the frequency dependent dust opacities in Weingartner and Draine (2001) (their $R_{\rm v} = 5.5$ extinction curve) corresponding to a frequency of $\nu = kT_{\rm eff}/h = 1.21 \times 10^{14}$Hz, where we have assumed $T_{\rm eff} = 5800$ K (i.e, the peak color temperature of the Sun). Our moment method uses the gray opacities

from Semenov *et al.* (2003).

3.4.3.1 Irradiation of a Dense Clump by two Point Sources with *HARM*^{2}

We perform our first hybrid radiation test on a uniform $(256)^3$ grid, disabling the hydrodynamics but allowing for absorption of the radiative energy by the gas. We run this test for $t = 2 \times 10^6$ s for two cases. In the first case, we only include absorption by the direct radiation field, i.e., we do not use the moment method, and in the second case we use the *HARM*^{2} algorithm. Figure 3.4 shows the irradiation from the direct radiation field from point sources (left panel), the irradiation from the dust-reprocessed radiation field (middle panel), and the combined irradiation from the point sources and dusty gas (right panel). The white region for the source irradiation demonstrates that our adaptive ray tracing method can properly cast shadows. The dusty gas absorbs energy from the direct radiation field, heats up, and re-emits as shown in the middle panel of Figure 3.4.

Figure 5 compares the temperature distribution for our run using the full *HARM*^{2} algorithm (right panel) to a case where we use only the ray trace, and omit the moment method (left panel). The temperature is highest near the point sources due to the larger radiative flux, thus leading to a larger absorption rate by the low-density gas. As the irradiation decreases farther away from the source, the gas attains lower temperatures due to the decreased heating rate of the absorbing medium. The right panel of Figure 3.5 shows that the re-emission by dust leads to lower temperatures and smoothes the radiation field. Note the almost discontinuous change in the gas

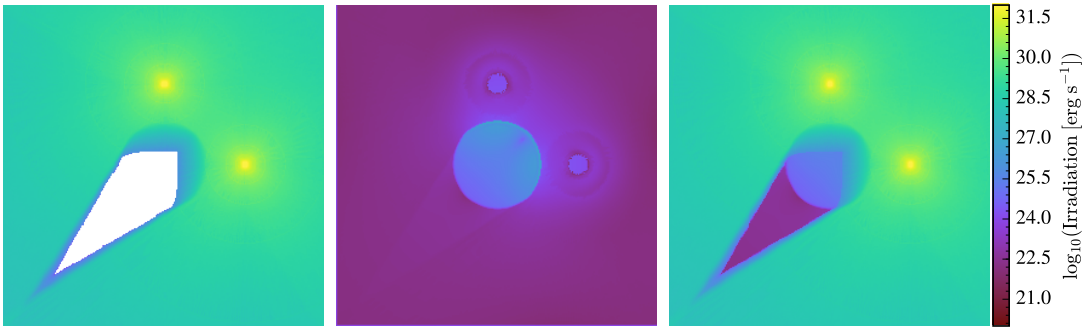

Figure 3.4 Irradiation of a dense clump by two point sources in an homogenous medium. The left panel shows the irradiation by the point sources' direct radiation fields while the middle panel shows the dust-reprocessed irradiation. The right panel shows the total irradiation by the stellar sources and dusty gas. The white region in the left panel, which shows where the direct irradiation is zero, demonstrates that our method can properly cast shadows.

temperature in the vicinity of the point sources in the full $HARM^2$ case. This is a result of a sharp drop in the opacity used for the moment method calculation, which causes a corresponding drop in the emissivity of the gas and thus a rise in its temperature. The physical origin of this discontinuity is sublimation of dust grains at temperatures above $\sim$ 1000 K (e.g., see Figure 4 of Semenov *et al.* (2003)), but from a numerical standpoint this is less important than the capability that this demonstrates. Our code can properly capture situations where the opacity that should be used for the direct radiation is very different than the opacity that is relevant for the reprocessed radiation field, for example because the direct and reprocessed radiation fields have very different color temperatures.

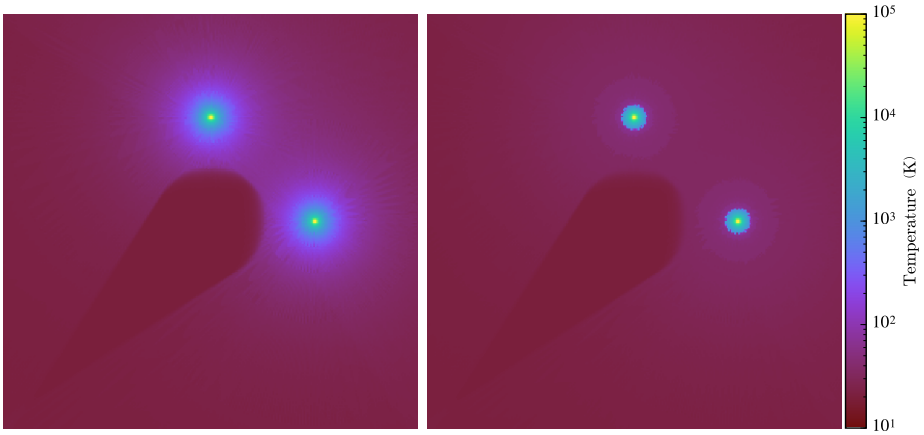

Figure 3.5 Same as the left and right panels of Figure 3.4, except showing the gas temperature where we only consider heating by the direct radiation field by including the adaptive ray trace (left panel) and where we consider heating by the direct radiation field and cooling by the dusty gas using *HARM*^{2} (right panel).

3.4.3.2 Irradiation of a Dense Clump by two Point Sources with *HARM*^{2}and Hydrodynamics

Our fourth validation test demonstrates our *HARM*^{2} algorithm operating in the context of a full radiation-hydrodynamic problem. We set the initial conditions to be exactly the same as the previous test except for the ambient gas temperature, which we set to 20×10^3 K so that the clump is initially in pressure balance with the ambient medium. Additionally, we enable the hydrodynamics and we also set the ambient medium to be transparent to the direct and diffuse radiation fields. Our base grid is $(128)^3$ and we refine the entire clump to one greater level of refinement (i.e., the clump has $(256)^3$ refinement).

Figure 3.6 shows the evolution of the density, temperature, and clump velocity of the simulation. This Figure demonstrates that the absorption of the point sources'

direct radiation field heats up the sides of the clump that are closest to the sources, causing the edges to expand. The momentum imparted by the direct radiation field to the clump also causes it to expand non-uniformly. We note that as the cloud becomes over-pressurized it expands into the ambient medium yielding large velocities along the edges of the cloud. As the simulation evolves the cloud is slowly disrupted leading to low density material expanding towards the point sources. The expansion of this low density material leads to instabilities as the clump material mixes with the low density gas. At late times the expansion of the low-density clump material closest to the point sources slows as the direct radiation field imparts momentum to the gas.

3.5 Performance Tests

It is important for our code to scale well with number of processors, especially for large simulations. Scaling tests demonstrate the efficiency of a parallel application when increasing the number of processors. In this section we present both weak and strong scaling tests to demonstrate the parallel performance of our adaptive ray trace algorithm. We also perform a strong scaling test for our hybrid radiation algorithm in section 3.5.2.3 in an AMR simulation to demonstrate the scaling capability of $HARM^2$ for a demanding, research application. For all tests, we set $\Phi_c = 4$ and also have the initial ray level set to 4 so that 3072 rays are initialized at the beginning of each ray trace step. All of the following performance tests were run on the Sandy Bridge nodes on the NASA NAS machine Pleiades.

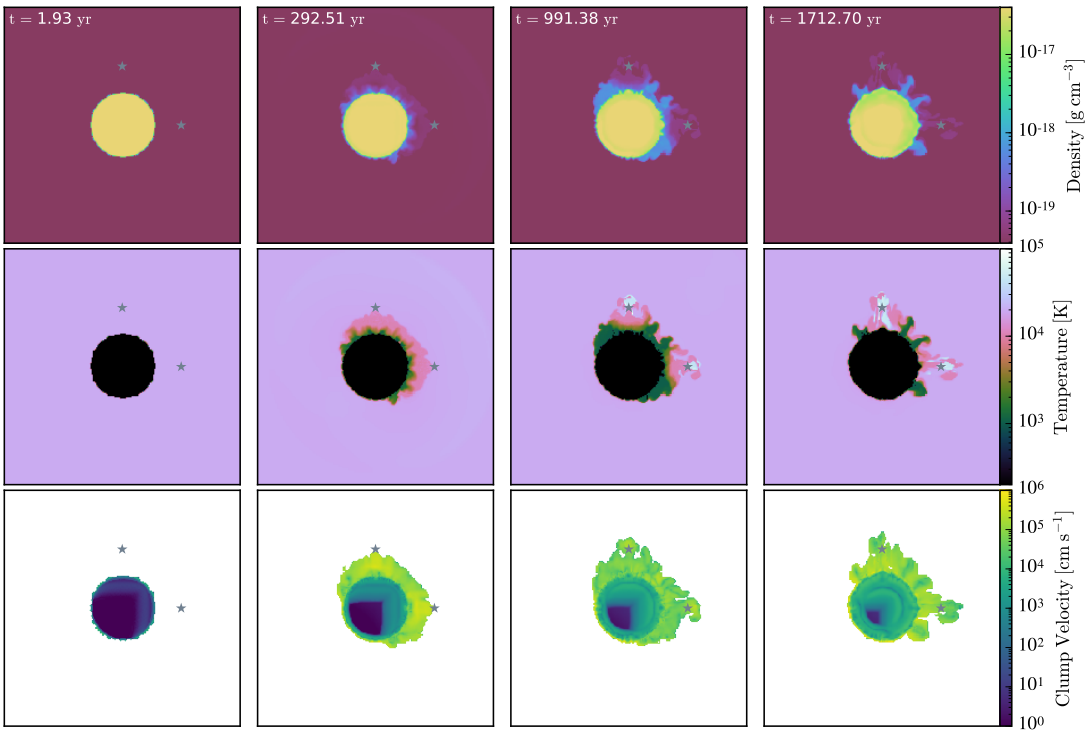

Figure 3.6 Snapshots of the radiation-hydrodynamical time evolution of a dense clump in a low-density transparent medium that is irradiated by two point sources using our *HARM*^{2} radiative transfer method. Different columns show different times, and different rows show different quantities: density (top), temperature (middle), and velocity magnitude (bottom). The heating and momentum deposition by the point sources' direct radiation fields cause the edges of the clump to expand. The gray stars denote the location of the radiating point sources.

3.5.1 Weak Scaling

Weak scaling tests demonstrate how well a parallel code scales with the number of processors while the workload assigned to each processor remains the same. For this purpose, we perform a weak scaling test on non-adaptive grids where each processor has one 32^3 grid and one radiating sink particle. Each 32^3 grid represents a $(1\ \mathrm{pc})^3$ domain with constant gas density, $n = 10^4\,\mathrm{cm}^{-3}$, with a radiating source placed at the

center. The physics modules we include are the adaptive ray trace and hydrodynamics. We set the opacity in all cells to zero so that no absorption of the radiation field occurs. To ensure that each processor performs the same amount of work with the ray trace, including the propagation of rays and the subsequent communication of rays to other processors, we terminate rays once they have traveled 0.6 pc from their originating source. This allows for rays to propagate to their neighboring grids and also enforces that all grids, except the grids along the domain edges, communicate the same number of rays to their neighbors. In short, the rays interact with the cells they cross but do not add energy or momenta to the fluid.

Our weak scaling tests were run on $N_{\rm CPU} = n^3$ processors, where n=[1,2,...,9, 10], for 50 time steps per weak scaling test. The weak scaling test results are presented in Figure 3.7 and show the total time spent per time step (black solid line) and the timing of the adaptive ray trace components: ray communication (gray dotted line), ray trace across cells (pink dashed line), adaptive ray trace overhead (i.e., locating ray grids, ray splitting, etc. – purple dot-dashed line), total adaptive ray trace (ray trace and associated overhead – blue dashed line), and the full adaptive ray trace which includes the ray communication (dot-dashed teal line). We note that a horizontal line denotes perfect weak scaling.

Our timing results show that the tracing of rays across cells has near-perfect weak scaling for all processor counts and that the adaptive ray trace overhead exhibits near perfect weak scaling until ∼216 processors. We also find that the costs associated with the overhead are more expensive than ray tracing alone. Finally, our ray commu-

nication algorithm is cheaper than the ray tracing up to ∼343 processors and cheaper than the costs associated with the adaptive ray trace overhead up to ∼729 processors. The ray communication only becomes as expensive as the adaptive ray trace at ∼1000 processors. This is because our asynchronous communication algorithm, described in section 3.3.3, has a $N_{\rm CPU}^{0.67}$ dependence. These results confirm that our communication algorithm is much more scalable and efficient when compared to previous methods. For example, the ray communication timing in Wise and Abel (2011) followed a $N_{\rm CPU}^{1.5}$ dependence and became the dominant cost of the ray trace at only $\sim$ 200 CPUs, despite the fact that their weak scaling test uses 64^3 rather than 32^3 blocks, and thus is significantly less stringent than ours.

3.5.2 Strong Scaling

Strong scaling demonstrates how well the code performs as the number of processors for a given problem increases while the total workload remains the same. We perform three tests to demonstrate the strong scalability of the adaptive ray trace and the *HARM*^{2} algorithm in a demanding, research application. The first two tests are performed on non-adaptive grids. The first test measures the strong scalability of the adaptive ray trace based on the number of cells that interact with rays (see Section 3.5.2.1) while the second test focuses on the strong scalability of the adaptive ray trace as a function of the number of frequency bins used (see Section 3.5.2.2). The third test shows the parallel performance of *HARM*^{2} in a demanding, research AMR simulation. In addition to *HARM*^{2}, this test also includes other physics modules in ORION such

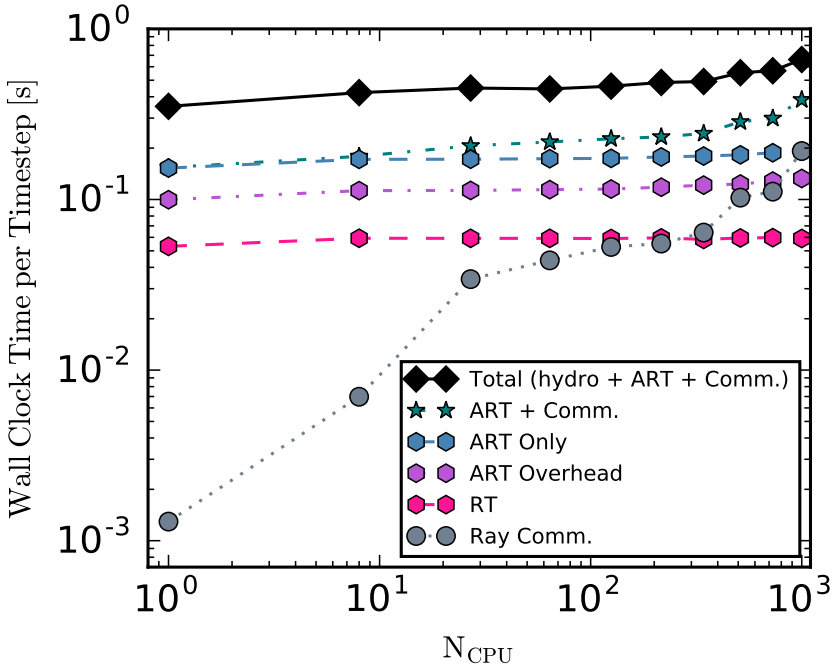

Figure 3.7 Weak scaling test with one 32^3 block per process. Each block is (1 pc)^3 and contains one radiating source at its center. Rays are terminated after they have traveled 0.6 pc from the source to ensure communication of rays to neighboring grids. Weak scaling results are shown for the ray communication (gray dotted line), ray tracing across cells (pink dashed line), overhead associated with the adaptive ray trace (purple dot-dashed line), adaptive ray trace excluding the communication of rays (blue line), the total cost of the adaptive ray trace including parallel communication of rays (teal dot-dashed line), and the total time spent on the hydrodynamics and adaptive ray tracing (solid black line). Ray communication is cheaper than the adaptive ray trace (ray trace and associated overhead) for $N_{\rm CPU} \lesssim 1000$ processors. The communication shows a $N_{\rm CPU}^{0.67}$ dependence.

as hydrodynamics, self-gravity, and sub-grid star particles. Each test and their results are described below.

3.5.2.1 Uni-grid Ray Trace Test with Varying Termination Lengths

We first use a setup similar to a single instance of our weak scaling test: a (1 pc)^3 domain with a single point source placed at its center. The resolution of the

computational domain is 256^3 cells and each grid consists of 16^3 cells yielding a total of 4096 grids, with no adaptivity. We perform three sub-tests with this setup in which the rays are destroyed after traveling 0.2 pc from their source, 0.4 pc from their source, or allowed to transverse the entire domain, respectively. These calculations were performed on $N_{\rm CPU} = 2^n$ processors with n=[2,...,9,10] for 5 time steps per test.

Our strong scaling results are presented in Figure 3.8, which shows the total CPU time per time step, $t_{\rm CPU}$, for the adaptive ray trace. (Note that, whereas in Figure 3.7 we plotted the time per processor, here we plot the total time summed over all processors, so that perfect scaling would again appear as a flat horizontal line.) To better quantify the results, we perform a χ^2 fit of our measured results to the functional dependence $t_{\rm CPU} \propto N_{\rm CPU}^a$; perfect strong scaling would be $a = 0$. We report these results in Table 3.2.

When we allow rays to traverse the entire computational domain, we find near-perfect strong scaling out to 1024 processors: $t_{\rm CPU} \propto N_{\rm CPU}^{0.084}$. As we lower the distance that rays propagate, the scaling deteriorates, for the obvious reason that processors which are assigned computational domains that rays do not reach are simply idle because they do not contribute to the ray trace computation. Indeed, we also report the fraction of the computational volume over which rays propagate in Table 3.2, and it is clear that the scaling is worse when this value is small.

Table 3.2 Fitted scaling results from our uni-grid strong scaling tests presented in Figure 3.8, together with the fraction of the computational volume over which the ray trace is performed. A value of $a = 0$ would imply perfect strong scaling.

$D_{\rm Ray}$	Ray-interaction Volume	a ($N^a_{\rm CPU}$)
0.2 pc	0.0335	0.52
0.4 pc	0.2681	0.27
Whole	1	0.084

3.5.2.2 Timing with Varying Frequency Bins

Our adaptive ray trace algorithm allows for an arbitrary number of frequency bins N_ν. Each ray has two arrays that contain N_ν doubles (size 8 bytes) that hold the ray's initial and current frequency-dependent luminosities, respectively. The choice of N_ν impacts the cost of the computation in two ways: (1) the ray trace operations must loop over all frequency bins when creating rays, advancing them across cells, and checking if they become extinct due to absorption by the fluid; and (2) MPI communication operations depend on the size of the message that is being sent and/or received. Therefore, increasing the number of frequency bins for the adaptive ray trace will lead to an increased cost in the overhead associated with the advancement and communication of rays.

To test the scaling efficiency of the adaptive ray trace as a function of N_ν we ran a series of tests where we vary the number of frequency bins. Our initial setup of our test problem is the same as the strong scaling test discussed in section 3.5.2.1 in which a radiating source is at the center of a (1 pc)^3 box. We terminate the rays after they have travelled 0.5 pc and perform tests for $N_\nu = (1, 2, 8, 16, 20, 32, 48, 64)$

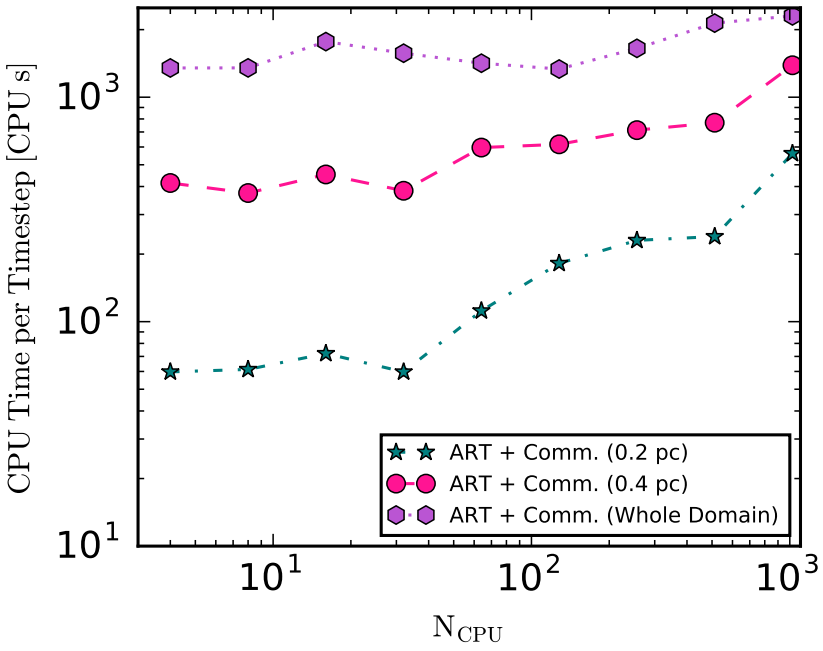

Figure 3.8 Strong scaling test with a 256^3 uni-grid calculation with a radiating point source at the center. We performed two tests where the rays are terminated after they travel 0.2 or 0.4 pc from their source and a third test where the rays transverse the entire domain. Perfect strong scaling would yield a flat line for each test. Our results show that the strong scaling performance improves as the volume that the rays interact with increases and that near-perfect strong scaling is attained when the rays transverse the entire domain.

frequency bins. Our base grid is 256^3 and we ran our scaling tests on 128 processors for 50 time steps per test. Perfect strong scaling on this test would be a computational cost proportional to N_ν, since the number of ray-cell interactions is linear in N_ν.

Our strong scaling results with varying N_ν are shown in Figure 3.9. We find that the wall clock time spent per ray trace increases with N_ν as expected, but that this increase is highly-sublinear, particularly at small N_ν. We find $t_\nu \propto N_\nu^{0.14}$ for 1-8 frequency bins and $t_\nu \propto N_\nu^{0.65}$ for 16-64 frequency bins. While these results might at first seem surprising, they make sense when we recall that the overhead associated with

the ray tracing – solving the geometric problem of finding the paths of rays through cells and grids, the probing and handshaking parts of the communication steps – does not scale with N_ν. As we increase N_ν, this overhead is "amortized" over a larger number of frequency bins, and thus we obtain what appears to be better-than-perfect strong scaling. As the number of frequency bins increases, this effect becomes less important, and the parts of the computation that do scale with N_ν – computing the opacities of cells and updating fluxes, transferring flux data between processors – begin to dominate. For sufficiently large N_ν we do begin to approach the expected $N_\nu^{1.0}$ scaling, but our results thus far demonstrate that we can use up to $\sim$ 10 frequency bins at near-zero additional cost, and several tens at only modest cost, compared to the single-frequency case.

3.5.2.3 AMR Simulation: Application to High-Mass Star Formation

Our final strong scaling test is an AMR simulation that includes hydrodynamics, self-gravity, radiative transfer, and radiating sink particles to demonstrate how our new *HARM*^{2} algorithm scales in a demanding research application. Here we perform strong scaling tests for two different outputs from an ORION AMR simulation of the formation of a high-mass stellar system. The results of this simulation are presented in Rosen *et al.* (2017) and Chapter 4 but we briefly summarize our problem setup here.

Our initial condition is a rotating, laminar 150 $M_\odot$ molecular core with radius 0.1 pc. The core follows a $\rho(r) \propto r^{-3/2}$ density profile. We use a domain size of 0.4 pc on each side, a base resolution of 128^3 and five levels of refinement which yields a

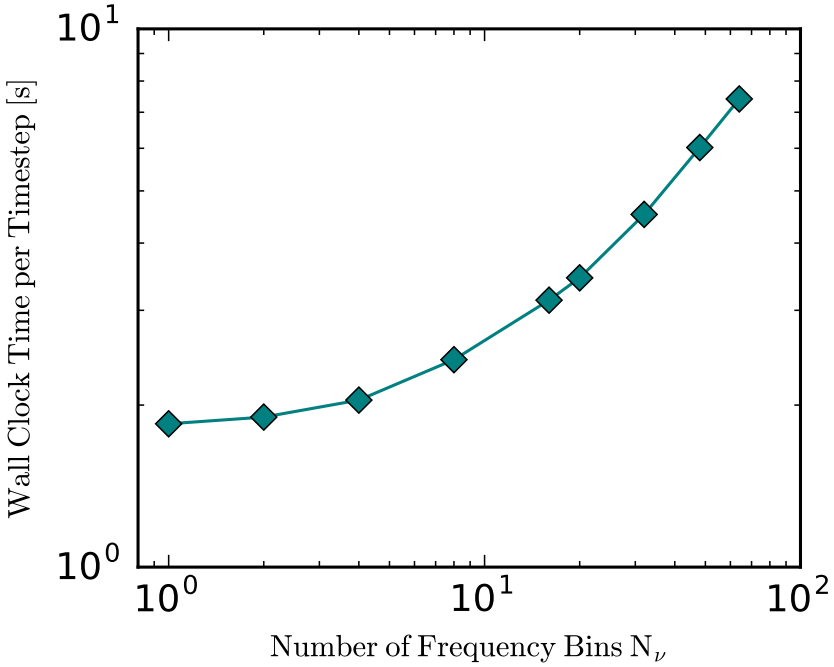

Figure 3.9 Frequency bin scaling test where we have varied the number of frequency bins N_ν. There is one source at the center of a $(128)^3$ domain and we truncate rays once they have traveled 0.5 pc. The cost of the ray trace rises with N_ν, as expected, but this effect is small for low N_ν.

maximum resolution of 20 AU on the finest level. To properly model the absorption of the direct radiation field from stars we use the frequency dependent stellar atmosphere profiles from Lejeune *et al.* (1997) to model the stellar spectra. Our choice of the opacities depend on whether the primary absorber is dust or molecular gas. Dust is the primary absorber for gas temperatures below $T_{\rm sub} = 1500$ K (i.e., the temperature at which dust sublimes) (Semenov *et al.*, 2003) while molecular hydrogen is the primary absorber for gas temperatures within $T_{\rm sub} \leq T < T_{\rm H\ II}$ where $T_{\rm H\ II} \approx 10^4$ K is the temperature at which we expect hydrogen to become fully ionized, and thus to have the usual Thompson opacity for electron scattering. If the primary absorber is dust

we use the frequency dependent dust opacities from Weingartner and Draine (2001) (their $R_{\rm v} = 5.5$ extinction curve), if it is molecular hydrogen we set the molecular gas opacity to 0.01 $\rm cm^2\,g^{-1}$, and if $T \geq T_{\rm H\ II}$ we set the opacity to zero. The last of these is a numerical convenience, because we have not implemented scattering or ionization chemistry, and because the regions in our computation with $T > T_{\rm H\ II}$ generally contain so little mass they will be optically thin anyway. We assume a dust-to-gas ratio of 0.01 and choose $N_\nu = 10$.

At $t = 0$ the molecular core begins to gravitationally collapse. As the core collapses a star forms at the center and continues to grow in mass via accretion. An accretion disk forms around the star due to conservation of angular momentum of the infalling material. Gravitational instabilities develop in the disk causing it to fragment into companion stars. The absorption of energy and momenta from the direct stellar radiation field and the diffuse dust-reprocessed radiation field from the fluid results in low-density, radiation pressure dominated bubbles near the poles of the most massive star that expand with time. Figure 3.10 shows slices parallel to the x-direction of the gas density (top panels) and absorbed direct radiation energy density (bottom panels) by the dust and gas for two different snapshots of this simulation at $t = 15.22$ kyrs and $t = 23.67$ kyrs. We only show the central $(8000\ {\rm AU})^2$ region of the computational domain because the majority of the domain is not affected by the direct radiation field. The most massive stars in these snapshots are 16.59 $M_\odot$ and 33.57 $M_\odot$, respectively. The early snapshot contains one star while the later snapshot contains eight stars where the companions range from $0.01 - 1.48\ M_\odot$ in stellar mass. These snapshots represent

typical "early" and "late" stages of the computation, with the latter being much more computationally expensive due to the larger number of sources and the greater distances that the direct radiation can propagate before being absorbed. We note that both the early and late stages are strong tests of the scalability, because the radiating sources are confined to a small portion of the computational volume, rather than being scattered throughout (c.f., the test presented in Wise and Abel (2011), which used a cosmological simulation where point sources were distributed nearly-isotropically.)

Our strong scaling results are shown in Figure 3.11, where we measure the time spent on the hydrodynamics, gravity, FLD, adaptive ray trace, and the total radiation module (adaptive ray trace and FLD). A horizontal line would correspond to perfect strong scaling. We ran each timing test for five time steps on $N_{\rm CPU} = 16 \times n$ processors where $n = [1, 2, ..., 8]$. The early snapshot contains 448 grids and the later snapshot contains 1137 grids at the beginning of each test. The top panel shows the timing results for the early snapshot and the bottom panel shows the results for the later snapshot. Comparison of the two panels show that the scalability for all modules in ORION become better at later times, especially for the adaptive ray trace when more grids are processing rays. This is due to the increase in number of grids per processor which reduces the MPI communication costs. A general rule of thumb for patch-based AMR methods such as ORION is that the the code is efficient at ~ 4 grids per CPU or more, and our tests are consistent with this. We find that our timing results for the adaptive ray trace follows $t_{\rm WC,ART} \propto N_{\rm CPU}^{0.97}$ for the early snapshot and $t_{\rm WC,ART} \propto N_{\rm CPU}^{0.56}$ for the later snapshot. These results agree with our strong scaling results from Section 3.5.2.1

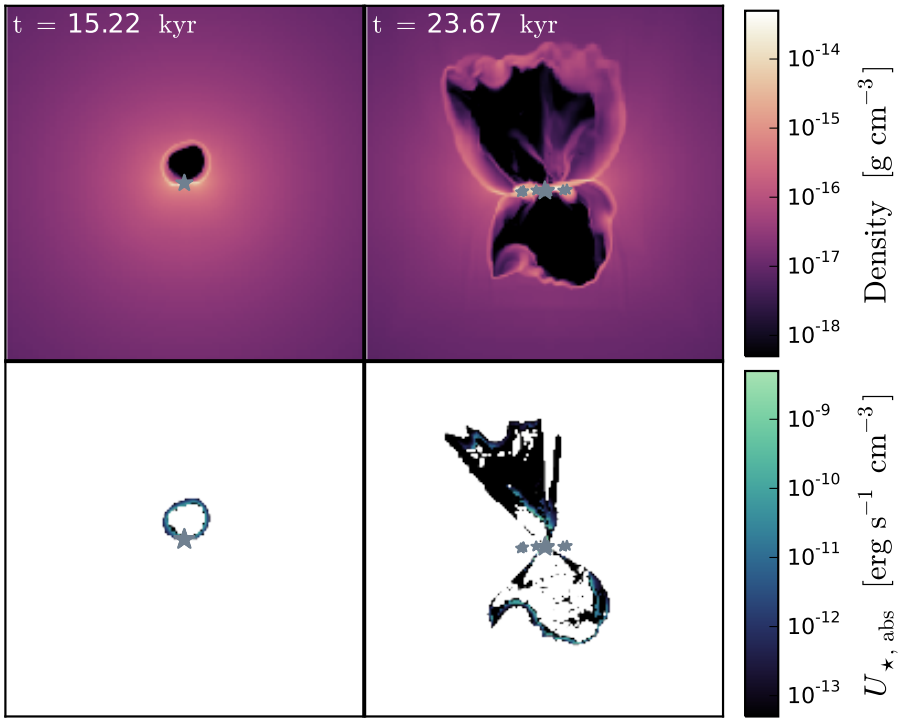

Figure 3.10 Example AMR simulation that uses our *HARM*^{2} algorithm. Here we show slice plots along the x-direction of the mass density (top) and absorbed direct radiation energy density (bottom) for two snapshots of a simulation of the formation a high mass star system. Gray stars denote the location of the stars, with the most massive star being largest. The left (right) panels show the snapshot when the simulation has progressed to 15.22 kyrs (23.67 kyrs) where the most massive star is 16.59 $M_\odot$ (33.57 $M_\odot$).

which showed that our parallelization procedure for the adaptive ray trace becomes more efficient as the number of grids that interact with rays increases. We find that the moment method, FLD in our case, is the most expensive module while gravity is the cheapest, and that the adaptive ray trace can be cheaper and/or about the same expense as the hydrodynamics.

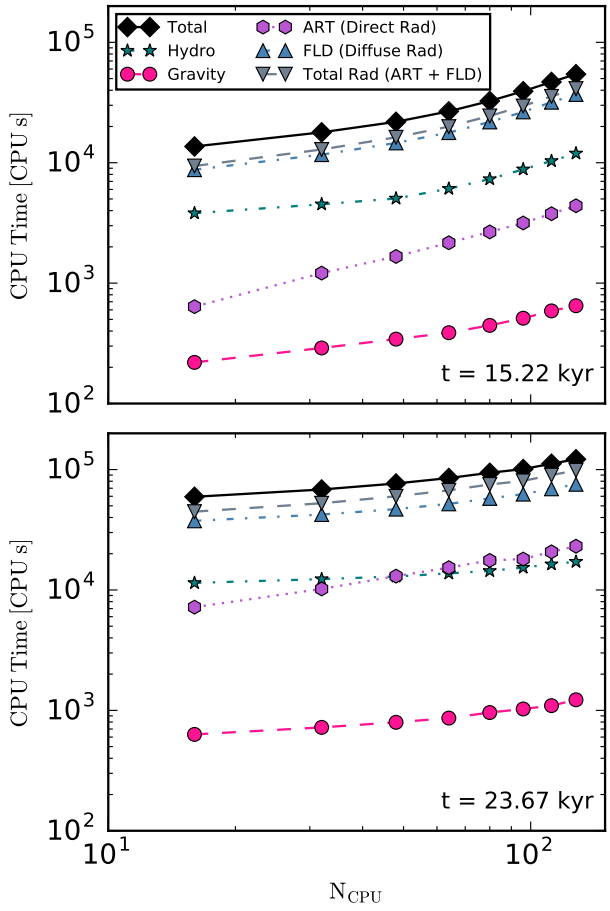

Figure 3.11 Strong scaling test with a 128^3 AMR simulation with 5 levels of refinement of the formation of a massive star system shown at two different simulation outputs from 15.22 kyrs (top) and 23.67 kyrs (bottom). The early (late) snapshot has 448 (1137) grids. The bottom panel shows that the scalability of the adaptive ray trace increases as the simulation progresses because rays interact with a larger volume of the computational domain (e.g., see Figure 3.10).

3.6 Summary

In this paper, we have presented our implementation of *HARM*^{2} – a new highly-parallel multi-frequency hybrid radiation hydrodynamics module that combines an adaptive long characteristics method for the (direct) radial radiation field from point

sources with a moment method that handles the (thermal) diffuse radiation field produced by a volume-filling fluid. Our new method is designed to be used with adaptive grids and is not limited to specific geometries. We have coupled $HARM^2$ to the hydrodynamics in the astrophysical AMR code ORION which includes flux limited diffusion, but our method can be applied to any AMR hydrodynamics code that has asynchronous time stepping and can incorporate any moment method. Although our implementation is not the first hybrid radiation scheme implemented in an AMR code, it is more accurate than previous methods because it uses long rather than hybrid characteristics. Furthermore, our new algorithm can be used in a variety of radiation hydrodynamics problems in which the radiation from point sources and diffuse radiation field from the fluid should be modelled. Such examples are the study of the formation of isolated high-mass stars and clustered star formation in the dusty interstellar medium.

One of the major difficulties with incorporating a long characteristics method in an AMR code that allows for a general geometry, where the hydrodynamics is parallelized by domain decomposition, is the parallel communication of rays. This is because ray tracing is a highly serial process and each ray will usually cross multiple processor domains. In order to avoid significant communication overheads and serial bottlenecks that often occur with long characteristics methods we have implemented a new completely asynchronous and non-blocking communication algorithm for ray communication. We performed a variety of weak and strong scaling tests of this method, and found that its performance is dramatically improved compared to previous long characteristics methods. In idealized tests without adaptive grids we obtain near-perfect weak scaling

out to > 1000 cores, and, in problems where the characteristic trace covers the entire computational domain, near-perfect strong scaling as well. Previous implementations became communications-bound at processor counts a factor of ~ 4 smaller than this. In a realistic, demanding research application with a complex, adaptive grid geometry, and using 10 frequency bins for the characteristic trace, we find excellent scaling as long as there are at least $\sim 3 - 4$ grids per CPU, and we find that the cost of adaptive ray tracing is smaller than or comparable to hydrodynamics, and significantly cheaper than flux limited diffusion.

Since *HARM*^{2} works for adaptive grids in a general geometry, it can be used in a variety of high-resolution simulations that require radiative transfer. Our implementation in ORION will be made public in an upcoming release of the ORION code, and the *HARM*^{2} source code will be made available immediately upon request to any developers who are interested in implementing *HARM*^{2} in their own AMR codes.

Chapter 4

The Formation of Massive Stars with Hybrid Radiative Transfer

A version of this chapter has been published as "An Unstable Truth: How Massive Stars get their Mass," Rosen, A. L., Krumholz, M. R., McKee, C. F., Klein, R. I. 2016, *Monthly Notices of the Royal Astronomical Society*, 463, 2553.[1]

4.1 Introduction

Massive stars live fast and die young. They are the major contributors to heavy element production in the Universe through their explosive deaths enriching the interstellar medium (ISM). Massive stars are rare, representing only $\sim 1\%$ of the stellar population by number, yet they dominate the energy budget in the Milky Way and other star-forming galaxies because of their strong radiation fields, stellar winds, and

[1] ©2016. Oxford University Press on behalf of the Royal Astronomical Society. All rights reserved. Reprinted here with permission.

supernova explosions. This stellar feedback – the injection of energy and momentum by stars into the ISM – limits their masses thereby affecting nuclear yields, slows down nearby star formation, and affects galaxy evolution.

Recent studies suggest that the pressure exerted by massive stars' radiation fields may be the dominant feedback mechanism during their formation (Krumholz *et al.*, 2009; Kuiper *et al.*, 2011, 2012; Klassen *et al.*, 2016). Massive stars have short Kelvin-Helmholtz timescales (the time required for a star to radiate away its gravitational binding energy) and contract to the main-sequence while they are accreting (Palla and Stahler, 1991, 1992; Behrend and Maeder, 2001; Hosokawa and Omukai, 2009). Therefore they attain their main sequence luminosities while they are still actively accreting and the radiation pressure associated with their high luminosities can oppose gravity and halt accretion (Larson and Starrfield, 1971; Yorke, 1979; Yorke *et al.*, 1995; Wolfire and Cassinelli, 1986, 1987; Yorke and Bodenheimer, 1999).

The relative importance of the radiative force ($f_{\rm rad}$) and the gravitational force ($f_{\rm grav}$) can be described in terms of the Eddington ratio, $f_{\rm edd} = f_{\rm rad}/f_{\rm grav}$, which simplifies to

$$f_{\rm edd} = 7.7 \times 10^{-5} \left(1 + f_{\rm trap}\right) \left(\frac{L_\star}{M_\star}\right)_\odot \left(\frac{\Sigma}{1 \text{ g cm}^{-2}}\right)^{-1} \tag{4.1}$$

where Σ is the surface density of the optically thick infalling material and $(L_\star/M_\star)_\odot$ is the stellar light-to-mass ratio in solar units. The factor $(1 + f_{\rm trap})$ included in $f_{\rm rad}$ denotes the combined contribution from the direct radiation pressure associated with the first absorption of the stellar radiation field and the reprocessed thermal, diffuse radia-

tion pressure associated with the re-emission by interstellar dust, respectively. Here $f_{\rm trap}$ denotes the trapping factor at which the radiation field is enhanced by the subsequent absorption and re-emission by interstellar dust. For spherically symmetric accretion, Equation (4.1) exceeds unity for stars with masses above $\sim 15-20\ M_{\odot}$ (Pollack *et al.*, 1994; Krumholz *et al.*, 2009). If accretion onto the star were isotropic then stars with masses in excess of this limit should not form, a problem commonly known as "the radiation pressure barrier problem." However, recent studies suggest that massive stars with initial masses well in excess of 150 $M_{\odot}$ exist and can have a dramatic impact on their environments (Crowther *et al.*, 2010, 2016).

Given the existence of massive stars, a number of solutions to the radiation pressure problem have been proposed in the literature. Nakano (1989) and Jijina and Adams (1996) present analytic models suggesting that accretion through a disk could circumvent the radiation pressure barrier, while McKee and Tan (2003) suggest that high accretion rates could provide sufficient ram pressure even in spherical symmetry. Krumholz *et al.* (2005) showed that escape of radiation through outflow channels could ease the radiation pressure problem. Numerical simulations within the last several decades generally support these hypotheses. Most of these simulations model the collapse of isolated, slowly rotating, and initially laminar pre-stellar massive cores (Yorke and Bodenheimer, 1999; Yorke and Sonnhalter, 2002; Krumholz *et al.*, 2009; Kuiper *et al.*, 2011, 2012; Klassen *et al.*, 2016). In these idealized simulations, the radiation pressure barrier is circumvented by the formation of an optically thick accretion disk that surrounds the massive star. With this anisotropy, the radiative flux easily escapes

along the polar directions of the star, launching radiation pressure dominated bubbles both above and below the star. This "flashlight" effect allows material to be funneled to the star by the accretion disk and gravitational instabilities present in the disk can enhance the accretion rate onto the star (Yorke and Sonnhalter, 2002; Krumholz *et al.*, 2009; Kuiper *et al.*, 2011, 2012; Klassen *et al.*, 2016).

Whether material is supplied to the star via disk accretion alone has been heavily debated in the literature (Krumholz *et al.*, 2009; Kuiper *et al.*, 2011, 2012; Klassen *et al.*, 2016). Krumholz *et al.* (2009) performed the first adaptive mesh refinement (AMR) 3D radiation-hydrodynamic simulation of the formation of a massive stellar system and found that the dense shells that surround the radiation pressure dominated bubbles become radiative Rayleigh-Taylor (RT) unstable. In this configuration, the dense shells that surround the rarefied radiation pressure dominated bubbles develop perturbations at the interface that grow exponentially, leading to "fingers" in the heavier fluid (the accreting gas) that sink into the lighter, more buoyant fluid (represented by the radiation field; Jacquet and Krumholz (2011)). These RT "fingers" can reach the star-disk system if they are not pushed back by radiation pressure, and deliver a significant amount of mass to the accretion disk that can then be incorporated into the star.

The presence of these instabilities can allow stars to grow beyond their Eddington limit but their development and growth is sensitive to how the radiation pressure is treated. Krumholz *et al.* (2009) only included the dust-reprocessed radiation pressure, which was modeled with the gray flux limited diffusion (FLD) approximation, and as-

sumed that the stellar radiation energy was deposited within the vicinity of the star, which underestimated the true radiation pressure. If the radiation pressure, especially the component of the radiative force that is anti-parallel to the gravitational force, is underestimated then the gas is less likely to be pushed away by radiation. Furthermore, an anisotropic radiation field can lead to density perturbations in the dense shells of the radiation pressure dominated bubbles that can then amplify and become RT unstable. These instabilities can grow and deliver material to the star-disk system.

To better represent the true radiation field in massive star formation simulations Kuiper *et al.* (2010) developed a hybrid radiation algorithm that included a multi-frequency raytracer, in which a series of rays travel radially away from the star and transfer energy and momentum to the absorbing dust, coupled to gray FLD to model the diffuse dust-reprocessed radiation field. With this method, Kuiper *et al.* (2011, 2012) performed a series of 3D simulations of the formation of massive stars from the collapse of laminar pre-stellar cores on a non-adaptive spherical non-uniform grid with resolution increasing logarithmically towards the center. The authors find that the star is fed through disk accretion only and that the radiation pressure dominated bubbles do not become RT unstable. They conclude that inclusion of the direct radiation pressure is responsible for maintaining stability of the expanding bubble shells.

The work of Krumholz *et al.* (2009) and Kuiper *et al.* (2011, 2012) both have their advantages and disadvantages. AMR simulations with a general Cartesian geometry, such as the simulation presented in Krumholz *et al.* (2009), can handle an arbitrary number of moving stars. The resulting gravitational interaction of the massive star with

its accretion disk can induce gravitational instabilities leading to disk fragmentation. In addition, movement of the massive star within the accretion disk can lead to shielding of the stellar radiation field resulting in a greater asymmetry in the direct radiation pressure, potentially seeding RT instabilities. One key advantage in AMR simulations, as compared to a non-adaptive grid, is that instabilities that may develop in the dense bubble shells can be resolved dynamically throughout the bubble evolution. In classical RT theory, the smallest perturbations grow fastest in the linear regime and these perturbations can only grow if they are resolved. The bubble shells in the work of Krumholz *et al.* (2009) are resolved to the finest level, likely allowing for small RT instabilities to grow large enough to deliver material to the star-disk system.

In contrast, the bubble shells in the work of Kuiper *et al.* (2011, 2012) are poorly resolved because they use a non-adaptive spherical grid. Furthermore, the star is artificially held at the origin of the grid, thereby suppressing potentially-important instabilities that could seed RT instabilities. However, these simulations included a much better treatment of the radiation field by incorporating a multi-frequency raytracer to model the direct radiation field. In such a geometry raytracing becomes trivial because the rays travel radially from the non-moving star, but this geometry can not support additional stars or disk asymmetries induced by stellar movement. Hence, the next generation of massive star formation simulations must include the advantages of both methods to better understand how massive stars can overcome the Eddington limit by including hybrid radiative transfer on adaptive grids.

The question of whether RT instability is important for massive star formation

has been muddied further by studies of radiation pressure-driven instabilities in the context of galactic winds. Krumholz and Thompson (2012); Krumholz (2013) study the ability of radiation to drive galactic winds using the same FLD methods as Krumholz *et al.* (2009), and find that RT instabilities arise and prevent the onset of winds entirely. Rosdahl and Teyssier (2015) reach the same conclusion using an M1 closure to treat the radiation. Davis *et al.* (2014), using a variable Eddington tensor method on a fixed grid, and Tsang and Milosavljević (2015), using implicit Monte Carlo, concur that RT instability occurs, but find that it does not prevent a wind from being launched, contrary to the results of Krumholz and Thompson and Rosdahl and Teyssier. Moreover, none of these calculations included a treatment of the direct radiation field.

The conflicting results discussed thus far have motivated the implementation of a new generation of hybrid radiation solvers in AMR simulation codes. Both Klassen *et al.* (2014) and Rosen *et al.* (2017) developed novel hybrid radiation schemes in the `FLASH` and ORION AMR simulation codes, respectively. Both implementations model the direct radiation field with a raytracer while the diffuse component is handled by a FLD solver, and can be used with an arbitrary number of moving stars. The raytracer employed in the Hybrid Adaptive Ray-Moment Method ($HARM^2$) algorithm developed by Rosen *et al.* (2017) (presented in Chapter 3) uses the method of long characteristics, which traces rays on a cell by cell basis thus providing maximum possible accuracy. Their method is adaptive, in which rays are allowed to split as they travel away from their source, greatly reducing the computational cost; and is capable of representing multi-frequency stellar irradiation (Abel and Wandelt, 2002; Wise and

Abel, 2011; Rosen *et al.*, 2017). The multi-frequency treatment is ideal for stars since they have color temperatures much higher than the absorbing medium. The raytracer employed in Klassen *et al.* (2014) models only single frequency irradiation and uses hybrid characteristics, which is a combination of long characteristics within individual grids and short characteristics between grids (i.e., in which only neighboring grid cells are used to interpolate incoming intensities; Rijkhorst *et al.* (2006)). The method of short characteristics is typically faster but more diffusive than long characteristics. Because of this limitation the long characteristics method employed in Rosen *et al.* (2017) has been highly optimized.

To revisit the problem of massive star formation and whether or not mass is delivered to the star via RT instabilities, Klassen *et al.* (2016) simulated the collapse of initially laminar pre-stellar cores with the new hybrid radiation algorithm presented in Klassen *et al.* (2014). Like the work of Kuiper *et al.* (2011, 2012) they find that their radiation pressure dominated bubbles remain stable and that the massive star is fed by disk accretion alone. However, the authors employ poor refinement criteria in their simulations, which results in the bubble shells being poorly resolved, potentially suppressing RT instabilities that are not resolved. To address this, we perform similar simulations of the collapse of a laminar massive pre-stellar core in which we choose to resolve the bubble shells, like that of Krumholz *et al.* (2009), and use the $HARM^2$ hybrid radiation algorithm to determine if RT instabilities are a real effect or if the direct radiation pressure inhibits their growth. As we will show, the development of RT instabilities is resolution dependent and therefore we find that authors can arrive

at conflicting results if the bubble shells are not properly refined.

The simulations discussed thus far were highly idealized. To date only the collapse of initially laminar massive pre-stellar cores have been studied numerically with a detailed treatment of the direct and diffuse radiation fields, yet observations of star forming regions show that star-forming cores are turbulent (Tatematsu *et al.*, 2008; Sánchez-Monge *et al.*, 2013). In such a configuration, the initial turbulence should act as seeds for RT instabilities. Furthermore, the asymmetric gas distribution in turbulent cores can yield low-density channels where radiation can easily escape, even in the absence of channels cut by outflows.

The purpose of this chapter is to study how radiation pressure affects the formation of massive stars via direct numerical simulation. For this work, we use the new highly accurate $HARM^2$ algorithm described in Rosen *et al.* (2017), which treats the direct radiation field from stars and the indirect radiation field associated with the re-emission and processing by interstellar dust. In this work, we simulate the collapse of both initially laminar and turbulent pre-stellar cores to determine how massive stars attain their mass. For the laminar cores, we also examine how resolution and treatment of radiation pressure can affect the onset of RT instabilities. We simulate the collapse of an initially turbulent core to model a more realistic setup of how massive stars form to show that RT instabilities are a common occurrence in their formation. The simulations presented in this work are still highly idealized since we do not include magnetic fields or outflows. This chapter is organized as follows: we describe our numerical methodology and simulation design in Section 4.2, we present and discuss our results in Sections 4.3

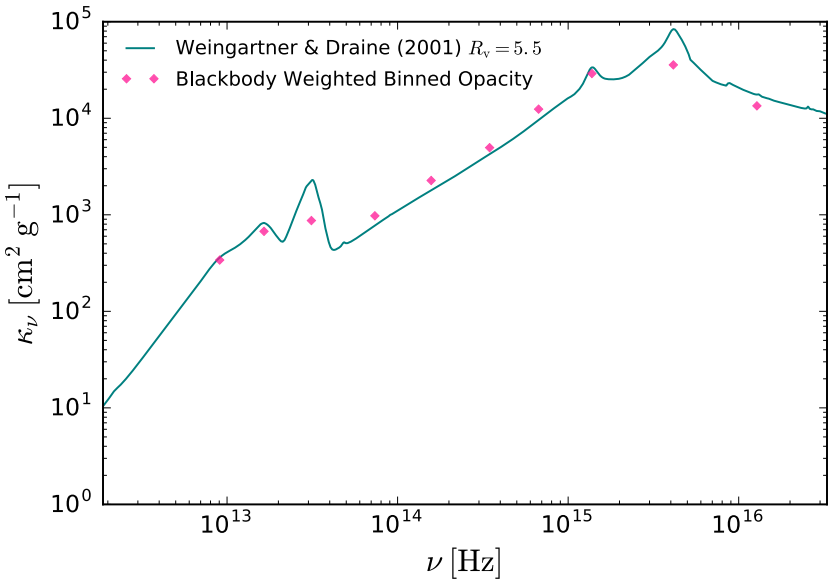

Figure 4.1 Specific frequency dependent dust opacities (per gram of dust) from Weingartner and Draine (2001) for their $R_v = 5.5$ extinction curve (teal line) with black body weighted binned opacities (pink diamonds) over-plotted for ten frequency bins used in the simulations presented in this work.

and 4.4, respectively, and conclude in Section 4.5.

4.2 Numerical Method

In this chapter, we simulate the collapse of isolated laminar and turbulent massive pre-stellar cores with the ORION adaptive mesh refinement (AMR) code. ORION includes hydrodynamics (Klein, 1999), radiative transfer (Howell and Greenough, 2003; Krumholz *et al.*, 2007b; Shestakov and Offner, 2008; Rosen *et al.*, 2017), self-gravity (Truelove *et al.*, 1998), accreting sink particles (Truelove *et al.*, 1997; Krumholz *et al.*, 2004), a protostellar evolution model used to represent the sink particles as radiating protostars (Offner *et al.*, 2009), protostellar outflows (Cunningham *et al.*, 2011), and

magnetic fields (Li *et al.*, 2012). In order to treat both the direct (stellar) and indirect (dust-reprocessed) radiation fields we use the multi-frequency Hybrid Adaptive Ray-Moment Method ($HARM^2$) described in Rosen *et al.* (2017), which combines direct solution of the frequency-dependent radiative transfer equation along long characteristics launched from stars to treat the direct stellar radiation field with a gray flux-limited diffusion (FLD) method to treat the radiation field produced by thermal emission from dust (Krumholz *et al.*, 2007b). We describe the equations solved by our code in Section 4.2.1, our stellar radiation feedback prescription in Section 4.2.2, the initial and boundary conditions for our simulations in Section 4.2.3, and our refinement criteria and sink creation requirements in Section 4.2.4.

4.2.1 Evolution Equations

ORION uses a Cartesian adaptive grid in which every cell has a state vector of conserved quantities (ρ, $\rho\mathbf{v}$, ρe, $E_{\rm R}$). Here ρ is the density, $\rho\mathbf{v}$ is the momentum density, ρe is the total internal plus kinetic gas energy density, and $E_{\rm R}$ is the radiation energy density in the rest frame of the computational domain. In addition to the fluid, ORION contains Lagrangian radiating sink particles that accrete from the gas and interact with it via gravity and radiation. The star particles, indexed by subscript i, are characterized by their position $\mathbf{x}_i$, momentum $\mathbf{p}_i$, mass M_i, and luminosity L_i, as determined by the protostellar evolution model described in McKee and Tan (2003) and Offner *et al.* (2009). They accrete mass, momentum, and energy from the computational grid at rates $\dot{M}_i$, $\dot{\mathbf{p}}_i$, and $\dot{\varepsilon}_i$; the distribution of these quantities over cells in the computational grid is

described by a weighting kernel $W(\mathbf{x}-\mathbf{x}_i)$, which is non-zero only within 4 computational zones of each particle. Both the value of $\dot{M}_i$ and $\dot{\mathbf{p}}_i$ and the weighting kernel function are determined via the sink particle algorithm of Krumholz *et al.* (2004). Each star particle also produces a direct radiation field that injects energy and momentum into the gas at a rate per unit volume $\dot{\mathbf{p}}_{\mathrm{rad},i}$ and $\dot{\varepsilon}_{\mathrm{rad},i}$; we defer discussion of how these two quantities are computed to Section 4.2.2. With these quantities the equations governing the evolution of the RHD fluid-particle system are

$$\frac{\partial \rho}{\partial t} = -\nabla \cdot (\rho \mathbf{v}) - \sum_i \dot{M}_i W(\mathbf{x}-\mathbf{x}_i) \tag{4.2}$$

$$\begin{aligned}\frac{\partial (\rho \mathbf{v})}{\partial t} &= -\nabla \cdot (\rho \mathbf{v}\mathbf{v}) - \nabla P - \rho \nabla \phi - \lambda \nabla E_{\mathrm{R}} \\ &\quad + \sum_i \left[\dot{\mathbf{p}}_{\mathrm{rad},i} - \dot{\mathbf{p}}_i W(\mathbf{x}-\mathbf{x}_i)\right]\end{aligned} \tag{4.3}$$

$$\begin{aligned}\frac{\partial (\rho e)}{\partial t} &= -\nabla \cdot [(\rho e + P)\mathbf{v}] - \rho \mathbf{v} \cdot \nabla \phi - \kappa_{0\mathrm{P}} \rho (4\pi B - c E_{\mathrm{R}}) \\ &\quad + \lambda \left(2\frac{\kappa_{0\mathrm{P}}}{\kappa_{0\mathrm{R}}} - 1\right) \mathbf{v} \cdot \nabla E_{\mathrm{R}} - \left(\frac{\rho}{m_{\mathrm{p}}}\right)^2 \Lambda(T_{\mathrm{g}}) \\ &\quad + \sum_i \left[\dot{\varepsilon}_{\mathrm{rad},i} - \dot{\varepsilon}_i W(\mathbf{x}-\mathbf{x}_i)\right]\end{aligned} \tag{4.4}$$

$$\begin{aligned}\frac{\partial E_{\mathrm{R}}}{\partial t} &= \nabla \cdot \left(\frac{c\lambda}{\kappa_{0\mathrm{R}} \rho} \nabla E_{\mathrm{R}}\right) + \kappa_{0\mathrm{P}} \rho \left(4\pi B - c E_{\mathrm{R}}\right) \\ &\quad - \lambda \left(2\frac{\kappa_{0\mathrm{P}}}{\kappa_{0R}} - 1\right) \mathbf{v} \cdot \nabla E_{\mathrm{R}} - \nabla \cdot \left(\frac{3-R_2}{2} \mathbf{v} E_{\mathrm{R}}\right) \\ &\quad + \left(\frac{\rho}{m_{\mathrm{p}}}\right)^2 \Lambda(T_{\mathrm{g}})\end{aligned} \tag{4.5}$$

Equations (4.2)-(4.5) describe conservation of gas mass, gas momentum, gas total energy, and radiation total energy. They include terms describing the exchange of these quantities with the star particles, and exchange of energy between radiation and gas.

The gas-radiation exchange terms are written in a mixed-frame formulation that allows conservation of total energy to machine precision (Mihalas and Klein, 1982; Krumholz *et al.*, 2007b). We assume an ideal equation of state so that the gas pressure is

$$P = \frac{\rho k_{\rm B} T}{\mu m_{\rm H}} = (\gamma - 1)\, \rho e_{\rm T}, \tag{4.6}$$

where T is the gas temperature, μ is the mean molecular weight, γ is the ratio of specific heats, and $e_{\rm T}$ is the thermal energy of the gas per unit mass. We take $\mu = 2.33$ and $\gamma = 5/3$ that is appropriate for molecular gas of solar composition at temperatures too low to excite the rotational levels of H_2; in practice the exact value of γ matters little for our computation, because the gas temperature is set almost entirely by radiative effects, with minimal influence from adiabatic compression or expansion. The fluid is a mixture of gas and dust, and at the high densities that we are concerned with the dust will be thermally coupled to the gas, allowing us to assume that the dust temperature is the same as the gas temperature.

In addition to updating fluid quantities, at each time step we also update the properties of the star particles. These change according to

$$\frac{dM_{\rm i}}{dt} = \dot{M} \tag{4.7}$$

$$\frac{d\mathbf{x_i}}{dt} = \frac{\mathbf{p}_{\rm i}}{M_{\rm i}} \tag{4.8}$$

$$\frac{d\mathbf{p_i}}{dt} = -M_i \nabla\phi + \dot{\mathbf{p}}_i, \tag{4.9}$$

where ϕ is the gravitational potential that obeys the Poisson equation including contributions from both the fluid and star particles:

$$\nabla^2\phi = 4\pi G\left[\rho + \sum_i M_i\delta(\mathbf{x}-\mathbf{x_i})\right]. \tag{4.10}$$

Our sink particle algorithm destroys information within four fine-level cells around each star particle (i.e., the particle's accretion radius) and thus we are unable to properly determine if two sink particles will merge when they approach within one accretion radius of one another (i.e., 80 AU). In light of this limitation, we employ the following merging criteria: when two star particles pass within one accretion radius of each other we merge them together if the smaller particle has a mass less than 0.05 $M_\odot$ (Myers *et al.*, 2013). This threshold corresponds to the largest plausible mass at which second collapse occurs for the protostar (Masunaga *et al.*, 1998; Masunaga and Inutsuka, 2000). At masses lower than this value the protostar represents a hydrostatic core that is several AU in size and will likely be accreted by the more massive star. Larger mass protostars will have collapsed down to sizes of roughly several $R_\odot$ and will unlikely merge with the nearby protostar.

Finally, the radiation-specific quantities are the blackbody function $B = \frac{ca_{\rm R}T^4}{4\pi}$, the co-moving frame specific Planck- and Rosseland-mean opacities $\kappa_{0\rm P}$ and $\kappa_{0\rm R}$, a dimensionless number λ called the flux-limiter, and the Eddington factor R_2. The last two quantities appear in Equation (4.5) and originate from the FLD approximation, which assumes that the radiative flux in the co-moving frame is related to the gradient

of the radiation energy density (Fick's Law)

$$\mathbf{F} = -\frac{c\lambda}{\kappa_{0\mathrm{R}}}\nabla E_{\mathrm{R}}. \tag{4.11}$$

ORION adopts the Levermore and Pomraning (1981) approximation for λ and R_2 as given by

$$\lambda = \frac{1}{R}\left(\coth R - \frac{1}{R}\right) \tag{4.12}$$

$$R = \frac{|\nabla E_{\mathrm{r}}|}{\kappa_{0R}\rho E_{\mathrm{R}}} \tag{4.13}$$

$$R_2 = \lambda + \lambda^2 R^2. \tag{4.14}$$

The flux limiter, λ, has the advantage that in an optically thick medium $\lambda \rightarrow 1/3$, thereby giving $\mathbf{F} \rightarrow -\left[(c/3\kappa_{0\mathrm{R}})\,\nabla E_{\mathrm{r}}\right]$, the correct value for diffusion. In an optically thin medium $\lambda \rightarrow (\kappa_{0\mathrm{R}} E_{\mathrm{R}}/|\nabla E_{\mathrm{R}}|)\,\mathbf{n}_{\mathrm{R}}$, where $\mathbf{n}_{\mathrm{R}}$ is a unit-vector that is anti-parallel to ∇E_{R}, yielding $\mathbf{F} \rightarrow cE_{\mathrm{R}}\mathbf{n}_{\mathrm{R}}$ for the free-streaming limit (Krumholz *et al.*, 2007b).

4.2.2 Treatment of Stellar Radiation

In star-forming environments radiation from stars will be absorbed by the dusty gas and deposit momentum and energy (e.g., see Equations (4.3)-(4.5)). The dust, which is highly coupled to the gas, will re-emit thermal radiation at infrared wavelengths and transfer energy and momentum to the gas via collisions. At the high densities with which we are concerned, thermal coupling is strong enough that we can safely assume

that the gas and dust are at the same temperature. In order to properly model this, we must know the magnitude and direction of the intervening stellar radiation field. With this in mind we use the new $HARM^2$ algorithm described in Rosen *et al.* (2017) to treat the first absorption of the (direct) stellar radiation field from stars and subsequent re-emission of radiation from the fluid. $HARM^2$ is a new hybrid radiative transfer tool developed for adaptive grids that employs an adaptive long-characteristics ray tracing method, first introduced by Abel and Wandelt (2002) and extended to adaptive grids by Wise and Abel (2011), to model the radiative flux from point sources. It is coupled to a moment method, in our case FLD (e.g., see Section 4.2.1), which models the re-processed diffuse radiation field intrinsic to the fluid. In short, $HARM^2$ is used to model both the direct and indirect radiation pressure in numerical simulations.

The method of long characteristics solves the radiative transfer equation along specific rays on a cell by cell basis that originate from the point source. This method provides the best possible accuracy for the radiative flux for point sources that represent stars because it is less diffusive than short and hybrid characteristic methods (Rijkhorst *et al.*, 2006; Klassen *et al.*, 2014). $HARM^2$ has the advantage that it can be used to model any number of moving point sources, handles multi-frequency radiation, and is highly parallelizable as compared to previous long-characteristic methods developed for adaptive grids (Wise and Abel, 2011). We choose to represent the luminosities of stars by a spectrum of frequency-dependent luminosities rather than a bolometric luminosity, $L_\star$, because the color temperatures of stars are much higher than the temperature of the absorbing medium. In what follows, we briefly summarize the basic components of

HARM[2], and refer the reader to Chapter 3. for a full description of the algorithm.

We describe the deposition of energy and momentum to the fluid from the radiation field of a single star but the generalization to multiple point sources is trivial. Each star has a specific luminosity L_ν, and bolometric luminosity given by $L_\star = \int_0^\infty L_\nu d\nu$. We discretize the stellar spectrum in frequency into N_ν frequency bins, with the jth bin covering a range in frequency $(\nu_{j-1/2}, \nu_{j+1/2})$. The luminosity of the point source integrated over the jth frequency bin is $L_{\star,\mathrm{j}} = \int_{\nu_{j-1/2}}^{\nu_{j+1/2}} L_\nu \, d\nu$ where $\sum_{j=0}^{N_\nu} L_{\star,\mathrm{j}} = L_\star$. We choose $N_\nu = 10$ for the simulations presented in this paper because this number of frequency bins does not significantly increase the cost of the adaptive ray trace (e.g., see Figure 6 of Rosen *et al.* (2017)) and provides an adequate frequency sampling of L_ν. The frequency bins were hand-chosen to align with important features of the dust opacity curve as shown in Figure 4.1.

We use the frequency dependent stellar atmosphere profiles from Lejeune *et al.* (1997) to model the stellar spectrum of stars that form in our simulations. These profiles provide the frequency dependent radiative flux of stars on a grid of values in $\log g$ and T_{eff} space, where g is the star's surface gravity and T_{eff} is the star's surface temperature, both of which are supplied by the sub-grid protostellar model in ORION (Offner *et al.*, 2009). At each raytracing step, we compute $\log g$ and T_{eff} for each star and interpolate between the frequency-dependent stellar atmosphere profiles that match most closely to the star's properties. The accretion of material onto the star will also contribute an

accretion luminosity

$$L_{\rm acc} = f_{\rm rad}\frac{GM_\star \dot{M}_\star}{R_\star}, \tag{4.15}$$

and we model the accretion luminosity, $L_{{\rm acc},\nu}$, as a blackbody with temperature $T_{\rm acc} = \left(L_{\rm acc}/(4\pi R_\star^2\sigma)\right)^{1/4}$ such that $L_{\rm acc} = \int_0^\infty L_{{\rm acc},\nu}d\nu$. The resulting luminosity from the star and accretion is $L_{\rm tot} = \sum_{j=0}^{N_\nu}(L_{\star,{\rm j}} + L_{{\rm acc,j}})$. The quantity $f_{\rm rad}$ is the fraction of the gravitational potential energy of the accretion flow that is converted to radiation rather than being used to drive a wind or advected into the stellar interior; we adopt $f_{\rm rad} = 3/4$, following the standard treatment in Offner *et al.* (2009) and this value is reasonably consistent with x-wind models of the launching of stellar outflows (Ostriker and Shu, 1995).

We wish to solve the time-independent radiative transfer equation

$$\mathbf{n}\nabla I(\nu,\mathbf{n}) = -\kappa(\mathbf{n},\nu)\rho I(\mathbf{n},\nu) + \eta(\mathbf{n},\nu)\rho \tag{4.16}$$

along specific rays that originate from point sources and transverse the computational domain in the radial direction to model the absorption of the direct radiation field from stars. Here $I(\mathbf{n},\nu)$ is the specific intensity of the stellar radiation field at frequency ν in direction $\mathbf{n}$ and $\kappa(\mathbf{n},\nu)$ and $\eta(\mathbf{n},\nu)$ are the direction and frequency-dependent specific absorption and emission coefficients. We set $\eta(\mathbf{n},\nu)$ to zero because the direct radiation field has zero emissivity except at the location of stars. We also neglect the effects of scattering because absorption is the dominant transfer mechanism in these simulations. Finally, we note that we can neglect the time dependence of the radiative

transfer equation because the light crossing time of a ray ($t_{\rm lc}$) will be much shorter than the opacity variation time scale (i.e., $t_{\rm lc} \ll \kappa/\left(d\kappa/dt\right)$) for the scales and time steps considered in our simulations.

We discretize the transfer equation in angle on a series of rays originating at the star and traveling radially outward. Each ray is characterized by a direction $\mathbf{n}$ and solid angle $\Omega_{\rm ray}$ that it subtends. Multiplying both sides of Equation (4.16) by $4\pi r^2/\Omega_{\rm ray}$, yields an integrated form of the transfer equation

$$\frac{\partial L_{{\rm ray},j}}{\partial r} = -\kappa_j \rho L_{{\rm ray},j}, \tag{4.17}$$

where $L_{{\rm ray},j}(r)$ is the luminosity for the jth frequency bin at a distance r from the point source and κ_j is the specific absorption opacity for the jth frequency bin. This equation is subject to the boundary condition $L_{{\rm ray},j}(0) = L_{{\rm tot},j}/N_{\rm pix}$, where $N_{\rm pix} = 4\pi/\Omega_{\rm ray}$. In order to reduce cost we initially sample the radiation field for each star with 3072 rays and adaptively split each ray into four sub-rays when the following condition is satisfied

$$\frac{\Omega_{\rm cell}}{\Omega_{\rm ray}} < \Phi_{\rm c}, \tag{4.18}$$

where $\Omega_{\rm cell} = (\Delta x/r)^2$ is the solid angle subtended by a cell of linear size Δx at a distance r from the point source. The quantity $\Phi_{\rm c}$ is the minimum number of rays required to go through each cell, which we set to 3 in our simulations. This refinement criterion ensures that the cells that interact with rays are adequately resolved.

Our choice for $\kappa_{\rm j}$ depends on whether the primary absorber is dust or molecular gas. Dust is the primary absorber for gas temperatures below $T_{\rm sub} = 1500$ K (i.e., the temperature at which dust sublimes; Semenov *et al.* (2003)) while molecular hydrogen is the primary absorber for gas temperatures within $T_{\rm sub} \leq T < T_{\rm H\ II}$ where $T_{\rm H\ II} \approx 10^4$ K is the temperature at which we expect hydrogen to become fully ionized, and thus to have the usual Thompson opacity for electron scattering. If the primary absorber is dust we use the frequency dependent dust opacities from Weingartner and Draine (2001) (their $R_{\rm v} = 5.5$ extinction curve, e.g., see Figure 4.1) and assume a constant dust-to-gas ratio of $M_{\rm dust}/M_{\rm gas} = 0.01$. If it is molecular hydrogen we set the molecular gas opacity to 0.01 $\rm cm^2\,g^{-1}$, and if $T \geq T_{\rm H\ II}$ we set the opacity to zero. The last of these is a numerical convenience, because we have not implemented scattering or photoionization chemistry, and because the regions in our computation with $T > T_{\rm H\ II}$ will contain so little mass they will be optically thin to the direct radiation field. We assume a dust-to-gas ratio of 0.01.

We solve equation (4.17) by discretizing it along the line segments defined by the intersection of the ray with the cells of the computational mesh, considering only the most highly spatially resolved data at any given position. Specifically, when a ray with luminosity $L_{{\rm ray},j}$ passes through a cell along a segment of length dl, the optical depth of the segment is $\tau_j = \kappa_j \rho\, dl$ where ρ is the dust (gas) density when the primary absorber is dust (molecular gas); and the luminosity of the ray decreases by an amount

$$dL_{{\rm ray},j} = L_{{\rm ray},j}\left(1 - e^{-\tau_j}\right). \tag{4.19}$$

Here we compute *dl* following the method of Wise and Abel (2011) as the ray transverses a cell. In the process, the cell absorbs an amount of energy and momentum at a rate

$$\dot{\varepsilon}_{\mathrm{rad,\,ray}} = \sum_{j=1}^{N_\nu} dL_{\mathrm{ray},j} \tag{4.20}$$

$$\dot{\mathbf{p}}_{\mathrm{rad,\,ray}} = \sum_{j=1}^{N_\nu} \frac{dL_{\mathrm{ray},j}}{c}\mathbf{n}. \tag{4.21}$$

The total energy and momentum absorption rates for each cell, $\dot{\varepsilon}_{\mathrm{rad}}$ and $\dot{\mathbf{p}}_{\mathrm{rad}}$, that are supplied to Equations (4.2) and (4.4), are simply the sum of $\dot{\varepsilon}_{\mathrm{rad,\,ray}}$ and $\dot{\mathbf{p}}_{\mathrm{rad,ray}}$ over all rays from all stars that pass through it, respectively. We terminate a ray when $L_{\mathrm{ray},j}(r) < 0.001 L_{\mathrm{ray},j}(0)$, i.e., when 99.9% of the energy originally assigned to that ray has been absorbed, if it exits the computational domain, or has left the collapsing core. The last deletion criterion significantly reduces the cost of the ray tracing step if rays leave the core because the ambient medium will not absorb any energy or momentum from the rays, and deleting rays after they have traveled at least ten cells in the ambient medium without encountering core material therefore saves the need to continue following them through the remainder of the computational volume.

4.2.3 Initial and Boundary Conditions

Our initial setup for all runs is as follows. We begin with an isolated sphere of molecular gas and dust with mass $M_{\mathrm{c}} = 150\ \mathrm{M}_\odot$, radius $R_{\mathrm{c}} = 0.1$ pc, temperature $T_{\mathrm{c}} = 20$ K, and density profile $\rho \propto r^{-k_\rho}$ with $k_\rho = 1.5$. The resulting surface density, $\Sigma = M_{\mathrm{c}}/(\pi R_{\mathrm{c}}^2) = 1\ \mathrm{g\,cm^{-2}}$, is consistent with typical values observed in Galactic

massive star forming regions (McKee and Tan, 2003; Swift, 2009; Sánchez-Monge *et al.*, 2013; Tan *et al.*, 2014). The resulting mean density of the core is $\bar{\rho} = 2.4 \times 10^{-18}$ g cm^{-3} (1.2×10^6 H nuclei cm^{-3}) and the characteristic free-fall collapse time scale is

$$t_{\rm ff} = \sqrt{\frac{3\pi}{32 G \bar{\rho}}} \approx 42.6 \text{ kyr}. \tag{4.22}$$

Our choice of $k_\rho = 1.5$ for the core density profile is in agreement with observations of star-forming regions at the ~ 1 pc clump scale (Caselli and Myers, 1995; Mueller *et al.*, 2002; Beuther *et al.*, 2007) and the ~ 0.1 pc scale (Zhang *et al.*, 2009; Longmore *et al.*, 2011; Butler and Tan, 2012; Stutz and Gould, 2016), which typically have k_ρ values within the range of 1.5-2.0.

Each core is placed at the center of a 0.4 pc box that is filled with a hot, diffuse ambient medium with a density equal to 1% of the core edge material and a temperature of 2000 K so that the core is in thermal pressure equilibrium with its surroundings. We set the opacity of the ambient medium to zero so that the ambient gas is unable to cool. The base resolution for each run is 128^3 and we allow for five levels of factors of two in refinement giving a maximum resolution of 4096^3 cells on the finest level ($\Delta x_{\rm min}$ = 20 AU). We initially fill the entire domain with a blackbody radiation field equal to $E_0 = 1.21 \times 10^{-9}$ erg cm^{-3} corresponding to a 20 K blackbody.

We consider two classes of initial condition: laminar cores and turbulent cores. For the laminar core we impose initial solid-body rotation at a rate such that the rotational energy of the core is 4% of its gravitational binding energy (i.e., $E_{\rm rot}/|E_{\rm grav}| =$

0.04). Our choice follows from the work of Goodman *et al.* (1993), which found that dense cores have values of $E_{\rm rot}/|E_{\rm grav}|$ within $\sim 0.01 - 0.09$ with a typical value of 0.02 where the authors assumed the cores followed a uniform density profile. For the case of cores that follow a $\rho \propto r^{-3/2}$ density profile, like the cores simulated in this work, these values are reduced by a factor of two. We do not impose a net rotation for the turbulent core run and instead give the gas an initial weakly turbulent velocity field with a non-thermal one-dimensional velocity dispersion $\sigma_{\rm 1D} = 0.4$ km s^{-1} corresponding to a virial ratio $\alpha_{\rm vir} \approx 5\sigma_{\rm 1D}^2 R_{\rm c}/GM_{\rm c} = 0.12$ and we allow the turbulence in the core to decay freely, ensuring the core will undergo immediate collapse. The velocity power-spectrum imposed follows a Burger's turbulence spectrum, $P(k) \propto k^{-2}$, as is expected for supersonic turbulence (Padoan and Nordlund, 1999; Boldyrev, 2002; Offner *et al.*, 2009). We include modes between $k_{\rm min} = 1$ and $k_{\rm max} = 256$ and our turbulence mixture is chosen to be a mix of 2/3 solenoidal and 1/3 compressive modes, which is the natural mixture for a 3D fluid (Federrath *et al.*, 2010b). Although the turbulence should decay freely as the core is assembled, physical processes such as converging flows and accretion onto the core as it is assembled could sustain the turbulence as the core grows in mass (Schneider *et al.*, 2010; Matzner and Jumper, 2015).

Our boundary conditions for the radiation, gravity, and hydrodynamic solvers are as follows. For each radiation update, we impose Marshak boundary conditions that bathe the simulation volume with radiation from a 20 K blackbody but allows radiation generated within the simulation volume to escape freely (Krumholz *et al.*, 2009; Cunningham *et al.*, 2011; Myers *et al.*, 2013). We set the gravitational potential,

ϕ, to zero at all boundaries when solving Equation (4.10) (Myers *et al.*, 2013). Although this choice of boundary conditions for the gravitational potential can lead to square artifacts near the boundaries we do not expect this choice to make any significant difference since the collapsing core is far removed from the boundaries. Finally, we impose outflow boundary conditions for the hydrodynamic update, meaning that we set the gradients of the hydrodynamic quantities (ρ, $\rho\mathbf{v}$, ρe) to be zero at the domain when advancing the hyperbolic subsystem of equations (Cunningham *et al.*, 2011; Myers *et al.*, 2013).

We conduct four simulations. The first, which we call `LamRT+FLD` (where `RT` denotes that this simulation includes ray tracing), follows the collapse of a laminar pre-stellar core with the setup described above and includes our *HARM*^{2} hybrid radiation scheme to model the direct (with an adaptive raytracing scheme) and indirect radiation pressure (with FLD). Our second run, named `LamFLD`, is identical to `LamRT+FLD` except that it only includes the FLD approximation for the indirect radiation field and assumes that the stellar radiation energy is deposited close to the star. In this run we set the terms $\dot{\varepsilon}_{\rm rad}$ and $\dot{\mathbf{p}}_{\rm rad}$ to zero and add the source term $\sum_i L_{\star,i} W(\mathbf{x} - \mathbf{x}_i)$, where $L_{\star,i}$ is the combined accretion and stellar luminosity for star i, to Equation (4.5). This term simply adds the radiation energy injected by stars to the radiation energy density over the window kernel $W(\mathbf{x} - \mathbf{x}_i)$, which extends to a radius of four fine-level cells around each sink particle. We include this run to compare how the choice of the treatment of the radiation field can affect our results. The third run, named `LamRT+FLD_LR`, is a repeat of run `LamRT+FLD` but with a factor of 2 worse resolution ($\Delta x_{\rm min} = 40$ AU rather than

20 AU), and with significantly less stringent refinement criteria, as discussed in the next section. We include this run to determine how the results depend on the resolution. Our final run, which is called `TurbRT+FLD`, aims to be a better representation of massive star formation because star forming cores are turbulent, and this run follows the collapse of a turbulent pre-stellar core with the properties described above and includes our hybrid radiative transfer treatment. The initial numerical conditions for our simulations are summarized in Table 4.1.

4.2.4 Refinement Criteria and Sink Creation

The major advantage of AMR codes over fixed codes is that the user can adaptively refine on areas of interest. This is advantageous in astrophysical simulations, especially star formation simulations, which have large dynamic range but within which only certain regions of the domain require high resolution (e.g., high density regions in a molecular cloud that can undergo gravitational collapse to form stars). As the simulation evolves the AMR algorithm automatically adds and removes finer grids based on certain refinement criteria set by the user.

For each simulation we begin with a base grid with volume $(0.4\text{ pc})^3$ discretized by 128^3 cells and allow for five levels of refinement. This choice leads to a maximum resolution of 20 AU on the finest level. As the simulation evolves we continuously flag cells for refinement so that we can resolve areas in which stars may form or where instabilities may develop, such as gravitational and Rayleigh Taylor instabilities. In all simulations presented in this paper we flag cells for refinement if they meet one or more

Table 4.1 Simulation Parameters

Run		`LamFLD`	`LamRT+FLD`	`LamRT+FLD_LR`	`TurbRT+FLD`
Physical Parameter					
Cloud Mass [$M_\odot$]	M_c	150	150	150	150
Cloud Radius [pc]	R_c	0.1	0.1	0.1	0.1
Surface Density [$\mathrm{g\,cm^{-2}}$]	Σ	1	1	1	1
Temperature [K]	T_c	20	20	20	20
Mean Density [$10^{-18}\,\mathrm{g\,cm^{-3}}$]	$\bar{\rho}_\mathrm{cl}$	2.4	2.4	2.4	2.4
Mean Free-fall Time [kyr]	t_ff	42.6	42.6	42.6	42.6
Power Law Index	k_ρ	1.5	1.5	1.5	1.5
Rotational Energy Ratio	$E_\mathrm{rot}/\lvert E_\mathrm{grav}\rvert$	0.04	0.04	0.04	–
Velocity Dispersion [$\mathrm{km\,s^{-1}}$]	σ_1D	–	–	–	0.4
Numerical Parameter					
Rad. Trans. Scheme		FLD	*HARM*^{2}	*HARM*^{2}	*HARM*^{2}
Domain Length [pc]	L_box	0.4	0.4	0.4	0.4
Base Grid Cells	N_0	128^3	128^3	128^3	128^3
Maximum Level	l_max	5	5	4	5
Minimum Cell Size [AU]	$\Delta x_{l_\mathrm{max}}$	20	20	40	20
Jeans Length Refinement	J_max	0.125	0.125	0.125	0.125
E_R Gradient Refinement	$E_\mathrm{R}/\Delta x$	0.15	0.15	–	0.15
Simulation Outcome					
Simulation Time [t_ff]		0.87	0.70	0.70	0.87
Massive Star Mass [$M_\odot$]		44.07	40.40	48.47	61.63
Number of Sinks with $M_\star > 0.01 M_\odot$		13	30	6	4

of the following criteria.

1. We refine any cell on the base level (i.e., level 0) that has a density equal to or greater than the core's edge density. This ensures that the entire pre-stellar core is refined to level 1 at the start of the simulation.

2. We refine any cell where the density in the cell exceeds the Jeans density given by

$$\rho_{\rm max,J} = \frac{\pi J_{\rm max}^2 c_{\rm s}^2}{G \Delta x_l^2} \tag{4.23}$$

   where $c_{\rm s} = \sqrt{k_B T/(\mu m_{\rm H})}$ is the isothermal sound speed, Δx_l is the cell size on level l, and $J_{\rm max}$ is the maximum allowed number of Jeans lengths per cell (Truelove *et al.*, 1997). Throughout this work we take $J_{\rm max} = 1/8$.

3. We refine any cell that is located within at least 8 cells of a sink particle.

4. We refine any cell within which the radiation energy density gradient exceeds

$$|\nabla E_{\rm R}| > 0.15 \frac{E_{\rm R}}{\Delta x_{\rm l}}, \tag{4.24}$$

   i.e., where the radiation energy density changes by more than 15% over the size of a single cell. This criterion is critical to ensuring that potentially-unstable interfaces are adequately resolved, and will become critical in our discussion later. Indeed, at late times in our simulations this criterion is responsible for refining more of the computational domain than any other one. We do not enforce this

criterion for run `LamRT+FLD_LR` because this run aims to see how the development of RT instabilities depends on simulation resolution.

This procedure is repeated recursively on all levels after every two level updates. A sink particle can only be created when the Jeans density is violated on the finest level. When we check this criterion on the finest level we set $J_{\rm max} = 1/4$ in Equation (4.23) following the artificial fragmentation tests of Truelove *et al.* (1997). If a cell is flagged on the finest level because it exceeds the Jeans density we place a sink particle in that cell whose mass is the excess matter in that cell. The new sink particle will evolve according to the equations in Section 4.2.1.

4.2.5 Overall Algorithm

We solve the equations described in Section 4.2.1 with the astrophysical AMR code ORION in a number of steps that we summarize below. First, we solve the equations of hydrodynamics using a Godunov-type scheme with the HLLD approximate Riemann solver (Klein, 1999; Miyoshi and Kusano, 2005). Next, we incorporate self-gravity following the methods of Truelove *et al.* (1998) and Klein (1999) by solving the Poisson equation (Equation (4.10)) with an iterative multigrid scheme provided by the Chombo AMR Library (Adams *et al.*, 2015). In the third step we apply the $HARM^2$ radiative transfer algorithm described in Rosen *et al.* (2017). The $HARM^2$ update algorithm first applies an adaptive ray trace step for all star particles that belong to the computational domain to inject the stellar radiation energy and momenta (Equations (4.20)-(4.21)) from stars to the absorbing fluid and then performs the FLD step to evolve

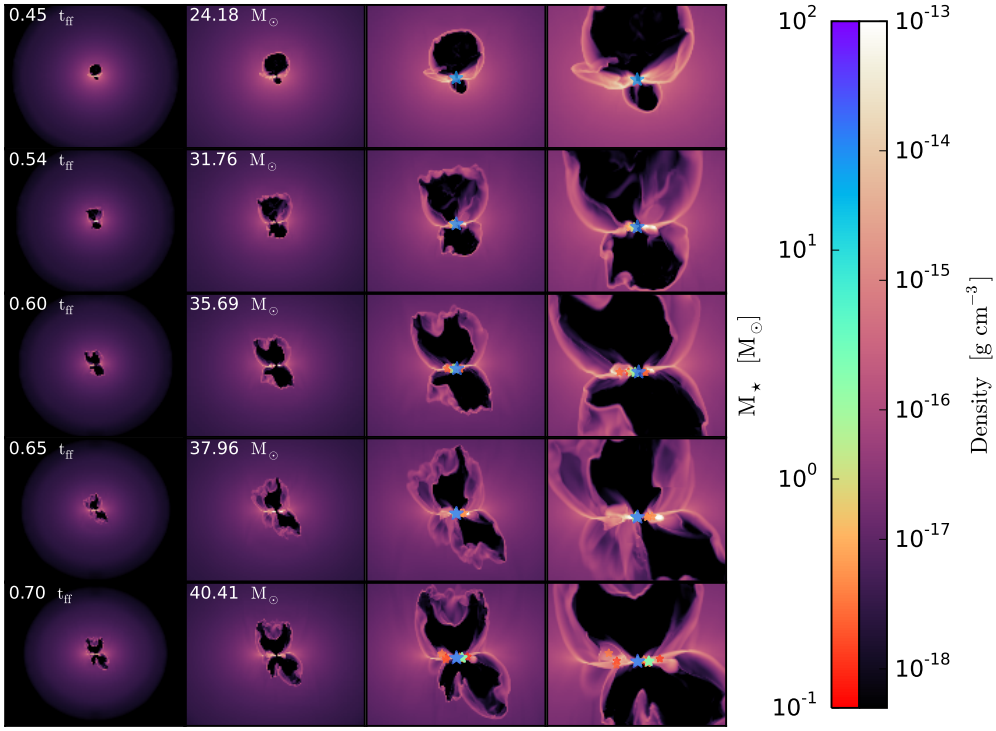

Figure 4.2 A series of density slice plots along the yz-plane (edge-on views) showing the time evolution for our `LamRT+FLD` simulation. Each row corresponds to a specific snapshot where each panel is a zoom in of the previous panel by a factor of two from $(40{,}000)^2$ down to $(5{,}000\ \mathrm{AU})^2$. The center of each panel corresponds to the center of the computational domain; stars with masses greater than $0.1\,M_\odot$ are over-plotted. The stars are color-coded by mass with the most massive being largest in size. The time of the simulation and mass of the most massive star are given in the top-left corner of the first and second panels of each row, respectively.

the radiation energy density and compute the radiation specific terms in Equations (4.3)-(4.5) (Rosen *et al.*, 2017). The FLD step uses an operator split approach that first solves the radiation pressure, work, and advection terms explicitly, and then implicitly updates the gas and radiation energy densities for terms that involve diffusion and the emission/absorption of radiation (Krumholz *et al.*, 2007b). The implicit solve update is handled by the iterative process described in Shestakov and Offner (2008) that uses

pseudo-transient continuation to reduce the number of iterations. Finally, we update the sink particle states with Equations (4.7)-(4.9) by computing their interactions with the fluid.

4.3 Results

In this section we describe the results from our simulations presented in Section 4.2.3 and summarized in Table 4.1. In Section 4.3.1 we first discuss our results for our laminar core run `LamRT+FLD`, which includes our new hybrid radiation transfer scheme. We then compare this simulation to run `LamFLD`, which only includes the radiation pressure associated with the diffuse dust-reprocessed radiation field. We defer discussion of our comparison low-resolution run, `LamRT+FLD_LR` to Section 4.4.1. Next in Section 4.3.2 we discuss our results from run `TurbRT+FLD`, which simulates the collapse of an initially turbulent core with our $HARM^2$ algorithm. All simulations presented here were run on the NASA supercomputer Pleiades located at NASA Ames or the Hyades supercomputer located at UCSC. We run each simulation to the point where the timestep either becomes too short to be practical (as in the case of run `LamFLD`) or until the point that the simulation takes too long to evolve because the majority of the bubble shells are refined to the finest level, severely increasing the computational cost of the simulation (as in runs `LamRT+FLD` and `TurbRT+FLD`). We use the `yt` package (Turk *et al.*, 2011) to produce all the figures and quantitative analysis shown below.

4.3.1 Collapse of Laminar Pre-stellar Cores

Here we present the results of run `LamRT+FLD`. At the end of this simulation the most massive star has a mass of 40.40 $M_{\odot}$. We ran the simulation for a time of $t = 0.70\ t_{\rm ff}$.

4.3.1.1 Evolution of Radiation Pressure Dominated Bubbles

We show a series of density slices at various times for run `LamRT+FLD` in Figure 4.2. We find that a radiation pressure dominated bubble begins to expand in the polar direction above the star, but not below, when the star has reached a mass of $\sim 14.5\ M_{\odot}$ at time $t = 0.34\ t_{\rm ff}$ (not shown). A radiation pressure dominated bubble only begins to expand below the star when it reaches a mass of $\sim 22.3\ M_{\odot}$ at time $t = 0.43\ t_{\rm ff}$ (not shown). As the radiation pressure dominated bubbles continue to expand small-scale RT instabilities begin to develop in the dense shells, but their growth is slow initially. This is likely due to the fact that the radiation pressure is able to push back on these instabilities, inhibiting their non-linear growth when the shell is optically thick to the direct stellar radiation field. For example, the absorption of the high-energy stellar radiation field is not fully resolved because the minimum optical depth through a 20 AU cell (the resolution on the finest level) is of order unity, where we have assumed that the shell density is $\rho \sim 10^{-16}$ cm^{-3} and the dust opacity to the high energy radiation is $\kappa_{\rm UV} \sim 10^{4}$ cm^{2} g^{-1} (e.g., see Figure 4.1).

When the primary star has a mass of $\sim 26.3\ M_{\odot}$ at time $t = 0.48\ t_{\rm ff}$ the right side of the disk becomes flared and material is blown off the accretion disk by the

direct radiation pressure. This injection of material into the upper bubble leads to an asymmetric absorption of the direct radiation field. This asymmetry and the resulting shielding of the direct radiation field causes RT instabilities to grow faster on the right side of the bubble shell while suppressing the non-linear growth of RT instabilities on the left side. Our results demonstrate that the seeding of RT instabilities and their resulting non-linear growth is a direct result of the asymmetric absorption of the energy and momentum from the direct radiation field across the bubble shell. Regions that feel a weaker radiative force are thus more likely to allow RT instabilities to grow non-linearly, leading to asymmetries in the bubble shells. These instabilities continue to grow as the simulation evolves. Once these unstable regions grow large enough gas is able to collapse directly onto the star-disk system if the material becomes sub-Eddington, delivering mass to the accreting protostar. We first see this behavior begin when the star reaches $\sim 30\ M_{\odot}$ at time $t = 0.51\ t_{\rm ff}$. At this time RT instabilities that develop on the right side of the bubble shell become sub-Eddington and grow large enough that the right edge of the shell deposits material onto the disk.

As the simulation progresses RT instabilities continue to develop across the top and bottom shells at an accelerating rate. This is a result of the star's movement in the disk, which causes the disk to shadow the direct radiation field (see Section 4.3.1.2) and is also due to the increasing surface density of the bubble shells as the core collapses. The bottom shell goes unstable and begins to collapse when the star is $\sim 34.3\ M_{\odot}$ at time $t = 0.57\ t_{\rm ff}$ and this material reaches the disk at time $t = 0.62\ t_{\rm ff}$. Material from the collapsed left side of the bottom bubble shell continues to deliver mass to the

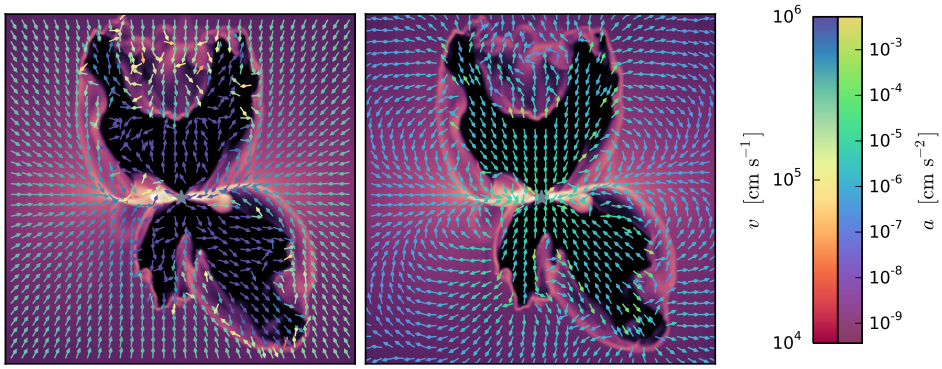

Figure 4.3 Density slices along the yz-plane with the velocity field (left panel) and net acceleration due to gravity and radiation (right panel) over-plotted when the most massive star is 40.4 $M_\odot$ at $t = 0.7\,t_{\rm ff}$ for run `LamRT+FLD`. The region plotted is (8,000 AU)^2 and the center of each panel corresponds to the center of the computational domain. The gray star denotes the position of the most massive star.

star-disk system until the star has reached a mass of $\sim 38.6\ M_\odot$ at time $t = 0.66\ t_{\rm ff}$. At this point the direct radiation pressure causes the left side of the bottom bubble to expand again.

At the end of the simulation we see that regions of the top and bottom bubbles are collapsing towards the star (bottom panel of Figure 4.2). To demonstrate this, we show the velocity (left panel) and net acceleration of the gas due to radiative and gravitational forces (right panel) in Figure 4.3 at the end of run `LamRT+FLD`. This Figure shows that the gas velocities in some of the densest regions of the shell are in the direction of the star-disk system even though the net acceleration along the majority of the bubble shells tend to point away from the star. The regions that experience a weaker net acceleration are more likely to go unstable while the regions that feel a larger net force will expand away from the star at a faster rate leading to more asymmetries in the bubble shells. It is these regions that go unstable and grow non-linearly, allowing

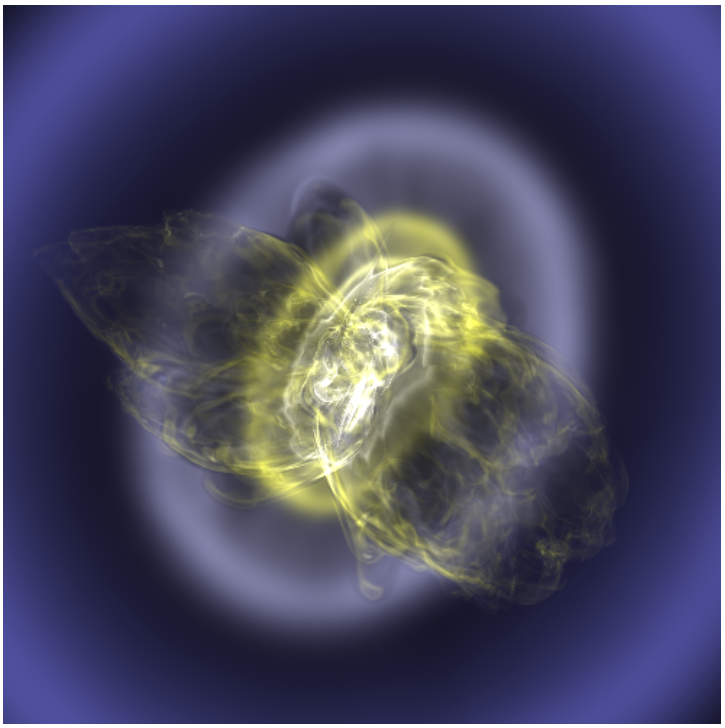

Figure 4.4 Volume rendering of a snapshot from run `LamRT+FLD` when the star is 40.1 $M_\star$ at time $t = 0.69\ t_{\rm ff}$ that shows RT instabilities are common throughout the radiation-pressure dominated bubbles.

material to continue to fall towards the star. This process may ultimately supply mass to the star-disk system and be accreted onto the star. Figure 4.4 shows that the majority of the bubble shells have become RT unstable.

Run `LamRT+FLD` also shows that throughout the collapse of the laminar core and growth of the massive protostar, a considerable amount of material is delivered from the edges of the radiation pressure dominated bubbles to the accretion disk via RT instabilities because these regions are shielded from the direct radiation field. We find that shielding of the direct radiation field promotes RT instabilities because the asymmetric absorption of the direct radiation field, which causes the direct radiation

force to vary over the inner surface of the bubble shells, can lead to perturbations that will then amplify and become RT unstable. This can be seen by observing where the stellar radiation field is absorbed in the bubble shells. The left panel in Figure 4.5 shows a zoomed-in density slice plot of the star at the end of the simulation along the yz-plane. Vectors showing the direction and magnitude of the direct radiation momentum deposition are over-plotted. The right panel shows the acceleration from the diffuse dust-reprocessed radiation field. Stellar radiation is able to stream freely along the polar directions that are not shielded by the accretion disk and gas within the bubble. In contrast, the accretion disk shields part of the radiation field near the left and right sides of the star. Furthermore, the radiation is shielded to a greater degree on the left side of the star because the disk is flared. Indeed, Figure 4.5 shows that the left side of the top and bottom bubbles experience a greater degree of instability than the right side of the bubbles suggesting that the growth and subsequent collapse of these RT instabilities depends on the shielding and resulting patchiness of the direct radiation field.

We find that throughout the simulation regions of the bubble shells that are shielded by the accretion disk feel a weaker direct radiative force and are more likely to go unstable and bring material to the star-disk system. This can be seen in Figure 4.6 that shows the same snapshot with the acceleration vectors over-plotted. In this figure, the color of each vector is the value for the Eddington ratio, $f_{\rm edd} = |\mathbf{f}_{\rm rad}|/|\mathbf{f}_{\rm grav}|$, where we have included the contribution from both the direct and dust-reprocessed radiation fields. Values of $f_{\rm edd} \lesssim 1$ are subject to collapse. The bubble interiors have $f_{\rm edd} \ll 1$

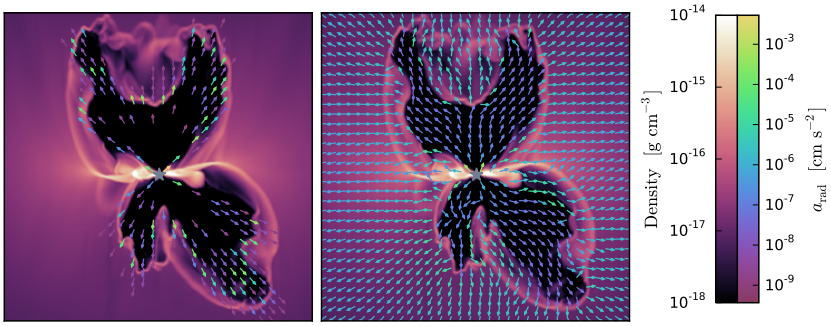

Figure 4.5 Same as Figure 4.3, but now the vectors show the acceleration due to the direct (left panel) and diffuse (right panel) radiation fields.

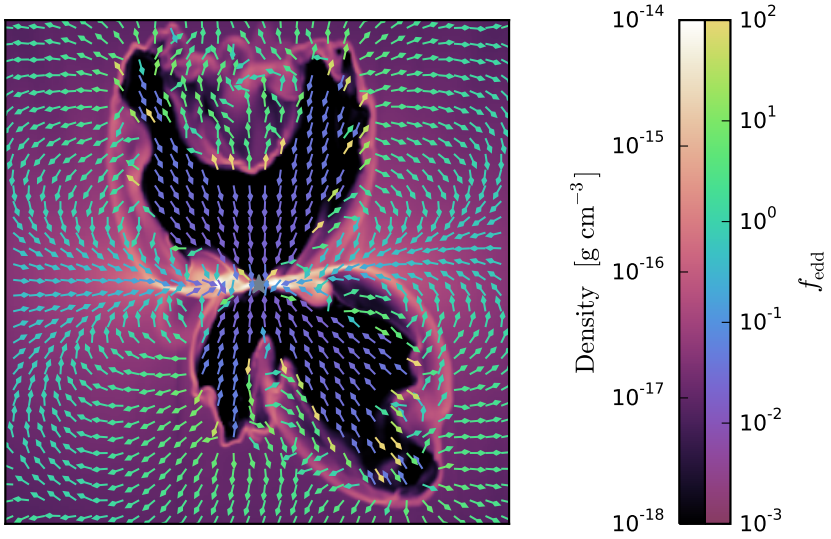

Figure 4.6 Same as Figure 4.3, but here arrows show the direction of the net (gravitational plus radiative) acceleration. Vector colors show the Eddington ratio, $f_{\rm edd} = |\mathbf{f}_{\rm rad}|/|\mathbf{f}_{\rm grav}|$, where $\mathbf{f}_{\rm rad}$ is the total radiative force due to both the direct and diffuse components.

because the bubble interiors are optically thin whereas regions of the bubble shells that become unstable have $f_{\rm edd} \lesssim 1$. Our results demonstrate that RT instabilities, along with disk accretion, deliver mass to the star, and that these instabilities become more important as the system evolves.

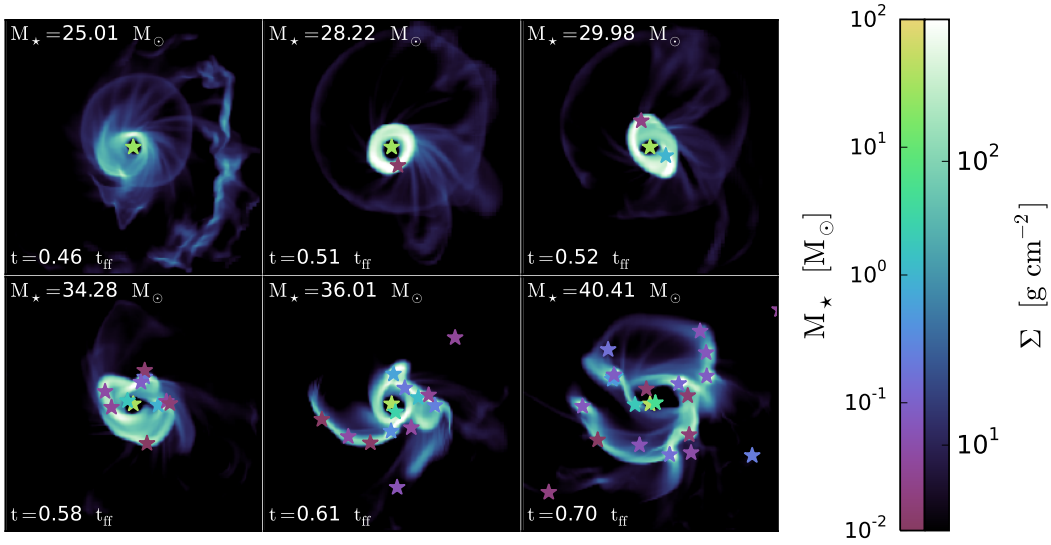

Figure 4.7 Surface density projections of the accretion disk in run `LamRT+FLD` showing the disk's time evolution. Each panel represents a projection of the accretion disk, with the most massive star at the center of the panel, that is (3000 AU)^2 in size. The projection is taken over a height of 1000 AU above and below the massive star. Stars with masses greater than 0.01 $M_\odot$ are over-plotted on all panels.

4.3.1.2 Accretion Disk Evolution

Next we examine the behavior and growth of the accretion disk. Figure 4.7 shows a series of surface density plots along the plane perpendicular to the core's rotation axis (xy-plane) that show the growth and evolution of the accretion disk around the massive star. The top left hand panel of Figure 4.7 shows that a noticeable thick accretion disk begins to form when the star reaches $\sim$ 25 $M_\odot$ (i.e., an accretion disk with a radius larger than the 80 AU accretion zone radius of the sink particle). The accretion disk continues to grow in size as the core undergoes inside-out collapse because material with a higher starting radius and thus a larger specific angular momentum is circularized farther away from the star. As the disk evolves it develops spiral arms

that become unstable and fragment into companions. The first companion star forms at time $t = 0.51\ t_{\rm ff}$ when the primary star has a mass of $\sim 28.2\ M_{\odot}$. The combined interaction of the primary star, accretion disk, and companions induces gravitational torques leading to even more companions. By the end of the run the primary has a mass of $\sim 40.4\ M_{\odot}$ and has 29 companion stars with masses greater than $0.01\ M_{\odot}$. The most massive companion is only $4.43\ M_{\odot}$; sixteen of the companion stars have masses greater than $0.1\ M_{\odot}$, but only four of these have masses greater than $1\ M_{\odot}$. Thus at the end of run `LamRT+FLD` we do not have a massive binary system, but rather a hierarchical system consisting of a massive primary and a series of low mass companions. Figure 4.8 shows the total growth in mass of the primary star and its companions as a function of time (top panel).

4.3.1.3 Comparison to Run `LamFLD`

To determine how the results depend on our treatment of the direct radiation field, we perform run `LamFLD`, a comparison run that does not include the direct radiation field and instead deposits the stellar radiation near the star. This method does not properly model the momentum deposition by the stellar radiation field and only includes gray dust opacities, which underestimates the true optical depth associated with the stellar radiation field. For example, the frequency dependent dust opacities range from $\sim 10 - 1000\ {\rm cm}^2/{\rm g}$ for molecular gas (i.e., assuming a dust-to-gas fraction of 0.01) for the high-frequency stellar radiation (e.g., see Figure 4.1) while the Semenov *et al.* (2003) opacities used for the FLD method in ORION range from $\sim 1 - 10\ {\rm cm}^2/{\rm g}$ for

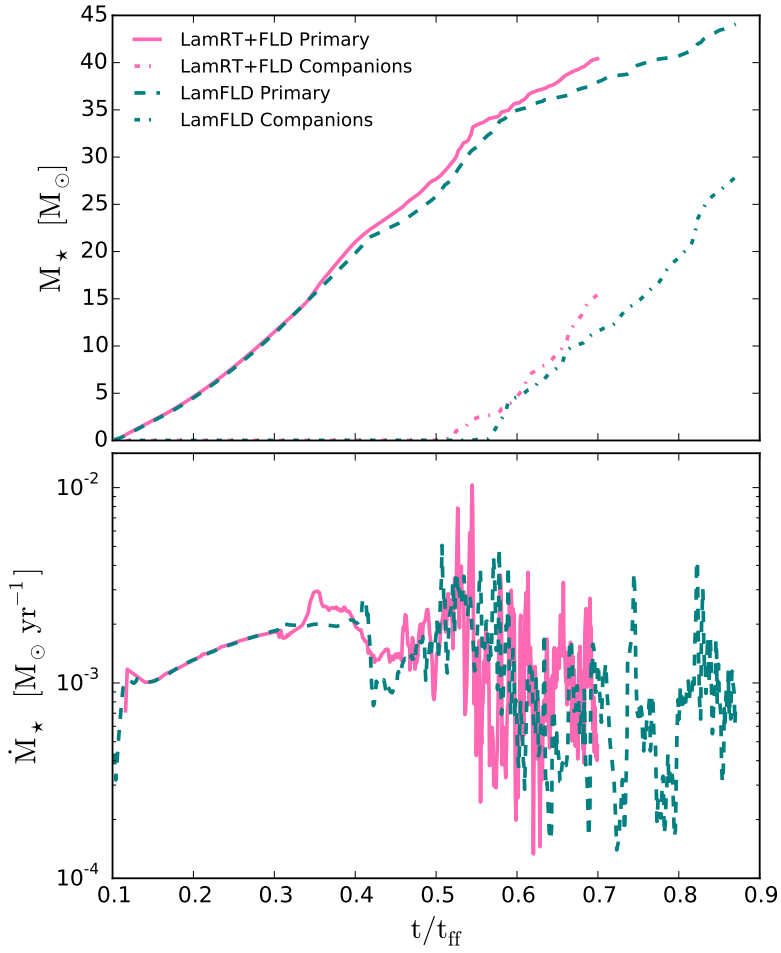

Figure 4.8 Stellar mass and accretion rates for runs `LamRT+FLD` and `LamFLD`. Top panel: Total mass in primary and companion stars as a function of time for run `LamRT+FLD` (pink solid and dot-dashed lines, respectively) and run `LamFLD` (teal dotted and dot-dashed lines, respectively). Bottom panel: Primary star accretion rate as a function of time for run `LamRT+FLD` (pink solid line) and run `LamFLD` (teal dashed line).

molecular gas at temperatures below $T \lesssim 1500$ K. Run `LamFLD` follows the same initial conditions as run `LamRT+FLD` but does not include the adaptive ray tracing from the *HARM*^{2} algorithm. Figures 4.9 and 4.10 show the time evolution for run `LamFLD`, and are analogous to Figures 4.2 and 4.7 for run `LamRT+FLD`.

In run `LamFLD` the radiation pressure dominated bubbles begin to expand along

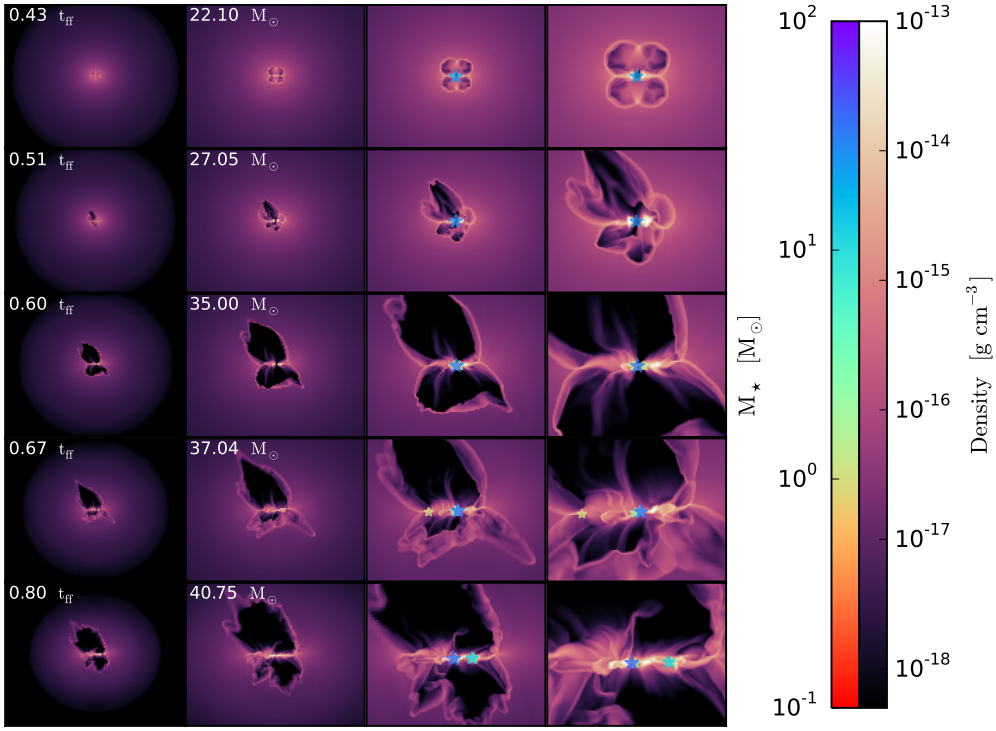

Figure 4.9 Same as figure 4.2, but for run `LamFLD`.

the polar directions (both above and below the star) when the star reaches $\sim 18\ M_\odot$ (not shown in Figure 4.9) whereas in run `LamRT+FLD` a radiation-pressure driven bubble began to expand above (below) the star when it reached a mass of $\sim 15\ M_\odot$ ($\sim 22\ M_\odot$). Similarly, Kuiper *et al.* (2012) also found that their massive star formation simulation, which only included FLD, launched radiation driven bubbles earlier than their comparison run that included both ray tracing and FLD. Comparison of Figures 4.2 and 4.9 also shows that the direct radiation pressure is more efficient at evacuating material interior to the bubble walls while also causing substantial RT instabilities to begin to develop later. This is also demonstrated in the top panel of Figure 4.11, which shows the volume weighted mass density as a function of radial distance of a three-dimensional

cone above the center of the computational domain. In run `LamFLD`, the bottom bubble becomes unstable and collapses onto the disk when the star has reached a mass of ∼23.7 $M_{\odot}$ while the bottom bubble first becomes unstable in run `LamRT+FLD` and begins to collapse when the star has a mass of $\sim 35\ M_{\odot}$. This difference is due to the fact that the direct radiation force falls off as r^{-2} so infalling material will feel a greater force as it falls towards the star, causing the direct radiation to push the material back towards the shell; whereas the diffuse radiation pressure is roughly constant in the bubbles because it follows the radiation energy density. Therefore, the diffuse radiation pressure is less likely to inhibit the non-linear growth of RT instabilities allowing the shells to collapse earlier. As the star becomes more luminous in both runs the bottom bubbles re-expand. However, we find that, regardless of the radiation treatment, the radiation dominated bubbles eventually become unstable and deliver mass to the star-disk system through RT instabilities.

In agreement with Kuiper *et al.* (2012) we also find that neglecting the direct radiation field leads to underestimating the true radiation force density. Figure 4.12 shows volume weighted projection plots of the direct (top left panel), diffuse (top right panel), and total radiation force densities (bottom left panel) for a snapshot of run `LamRT+FLD` when the primary star has a mass of 36.1 $M_{\odot}$. The bottom right panel of Figure 4.12 shows the total radiation force density for run `LamFLD` at the same stellar mass for comparison. The top two panels show that the radiation force density associated with the direct radiation field is much greater than the diffuse component in regions of the bubble shells where the direct component is absorbed while comparison of

the bottom two panels demonstrate that the radiation force density is greatly underestimated at the location of the bubble shells where the direct radiation is absorbed. This is also observed in the bottom panel of Figure 4.11 which shows the volume weighted averaged direct, diffuse, and total radiation force densities as a function of radius for a three-dimensional cone above the center of the computational domain for the snapshots shown in Figure 4.12. We also find the integrated radiative force over a spherical volume with radius 7000 AU around the primary star in run `LamRT+FLD` is a factor of ~ 2 larger than run `LamFLD` when the star is 36.1 $M_{\odot}$. Thus, we find that inclusion of the direct radiation field leads to a larger total radiation force as expected but regions of the bubble shells still become RT unstable regardless.

Although the development of RT instabilities is qualitatively the same for runs `LamRT+FLD` and `LamFLD`, the structure of the accretion disk and the consequent creation of companions is not. Comparison of Figures 4.7 and 4.10 show that the accretion disk in run `LamFLD` is more extended and has an overall lower surface density than in run `LamRT+FLD`. It also undergoes less fragmentation resulting in fewer companions. For example, the primary star in run `LamFLD` has eight companion stars with masses greater than 0.01 $M_{\odot}$ when the primary has a mass of 40.4 $M_{\odot}$, whereas the primary star in run `LamRT+FLD` has 29 companion stars when the primary has a mass of 40.4 $M_{\odot}$. Furthermore, the most massive companion in run `LamFLD` is 11.28 $M_{\odot}$ when the primary has a mass of 40.4 $M_{\odot}$, a factor of $\sim$2.5 larger than the most massive companion in run `LamRT+FLD` for the same primary stellar mass.

Figure 4.8 shows the evolution of the primary and total companion star mass

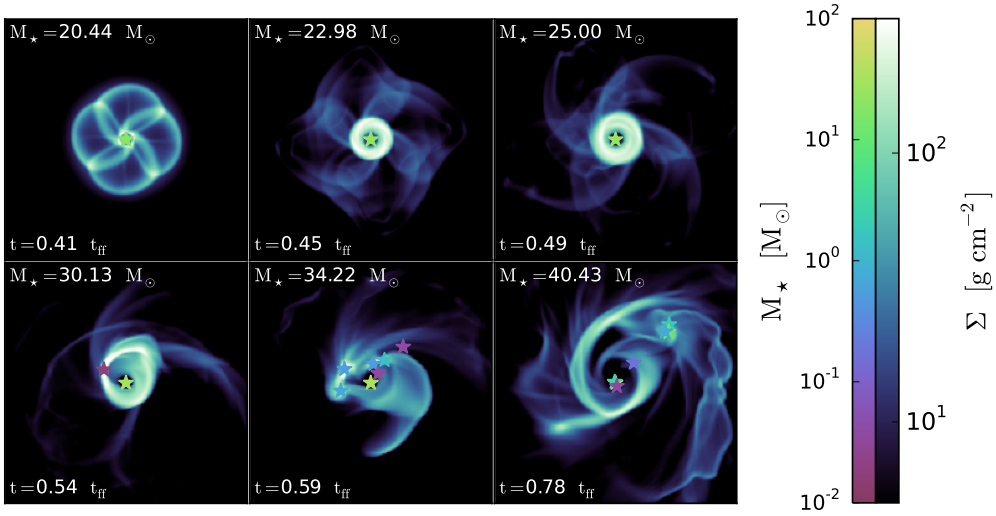

Figure 4.10 Same as figure 4.7, but for run `LamFLD`.

for both runs (top panel) and accretion rate onto the primary star (bottom panel). We find that although the number of companion stars formed is different for each run, the total mass contained in the companion stars is qualitatively similar when the primary star has a mass of 40.4 $M_\odot$ (i.e., the final stellar mass in run `LamRT+FLD`). The accretion rate onto the primary star in each run is also qualitatively similar. Initially the accretion rate onto the primary star is smooth for both simulations, but it becomes chaotic once the disk becomes gravitationally unstable and forms companion stars. This chaotic behavior can be attributed to disk gravitational instabilities and RT instabilities funneling material to the stars. Since run `LamRT+FLD` undergoes a greater degree of disk fragmentation, we find that the total stellar mass in run `LamRT+FLD` is larger than that of run `LamFLD` at $t = 0.70\ t_{\rm ff}$ (the final time in run `LamRT+FLD`). The total stellar mass at this time is 55.80 and 49.68 $M_\odot$ for run `LamRT+FLD` and run `LamFLD`, respectively.

The decrease in disk fragmentation in run `LamFLD` can be understood by looking

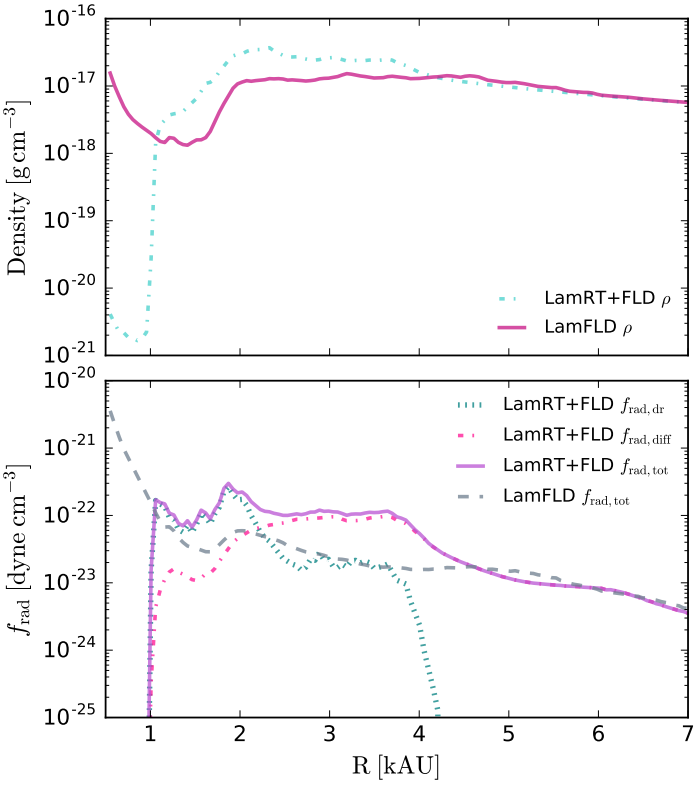

Figure 4.11 Volume-weighted averaged mass densities (top panel) and direct, diffuse, and total radiation force densities (bottom panel) as a function of radius for a three-dimensional cone above the center of the computational domain for runs `LamRT+FLD` and `LamFLD` when the primary star has a mass of 36.1 $M_\odot$.

at the temperature structure of the accretion disks as shown in Figure 4.13. Collapse can only occur in regions that become Jeans unstable, and this instability depends on both the density and temperature of the gas. A hotter, lower density region is less likely to fragment (e.g., see Equation (4.23)). Run `LamFLD` has a hotter accretion disk because the radiation is deposited in the immediate vicinity of the stars, and it subsequently diffuses through the disk, heating up the gas as shown in the bottom right panel of Figure 4.12. In contrast, the absorption of radiation for run `LamRT+FLD` is highly dependent on

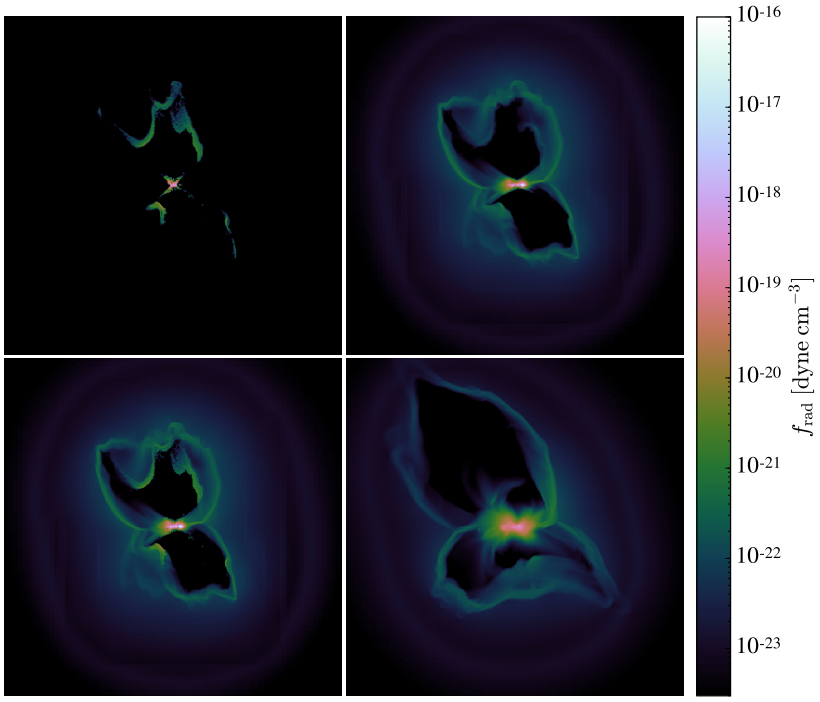

Figure 4.12 Volume-weighted projection plots of the radiation force densities along the yz-plane for the direct radiation field (top left panel) and diffuse radiation field (top right panel) in run `LamRT+FLD` and total radiation field in runs `LamRT+FLD` (lower left panel) and `LamFLD` (lower right panel), respectively, when the star has a mass of 36.1 $M_\odot$. Each projection covers a depth of 500 AU and area of (12,000 AU)^2. The center of each panel corresponds to the location of the most massive star.

the frequency-dependent optical depth of the cells that the rays transverse. Once an evacuated region appears above and below the disk, much of the stellar radiation energy is deposited in the bubble walls at a considerable distance from the disk, allowing the disk to remain cooler. Furthermore, the accretion rate onto the stars depends on the disk temperature, $\dot{M} \propto c_{\rm s}^3$ (Shu, 1977). Thus the hotter gas in the accretion disk in run `LamFLD` produces more massive companion stars, consistent with what we observe.

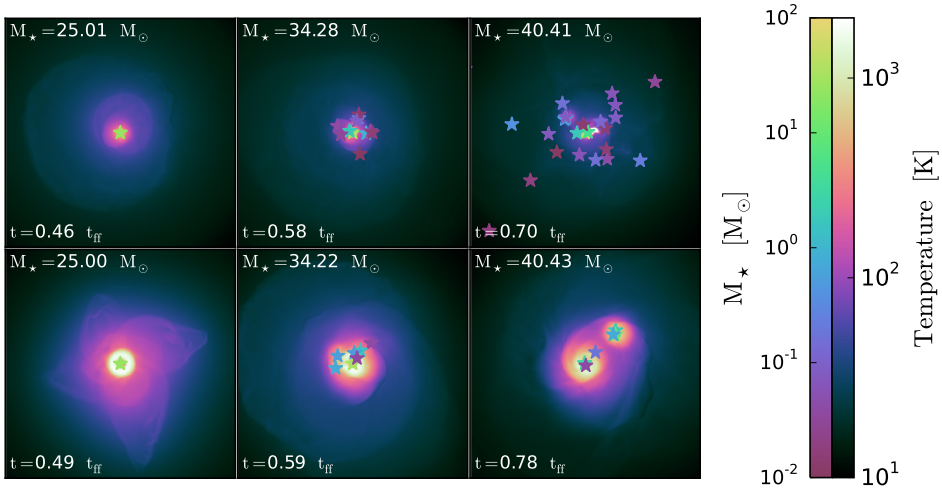

Figure 4.13 Density-weighted mean projected temperature for the accretion disks formed in runs `LamRT+FLD` (top row) and `LamFLD` (bottom row), respectively. Each panel is a projection that is $(5000\ \mathrm{AU})^2$ in size and is projected over a height of 1000 AU above and below the massive star. The most massive star is at the center of each panel, and stars with masses greater than 0.01 $M_\odot$ are over-plotted.

4.3.2 Collapse of Turbulent Pre-stellar Cores

Next we describe our results for run `TurbRT+FLD`, which follows the same initial conditions as run `LamRT+FLD` except that the core is not initially placed in solid-body rotation and is instead seeded with a weakly turbulent velocity profile with a 1D velocity dispersion of $\sigma_{1\mathrm{D}} = 0.4\ \mathrm{km\,s^{-1}}$. At the end of this simulation the most massive star has a mass of 61.63 $M_\odot$. We ran the simulation for a time of $t = 0.87\ t_{\mathrm{ff}}$.

4.3.2.1 Evolution of Radiation Pressure Dominated Bubbles

Figure 4.14 shows density slices along the yz-plane for a series of snapshots from run `TurbRT+FLD`. The initial turbulence leads to a clumpy and filamentary core density structure that begins to collapse and forms a star. As the core continues to

collapse the star is primarily fed by dense filaments and clumpy material. We first see a radiation pressure dominated bubble begin to expand when the star is $\sim 10\ M_{\odot}$ but it is quickly quenched by the dense, inflowing material. Furthermore, these bubbles instantly go RT unstable and deliver material to the star (i.e, within the 80 AU accretion radius of the sink particle). This can be seen within the radiation pressure dominated bubble interiors shown in Figure 4.14 because the size scale of the density fluctuations within the bubbles is smaller than the density perturbations in the initial turbulence surrounding the bubbles, thus suggesting that the interior bubble material has become RT unstable. We find that the growth of a radiation driven bubble is continuously suppressed by the flux of the infalling filamentary and RT unstable material until the star reaches a mass of $\sim 21.7\ M_{\odot}$ at time $t = 0.42\ t_{\rm ff}$. At this time the direct radiation pressure from the accreting star is able to effectively push material away from the star. However, material is not fully evacuated along the polar directions of the star.

This quick onset of RT instabilities can be attributed to the initial turbulence. The turbulent gas seeds the growth of these instabilities. In addition, when the star is below $\sim 30\ M_{\odot}$ the star is moving rapidly in the core because the accreting material carries momentum. Figure 4.15 shows that the stellar velocity decreases as the stellar mass increases. The overall accretion flow onto the star is not spherically symmetric and thus the asymmetrical momentum deposition to the star by the accreting gas causes the star to move a significant distance in the collapsing core, a property also observed in the massive star formation simulations presented in Cunningham *et al.* (2011). Throughout the simulation the star travels a distance of 1968 AU from its initial position. The

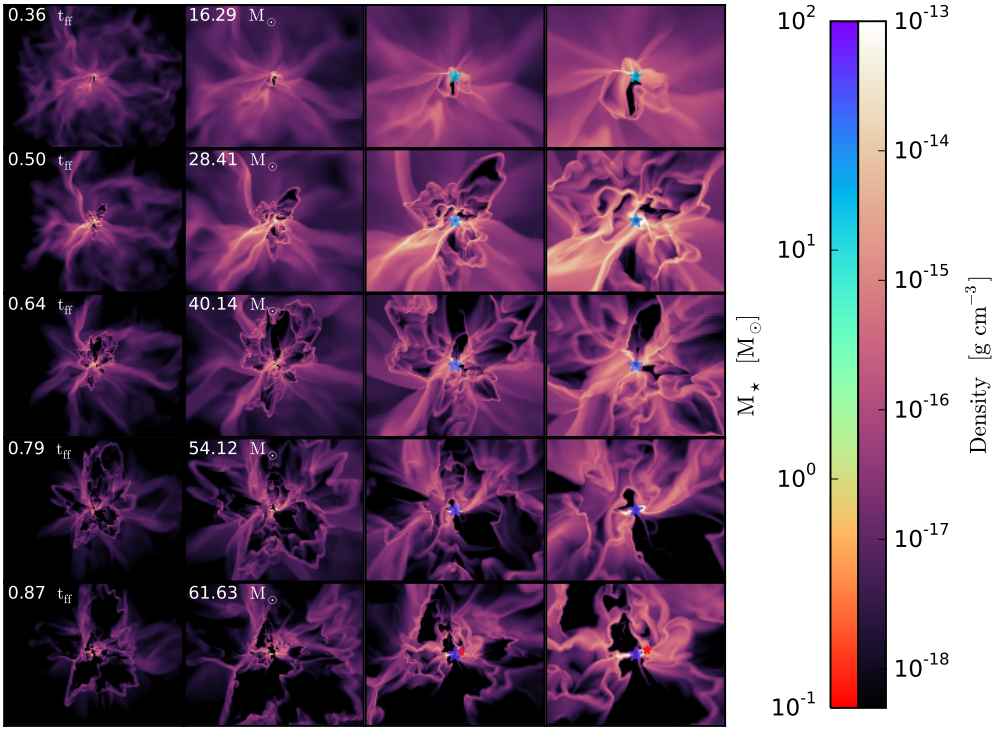

Figure 4.14 Same as Figure 4.2, but for run `TurbRT+FLD`. The center of each panel corresponds to the position of the most massive star.

combination of the movement of the star, dense filaments accreting onto the star, and RT instabilities delivering material to the star limit the growth and stability of radiation pressure dominated bubbles around the star. When the star has a mass greater than $\sim 30\ M_\odot$ radiation pressure begins to evacuate low-density material away from the star but dense filaments and material that become RT unstable continue to fall onto the star. This effect is demonstrated in Figure 4.16 that shows density slices along the yz-plane for a series of snapshots from run `TurbRT+FLD` with velocity vectors over-plotted.

Low density bubbles do not begin to appear until the star has reached a mass of $\sim 35\ M_\odot$ at time $t = 0.59\ t_{\rm ff}$ and these bubbles are larger than those in run `LamRT+FLD`

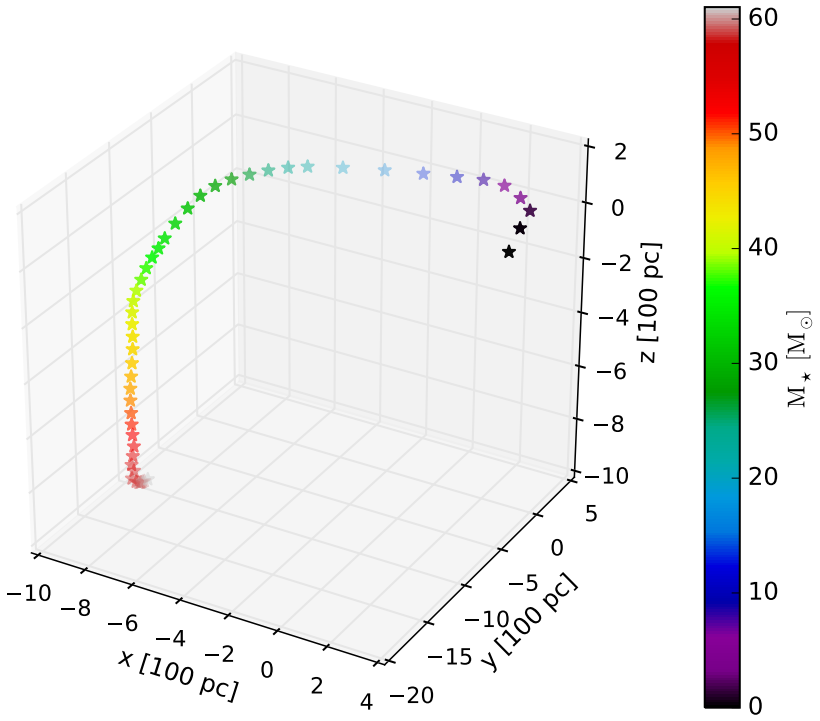

Figure 4.15 Three-dimensional position of the primary star in run `TurbRT+FLD`.

at a similar mass (∼4000 AU versus ∼3000 AU in run `LamRT+FLD`). At this mass the stellar luminosity is large enough to push away the infalling material more effectively. The bubbles then become episodic, expanding and collapsing as the ram pressure of the inflow rises and falls due to the turbulence. This behavior continues throughout the rest of the simulation but the bubbles survive longer and expand as the stellar luminosity increases. At the end of run `TurbRT+FLD`, when the star has a mass of 61.63 $M_\odot$ at time $t = 0.87\ t_{\rm ff}$, most of core has been evacuated by radiation pressure along the polar directions of the star but material is still being fed to the star along directions that are perpendicular to the poles of the star (e.g., see bottom panel of Figure 4.14).

To understand this behavior quantitatively, it is helpful to compare the pres-

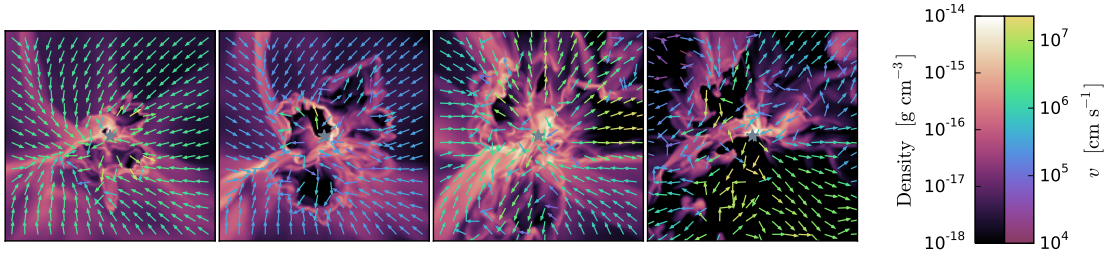

Figure 4.16 Density slices along the yz-plane with velocity vectors over plotted for run `TurbRT+FLD` when the massive star is (from left to right) 23.82 $M_\odot$ at $t = 0.43\,t_{\rm ff}$, 30.03 $M_\odot$ at $t = 0.53\,t_{\rm ff}$, 41.08 $M_\odot$ at $t = 0.65\,t_{\rm ff}$, and 61.63 $M_\odot$ at $t = 0.87\,t_{\rm ff}$, respectively. The region plotted is (10,000 AU)^2 with the most massive star (over plotted gray star) located at the center of each panel.

sure of the stellar radiation field to the ram pressure of the inflow. Consider a sphere 1000 AU in radius centered on the most massive star. To understand the force balance in the problem, we compute three mean pressures on this sphere: the direct radiation pressure (including the accretion and stellar luminosities, averaged over area), the area-weighted mean ram pressure, and the mass-flux weighted mean ram pressure for inflowing material. The former quantity is defined as

$$P_{\rm rad} = \frac{L_\star + L_{\rm acc}}{4\pi r^2 c} \tag{4.25}$$

and the latter two quantities are defined by

$$\langle P_{\rm ram} \rangle = \frac{\int \rho v_r^2 w \, dA}{\int w \, dA}, \tag{4.26}$$

where v_r is the radial velocity, and the weighting function w is unity for the area-weighted average, and is ρv_r for the mass flux-weighted average where we only include

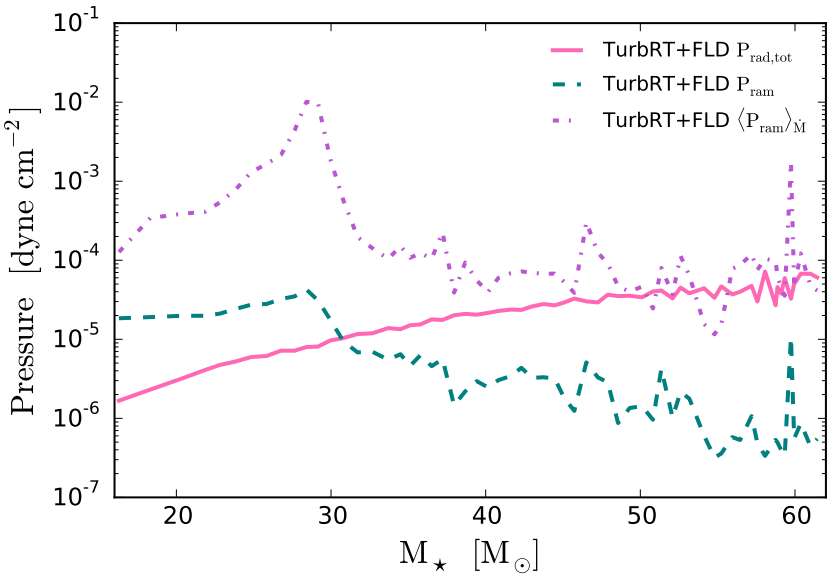

Figure 4.17 Comparison of the direct radiation pressure including contributions from the stellar and accretion radiation fields (pink solid line) and the area-weighted and mass-weighted ram pressure (teal dashed and purple dot-dashed lines, respectively) from inflowing material taken over a 1000 AU sphere surrounding the accreting primary star for run `TurbRT+FLD`. See main text for full details on how these averages are defined.

contributions from inflowing material. We include the mass-flux weighted mean ram pressure because it is a better representation of the ram pressure of the material that can be accreted onto the star. We plot these three quantities as a function of time in Figure 4.17. We see that the radiation pressure overwhelms the area-averaged ram pressure by the time the star reaches $\sim 30\ M_\odot$, but that the mass flux-weighted mean ram pressure is roughly an order of magnitude higher. Thus, even though the radiation pressure is stronger than gas pressure when averaged over 4π sr, turbulence causes the mass flow onto the star to be concentrated in narrow filaments that have much greater ram pressure, and are much harder to stop. It is not until the star reaches $\sim 50\ M_\odot$ that its radiation pressure becomes comparable to the mass flux-weighted ram pressure, and

even then there are still periods when the ram pressure rises and is sufficient to punch through the radiation and deliver mass. This episodic rise in the ram pressure (which is mirrored in the density field by the episodic collapse of the radiation-dominated bubbles) is a direct result of RT instability, accelerated and seeded by the pre-existing turbulence.

4.3.2.2 Accretion Disk Evolution

Figure 4.18 shows the growth and evolution of the accretion disk that forms around the massive star in run `TurbRT+FLD`. Our results show that a thick accretion disk begins to form around the massive star when it has reached a mass of $\sim 41\ M_{\odot}$ at time $t = 0.65\, t_{\rm ff}$ (i.e., an accretion disk with a radius larger than the 80 AU accretion zone radius of the sink particle). Up until this point material is primarily fed to the star through dense filaments and RT instabilities whose infall is not suppressed by radiation pressure. Figure 4.19 shows the primary stellar mass and accretion rate onto the primary star as a function of time. The accretion rate is relatively smooth up until a time of $t = 0.5\ t_{\rm ff}$. After this time, when the star has a mass of $\sim$28 $M_{\odot}$, RT instabilities and dense filaments supply most of the mass onto the star leading to a chaotic accretion flow onto the star. However, when a thick accretion disk forms, at $t \approx 0.65\ t_{\rm ff}$, the accretion rate onto the star becomes much more chaotic because gravitational instabilities in the disk funnel gas to the star while dense filaments and RT unstable material are delivered to the disk. The disk soon becomes unstable and begins to fragment when the primary star has a mass of 57.62 $M_{\odot}$ at time $t = 0.83\ t_{\rm ff}$. At the end of run `TurbRT+FLD` the primary star has three low-mass companion stars with masses between 0.034-0.11 $M_{\odot}$.

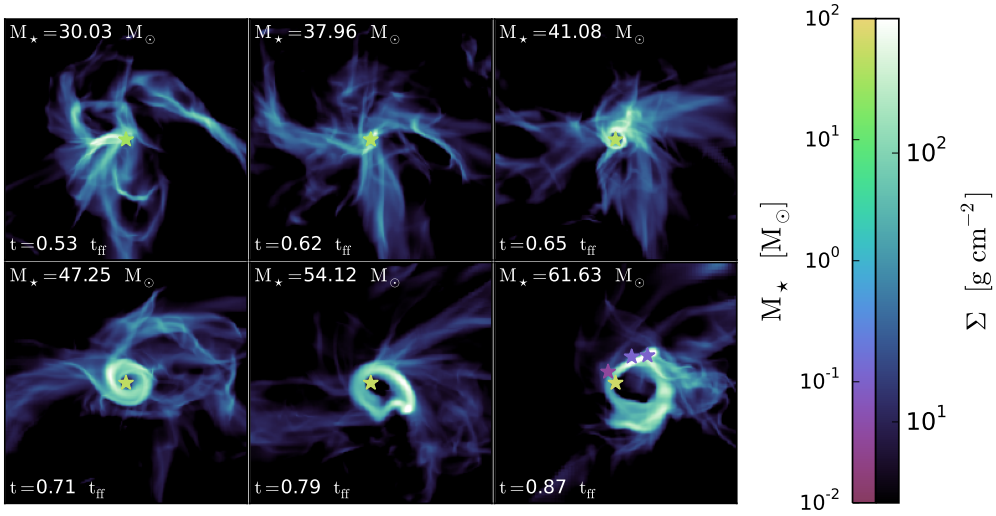

Figure 4.18 Same as Figure 4.7, but for run `TurbRT+FLD`.

Again we form a hierarchical system consisting of a massive primary and a series of much less massive mass companions similar to run `LamRT+FLD`.

4.4 Discussion

The purpose of this work is to understand how mass is delivered to massive stars during their formation. Primarily, we are interested in determining if the radiation pressure dominated bubbles that expand away from the star become RT unstable and if these instabilities contribute to disk accretion or direct accretion onto the star. To answer this question, and compare our work with previous 3D simulations of the formation of massive stars, we developed a new highly parallel hybrid radiation algorithm that models the direct radiation pressure from stars with a multi-frequency long-characteristics ray tracing solve coupled to (gray) flux-limited diffusion to model the re-emission and processing by interstellar dust in the ORION radiation-hydrodynamics

simulation code (Rosen *et al.*, 2017). With this new tool we have performed the collapse of initially laminar and turbulent massive star-forming cores.

Our results lead to two key differences from the simulations presented in Kuiper *et al.* (2011, 2012) and Klassen *et al.* (2016). The first crucial difference, which we discuss in Section 4.4.1, is that we find that the radiation pressure dominated bubbles that expand around the accreting massive star become unstable and deliver mass to the star-disk system for both initially laminar and turbulent cores. The second difference we find, which we address in Section 4.4.2, is that inclusion of direct radiation pressure leads to unstable accretion disks that fragment into a hierarchical system consisting of a massive primary and a series of much less massive companions. Finally, we also find if the pre-stellar core is initially turbulent the growth of radiation pressure dominated bubbles are suppressed at early times as compared to massive stars that form out of initially laminar cores. For initially turbulent cores, we find that most of the mass is supplied to the star via dense filaments and RT instabilities rather than extended disk accretion. We discuss these differences in Section 4.4.3.

4.4.1 Revisiting Rayleigh Taylor Instabilities

Kuiper *et al.* (2011, 2012) and Klassen *et al.* (2016) find that the expanding radiation pressure dominated bubbles that form around accreting massive stars are stable and the massive star is only fed by disk accretion. They suggest that the bubbles that form in the simulation presented in Krumholz *et al.* (2009) develop RT instabilities because only the diffuse dust-reprocessed radiation field is modeled and therefore the

true radiation pressure is underestimated. These authors conclude that inclusion of the direct radiation field from the star leads to a larger radiation pressure resulting in stable bubbles that are not subject to collapse. In contrast, we find that, while an improved treatment of the direct radiation field does lead to a larger radiation pressure it only *delays* the onset of substantial RT instabilities that are capable of delivering mass to the star-disk system in the case of a laminar core, it does not prevent them entirely. At late times these instabilities grow non-linearly in regions that are shielded from the direct radiation field and deposit material to the star-disk system. This material can then be fed to the accreting star. We would like to understand the origin of this difference in results, though we caution that, in the light of our results for run `TurbRT+FLD`, this discussion is somewhat academic. This run shows that, in a realistic, turbulent core, the flow is "born" RT unstable, in the sense illustrated by Figure 4.17 – a configuration whereby the angle-averaged radiation force is stronger than gravity and ram pressure, but the majority of the mass flux arrives over a small solid angle where the ram pressure force is stronger than the radiation force.

Since Kuiper *et al.* (2011, 2012) and Klassen *et al.* (2016) hypothesize that the absence of RT instability in their simulations was due to the direct radiation force, we begin this investigation by examining when the presence of direct radiation pressure could possibly make a difference to the outcome. We therefore investigate when the gravitational force per unit area, $f_{\rm grav}(r) = GM_\star\Sigma/r^2$, exceeds the direct radiative force per unit area, $f_{\rm rad,dir}(r) = L_\star/(4\pi r^2 c)$. Here $M_\star$ and $L_\star$ are the mass and luminosity of the massive star, respectively; and $\Sigma(r) = \int_0^r \rho(r')dr'$ is the column density of a

slab of core material as seen by the star. The relative importance of direct radiation force and gravity can be described in terms of the Eddington ratio given in Section 4.1 where we now ignore the contribution of the trapped diffuse radiation force, $f_{\rm edd,dir} = f_{\rm rad,dir}/f_{\rm grav}$, given by

$$f_{\rm edd,dir} = 7.7 \times 10^{-5} \left(\frac{L_\star}{M_\star} \right)_\odot \left(\frac{\Sigma}{1 \text{ g cm}^{-2}} \right)^{-1}. \tag{4.27}$$

The notation $(...)_\odot$ denotes that $L_\star$ and $M_\star$ are in units of $L_\odot$ and $M_\odot$, respectively. A value of $f_{\rm edd,dir} \gtrsim 1$ implies that direct radiation pressure is dynamically dominant, while a value of $f_{\rm edd} < 1$ implies that gravity dominates. In the latter regime the force exerted by the *diffuse* radiation field may still exceed the force of gravity, but in such regions we expect RT instability to occur (Jacquet and Krumholz, 2011). Locations where $f_{\rm edd,dir} < 1$ can therefore collapse and deliver mass to the star-disk system.

We compute $f_{\rm edd,dir}$ as a function of position within the initial pre-stellar cores modeled by Krumholz *et al.* (2009), Kuiper *et al.* (2011), Kuiper *et al.* (2012), Klassen *et al.* (2016), and this work (using the core properties listed in Table 4.2) for light to mass ratios appropriate for zero age main sequence stars with masses $M_\star = 35 - 45\ M_\odot$, and plot the results in Figure 4.20. For the purposes of this computation, note that the core density profile in all of these simulations is $\rho(R) = \rho_{\rm edge}(R/R_c)^{-k_\rho}$ where $\rho_{\rm edge} = (3 - k_\rho)M_{\rm c}/(4\pi R_{\rm c}^3)$ for a pre-stellar core with mass $M_{\rm c}$ and radius $R_{\rm c}$. The resulting column density, as seen by the star at a distance R, is $\Sigma(R) = \rho_0 R_c^{k_\rho} R^{1-k_\rho}/(k_\rho - 1)$. Of these simulations only those presented in Krumholz *et al.* (2009) and this work find

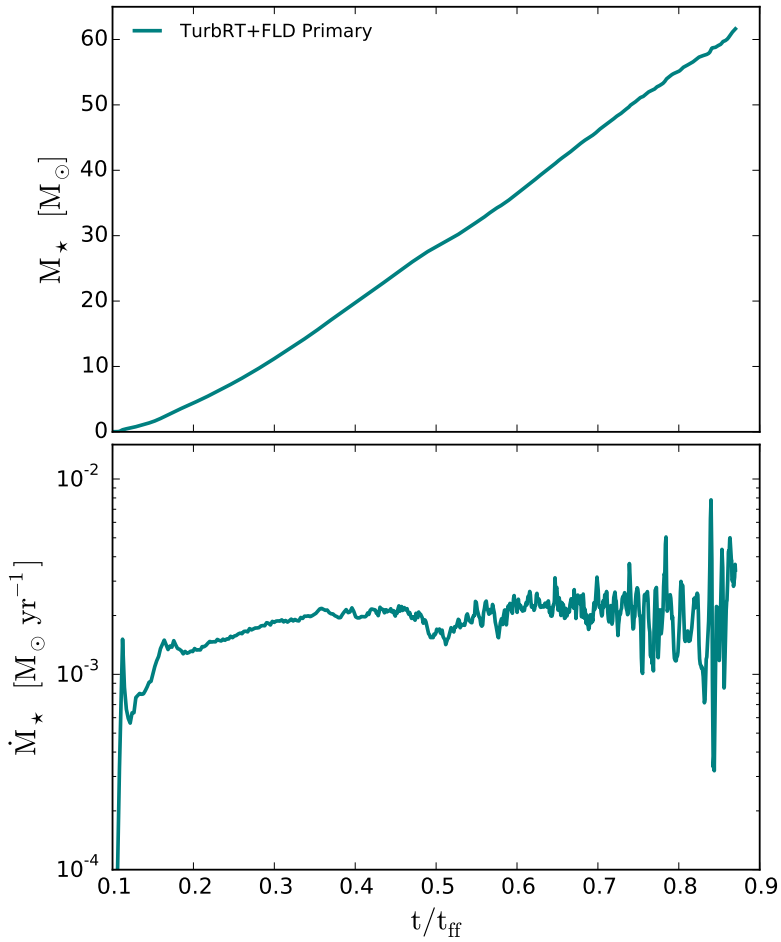

Figure 4.19 Stellar mass (top panel) and accretion rate (bottom panel) for the primary star in run `TurbRT+FLD`.

that the radiation-pressure dominated bubble shells become RT unstable, and Figure 4.20 makes it clear that at least part of this discrepancy is simply a matter of initial conditions. We find that the cores with $k_\rho = 2$ presented in Kuiper *et al.* (2011) and Kuiper *et al.* (2012) have $f_{\rm edd,dir} > 1$ over a substantial portion of their radial extent, as a result of the cores' steeper density profile, and lower overall surface density. As a result, direct radiation pressure alone, without any assistance from the diffuse reprocessed radiation field, is sufficient to expel material from the cores simulated by

Kuiper *et al.* (2011), and possibly also Kuiper *et al.* (2012). It is not surprising, given such a setup, that RT instability does not develop – the diffuse radiation field never matters, because direct radiation alone guarantees a net positive radial acceleration.

While this simple argument explains why the cores simulated by Kuiper *et al.* (2011) and perhaps Kuiper *et al.* (2012) never develop RT instabilities, it does not explain the discrepancy between our results and those of Klassen *et al.* (2016), who have direct Eddington ratios comparable to those in our simulation. One key difference between the work of those authors and the simulations we present here is refinement of the bubble shell. Refining the bubble shell is crucial for studying the growth of RT instabilities in massive star formation simulations because the amplitude η of linear perturbations (which is the relevant regime for the non-turbulent simulations) grows with time as $\eta(t) \propto \exp(\omega t)$, where $\omega \propto \lambda^{-1/2}$ and λ is the wavelength of the perturbation (Jacquet and Krumholz, 2011). Thus for radiation RT instability, as for classical hydrodynamic RT instability, the smallest perturbations grow fastest. However, perturbations can only grow if they are resolved, and we warn that RT instabilities with wavelengths smaller than the cell size on the finest level can not be resolved, thereby suppressing smaller scale perturbations that will grow faster in the linear regime.

Based on this analysis, the lack of RT instability in the work of Kuiper *et al.* (2012) and Klassen *et al.* (2016), and its presence in our simulations, is likely a resolution effect. We can make this point quantitatively as follows. In this work, and the work of Krumholz *et al.* (2009), we adaptively refine on the Jeans length and locations where the gradient of the radiation energy density exceeds 15%. Figure 4.21 shows density

and radiation energy density slices, with the level 4 and 5 grids over-plotted, at the time when the star in run `LamRT+FLD` has a mass of 40.4 $M_{\odot}$ at time 0.7 $t_{\rm ff}$. This Figure shows that the radiation pressure dominated bubbles are refined up to level 4 (40 AU resolution) and that most of the bubble shells have level 5 refinement (20 AU resolution). The level 5 refinement for the bubble shell is due to our radiation energy density gradient refinement criterion, because this refinement condition is triggered by the sharp gradient in the radiation energy density at the shell location (i.e., where it transitions from optically thin to optically thick material).

In contrast, Kuiper *et al.* (2012) use a non-adaptive spherical grid that provides much higher resolution than we achieve near the star, but that coarsens rapidly at large distances. The grid has a resolution of 5.625° in the θ direction, which at a distance of 4,000 AU, roughly the sizes of our bubbles at the point where they become unstable, corresponds to $\approx$ 400 AU. Thus their resolution is a factor of $\sim$ 20 lower than ours, and the linear growth rate is a factor of $\approx$ 4.5 lower. This may push the development of the instability back to times longer than the time required for all the mass to be accreted. The situation for Klassen *et al.* (2016) is similar. While they do have adaptivity, they refine only on Jeans length and not on gradients in the radiation energy density, and thus their bubble walls are at much lower resolution than the peak they achieve. Visual inspection of their published results (their Figure 12) suggests that a typical resolution in their bubble walls is 160 AU, giving a growth time $\approx$ 3 times longer than we have.

We can also test the resolution hypothesis directly. To do so, we perform a low resolution run, run `LamRT+FLD_LR`, which has four levels of refinement (40 AU maximum

Table 4.2 Comparison of the initial laminar pre-stellar core conditions from this work and previous numerical work.

Work	$M_{\rm c}$ [$M_\odot$]	$R_{\rm c}$ [pc]	k_ρ	$\Sigma_{\rm c}$[a][g cm^{-2}]	RTI?[b]
This work	150	0.1	1.5	1	Yes
Klassen *et al.* (2016)	100, 200	0.1	1.5	0.67, 1.33	No
Kuiper *et al.* (2012)	100	0.1	1.5, 2	0.67	No
Kuiper *et al.* (2011)	120	0.2	2	0.2	No
Krumholz *et al.* (2009)	100	0.1	1.5	0.67	Yes

[a] $\Sigma_c \equiv M_c/\pi R_c^2$

[b] Rayleigh Taylor instabilities present?

References. — Krumholz *et al.* (2009); Kuiper *et al.* (2011, 2012); Klassen *et al.* (2016)

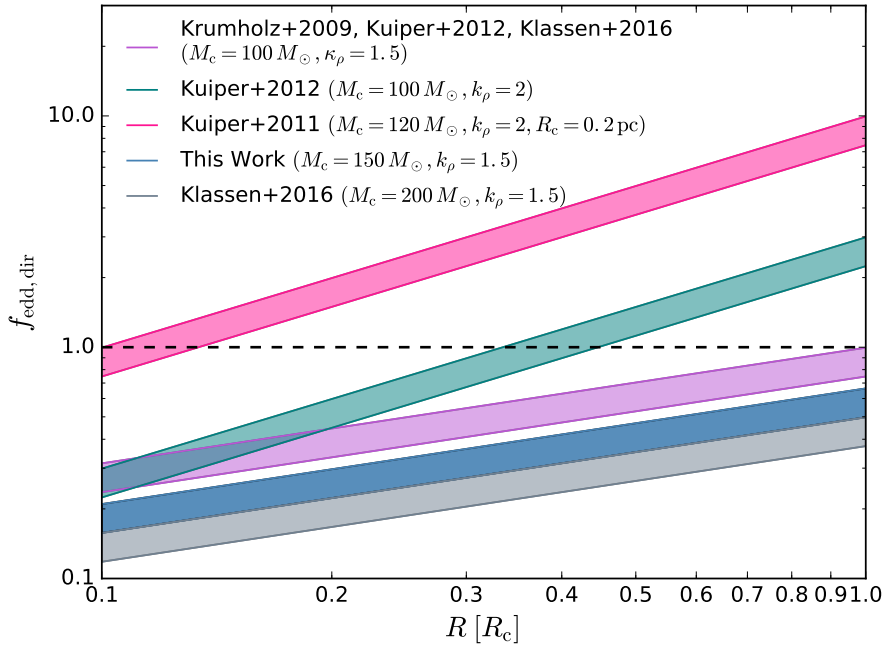

Figure 4.20 Eddington ratio associated with the direct radiation field ($f_{\rm edd,dir}$) for the initial core properties listed in Table 4.2 as a function of radius within the core. Shaded regions denote $L_\star/M_\star$ values computed for a zero age main sequence star between 35 (bottom line) and 45 (top line) $M_\odot$ in mass. The horizontal black dashed line denotes where $f_{\rm edd,dir} = 1$.

resolution) and only refines on the Jeans length. Thus run `LamRT+FLD_LR` uses the same refinement criteria as Klassen *et al.* (2016). This reduction in refinement criteria ensures that the shell will be poorly resolved. Figure 4.22 shows density slices along the yz-plane showing the evolution of the expanding radiation dominated pressure bubbles for run `LamRT+FLD_LR`. Comparison of Figure 4.22 with Figure 4.2 demonstrates that when the shell is poorly resolved RT instabilities are unlikely to develop. In run `LamRT+FLD` we found that RT instabilities began to have noticable growth when the star was $\sim 30\ M_{\odot}$ whereas the bubbles in run `LamRT+FLD_LR` remain stable until the star has reached a mass of $\sim 37.5\ M_{\odot}$, and even after this point the instability is clearly less violent and delivers less mass than in the higher resolution run. Clearly resolution matters a great deal for the development of RT instability.

The late-onset instability in our low resolution run also points to one more potentially important difference between our simulations and those of Klassen *et al.* (2016). The instability in run `LamRT+FLD_LR` first appears when the left side of the disk becomes flared and most of the direct radiation is absorbed by the disk, shadowing the left side of the bubble. Shadowing of the direct radiation field is clearly an important process. Our direct radiation treatment uses the method of long characteristics which is more accurate than the method of hybrid characteristics used in Klassen *et al.* (2016). Far away from the source, as the rays cross many grids, this method will not resolve sharp shadows as well as long characteristics, and will likely underestimate the asymmetry in the direct radiation field thus suppressing the development of RT instabilities.

4.4.2 Revisiting Disk Fragmentation

Most massive stars are found in multiple systems. Chini *et al.* (2012) performed a spectroscopic study of massive stars and found that $> 82\%$ of stars with masses greater than 16 $M_{\odot}$ belong to close binary systems. Likewise, Sana *et al.* (2014) found that all massive main-sequence stars in their sample are in tight binaries or higher order multiples. Both authors conclude that this large binary fraction originates from the formation process rather than direct capture. In agreement with these observations, we formed multiple systems in runs `LamRT+FLD` and `TurbRT+FLD` where companions form from disk fragmentation. At the end of each run we are left with a hierarchical system consisting of a massive primary and a series of low-mass companions. Contrary to our results, Klassen *et al.* (2016) only form a single massive star in each of their simulations while Krumholz *et al.* (2009) form a massive binary system. We attribute these differences in stellar multiplicity to be due to the different sink particle creation and merging algorithms employed.

The accretion disks formed in the work of Klassen *et al.* (2016) become gravitationally unstable but do not fragment. This result is likely attributed to their stricter sink particle creation algorithm while our production of many low-mass companions may be due to our more lenient algorithm. In this work, sink particles are created following the algorithm described in Krumholz *et al.* (2004), which allow sinks to form in regions that are Jeans unstable on the finest level and are undergoing gravitational collapse. The sink particle algorithm employed in Klassen *et al.* (2016) includes these

requirements but also enforces additional criteria following the work of Federrath *et al.* (2010a). These additional requirements for sink particle creation are: (1) the flow must be convergent, (2) the location at which a sink can form must be a minimum for the gravitational potential, and (3) the total energy within a control volume around the potential sink particle be negative ($E_{\rm grav} + E_{\rm th} + E_{\rm kin} < 0$). These additional requirements are essentially untested in the context of an unstable accretion disk, and it is not clear if they help prevent artificial fragmentation, or if they suppress the formation of fragments that would in fact form if the simulation had been carried out at higher resolution.

In contrast to our hierarchical systems, Krumholz *et al.* (2009) form a massive binary with a mass ratio of $q = m_2/m_1 \approx 0.7$. One key difference between the work of Krumholz *et al.* (2009) and run `LamRT+FLD` presented in this work, besides the method of radiative transfer used, is the criterion used for merging sink particles. As described in Section 4.2.1 we allow two sink particles to merge when the lower mass particle has a mass less than 0.05 $M_\odot$. Krumholz *et al.* (2009) use the same sink particle creation algorithm as our work but allow particles to merge once two particles are within an accretion radius (i.e., 4 cells) of one another regardless of their mass. This lenient merging criteria allows for a series of disk-borne companions to merge together to form a more massive companion star, eventually resulting in a massive binary system. Furthermore, as run `LamFLD` demonstrated, the disk properties are highly dependent on the radiative transfer method employed. When the direct radiation pressure is neglected, we are left with hotter accretion disks that are less prone to fragmentation. The hotter

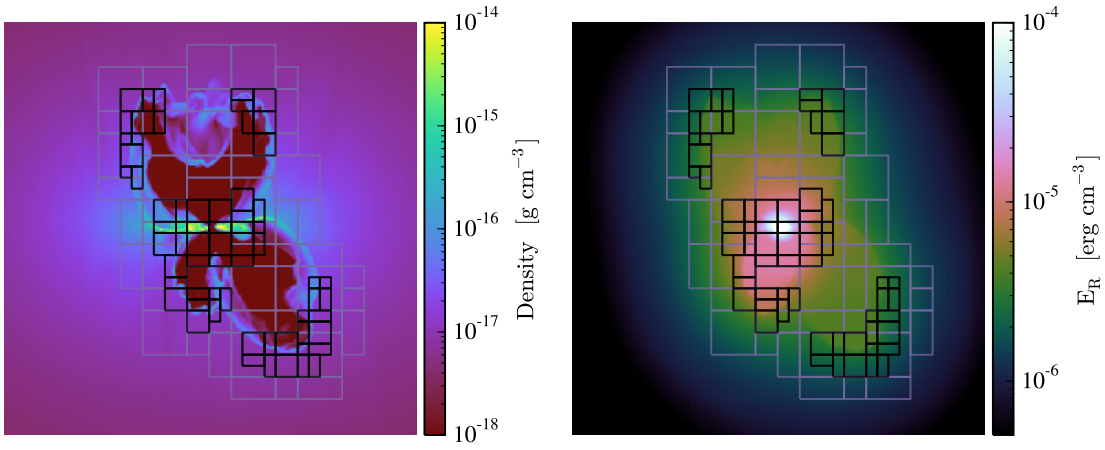

Figure 4.21 Density and radiation energy density slices along the yz-plane for run `LamRT+FLD` when the star has a mass of 40.4 $M_\odot$ at $t = 0.7\ t_{\rm ff}$. Level 4 grids (40 AU resolution – gray rectangles) and level 5 grids (20 AU resolution – black rectangles) are over-plotted. The region plotted is (12,000 AU)^2 and the center of each panel corresponds to the primary star location.

gas yields higher accretion rates onto the companion stars, leading to larger masses.

Comparison of our results with previous work demonstrates that the multiplicity and companion mass distribution produced in massive star formation simulations is highly sensitive on the simulation resolution, radiative transfer, and algorithms used to create and merge sink particles. Since the fragmentation and resulting system multiplicity is sensitive to the numerics, we advise the reader that the fragmentation produced in our idealized numerical simulations and other simulations does not provide an adequate solution to the multiplicity of observed massive stars. Future work must include additional physics, such as magnetic fields and outflows, to further understand the observed multiplicity of massive stellar systems.

4.4.3 Revisiting the Flashlight Effect

In agreement with previous work, we find that disk accretion supplies most of the mass to the primary star in run `LamRT+FLD`. The presence of an optically thick accretion disk shields the stellar radiation field leading to the "flashlight" effect in which the radiative flux escapes along the polar axis and into the polar cavities, launching radiation pressure dominated bubbles above and below the star (Yorke and Sonnhalter, 2002; Krumholz *et al.*, 2009; Kuiper *et al.*, 2011, 2012; Klassen *et al.*, 2016). As the bubbles expand they become unstable and deliver material to the star-disk system that can then be accreted onto the star. The asymmetry induced by the flashlight effect allows radiative flux to escape while mass from the disk can be accreted onto the star.

In run `TurbRT+FLD`, however, we find that the flashlight effect is less important and that the initial turbulence allows for asymmetry in the radiation field. Instead of extended disk accretion the majority of the mass is delivered to the star by dense filaments and RT instabilities that are not destroyed by radiation pressure. The radiation freely escapes through low density channels that are not necessarily located along the polar directions of the primary star. The rapid infall of dense material inhibits the growth and stability of radiation pressure dominated bubbles at early times thus only allowing the "flashlight" effect to occur at late times when the star has a larger luminosity. Therefore, we find that if the matter distribution of the core is asymmetric to begin with then the flashlight effect is not necessary for the formation of massive stars out of turbulent cores. However, our simulations neglect the effect of bipolar stellar outflows

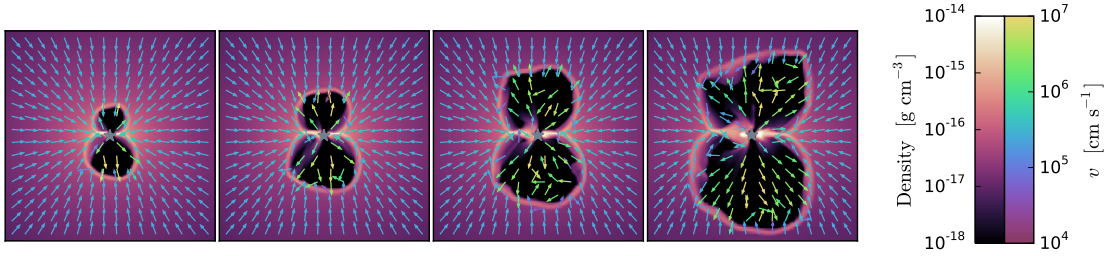

Figure 4.22 Density slices along the yz-plane with velocity vectors over-plotted for run `LamRT+FLD_LR` when the massive star is (from left to right) 24.70 $M_\odot$ at $t = 0.43\,t_{\rm ff}$, 30.05 $M_\odot$ at $t = 0.46\,t_{\rm ff}$, 34.22 $M_\odot$ at $t = 0.50\,t_{\rm ff}$, and 40.34 $M_\odot$ at $t = 0.57\,t_{\rm ff}$, respectively. The region plotted is (8,000 AU)^2 with the most massive star (over plotted gray star) located at the center of each panel.

that have been shown to enhance the flashlight effect (Cunningham *et al.*, 2011; Kuiper *et al.*, 2015).

For example, Cunningham *et al.* (2011) were the first to perform 3D radiation-hydrodynamic simulations of the collapse of initially turbulent pre-stellar cores that included feedback from bipolar stellar outflows and radiation, but they neglected the direct radiation field. They found that inclusion of bipolar outflows from the massive protostar increases the ejection of ambient material along the polar directions of the star, enhancing the flashlight effect. This effect is enhanced because regions of the core that are expected to experience a large net force by the outward radiation force lie within the outflow cavity. The stellar outflows evacuate material along the polar directions of the primary star. These outflow cavities provide significant focusing of the radiative flux in the polar directions, resulting in the radiative flux to escape while accretion continues through regions of the infalling envelope uninhibited by the radiative force.

4.5 Conclusions

In this paper, we have used our powerful new hybrid radiation transfer tool, $HARM^2$, in a suite of radiation-hydrodynamic simulations that followed the collapse of initially laminar and turbulent massive pre-stellar cores to study the formation of massive stars. $HARM^2$ uses a multi-frequency adaptive long-characteristics ray tracing scheme to capture the first absorption of the direct radiation from stars by the intervening interstellar dust and molecular gas, and flux limited diffusion to model the diffuse radiation field associated with the subsequent re-emission by interstellar dust. Our method is highly optimized and can run efficiently on hundreds of processors, works on adaptive grids, can be coupled to any moment method, and can be used for an arbitrary number of moving stars (Rosen *et al.*, 2017).

The primary goal of our work is to determine how massive stars attain their mass when radiation pressure is the only feedback mechanism considered (i.e., in the absence of magnetic fields, outflows, and photoionization). Do massive stars obtain their mass through disk accretion alone? Or do radiative Rayleigh Taylor instabilities that develop in the radiation pressure dominated bubble shells, which are launched by the stars' intense radiation fields, deliver material directly via collapse onto the stars or star-disk systems? Or is it a combination of both of these processes?

For initially laminar cores, we find that the majority of mass delivered to the massive star is due to disk accretion, but that RT instabilities are responsible for bringing material onto the disk before it is subsequently incorporated into the star.

For initially weakly turbulent cores, in contrast, we find that dense filaments and RT unstable material supply most of the mass to the accreting massive star directly, without mediation by an extended disk (i.e., an accretion disk with a radius larger than the 80 AU accretion zone radius of the sink particle) for the run time considered. However, we find that once an extended disk formed, disk accretion supplies material to the primary star. Our results show that the radiation escapes through low density channels that are not necessarily located along the polar directions of the star and that sustained radiation pressure dominated bubbles do not appear until late times when a significant accretion disk develops. For stronger turbulence at the level seen in many massive cores, we would expect this effect could be enhanced. Our results suggest that the "flashlight" effect that occurs in our laminar runs, which allows the radiative flux to escape along the polar directions of the star and material to be accreted onto the star by an optically thick accretion disk, is not required for massive stars that form from turbulent cores. Instead, the asymmetric density distribution allows the radiation to escape through the path(s) of least resistance, allowing the dense infalling material to fall onto the star regardless of its location.

Our results also demonstrate that RT instabilities are a natural occurrence in the formation of massive stars regardless of whether the star-forming core is initially turbulent or laminar. These instabilities arise immediately for turbulent cores because the initial turbulence seeds the instabilities. RT instabilities develop later for laminar cores because the initially symmetric gas distribution must be perturbed. These perturbations can then seed RT instabilities that grow in time and can eventually deliver

material to the star-disk system. We find that the development of an accretion disk and gravitational torques induced within the disk destroy the symmetry of the gas distribution and seed the initial perturbations that lead to RT instabilities in the bubble shells as first shown by Krumholz *et al.* (2009). Our work suggests that the seeds for RT instabilities that arise in initially laminar pre-stellar cores are asymmetries induced by the shielding of the direct radiation field by the accretion disk and the non-symmetric distribution of material within the bubbles. These asymmetries arise from disk flaring, disk fragmentation, and the gravitational interaction of the massive star with the accretion disk and companions.

Previous work that simulated the collapse of initially laminar cores concluded that the direct radiation field inhibited the growth of RT instabilities (Kuiper *et al.*, 2012; Klassen *et al.*, 2016). Contrary to their results we find that inclusion of the direct radiation field only suppresses the non-linear growth of these instabilities at early times. As the asymmetry in the system grows, these instabilities can grow non-linearly and become dense enough to overcome the radiation-pressure barrier and deliver material to the star-disk system. We argue instead that poor shell resolution is the likely culprit as to why Kuiper *et al.* (2012) and Klassen *et al.* (2016) do not obtain bubble shells that become RT unstable. We check this hypothesis directly by conducting a resolution study where we intentionally de-resolve the bubble shell to the point where our resolution is comparable to that used in earlier work, and we show that doing so both delays the onset of instability and reduces its intensity. We further find in the work of Kuiper *et al.* (2012), that limitations of their fixed grid approach with a star that is centrally fixed

in a spherical grid does not permit the movement of the star-disk system that would naturally allow asymmetries to arise and lead to seeding the RT instability.

We find that both turbulent and laminar cores lead to hierarchical star systems that consist of a massive primary star and several low-mass companions. We find that our multiplicity results are sensitive to the physics included, radiative transfer treatment used, and sink creation and merging criteria employed. Inclusion of the direct radiation pressure leads to cooler disks that are prone to greater fragmentation when compared to our comparison run that neglected the direct radiation field and assumed that the stellar radiation was immediately absorbed within the vicinity of the stars. However, given the idealized nature of our simulations, we cannot address the true multiplicity properties of massive stars.

Despite this limitation, our work settles a long-debated question in massive star formation: how does radiation pressure limit the masses of stars? We find that radiation pressure is still an important feedback mechanism that must be considered in massive star formation, but RT instabilities can overcome the radiation pressure barrier, at least in the context of the idealized numerical experiments performed thus far. However, there are still many other physical processes at play that we neglect. These include collimated outflows, fast stellar winds, and magnetic fields. Future work will include these other feedback mechanisms to determine a more complete picture of how massive stars form and how their associated feedback can limit stellar masses.

Chapter 5

Gone With the Wind: Where is the Missing Wind Energy from Massive Star Clusters?

A version of this chapter has been published as "Gone With the Wind: Where is the Missing Wind Energy from Massive Star Clusters?," Rosen, A. L., Lopez, L. A., Krumholz, M. R., Ramirez-Ruiz, E. 2014, *Monthly Notices of the Royal Astronomical Society*, 442, 2701.[1]

5.1 Introduction

Massive star clusters (MSCs; $M_\star \gtrsim 10^3$ $M_\odot$) are born in the dense regions of giant molecular clouds (GMCs). The resulting injection of energy and momentum by

the young stars (i.e., stellar feedback) terminates star formation and expels gas from the MSC. These feedback processes are likely responsible for the low star formation efficiencies observed in GMCs (Matzner and McKee, 2000; Krumholz and Tan, 2007), they control the dynamics of the H II regions surrounding these young clusters (Krumholz and Matzner, 2009; Lopez *et al.*, 2011, 2013a), and they may be responsible for the dissolution and ultimate disruption of their host molecular clouds. For recent reviews, see Krumholz (2014) and Krumholz *et al.* (2014).

Newborn stars in these clusters dramatically affect the surrounding interstellar medium (ISM) via photoionization flows (e.g., Dale *et al.* 2013), direct stellar radiation pressure (e.g., Krumholz and Matzner 2009; Fall *et al.* 2010; Murray *et al.* 2010), dust-reprocessed radiation pressure (e.g., Thompson *et al.* 2005; Murray *et al.* 2010), protostellar outflows (e.g., Cunningham *et al.* 2011), and hot gas shock-heated by stellar winds (e.g., Castor *et al.* 1975; Weaver *et al.* 1977; Cantó *et al.* 2000; Stevens and Hartwell 2003; Harper-Clark and Murray 2009) and supernovae (SNe; e.g., McKee and Ostriker 1977; Chevalier and Clegg 1985). The expansion of a cool, dense shell of interstellar material surrounding the H II region is driven by these processes (Castor *et al.*, 1975; Weaver *et al.*, 1977; McKee and Ostriker, 1977; Krumholz and Matzner, 2009).

It is still uncertain which of these processes dominate stellar feedback and thus drive the subsequent expansion of the H II region shell. Recent studies of H II regions that host MSCs suggest that the thermal pressure of the warm ($\sim 10^4$ K) ionized gas dominates H II region dynamics at late times, while radiation pressure may dominate during H II regions' infancy (for $R_{\rm HII} \lesssim 1 - 100$ pc; Krumholz and Matzner, 2009;

Fall *et al.*, 2010; Lopez *et al.*, 2011, 2013a). However, the importance of stellar winds remains uncertain (Lopez *et al.*, 2011; Pellegrini *et al.*, 2011; Rogers and Pittard, 2013; Lopez *et al.*, 2013a). The total energy injected by stellar winds is quite large for MSCs (Kudritzki *et al.*, 1999; Repolust *et al.*, 2004), but whether this energy contributes significantly to the dynamics of the shell, or if most of it escapes or is radiated away, remains unresolved.

Massive stars have mass-loss rates on the order of $\dot{M}_{\rm w} \sim 10^{-6}$ M$_\odot$ yr^{-1} (Repolust *et al.*, 2004). This mass escapes the stellar surface at velocities of $v_{\rm w} \sim 1000$ km s^{-1} (Leitherer *et al.*, 1992), resulting in an energy injection rate of $(1/2)\dot{M}_{\rm w}v_{\rm w}^2 \sim 100\ L_\odot$ per massive star. In a MSC, these fast stellar winds collide with the winds of nearby stars, producing multiple shocks with complex morphologies. The hot, collective stellar wind will then produce an outward-directed "cluster wind" as the hot gas adiabatically expands and ultimately leaves the cluster (Cantó *et al.*, 2000; Stevens and Hartwell, 2003). The resulting "super-bubble" (Bruhweiler *et al.*, 1980) fills the surrounding H II region with hot, shocked stellar wind material at temperatures of $\sim 10^7$ K, and produces diffuse X-ray emission. This X-ray emission has been detected from numerous MSCs in the Milky Way (MW; Moffat *et al.* 2002; Townsley *et al.* 2003, 2006, 2011a) and the Large Magellenic Cloud (LMC; Lopez *et al.* 2011, 2013a).

While the source of the X-ray emission is well understood, its luminosity is not: the X-ray luminosity of H II regions associated with MSCs is less than expected if the kinetic energy supplied by winds was retained within the super-bubbles. There are several competing theoretical models to account for the X-ray luminosity in bubbles

around MSCs, and these models imply different dynamical importance for stellar winds (and SNe, which also produce shocked hot gas). Castor *et al.* (1975) and Weaver *et al.* (1977) assume that the hot gas in the bubble is fully confined by a cool shell expanding into a uniform density ISM, whereas Chevalier and Clegg (1985) ignore the surrounding ISM and simply assume a steady, freely-expanding wind. Compared to observations of M17 (Townsley *et al.*, 2003), the Carina Nebula (Townsley *et al.*, 2011b), and 30 Doradus (30 Dor; Townsley *et al.* 2006; Lopez *et al.* 2011), the models of Castor *et al.* (1975) and Weaver *et al.* (1977) over-predict the observed X-ray luminosity, while that of Chevalier and Clegg (1985) under-predicts it (Dunne *et al.*, 2003; Harper-Clark and Murray, 2009; Lopez *et al.*, 2011). This result led Harper-Clark and Murray (2009) to introduce an intermediate model, where the hot gas expands into a non-uniform ISM, producing a "porous" shell from which the hot gas can leak. This model is capable of fitting the observed X-ray luminosities, but the porosity is treated as a free parameter, not independently predicted.

The model of Harper-Clark and Murray (2009) assumes the low X-ray luminosities are caused by hot gas leakage, but there are several other channels by which the wind energy can be lost. One possibility is that hot and cold gas may also exchange energy via laminar or turbulent conduction; the latter process occurs when turbulence at the hot-cold interface produces small-scale mixing of hot and cold gas, greatly accelerating conductive transfer between the two (McKee *et al.*, 1984; Strickland and Stevens, 1998; Nakamura *et al.*, 2006). A closely related possibility is that turbulence at the hot-cold interface mixes dust grains into the hot gas, or that dust is produced *in situ* within

the super-bubble by evolved stars. Dust grains immersed in hot gas will eventually be destroyed by sputtering, but they will absorb thermal energy and radiate it in the IR before that. A final possibility is that the hot gas can transfer energy to the ISM by doing mechanical work on the cold, dense shell that bounds the H II region, leading to either coherent or turbulent motions (Breitschwerdt and Kahn, 1988).

As previously mentioned, the effect of leakage is intimately tied to the question of stellar wind feedback in MSC formation. The contribution of stellar winds to H II region dynamics, and their importance as a mechanism for limiting star formation efficiencies, depend on how much of the stellar wind energy is used to do work on the cold ISM, and how much energy is transferred to other channels. In this chapter, we attempt to determine this division of energy through observations. We examine four well-studied H II regions (30 Doradus, Carina, NGC 3603, and M17), and we evaluate how the energy stored in the hot gas is lost via these different mechanisms using X-ray observations coupled to ancillary radio data. By conducting this energy census, we estimate the wind energy which leaks from the H II shells, and we explore the implications regarding the role of stellar winds in regulating star formation in MSCs. This paper is organized as follows: Section 5.2 presents the theoretical framework by reviewing the many different avenues the hot X-ray emitting gas can lose energy. Section 5.3 discusses our source selection criteria and describes our resulting MSC sample. We present the results of our analysis of these regions in Section 5.4, and discuss their implications in Section 5.5. Finally, we summarize and conclude our analysis in Section 5.6.

5.2 Theory & Background: Energy Budgets

5.2.1 $L_{\rm w}$: Energy Injection by Stellar Winds

Consider an idealized, simple spherical H II region with a MSC at its center, injecting wind energy at a rate of

$$L_{\rm w} = \sum_{i=1}^{N} \frac{1}{2} \dot{M}_{{\rm w},i} v_{{\rm w},i}^2 \tag{5.1}$$

where $\dot{M}_{{\rm w},\,i}$ and $v_{{\rm w},\,i}$ are the mass-loss rate and wind velocity for star i, and N is the total number of massive stars in the MSC. For typical MSCs in the MW and LMC, $L_{\rm w}$ has values of $\sim 10^{37} - 10^{39}$ erg s^{-1} (Crowther and Dessart, 1998; Dunne *et al.*, 2003; Smith, 2006; Doran *et al.*, 2013). The region has a radius R, and is bounded by a shell of cold, dense material expanding at velocity $v_{\rm sh}$. It is filled with hot gas with temperature T and electron number density $n_{\rm X}$. We assume that its filling factor is unity to assess the global dynamical effect of the hot gas on the shell (Lopez *et al.*, 2011). This picture is an oversimplification of the structure of a real H II region around a MSC. However, as we shall see below, the missing wind energy is so large that even this simplified model is able to provide meaningful constraints on the missing kinetic energy carried by stellar winds.

For the purposes of this study, we only consider the energy injected by stellar winds and ignore the contribution by SNe. This assumption is reasonable for the following reasons. First, all of the H II regions considered in this paper have young MSCs

(of ages ∼1–3 Myr) so that SNe have not occurred yet. Second, the mechanical energy of one SN ($\sim 10^{51}$ erg) is comparable to the amount injected by winds over a single massive star's lifetime (Castor *et al.*, 1975). As a result, ignoring SNe amounts to, at most, a factor of 2 error in the total kinetic energy injection. Finally, as we demonstrate later, we cannot account for the total energy injection by winds alone. Including the heating contribution from SNe would only strengthen our conclusions. Therefore, by using the observed X-ray, stellar population, and kinematic properties of several H II regions, we examine the possible avenues that the hot gas can transfer energy in these H II regions. From our analysis we determine which processes, if any, can account for the missing kinetic energy. The remainder of this section discusses the various energy sinks for the hot gas.

5.2.2 $L_{\rm cool}$: Radiative Cooling of the Hot Gas

The energy injected by winds can be lost via several channels, the first of which is radiative cooling. The hot gas cools primarily via thermal bremsstrahlung and metal-line cooling. An optically thin "parcel" of hot gas with volume dV and electron and ion number densities of $n_{\rm X}$ and $n_{\rm i}$, respectively, loses energy via radiation at a rate

$$dQ = -n_{\rm X} n_{\rm i} \Lambda(T, x_{\rm i}, Z) dV dt, \tag{5.2}$$

where $\Lambda(T, x_{\rm i}, Z)$ is the radiative cooling function (with units of ergs $\rm s^{-1}$ $\rm cm^3$), which depends on the temperature T, ionization state $x_{\rm i}$, and metallicity Z of the hot gas. For

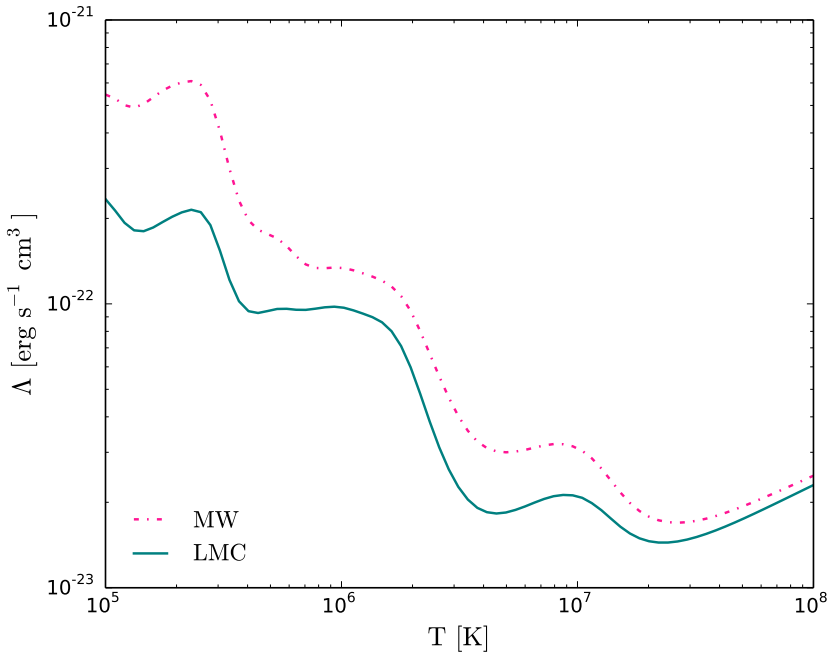

Figure 5.1 Radiative cooling functions from CHIANTI for MW ($Z = Z_\odot$; pink dash-dot line) and LMC ($Z = 0.5\ Z_\odot$; teal solid line) metallicities assuming that the hot gas is in CIE.

a fully ionized plasma of Solar composition, $n_\mathrm{i} = 0.9\, n_\mathrm{X}$. Since n_X is dominated by the free electrons liberated from H and He, the ratio of n_i/n_X is nearly identical for the LMC and MW sources. For a low-density, optically thin plasma, $\Lambda(T, x_\mathrm{i}, Z)$ is independent of density. We use CHIANTI (Dere *et al.*, 1997) to calculate $\Lambda(T, x_\mathrm{i}, Z)$ for MW and LMC metallicities, as shown in Figure 5.1 (Grevesse and Sauval, 1998; Russell and Dopita, 1992). The ionization state is determined by assuming the plasma is in collisional ionization equilibrium (CIE; we discuss deviations from CIE in Section 5.5.1), and that charge exchange, radiative recombination, and dielectronic recombination are the only processes altering the ionization balance (Draine, 2011). In this case, the ionization

fractions, $x_{\rm i}$, depend only on the gas temperature, and hence Λ only depends on T and Z. Under these assumptions, the total energy loss rate via cooling is

$$L_{\rm cool} = 0.9 n_{\rm x}^2 \Lambda(T, Z) V, \tag{5.3}$$

where V is the H II region volume. For typical shocked gas temperatures of H II regions ($\sim 10^7$ K), most of the photons produced by this cooling have $\sim$ keV energies, and thus are observable with X-ray telescopes, such as the *Chandra* X-ray Observatory.

We can use this result to place a constraint on the number density of the hot gas, since $L_{\rm cool} \propto n_{\rm X}^2$. If we assume that radiative cooling is the sole mechanism responsible for removing the kinetic energy injected by winds (i.e., $L_{\rm cool} = L_{\rm w}$), then the electron density of the hot gas is

$$n_{\rm cool} = \sqrt{\frac{L_{\rm w}}{0.9 \Lambda(T) V}}. \tag{5.4}$$

To illustrate our calculation, we consider two example H II regions with radii of 25 pc and 50 pc, respectively. Figure 5.2 shows the value of $n_{\rm cool}$ versus temperature (solid teal line) for these two example regions, using a kinetic energy input rate of $L_{\rm w} = 10^{38}$ erg s^{-1}. Energy conservation requires that the hot gas density and temperature must be at or below the $n_{\rm cool}$ versus T curve, since the gas cannot radiate more energy than is injected by stellar winds. The shaded region above the $n_{\rm cool}$ line denotes the disallowed region and highlights the combinations of thermodynamic properties that

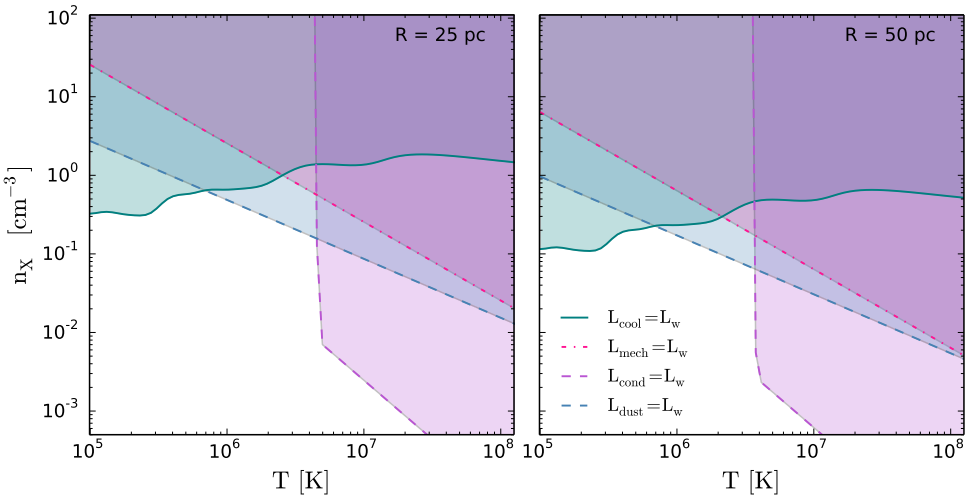

Figure 5.2 Allowed number densities and temperatures (white regions) for the plasma filling simulated H II regions with radii of 25 pc (left panel) and 50 pc (right panel), respectively. We take $L_{\rm w} = 10^{38}$ ergs s^{-1} and $v_{\rm sh} = 20$ km s^{-1}. Curves denote the loci in the $T - n_{\rm X}$ plane where each of the energy sinks discussed in Section 5.2 are capable of removing all of the energy injected by winds. Shaded regions denote values of $n_{\rm X}$ and T that are disallowed because the energy loss rate exceeds the energy input rate.

violate energy conservation.

5.2.3 $L_{\rm mech}$: Mechanical Work on the Dense Shell

The second channel by which the hot gas can transfer energy is by doing mechanical work on the cooler gas around it – either the cold neutral ISM, or the warm ($\sim 10^4$ K) gas produced by photoionization. Observations of H II regions show that they are generally undergoing coherent expansion at speeds comparable to or larger than their internal turbulent velocities (e.g., Balick *et al.*, 1980; Clayton *et al.*, 1985), so we can think of this process as the hot gas acting as a piston pushing on a dense shell bounding the H II region. The thermal pressure of the hot gas is given by $P_{\rm X} = 1.9 n_{\rm X} k_{\rm B} T$, and the rate at which this pressure does work W on the surrounding shell

is $dW/dt = 4\pi R^2 P_{\rm X} v_{\rm sh}$. The factor of 1.9 arises from the fact that the total number density (e.g., $n = n_{\rm i} + n_{\rm X}$) contributes to the pressure, and we have assumed that $n_{\rm X} = 0.9 n_{\rm i}$. We note that $P_{\rm X} = \frac{2}{3} u_{\rm X}$ where $u_{\rm X}$ is the energy density of the hot gas and $4\pi R^2 v_{\rm sh}$ is the rate that the volume increases as the H II region expands. Under these assumptions, the rate at which the hot gas does work on the bubble shell is

$$L_{\rm mech} = 7.6 \pi R^2 v_{\rm sh} n_{\rm X} k_{\rm B} T. \tag{5.5}$$

Note that it does not matter whether this work is being done on 10^4 K photoionized gas, ~ 100 K cold neutral gas, or some combination of the two, so long as the working surface at the hot-cold interface is roughly $4\pi R^2$, and the pressure of the hot gas greatly exceeds that of the cooler gas on which it is pushing. If the latter does not hold and the pressure of the cooler gas is actually greater than that of the hot gas, then the direction of energy flow will be reversed (i.e., the cold gas will do mechanical work on the hot gas), and our estimate of $L_{\rm mech}$ will be an upper limit.

As with radiative cooling, we can obtain an upper limit on the electron density by considering the highest value that it could have without the resulting work exceeding the available kinetic energy supply provided by the winds (i.e., $L_{\rm mech} = L_{\rm w}$). We find that the maximum allowed number density of the hot gas is given by

$$n_{\rm mech} = \frac{L_{\rm w}}{7.6 \pi R^2 v_{\rm sh} k_{\rm B} T}, \tag{5.6}$$

which is also shown in Figure 5.2 (dot-dashed pink line). For this example, we take $v_{\rm sh} = 20$ km s^{-1} which is typical for young H II regions (e.g., see Table 5.1). Similarly, since $L_{\rm mech}$ increases with increasing $n_{\rm X}$, the hot gas is only allowed to have number densities less than or equal to $n_{\rm mech}$. This result places another constraint on $n_{\rm X}$, and produces another disallowed region in the $n_{\rm X} - T$ plane.

We note that for temperatures below $\sim 10^6$ K, all wind energy is lost via radiation. At temperatures above a $\sim$few $\times 10^6$ K, mechanical work is more effective than cooling at removing the wind energy. This transition is easily discerned by calculating the ratio

$$\frac{L_{\rm cool}}{L_{\rm mech}} = 0.16 \frac{\Lambda(T, Z)\Sigma_{\rm X}}{k_{\rm B} T v_{\rm sh}}, \tag{5.7}$$

where $\Sigma_{\rm X} = n_{\rm X} R$ is the surface density of the hot gas. This ratio is less than unity for temperatures where $n_{\rm mech} < n_{\rm cool}$.

5.2.4 $L_{\rm cond}$: Thermal Conduction

Conduction is a third possible kinetic energy sink. In the absence of magnetic fields, thermal conduction by the hot electrons can be an efficient energy loss mechanism at the inner edge of the cool bubble shell, since the conductive heat flux from a fully ionized plasma depends sensitively on temperature ($\propto T^{7/2}$, Spitzer, 1962). This process creates a region of intermediate temperature gas ($T \sim 10^5$ K) between the hot bubble interior and the cold shell, and this region will shed energy rapidly via metal line cooling in the far-UV. This light would be extremely difficult to detect observationally, due to

the high opacity of the ISM at these wavelengths and the even greater opacity of the Earth's atmosphere.

For classical conductivity, the heat flux is $q_{\rm c} = -\kappa_{\rm c} \nabla T$, where

$$\kappa_{\rm c} = 0.87 \frac{k_{\rm B}^{7/2} T^{5/2}}{m_{\rm e}^{1/2} e^4 \ln \Lambda_{\rm C}} \tag{5.8}$$

is the thermal conductivity of the hot electrons with temperature T, and

$$\ln \Lambda_{\rm C} = 29.7 + \ln \left(n_{\rm X}^{-1/2} \frac{T}{10^6 \, {\rm K}} \right) \tag{5.9}$$

is the Coulomb logarithm for $T > 4.2 \times 10^5$ K (Spitzer, 1962; Cowie and McKee, 1977; Draine, 2011). Cowie and McKee (1977) find that when the electron mean free path becomes comparable to or greater than the temperature scale height, $T/|\nabla T|$, the heat flux saturates and takes on the value

$$q_{\rm s} = 0.4 \left(\frac{2 k_{\rm B} T}{\pi m_{\rm e}} \right)^{1/2} n_{\rm X} k_{\rm B} T. \tag{5.10}$$

The total energy loss rate due to conduction for an H II region with radius R filled with hot gas at a temperature T is therefore

$$L_{\rm cond} = 4 \pi R^2 \min(\kappa_c |\nabla T|, q_s). \tag{5.11}$$

We further assume that $|\nabla T| \sim T/R$, which is true at the order of magnitude level.

If thermal conduction is responsible for removing the bulk of the energy injected by stellar winds ($L_{\rm cond} = L_{\rm w}$), then the required number density of the hot gas is

$$n_{\rm cond} = \left(\frac{T}{10^6{\rm K}}\right)^2 \exp\left(59.4 - 6.96\pi\frac{k_{\rm B}^{7/2}T^{7/2}R}{m_{\rm e}^{1/2}e^4L_{\rm w}}\right), \tag{5.12}$$

assuming that the heat flux is not saturated. This result follows from Equations (5.8), (5.9), and (5.11). However, if the temperature is large enough such that the conductive heat-flux becomes saturated, then the number density required for conduction to dominate the energy loss is

$$n_{\rm cond} = \left(\frac{m_{\rm e}}{2\pi}\right)^{1/2}\frac{L_{\rm w}}{1.6R^2k_{\rm B}^{3/2}T^{3/2}}, \tag{5.13}$$

which follows from Equations (5.10) and (5.11). These results are also shown in Figure 5.2 (purple dashed line). The shaded region to the right of this curve denotes the forbidden region where conductive losses exceed the wind energy input.

Finally, we note that Equation (5.11) is almost certainly a large overestimate of the true conductivity, because a non-radial magnetic field, even a dynamically subdominant one, will greatly reduce the heat flux (Soker, 1994). We address the effects of magnetic fields on conduction in more detail in Section 5.5.2. If the conductive heat flux is less than Equation (5.11), then $n_{\rm cond}$ will shift to higher temperatures, thereby reducing the size of the forbidden region.

5.2.5 $L_{\rm dust}$: Collisional Heating of Dust Grains

The next energy sink we consider is the transfer of thermal energy from the hot gas to dust grains via collisions, followed by thermal radiation from the grains. The molecular clouds out of which MSCs form are dusty, and this dust can mix with the hot gas in two ways. First, the dust in ISM material can mix with the shocked wind material. Second, the expanding shell around the H II region will become corrugated with instabilities (Strickland and Stevens, 1998), and the resulting turbulence at the hot-cold interface can mix dust grains into the hot gas. One final process by which dust can be supplied to and mixed with the hot gas is independent of the molecular cloud material: *in situ* formation of dust surrounding evolved stars such as red supergiants in the young MSC (Levesque, 2010). Regardless of its source, dust grains immersed in hot gas will eventually be destroyed by sputtering, but they will absorb thermal energy via inelastic collisions and radiate it in the IR before that.

The importance of these processes depends on how well the dust is mixed with the hot gas and on how the sputtering and destruction time scales compare (Smith *et al.*, 1996; Draine, 2011). These parameters depend on the properties of the dust grains and on the density and temperature of gas in the turbulent mixing layer. We address this question in detail in Section 5.5.3, but to be conservative we perform the calculation assuming that dust is able to survive in the hot gas with the same abundance as in the cold gas. Under this assumption, the gas-dust energy exchange rate by collisions with

dust grains per unit volume of the hot gas is given by

$$\Lambda_{\rm gd} = n_{\rm X} n_{\rm d} \sigma_{\rm d} \left(\frac{8 k_{\rm B} T}{\pi m_{\rm e}} \right)^{1/2} \bar{\alpha}_T \left(2 k_{\rm B} T_{\rm d} - 2 k_{\rm B} T \right) \tag{5.14}$$

where $n_{\rm d}$ is the dust grain number density, $T_{\rm d}$ is the dust temperature, T is the hot gas temperature, $\sigma_{\rm d} = \pi a^2 \gamma_e$ is the dust cross section where the factor γ_e allows for Coulomb focusing/repulsion of the hot electrons. Here $\bar{\alpha}_T$ is the averaged accommodation coefficient for an astrophysical mixture of gases which describes the fraction of kinetic energy of the impacting electron may be converted to heat (Burke and Hollenbach, 1983; Draine, 2011; Krumholz, 2013). For dust grains immersed in hot gas with temperatures greater than $\sim 10^6$ K, the electric potential is much less than the thermal energy of the impacting electrons, and thus the dust grain can be treated as neutral (i.e., $\gamma_{\rm e} = 1$; Dwek, 1987). We assume that the accommodation coefficient is equal for both H atoms and the hot electrons, with a value $\bar{\alpha}_{\rm T} = 0.3$ (Burke and Hollenbach, 1983; Dwek, 1987; Krumholz *et al.*, 2011). For canonical values of the dust-to-gas mass ratio and the dust grain cross section, assuming that the total surface area of grains is proportional to the metal abundance, we find that the total energy exchange rate from the hot gas to the dust is

$$L_{\rm dust} = \alpha_{\rm dg,\,e} n_{\rm X}^2 V T^{3/2}, \tag{5.15}$$

where

$$\alpha_{\rm dg,\,e} = 2.20 \times 10^{-31} \frac{Z}{Z_\odot} {\rm erg\ cm^3 K^{-3/2} s^{-1}} \tag{5.16}$$

is the grain-gas coupling parameter, which is proportional to $n_{\rm X}/m_{\rm e}^{1/2}$ (Krumholz *et al.*, 2011).

If heat exchange from the gas to the dust is primarily responsible for removing the bulk of the energy injected by winds, then the number density of the hot gas is

$$n_{\rm dust} = \sqrt{\frac{L_{\rm w}}{\alpha_{\rm dg,\,e} V T^{3/2}}}. \tag{5.17}$$

These results are also shown in Figure 5.2 (dashed blue line). Again, the shaded region above this curve denotes the forbidden region within which the energy loss rate exceeds the injection rate.

Finally, we warn the reader that Equation (5.15) is likely an overestimate of the true energy transfer rate of the hot gas colliding with dust. The value of $\alpha_{\rm dg,\,e}$ is dependent on the adopted dust-to-gas ratio. Here, we have assumed that the dust-to-gas ratio for the hot gas is the same as that of the neutral ISM, where dust is perfectly mixed with the gas. The true dust-to-gas ratio in the hot gas is likely to be smaller, and the value will depend on the competition between turbulent mixing at the hot-cold interface and the sputtering of grains in the high temperature medium.

5.2.6 $L_{\rm leak}$: Physical Leakage of the Hot Gas

The final energy sink that we will calculate is that associated with bulk motion of the hot gas. The hot gas may be only partially confined by the cold gas in the shell, either because the surrounding ISM is non-uniform or because stellar feedback punches

holes in the shell. In either case, the hot gas, which has a much larger sound speed than the cool gas, will flow out of the holes, expand adiabatically, and cool radiatively (Harper-Clark and Murray, 2009). In this scenario, the energy injected by stellar winds is ultimately radiated as low-surface brightness X-ray and far-UV emission over an area much larger than the observed H II region.

Harper-Clark and Murray (2009) define a confinement parameter $C_{\rm f}$ that describes the "porosity" of the cold shell, where $C_{\rm f} = 1$ describes a shell with no holes and $C_{\rm f} = 0$ describes a completely porous shell (i.e., no shell exists). The holes allow the hot gas to escape the H II region at its sound speed, $c_{\rm s}$, with an energy flux given by

$$L_{\rm leak} = (1 - C_{\rm f})\, 4\pi R^2 \frac{5}{2} \rho_{\rm h} c_{\rm s}^3 \tag{5.18}$$

where $\rho_{\rm h} = 1.9 \mu m_{\rm p} n_{\rm X}$ is the density of the hot gas, $\mu = 0.62$ assuming He is fully ionized and its mass fraction is 0.3, and $c_{\rm s} = \sqrt{k_{\rm B} T / \mu m_{\rm p}}$ is the sound speed of the hot gas. Note that since $L_{\rm leak} \propto c_{\rm s}^3$, a large amount of leakage can occur even if the shell has a large covering fraction.

5.2.7 Other Forms of Energy Loss

The energy losses by the mechanisms discussed previously in this section can be estimated easily under the stated assumptions. However, other avenues of energy loss also exist, including "turbulent conduction" and "turbulent work." As we shall see below, the former mechanism may likely dominate the energy loss of the hot gas.

Unfortunately, both channels are much harder to assess using observations, even at the order-of-magnitude level. Nonetheless, we summarize these underlying physical mechanisms here.

Turbulent conduction (McKee *et al.*, 1984) describes how cold gas can mix rapidly with hot gas via Kelvin-Helmholtz instabilities that occur as hot gas flows past cold clouds, either in the hot bubble interior or as it leaks out (Strickland and Stevens, 1998; Nakamura *et al.*, 2006). As with the estimate provided above for thermal conduction, this mixing will lead to rapid conductive transmission of the thermal energy, producing gas at temperatures of $\sim 10^5$ K which sheds energy rapidly via metal line cooling in the far-UV.

The difference between thermal conduction and turbulent conduction is that if a turbulent mixing layer is present, then the effective area of the hot-cold interface and the sharpness of the temperature gradient can be orders of magnitude larger than the laminar estimate given by Equation (5.11). Moreover, if the turbulent mixing layer produces mixtures of hot and cold gas on scales smaller than the electron gyro radius, then magnetic confinement of the electrons will not be able to restrict the rate of energy interchange between hot and cold gas. Thus, the presence of a turbulent mixing layer might lead to a conductive loss rate much higher than the simple laminar estimate presented in Section 5.2.4.

The final energy loss mechanism we consider is turbulent work, where hot gas collides with the cold ISM and does work on it, converting its thermal energy into a turbulent cascade in the cold gas (Breitschwerdt and Kahn, 1988). This process leads to

the formation of shocks and to the energy being radiated in the IR (if dust cooling of the cold ISM dominates) or radio (if molecular line cooling dominates). Turbulent work is related to the mechanical luminosity we have estimated above, but it would manifest as large incoherent velocities rather than the coherent expansion in the previous estimate. It is unlikely that turbulent work would dominate over mechanical work because the total amount of work done on the cold ISM depends on the total surface area of the working surface (i.e., the bubble shell). As the shell expands coherently, the work done on the shell will be much greater than that over the turbulent regions. We therefore conclude that turbulent work is not a dominant energy sink for the hot gas.

5.3 HII Region Sample

5.3.1 Sample Selection Criteria

In the previous section, we have reviewed the various physical processes that can contribute to the energy accounting problem. In the following sections, we derive constraints on the effectiveness of each process in depleting the injected wind energy from a sample of well-studied H II regions. We have selected this sample using several criteria. First, there must be X-ray data available to enable us to determine the physical properties of the hot gas and estimate the rate of radiative energy losses. Second, we require radio observations that allow us to characterize the dense shells bounding the H II regions, since the radius and velocity of this shell enter in our estimates for the mechanical luminosity.

Table 5.1 Table of the H II region properties in our sample. Properties listed are distance, H II region radius, shell velocity, MSC age, bolometric luminosity, integrated wind luminosity, observed unabsorbed X-ray luminosity, and spectral fitted temperatures for the hot X-ray emitting gas.
[a]Temperatures shown are surface-brightness weighted values from Townsley *et al.* (2011a).
References: **30 Doradus**: Lopez *et al.* (2011); Doran *et al.* (2013); Lopez *et al.* (2013a); **Carina**: Smith *et al.* (2000); Smith (2006); Smith and Brooks (2007); Harper-Clark and Murray (2009); Townsley *et al.* (2011a), **NGC 3603**: Balick *et al.* (1980); Crowther and Dessart (1998); Townsley *et al.* (2011a), **M17**: Clayton *et al.* (1985); Dunne *et al.* (2003); Townsley *et al.* (2003); Hoffmeister *et al.* (2008); Townsley *et al.* (2011a)

Name	D [kpc]	R_{sh} [pc]	v_{sh} [km/s]	t_{cl} [Myr]	$\log L_{bol}$ [$L_\odot$]	L_w [10^{37} erg/s]	L_x [10^{35} erg/s]	T_X [10^6 K]
30 Doradus	50	100	25	2	8.4	224	45.0	7.4
Carina	2.3	20	20	3	7.23	35.0	1.71	4.5[a]
NGC 3603	7.0	21	20	1	–	62.0	2.6	6.2[a]
M17	2.1	5.8	25	1	6.58	1	0.2	5.3[a]

Finally, we require robust observational estimates of the wind energy output by the stars. To obtain an accurate accounting of the wind energy, the spectral types of the majority of the luminous stars are necessary, so that star-by-star surface gravities and temperatures can be determined. Given these constraints, we have restricted our analysis to four well-studied H II regions in the LMC and MW, which we describe briefly below. All our sources have young aged clusters (∼1–3 Myr old), and thus their X-ray emission is predominantly powered by stellar winds from their MSCs.

5.3.2 Individual HII Regions

5.3.2.1 30 Doradus

30 Doradus (hereafter 30 Dor), located in the LMC (at a distance $D \sim 50$ kpc), is the most luminous and largest H II region in the Local Group, with a radius of ~ 100 pc and a bolometric luminosity of $\sim 2.3 \times 10^8\ L_\odot$ (Lopez *et al.*, 2013a; Doran *et al.*, 2013). It is primarily powered by NGC 2070 which contains ~ 2400 OB stars. At its center lies R136, a young ($t_{\rm age} \sim 1-2$ Myr) dense star cluster with a stellar mass density of 5.5×10^4 M$_\odot$ pc^{-3} (Parker, 1993; Hunter *et al.*, 1995). The total energy input by the stellar winds is 2.2×10^{39} erg s^{-1} (Doran *et al.*, 2013), and its bubble shell is expanding at an average speed of ~ 25 km s^{-1} (Chu and Kennicutt, 1994). The X-ray emission from 30 Dor was observed using the *Chandra* Advanced CCD Imaging Spectrometer (ACIS) for an integrated time of ≈ 94 ks (PI: L. Townsley). Lopez *et al.* (2011) found that the total diffuse unabsorbed X-ray luminosity of 30 Dor in the 0.5–2 keV band is 4.5×10^{36} erg s^{-1}. From the X-ray spectra, Lopez *et al.* (2011) found that the X-ray

emission can be characterized by a hot plasma with a temperature of 7.4×10^6 K.

5.3.2.2 The Carina Nebula

The Carina Nebula, located at a distance of $D \sim 2.3$ kpc, is one of the nearest regions of active massive star formation (Allen and Hillier, 1993; Smith, 2006). This complex is a "cluster of clusters", containing 8 open clusters. It hosts ∼70 O stars, of which 46 belong to the young star cluster Trumpler 16 ($t_{\rm cl} \sim 2 - 3$ Myr; Smith, 2006), the home of the well-known luminous blue variable η Carina. The total bolometric luminosity of the stars in the Carina Nebula is 2.5×10^7 $L_\odot$, and the total energy input by stellar winds is $\sim 3.5 \times 10^{38}$ erg s^{-1}, with 70% of the energy budget coming from Trumpler 16 (Smith, 2006; Harper-Clark and Murray, 2009). The nebula has a radius of ~ 20 pc (Harper-Clark and Murray, 2009; Townsley *et al.*, 2011a) and its outer shell is expanding at a velocity of ~ 20 km s^{-1} (Smith *et al.*, 2000; Smith and Brooks, 2007). Carina has been studied extensively with *Chandra*. Townsley *et al.* (2011b) obtained a 1.2 Ms, 1.42 deg^2 ACIS-I mosaic of the complex to characterize its diffuse emission and to identify thousands of X-ray point sources (e.g., low-mass pre-main sequence stars and massive stars). They found that the total integrated diffuse emission from the Carina Nebula in the 0.5–7 keV X-ray band is 1.7×10^{35} erg s^{-1}. To derive the temperature of the hot gas, Townsley *et al.* (2011a) fit the X-ray spectra with three non-equilibrium ionization (NEI) plasma components. For our purposes, we assume that the observed hot gas temperature is the surface-brightness weighted value taken from Townsley *et al.* (2011a). This yields a temperature of 4.5×10^6 K.

5.3.2.3 NGC 3603

The giant H II region NGC 3603, located at a distance of $D \sim 7$ kpc, contains the most compact and youngest ($t_{\rm cl} \approx 1$ Myr) massive "starburst" cluster located in the MW (HD 97950; Crowther and Dessart, 1998). With a mass density of $\sim 10^5$ $M_\odot$ pc^{-3}, HD 97950 is more compact than R136 (Hofmann *et al.*, 1995). Assuming a distance of $D \sim 8.4$ kpc (Goss and Radhakrishnan, 1969), Balick *et al.* (1980) found that the radius of NGC 3603 (i.e., the region which contains 90% of the radio flux) is 25 pc. Assuming a distance of 7 kpc, the radius of NGC 3603 reduces to ~ 21 pc. Balick *et al.* (1980) also studied the dynamics of NGC 3603 by measuring multiple emission lines, including Hα and N II. They found that the N II lines are double peaked and separated by ~ 20 km s^{-1}. Furthermore, they also measured the velocity dispersion of the Hα turbulent line widths to be 20 km s^{-1}. These results suggest that NGC 3603 is expanding at a rate of ~ 20 km s^{-1}. Performing a stellar census of the massive stars in NGC 3603, Crowther and Dessart (1998) estimate that the total mechanical energy input by stellar winds is 6.2×10^{38} erg s^{-1}. Smith (2006) suggest that the actual wind luminosity for NGC 3603 is smaller than this value because Crowther and Dessart (1998) do not consider the effect of wind clumping in their analysis. However, Smith (2006) does not quantify what this value is so we adopt the wind luminosity estimate from Crowther and Dessart (1998) and warn the reader that this may likely be an overestimate. NGC 3603 was observed with *Chandra* with 46 ks of usable time (Moffat *et al.*, 2002). Townsley *et al.* (2011a) re-analyzed these data and found 1328 X-ray point sources in the $17' \times 17'$

ACIS-I field. After removing these point sources, Townsley *et al.* (2011a) found that the diffuse emission of NGC 3603 in the 0.5–7 keV band is 2.6×10^{35} erg s^{-1}. Similarly to Carina, they fit the X-ray spectra by a multiple component plasma. Taking the surface-brightness weighted average of their results, we adopt a hot gas temperature of 6.2×10^6 K.

5.3.2.4 M17

The emission nebula M17, located at a distance of $D \sim 2.1$ kpc, is on the eastern edge of a massive molecular cloud, M17SW, and exhibits a blister-like structure with a radius of ∼5.8 pc (Townsley *et al.*, 2003). It is powered by the open cluster NGC 6616, which consists of a ring of seven O stars ~ 0.5 pc in diameter (Townsley *et al.*, 2003). NGC 6616 is quite young, with an estimated age of $\lesssim 1$ Myr (Hanson *et al.*, 1997). Assuming a distance of 2.1 kpc to the nebula, Hoffmeister *et al.* (2008) found that the total bolometric luminosity of the stellar population in M17 is 3.8×10^6 L$_\odot$. Dunne *et al.* (2003) estimate that $L_{\rm w} \sim 1 \times 10^{37}$ erg s^{-1}. The bubble shell of M17 is expanding at a rate of ~ 25 km s^{-1}(Clayton *et al.*, 1985). Townsley (2009) created a deep (total ACIS-I integration time of 320 ks) mosaic of M17. From these data, Townsley *et al.* (2011a) found that the total integrated diffuse emission from M17 in the 0.5–7 keV X-ray band is 2.0×10^{34} erg s^{-1}. They modeled the X-ray spectra by a multiple component plasma, and from their model we adopt the surface-brightness weighted value of 5.3×10^6 K for the hot gas temperature.

5.4 Results

In this section, we assess which sinks are responsible for removing the wind kinetic energy injected by MSCs in our four H II regions. We perform this analysis in several steps. First, in Section 5.4.1, we constrain the actual densities and temperatures of the hot gas in our sample H II regions using the available observations of their diffuse X-ray emission. Second, in Section 5.4.2, we evaluate all of the sink terms discussed in Section 5.2 to determine which of them, if any, might be responsible for removing the bulk of the wind energy. We use these calculations to evaluate the global energy budget for stellar wind energy injection in Section 5.4.3.

5.4.1 Observational Constraints on the Hot Gas Density and Temperature

The density and temperature of the hot gas are jointly constrained by the observed (absorption-corrected) X-ray luminosity, while the temperature is constrained by the shape of the X-ray spectrum. We focus on the former constraint first. A "parcel" of hot gas with temperature T, electron number density $n_{\rm X}$, and volume V will have an X–ray luminosity given by

$$L_{\rm X,\,obs} = 0.9 n_{\rm X}^2 V \int_{\nu_0}^{\nu_1} j_\nu(T, Z) d\nu \tag{5.19}$$

where $j_\nu(T, Z)$ is the emissivity of the hot gas and $(\nu_0,\ \nu_1)$ is the frequency band of the X-ray telescope. For our purposes, we focus on the soft (0.5–2 keV) X-ray band when

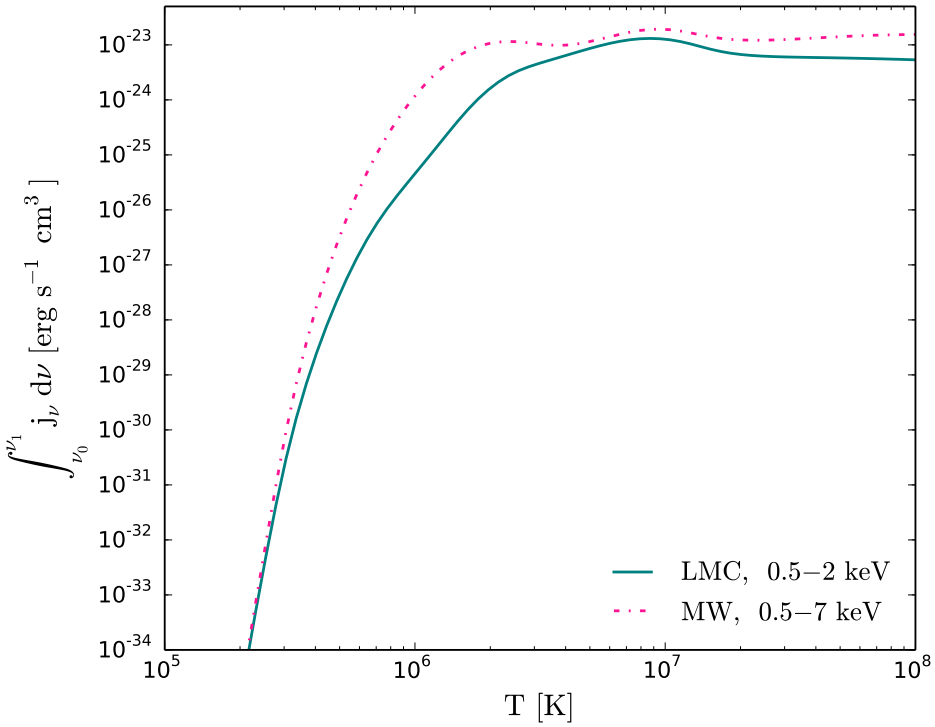

Figure 5.3 Frequency-integrated emissivities from CHIANTI for MW ($Z = Z_\odot$) and LMC ($Z = 0.5\ Z_\odot$) metallicities assuming that the hot gas is in CIE. The LMC emissivity is integrated over the 0.5-2 keV *Chandra* band and the MW emissivity is integrated over the 0.5-7 keV *Chandra* band.

available, since the luminosity at these energies originates from the diffuse structures created by the collision of stellar winds. These are brighter by an order of magnitude than the point sources (Townsley *et al.*, 2006). From the literature, we only have $L_{\rm X}$ for the 0.5–2 keV band for 30 Dor (Lopez *et al.*, 2011), whereas we have $L_{\rm X}$ for the 0.5–7 keV band for the MW H II regions (Townsley *et al.*, 2011a). We use CHIANTI to compute $j_\nu(T, Z)$ for both MW and LMC abundances (Russell and Dopita, 1992; Grevesse and Sauval, 1998), and we show the results in Figure 5.3. Under our simple assumption of

a uniform hot gas filling the H II region, we can then combine the observed luminosity with the approximate volume of the region to obtain the number density of the hot X-ray emitting gas,

$$n_{\rm X} = \sqrt{\frac{L_{\rm X,\,obs}}{0.9V \int_{\nu_0}^{\nu_1} j_\nu(T,Z)d\nu}}. \tag{5.20}$$

From the X-ray data, one can also determine the temperature of the hot gas by modeling the X-ray spectrum as an absorbed hot diffuse gas. For this purpose, we adopt the surface-brightness weighted temperatures derived from the observations, as discussed in Section 5.3.

Figure 5.4 illustrates the locus in the $T - n_{\rm X}$ plane allowed by the observed luminosities of our sample H II regions, with points marked along these curves corresponding to the temperatures inferred from the spectra. The $n_{\rm X}$ versus T curves for the MW sources have the same shape because they all use the same metallicity and bandpass for $j_\nu(T, Z)$, but have different observed luminosities. The curve for 30 Dor in the LMC has a slightly different shape due to the difference in both the frequency band used for the observations and in the gas metallicity.

5.4.2 Energy Sinks

We next estimate the energy sinks discussed in Section 5.2 for our sample H II regions, in order to produce for each one a plot of the same type as shown in Figure 5.2 (i.e., the loci in the $T-n_{\rm X}$ plane where each potential energy sink is capable of removing all of the kinetic energy injected by the winds). The inputs to these calculations are

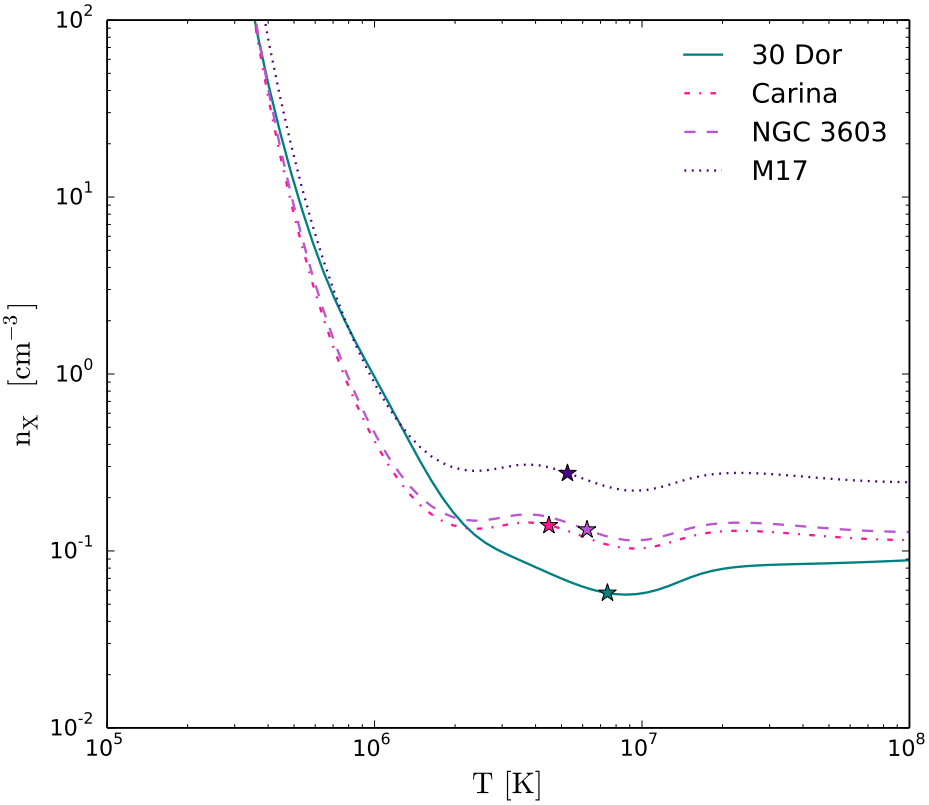

Figure 5.4 Allowed hot gas number density, n_X, versus temperature, T, constrained by X-ray observations for the 30 Dor, Carina, NGC 3603, and M17 H II regions. As can be seen, the allowed n_X for the MW H II regions (Carina, NGC 3603, and M17) follow the same shape but have different offsets due to their differing $L_{X,\,obs}$. The points denote the temperatures inferred by spectral fitting (see Table 5.1).

the observed H II region properties given in Table 5.1. We show the results of these calculations in Figure 5.5, with the curves of n_X versus T inferred from the observed X-ray emission overlaid.

The $L_{cool} = L_w$ curve (i.e., Equation (5.4) – the solid teal line) indicates density-temperature combinations such that all the kinetic energy injected by stellar winds is radiated away. We remind the reader that the hot gas can only lie on or below the n_{cool} line in order to conserve energy (i.e., the gas can not radiate more energy than

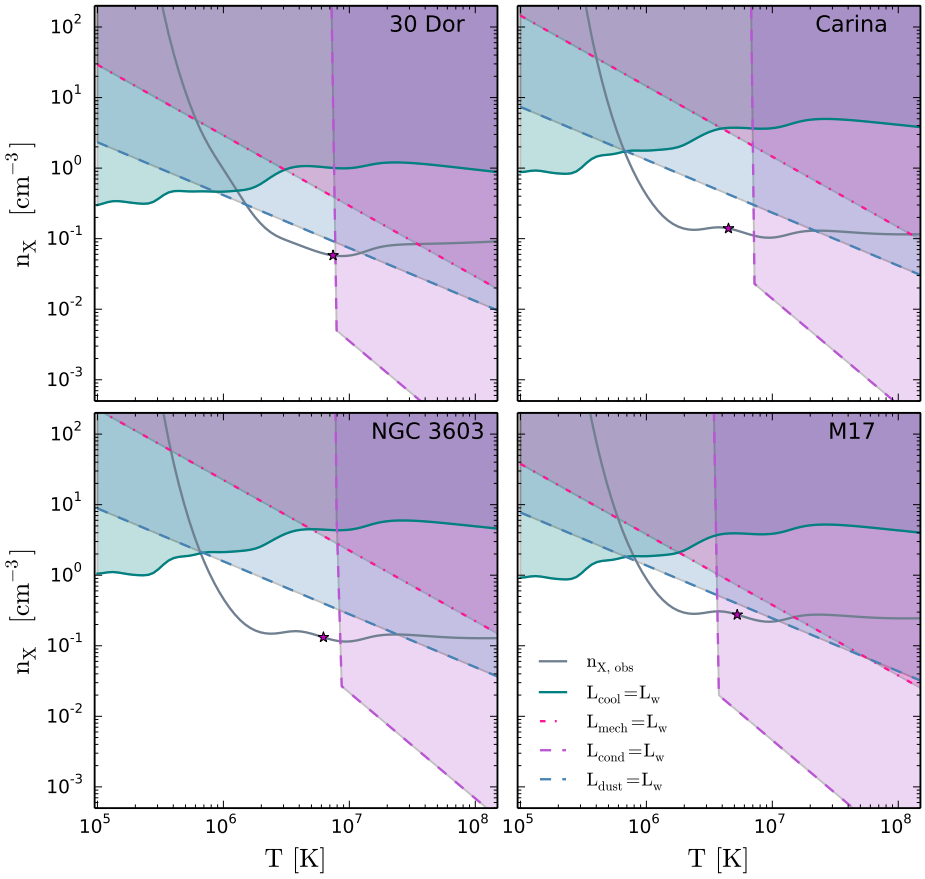

Figure 5.5 Same as Figure 5.2 but for the H II regions in our sample. The gray lines with stars along them indicate the values of n_X versus T constrained by the observed X-ray luminosities, with the stars indicating the temperatures inferred by spectral fitting (see Table 5.1).

is injected into it). Clearly, the required number densities for cooling to dominate the energy loss are much larger than the number density constrained by the observed X-ray emission for all H II regions in our sample for $T \gtrsim 10^6$ K. The observationally-inferred gas temperatures are well above this limit. We conclude that radiative cooling is not an important energy sink, consistent with previous results (Dunne *et al.*, 2003; Lopez *et al.*, 2011; Townsley *et al.*, 2011a).

Next, we consider the $L_{\rm mech} = L_{\rm w}$ curve (i.e., Equation (5.6) – the dot-dashed pink line), the locus of density-temperature combinations for which mechanical work on the dense shell removes the bulk of the wind energy. We find that for temperatures of $\gtrsim 1 - 2 \times 10^6$ K, mechanical work becomes more efficient at removing energy since the hot gas pressure increases with temperature and $L_{\rm mech} \propto n_{\rm X}$. Thus, the $L_{\rm mech} = L_{\rm w}$ curve requires lower number densities than radiative cooling to remove the wind energy. However, we find that $n_{\rm mech}$ is still larger than the number density constrained by the observed X-ray emission for all H II regions unless the hot gas temperature exceeds $\sim 0.2 - 1 \times 10^8$ K. None of the H II regions in our sample are in this temperature range. Thus, we conclude that mechanical work on the bubble shell is not responsible for removing the bulk of the wind energy.

The next energy sink we consider is thermal conduction. The $L_{\rm cond} = L_{\rm w}$ curve (i.e., Equations (5.12) and (5.13) – the dashed purple line) is nearly vertical at low temperatures because $L_{\rm cond}$ depends only weakly on density (e.g., Equation (5.9)) in the unsaturated regime. Only when the heat flux reaches the saturated value does the conductive luminosity exhibit any significant density dependence. We find that the observationally-constrained number densities and temperatures do lie in the region where conduction is capable of removing the bulk of the wind energy for 30 Dor and M17. However, we remind the reader that our estimate of the conductive heat flux is almost certainly a sizable overestimate, as we have entirely neglected the effects of magnetic fields. Thus, our results show that for densities and temperatures consistent with observations, thermal conduction can be an important energy sink for stellar wind

energy as long as it is not significantly inhibited by magnetic fields.

Lastly, we consider the energy transfer of the hot gas to dust via collisions. The $L_{\rm dust} = L_{\rm w}$ curve (i.e., Equation (5.17) – the dashed blue line) indicates the density-temperature combinations at which all of the energy injected by stellar winds is transferred to the dust via collisions with the hot gas. We find that the heating of dust is more effective at removing energy from the hot gas than cooling and mechanical work for $T \gtrsim 10^6$ K. We also find that the $L_{\rm dust} = L_{\rm w}$ curve is quite close to the observational constraint line $n_{\rm X,obs}$ for temperatures consistent with the observed spectrum in 30 Dor and M17. This result suggests that dust heating could be a significant energy sink for 30 Dor and M17, but probably not in NGC 3603 and Carina. However, as with conduction, our energy loss estimates for dust heating are likely to be large overestimates, since they assume that the dust content in the hot gas matches that in the cool ISM.

We defer a calculation of the rate of energy leakage via bulk motion to Section 5.4.4 since the confinement factor $C_{\rm f}$ is unconstrained observationally.

5.4.3 Implications for the Energy Budget

In order to better constrain the dominant source of kinetic energy removal, and to illustrate the problem of the missing wind energy, we next calculate the various energy sinks as a function of the hot gas temperature. We perform this calculation at each temperature T by using the observed X-ray luminosity to calculate the corresponding density $n_{\rm X,obs}$ from Equation (5.20). For each $T - n_{\rm X,obs}$ pair, we then compute all the energy sinks discussed in the previous Section: radiative cooling, mechanical work,

Name	$n_{\rm X}$ [cm^{-3}]	$\frac{L_{\rm cool}}{L_{\rm w}}$	$\frac{L_{\rm mech}}{L_{\rm w}}$	$\frac{L_{\rm cond}}{L_{\rm w}}$	$\frac{L_{\rm dust}}{L_{\rm w}}$	$C_{\rm f}$[a]	$C_{\rm f,\,all}$[b]
30 Doradus	0.058	0.37%	15%	$< 97\%$	$< 40\%$	> 0.84	–
Carina	0.14	0.16%	4.3%	$< 22\%$	$< 11\%$	> 0.36	< 0.58
NGC 3603	0.13	0.10%	3.7%	$< 41\%$	$< 11\%$	> 0.36	< 0.70
M17	0.27	0.55%	38%	$< 392\%$	$< 48\%$	> 0.95	–

Table 5.2 Inferred number densities, luminosities, and confinement factors.

Note. — For each H II region in the sample, $n_{\rm X}$ is the number density inferred from the observed X-ray luminosity and best-fitting temperature. The columns $L_{\rm cool}/L_{\rm w}$, $L_{\rm mech}/L_{\rm w}$, $L_{\rm cond}/L_{\rm w}$, and $L_{\rm dust}/L_{\rm w}$ show the radiative cooling, mechanical work, conduction, and dust cooling luminosities normalized to the wind energy injection rate; the latter two are upper limits. Finally, $C_{\rm f}$ ($C_{\rm f,\,all}$) is the confinement factor that would be required to remove the unaccounted-for wind energy via bulk motion.

[a] Derived $C_{\rm f}$ includes energy loss due to mechanical work and radiative cooling. These act as lower limits since the values obtained for these energy loss mechanisms are reasonable estimates.

[b] Derived $C_{\rm f,\,all}$ includes energy loss due to mechanical work, radiative cooling, thermal conduction, and dust heating via collisions. These act as upper limits since the values obtained for thermal conduction and dust heating via collisions are likely overestimates.

thermal conduction, and dust heating via collisions, and compare the sum of these cooling rates to the wind energy input rate.

Figures 5.6 - 5.9 show the results. Given the uncertainties in the true rates of conductive and dust heating, we perform this calculation both excluding them (left panels) and including them (right panels). The top panels show the absolute values of the individual and total energy loss rates, whereas the bottom panels show the energy loss rates as a fraction of the total energy injection rate by stellar winds. We remind the reader that values above the horizontal lines in these figures are not allowed due to energy conservation. The shaded regions illustrate how much energy is missing, i.e., what fraction of the injected wind energy cannot be accounted for by the sum of the various sinks we have been able to calculate. We also report these values, using the

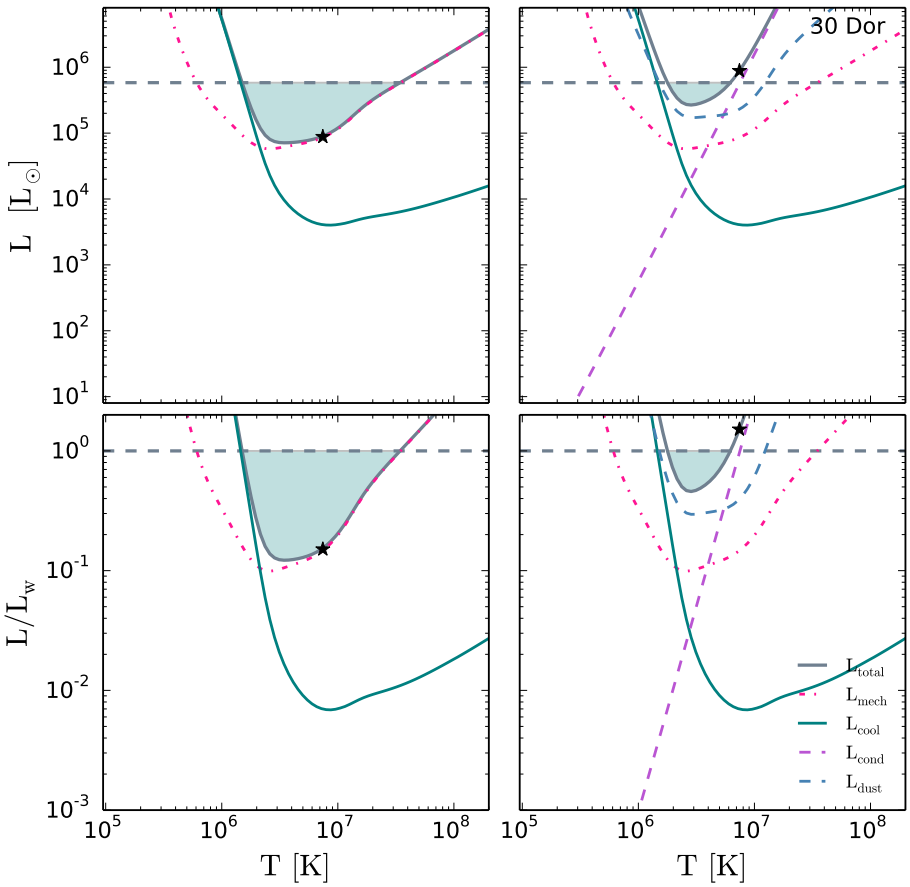

Figure 5.6 Hot gas temperature versus the energy loss rates for the energy loss mechanisms described in Section 2 for the observationally constrained hot gas number density for 30 Dor. The horizontal line in the top and bottom panels denote the stellar wind energy injection rate for 30 Dor. The left panels consider only $L_{\rm cool}$ and $L_{\rm mech}$, since these values are reasonable estimates whereas the left panels also include thermal conduction and dust heating via collisions, which are likely overestimates. Stars denote the values of $T_{\rm X}$ inferred by spectral fitting.

temperatures inferred from fitting the X-ray spectra, in Table 5.2.

For temperatures reasonably consistent with the observationally-inferred values (4.5×10^6 K $\lesssim$ T$_{\rm X,\,obs}$ $\lesssim 7.5 \times 10^6$ K, c.f. Table 5.1), we find that radiative cooling acts as a negligible energy sink, contributing to $< 1\%$ of the fractional energy loss for

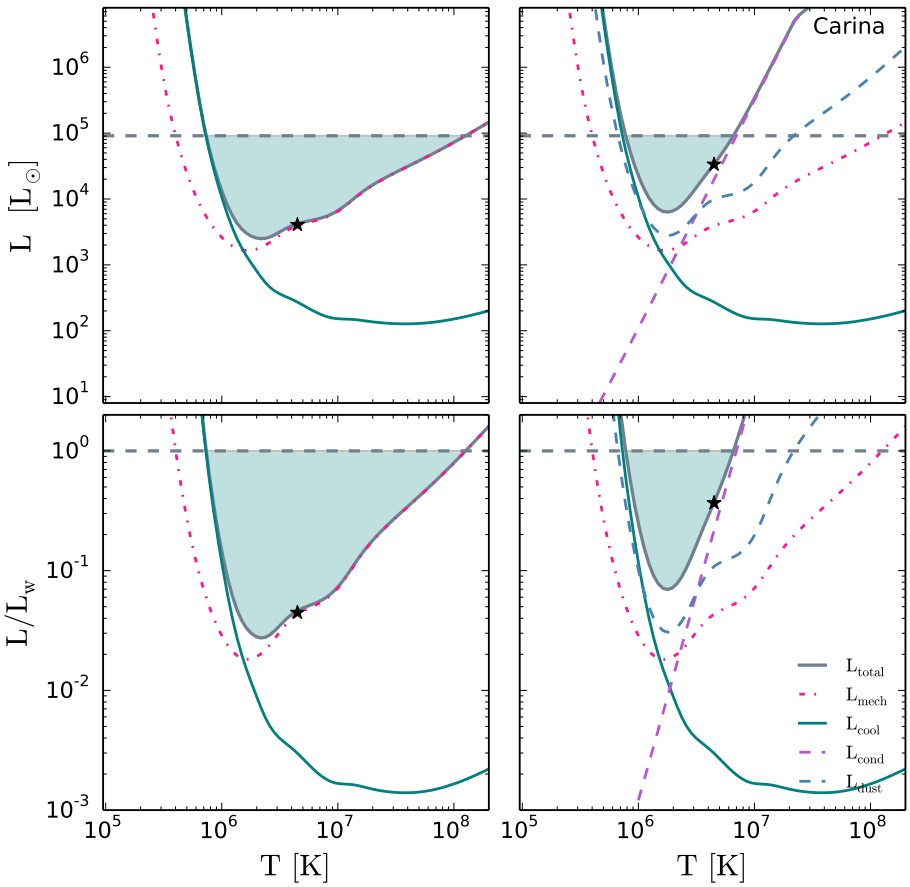

Figure 5.7 Same as Figure 5.6 but for Carina.

all H II regions. Mechanical work accounts for 3.7% – 38% of the energy injected by winds, and for < 15% in three of our four sample regions. We find that mechanical work can account for 38% of the stellar wind energy injected in M17. This large fraction of energy transferred to mechanical work is likely due to M17's small size. The inferred number density from the X-ray emission is inversely related to the H II region volume (i.e., $n_{\rm X} \propto V^{-1/2}$), thus a smaller volume for a given X-ray luminosity and plasma temperature would yield a larger inferred number density and hot gas pressure.

As illustrated in the right panels of Figures 5.6 - 5.9, the situation is different if we include dust heating and/or thermal conduction. By combining these energy sinks with mechanical and radiative losses in Carina and NGC 3603, we can account for 37% and 55% of the injected energy, respectively. In the remaining two H II regions, setting the conductive and dust cooling rates to their maximum would lead to a luminosity greater than that injected by winds. However, this assumption is only true if magnetic fields do not inhibit conductive losses in any way and the dust to gas ratio is the same in the hot gas as in the cold ISM. Neither of those assumptions are likely to be true, as we discuss further in Section 5.5, even at the order of magnitude level. Only in M17, where we find $L_{\rm cond}/L_{\rm w} \approx 4.8$ (see Table 5.2), is there a significant margin of error. In all the other regions, if the failure of these assumptions were to reduce the real conductive and dust luminosities by even a factor of a few compared to our upper limit, we would no longer be able to account for all the injected wind energy.

5.4.4 Ways Out: Where's the Missing Energy?

We have shown that the combined effects of radiative cooling and mechanical work cannot account for the missing energy of the hot post-shocked stellar wind material in our sample. Thermal conduction and dust heating via collisions might, but only if the assumptions described above are true. Are there other ways out?

One possible solution is that the hot gas acts as an energy reservoir for the winds. If storage in the thermal energy of the hot gas is significant, and has been over the cluster's lifetime, then the present-day thermal energy of the hot gas is of order of

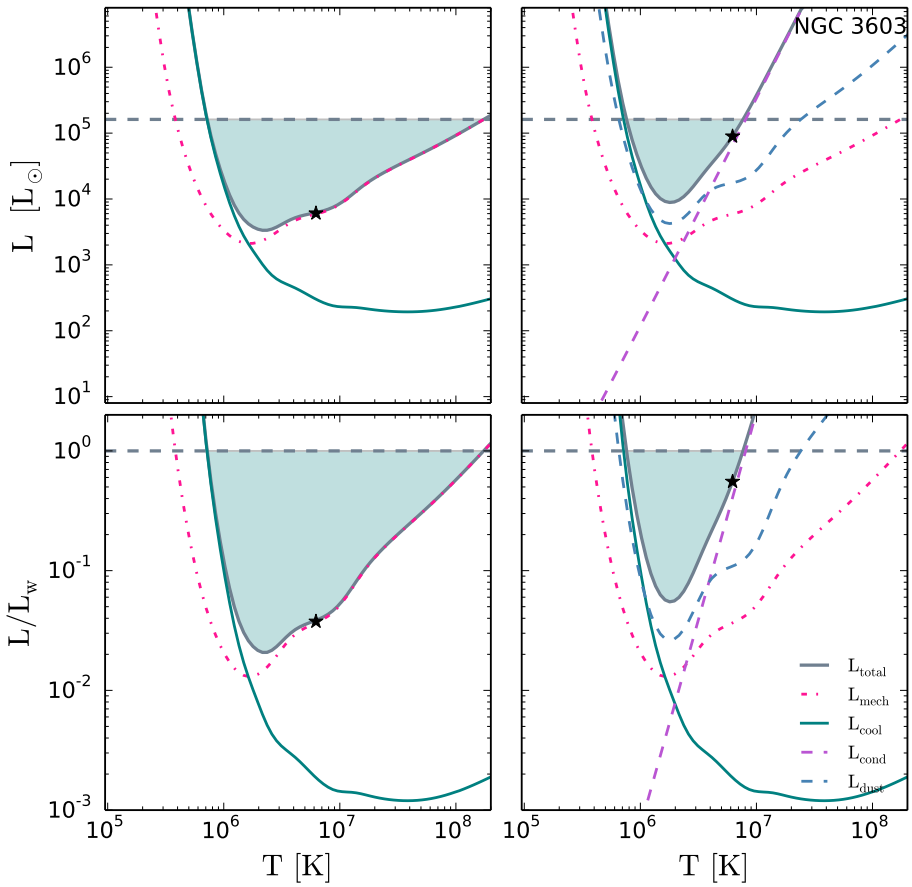

Figure 5.8 Same as Figure 5.6 but for NGC 3603.

the total energy that has been injected since the winds started blowing, $E_{\rm w} \sim L_{\rm w} t_{\rm cl}$. The resulting energy density for the stellar winds is $u_{\rm w} = L_{\rm w} t_{\rm cl}/V$. Equating the stellar wind energy density to the energy density of the hot gas, $u_{\rm X} = \frac{3}{2}(1.9 n_{\rm X} T)$, yields a number density of

$$n_{\rm w} = 0.05 \left(\frac{L_{\rm w}}{10^{38}\ {\rm erg\ s^{-1}}}\right) \left(\frac{t_{\rm cl}}{\rm Myr}\right) \left(\frac{T}{10^7\ {\rm K}}\right)^{-1} \left(\frac{R_{\rm sh}}{50\ {\rm pc}}\right)^{-3}. \qquad (5.21)$$

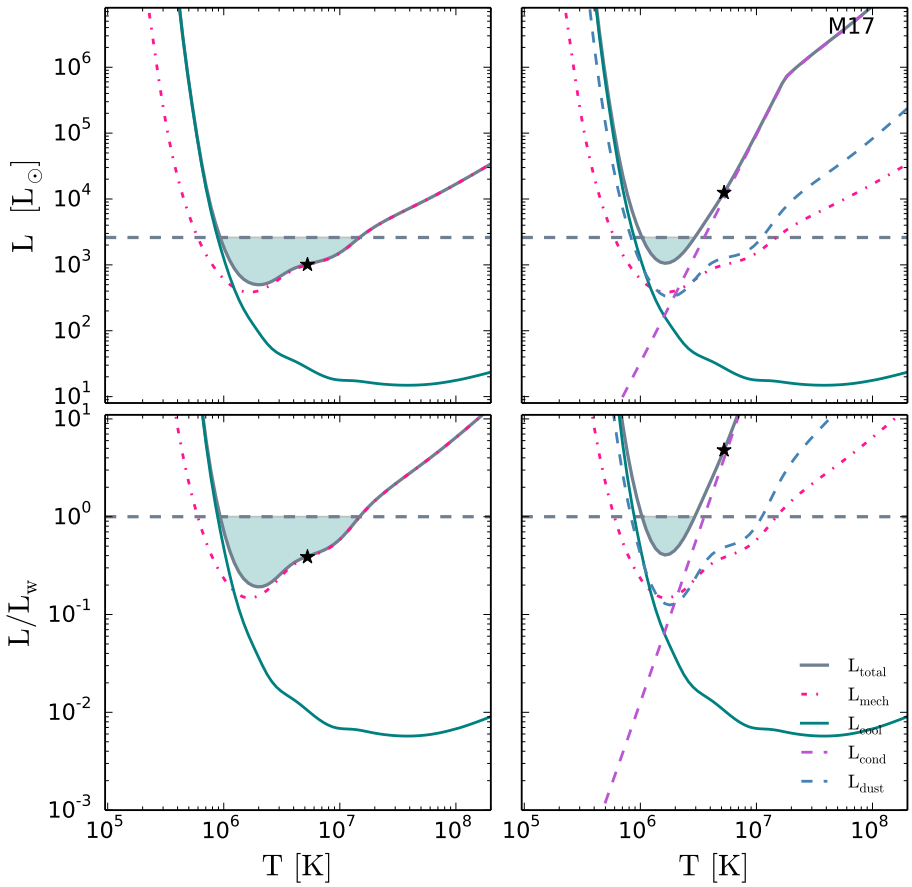

Figure 5.9 Same as Figure 5.6 but for M17.

Assuming that the wind energy is stored in the thermal energy of the hot gas, we find that the required $n_{\rm w}$ is 0.6, 17, 8.4, and 6.4 cm^{-3} for 30 Doradus, Carina, NGC 3603, and M17, respectively for $T = 5 \times 10^6$ K, roughly the observationally-inferred value. Figure 5.5 shows that these number densities are well above the observationally-constrained $n_{\rm X} - T$ curve and well into the forbidden region where one or more loss mechanisms would remove energy faster than it is injected. This immediately demonstrates that depositing the wind energy into the thermal reservoir of the hot gas is not a viable

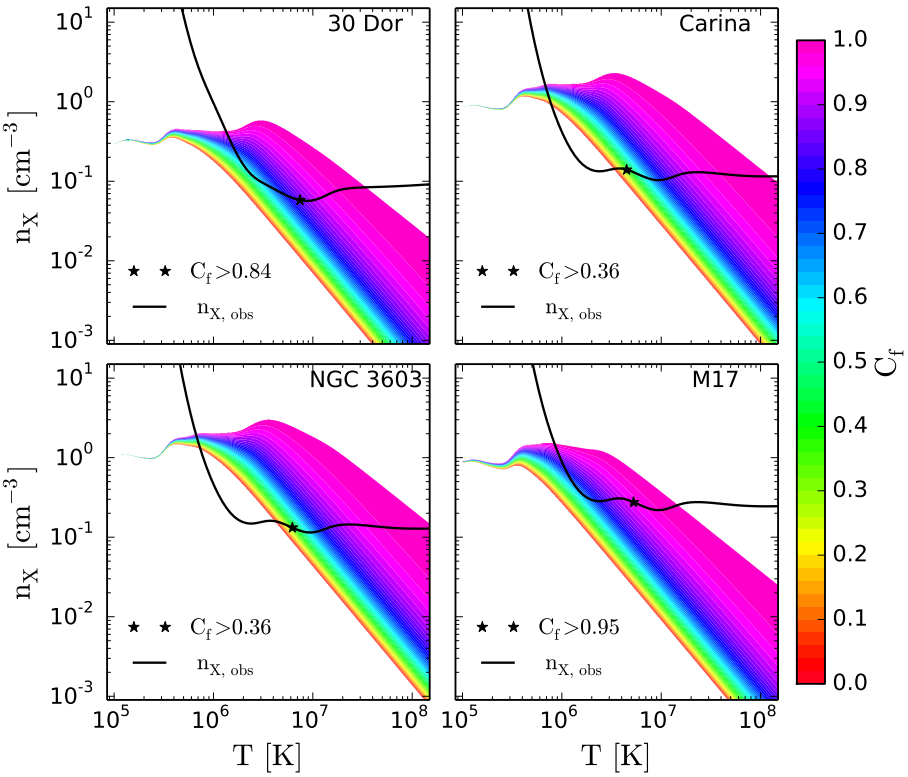

Figure 5.10 Contours of constant confinement parameter, C_f, for all H II regions in our sample. The value of C_f shown is that which would be required for physical leakage to account for all of the wind energy not removed by radiative cooling and mechanical work on the bubble shell. The curve of $n_{X,obs}$ versus T required for consistency with the observed X-ray emission is over-plotted. Stars denote the values of T inferred from the spectral fitting.

solution.

Since the above argument suggests that the wind energy is not stored in the hot gas another possible solution is physical leakage of the hot gas. If the bubble shell is porous, the hot gas can physically leak out since the sound speed of the hot gas is greater than the expansion rate of the bubble shell (as discussed in Section 2.5). The energy loss by physical leakage is controlled by the porosity of the bubble shell, which

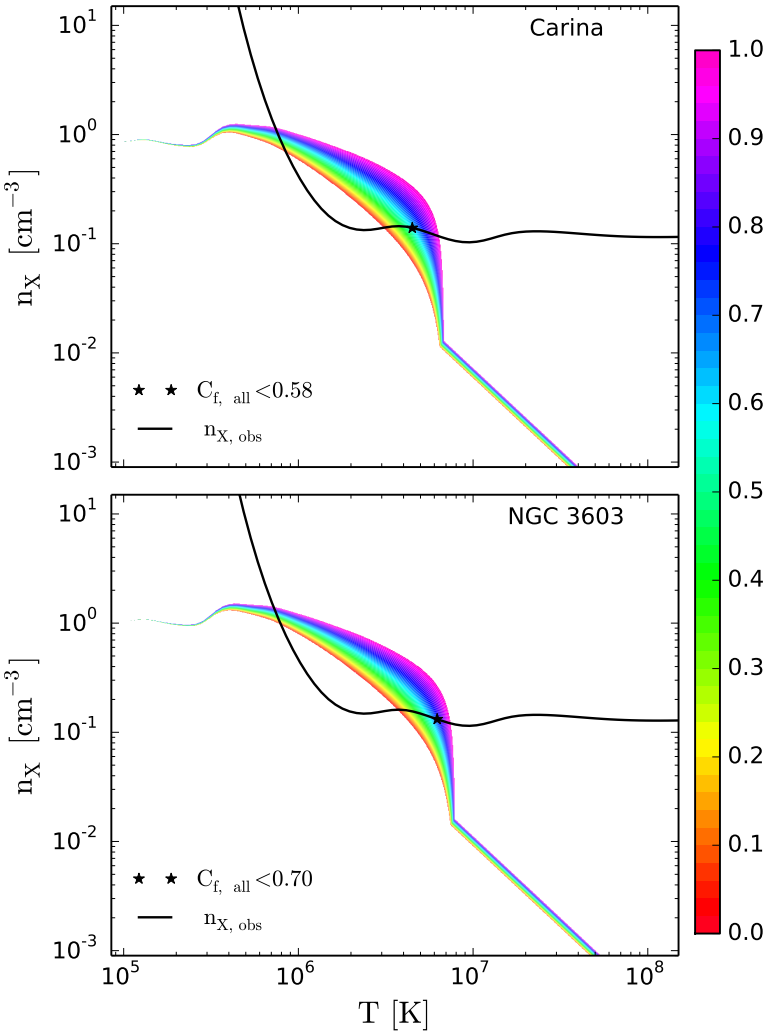

Figure 5.11 Same as Figure 5.10 for Carina and NGC 3603 but also including the energy transfer associated with thermal conduction and collisional heating of dust grains.

we can parameterize by the covering fraction C_f. If the shell is very porous, the shock-heated gas will escape easily, resulting in a significant loss of the wind energy from the bubble, greatly reducing the X-ray luminosity. From the energy loss processes discussed

in Section 2, we have that the total energy loss of the hot gas is

$$\frac{dE}{dt} = L_{\rm w} - L_{\rm cool} - L_{\rm mech} - L_{\rm cond} - L_{\rm dust} - L_{\rm leak}. \tag{5.22}$$

Using Equation (5.18) and assuming that these processes account for the total energy loss of the hot gas (i.e., $\frac{dE}{dt} = 0$), $C_{\rm f}$ is given by

$$C_{\rm f} = 1 - \frac{2}{5}\frac{[L_{\rm w} - L_{\rm cool} - L_{\rm mech} - L_{\rm cond} - L_{\rm dust}]}{4\pi R^2 \mu m_{\rm p} n_{\rm X} c_{\rm s}^3} \tag{5.23}$$

which depends on both $n_{\rm X}$ and T.

Figure 5.10 show contours of the values of $C_{\rm f}$ required to account for the missing energy as a function of hot gas density and temperature. To generate this figure, we solve Equation (5.23) at each point in the $T - n_{\rm X}$ plane, assuming that only radiative cooling, mechanical work, and physical leakage contribute to energy loss, i.e., that $L_{\rm cond} = L_{\rm dust} = 0$. We also show the loci in the $T - n_{\rm X}$ inferred from the observed X-ray emission. The plot shows that physical leakage can adequately account for the missing energy for these H II regions for plausible values of the confinement factor. For the observationally-favored temperature and the corresponding derived density values (denoted by points in the Figure), the required values of $C_{\rm f}$ are in the range $0.36 - 0.95$ (also see Table 5.2). Adopting non-zero values of $L_{\rm cond}$ or $L_{\rm dust}$ would increase these values as can be seen in Figure 5.11 and Table 5.2 for Carina and NGC 3603.

Finally, we note that there is one additional mechanism that we have not considered because we lack the ability to calculate it: turbulent mixing of the hot gas with

cooler gas followed by conduction. As the shell expands into the ISM, the bubble shell interface becomes corrugated by instabilities (Strickland and Stevens, 1998). These instabilities will lead to the addition of cooler, denser material in the bubble interior. This material can then mix with the hot gas, and the resulting large temperature variations over small scales will produce very rapid thermal conduction. For example, if the hot gas ($T \sim 10^6 - 10^7$ K) mixes with the surrounding warm, ionized gas ($T \sim 10^4$ K) the resulting mixture will have temperatures of $\sim 10^5$ K (Dunne *et al.*, 2003) and this gas will cool rapidly via metal-line cooling in the far-UV before adiabatically expanding and filling the whole H II region. Figure 5.5 shows that the cooling of the denser, mixed gas can effectively radiate all of the wind energy.

5.5 Discussion

5.5.1 Deviations from Collisional Ionization Equilibrium

Throughout our analysis we have assumed that the post-shocked wind material responsible for the diffuse X-ray emission in H II regions is in CIE. This assumption allows one to easily determine the allowed locus in the $T - n_{\rm X}$ plane for an optically thin plasma given its observed X-ray luminosity. This is because the ionization fractions of the plasma depend only on T and Z under the assumption of CIE, as does the emissivity, j_ν, and the radiative cooling function Λ. However, a hot plasma which was initially in equilibrium will deviate from equilibrium if the gas cools faster than it can recombine. The rapid cooling will cause the gas to become "over-ionized" (Gnat and

Sternberg, 2007). One such example is if the hot plasma undergoes rapid adiabatic expansion before significant radiative losses can occur (Breitschwerdt and Schmutzler, 1999) which has been observed in SN remnants (Lopez *et al.*, 2013b, and references therein). This scenario is likely the case for the hot gas we are considering in MSCs because the initial post-shock wind material will adiabatically expand and fill up the entire H II region before suffering drastic radiative losses.

Gnat and Sternberg (2007) studied the time-dependent behavior of a hot, low-density plasma and found that non-equilibrium effects cause the radiative cooling rate to be suppressed by a factor of $2-4$ as compared to an equilibrium plasma. This result leads to an increase in the cooling time of a non-CIE plasma, rendering radiative cooling even more unimportant than our fiducial analysis suggests. Hence, our assumption of CIE likely only over-estimates the cooling rate for a given density.

Similarly, the emissivity, j_ν, integrated over the X-ray band, is of order Λ for the temperatures that we consider (e.g., $T \gtrsim 10^6$ K). Thus, if Λ is suppressed by a factor of at most 4, then the integrated emissivity will decrease by a similar factor. This decrease in the emissivity will lead to the derived $n_{\rm X}$ to increase, at most, by a factor of 2, which would cause $L_{\rm mech}$ and $L_{\rm dust}$ to increase by factors of 2 and 4, respectively. Furthermore, $L_{\rm cool}$ will remain the same since the decrease in Λ will cancel the increase in $n_{\rm X}$. $L_{\rm cond}$ will remain approximately the same since the energy loss due to conduction in the unsaturated regime depends very weakly on density. Hence, we conclude that if the hot gas is not in CIE then radiative cooling is still an inefficient energy sink for the hot gas. The energy transfer due to mechanical work on the shell and dust heating via

collisions will be larger than our fiducial estimates, but only by factors of order unity.

5.5.2 Thermal Conduction and Magnetic Fields

In our analysis, we found that thermal conduction can remove a significant amount of energy from the hot gas, but only if we assume that it is not substantially suppressed by the presence of a magnetic field oriented with field lines parallel to the wall of the bubble. If such a magnetic field is present, it inhibits electron transport between the hot and cold gas, reducing the conduction coefficient compared to our fiducial value by a factor of order $(r_{\rm e}/\ell_{\rm e})^2$, where $r_{\rm e}$ is the electron gyroradius and $\ell_{\rm e}$ is the electron mean free path. In a plasma of 10^7 K gas with a density of 1 cm^{-3}, roughly our observationally-inferred values, $\ell_e \sim 0.04$ pc. In comparison, for a magnetic field of strength B, the gyroradius is $r_e = 10^8 \sqrt{T_7/B_0}$ cm, where $T_7 = T/10^7$ K and $B_0 = B/1$ μG, so the ratio $(r_e/\ell_e)^2 \sim 10^{-20}$ even for an extremely weak field of 1 μG. Thus even such a weak field will completely suppress conduction across field lines, and the only remaining question is the magnetic field geometry.

The molecular clouds out of which MSCs form are magnetized (Crutcher, 2012). A number of authors have simulated H II regions expanding into magnetized media (e.g., Krumholz *et al.*, 2007c; Wise and Abel, 2011; Arthur *et al.*, 2011; Gendelev and Krumholz, 2012), and a generic result of these simulations is that, as the H II region expands, advection of material out of the low-density interior into the surrounding swept-up dense shell results in a decrease in field strength in the H II region interior and an increase in field strength at the swept-up shell. This same phenomenon tends

to reconfigure the field orientation such that, over most of the swept-up shell, the field is oriented parallel to the shell wall, i.e., the configuration that should be most effective at suppressing thermal conduction between the hot and cold phases. Although measuring magnetic fields in the shells that bound H II regions is difficult, there is some observational evidence for this phenomenon operating. Pellegrini *et al.* (2007) measure the field strength in the photodissociation region (PDR) bounding the M17 H II region to be ~ 100 μG, far above the mean interstellar value, suggesting that field amplification has taken place and that conduction is being suppressed. Indeed, Dunne *et al.* (2003) conclude that such a strong field is required to explain the observed low X-ray luminosity of M17.

Although M17 is just one example, and in it we have only circumstantial observational evidence that the field is oriented parallel to the dense shell wall, that plus the simulation results is highly suggestive that magnetic suppression of conduction is probably very effective in most H II regions, with the effectiveness depending on the detailed magnetic field configuration. It is therefore likely that conduction is not a significant source of energy loss. Note that this statement does *not* apply to what we have termed turbulent mixing followed by conduction. The reason is that turbulence will cascade down to scales comparable to the electron gyroradius, and on such small scales conduction is no longer suppressed by magnetic fields. Magnetic fields suppress only laminar conduction, not conduction that is the end product of a turbulent cascade originating at an unstable interface.

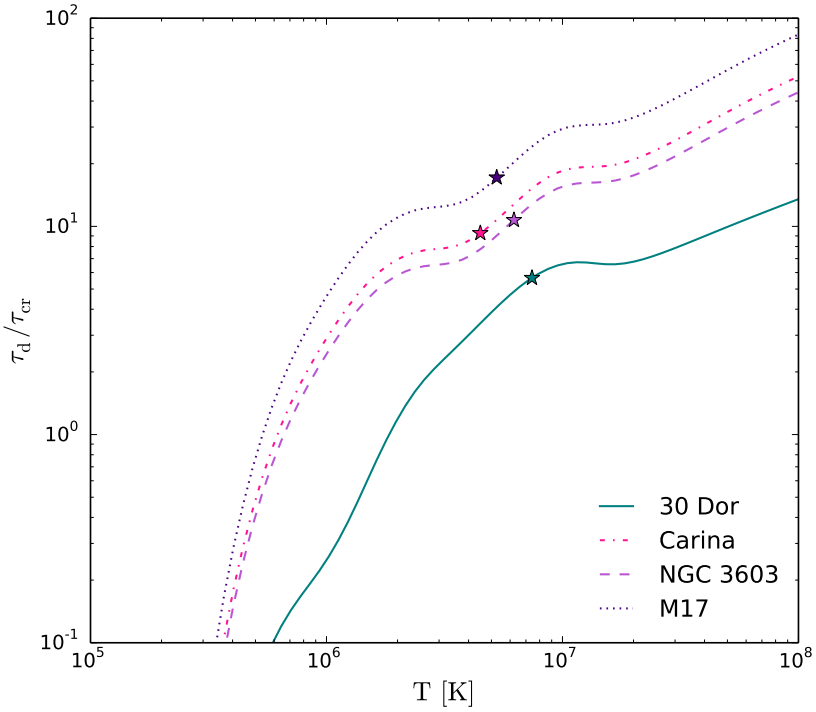

Figure 5.12 Ratio of the dust destruction time scales to the crossing times for our H II region sample. The points denote the observed T_X and the corresponding n_X values obtained from our derived $T - n_X$ plane.

5.5.3 Dust Sputtering and the Dust Cooling Rate

We also found that the heating of dust by collisions with the hot electrons can be an important energy sink for the hot gas, but to be conservative we performed this calculation assuming the same dust to gas ratio in the hot gas as in the cold ISM. This assumption is unlikely to be satisfied. To see why, it is helpful to compare the mixing timescale of the dust that is entrained into the hot gas with the timescale for this dust to be destroyed by sputtering. The mixing timescale will be of order the crossing time, $\tau_{cr} = R/c_s$, of the hot gas. In comparison, the approximate lifetime of dust grains

immersed in hot gas is

$$\tau_{\rm d} \approx 1 \times 10^5 \left[1 + \left(\frac{T}{10^6\ {\rm K}}\right)^{-3}\right] \left(\frac{a}{0.1\,\mu{\rm m}}\right) \left(\frac{n_{\rm i}}{{\rm cm}^{-3}}\right)^{-1}\ {\rm yr} \tag{5.24}$$

where a is the dust grain size (Draine, 2011).

Figure 5.12 shows the ratio of dust grain lifetimes and crossing times for the H II regions in our sample using our derived $n_{\rm X}$, where we have assumed a typical grain size of 0.1 μm in Equation (5.24). We find that under our derived conditions, the dust grains will survive from a few $\times 10^5$ years up to a couple Myrs. This results in the dust surviving from a few to $\sim$ 10 crossing time scales for the temperatures given in Table 5.1. This suggests that it is possible for dust grains with sizes greater than 0.1 μm to survive for some length of time in the hot gas. However, since the crossing and destruction timescales are not very different, our assumption that the dust abundance in the hot gas matches that in the cold gas is likely still a substantial overestimate. To keep the dust abundance so high, cold gas would have to be continually mixed into the hot H II region interior on times not much greater than the hot gas crossing timescale. Such rapid mixing would likely in itself be a major cooling source, rendering the dust of secondary importance.

5.6 Conclusion

In this chapter, we have examined the many different ways that MSCs can lose the kinetic energy injected by fast stellar winds from massive stars. These winds collide

with each other and the ISM, generating hot shock-heated material at temperatures of $\sim 10^7$ K, and the mechanical luminosity associated with the production of this gas is comparable to that provided by supernovae at later stages of stellar evolution. However, the effects of this gas on the ISM depend critically on where the energy ultimately ends up – does it go into bulk motion of the cold ISM, possibly disrupting gas clouds and halting star formation? Is it radiated away as X-ray emission? Is it lost in some other way?

To address these questions, we have used the empirically determined properties from four LMC and MW MSCs. For each of these, the set of observational constraints is sufficient to allow us to estimate the wind energy input, and conversely, to estimate the rates of energy loss due to radiative cooling, mechanical work on the dense H II region shell, thermal conduction, collisional dust heating, and physical leakage of hot gas out of the dense shell. We find that radiative cooling of the hot gas accounts for less than 1% of the total energy injected by stellar winds for the observed hot gas temperatures in the H II regions we have considered. While this might appear to favor a significant fraction of the energy going into mechanical work and thus being available as a form of feedback, our estimates of the rate of mechanical work on the dense H II region shell suggest that this is not the case. Instead, for all but one of the H II regions (M17), we find that at most $\sim 15\%$ of the injected wind energy goes into doing mechanical work on the ISM. This limits the potential importance of winds as a stellar feedback mechanism, since it suggests that the efficiency with which they can be converted to bulk motion is fairly low.

This raises the question: if the bulk of the wind energy does not go into radiation nor mechanical work, where does it go? We identify four possible scenarios. The first is that the energy could be lost via thermal conduction at the hot-cold shell interface, followed by line radiation from this gas at far-UV wavelengths. However, this scenario appears to be viable only under the most optimistic possible assumptions. Thermal conduction will be dramatically reduced if there is a magnetic field parallel to the hot-cold interface, a configuration that simulations suggest should be common. It is possible to check this possibility via observations in several ways. If thermal conduction is the dominant loss mechanism, then observations of far-UV radiation in H II regions should discover a significant mass of $\sim 10^5$ K gas in these objects. More indirectly, polarization studies and Zeeman line splitting measurements of the gas in H II regions and their shells can allow one to determine the orientation of the magnetic field and magnetic field strength. If the magnetic field is indeed parallel to the hot-cold interface, then thermal conduction will be strongly suppressed.

A second scenario is that wind energy stored in the hot gas is transferred to dust grains via collisions, and then radiated as infrared continuum. While this provides a sufficient energy sink to account for most of the injected wind energy if the dust content of the hot gas is the same as that of the cold gas, this too seems highly improbable. Grains ~ 0.1 μm in size will be destroyed by sputtering in the hot gas in a time that is only a factor of a few larger than the crossing timescale, which suggests that it would be difficult to maintain a large population of such grains. Observationally, one might be able to evaluate this possibility by checking for distortions in the dust continuum

spectrum. Since sputtering will preferentially destroy small grains, the infrared spectral energy distribution (SED) produced by the remaining grains should be shifted to longer wavelengths than the usual dust SED.

The third way the energy can be accounted for is if the hot gas physically leaks out of the H II region through holes in the bubble shell. These holes can be a result of stellar feedback punching holes in the dense H II region shell or because the shell expands into a non-uniform ISM. We find that, for plausible values of the confinement factor of the dense shell, this loss mechanism would be sufficient to account for the missing energy. In support of this scenario, Rogers and Pittard (2013) simulate the interaction of the mechanical energy input by stellar winds of three O-stars in a GMC and find that the hot gas generated by the shock heated stellar winds flows out of the GMC through low-density channels.

Our fourth and final scenario is that the hot gas can lose a significant amount of energy by mixing with the cold gas, followed by thermal conduction at the turbulent interface between the two – turbulent conduction. The resulting mixed gas will have temperatures of $\sim 10^5$ K and will drastically cool via radiation in the far-UV. There is one indirect piece of observational evidence for this scenario: Bowen *et al.* (2008) report high O VI absorption in Carina, suggesting an overabundance of $\sim 10^5$ K gas as compared to the normal ISM in the MW. Such an excess might also be evidence of laminar conduction without turbulent mixing, and one can distinguish between these scenarios by measuring the magnetic field strength and orientation. If a magnetic field parallel to the hot-cold interface is present, then the energy loss will most likely be dominated

by turbulent conduction. We conclude that the either this scenario or physical leakage is the most likely explanation for the missing energy.

These four possible scenarios suggest that one productive avenue for further investigation is three-dimensional simulations of stellar wind feedback. Simulations of wind feedback including self-gravity and a realistically-turbulent confining molecular medium are quite rare. Rogers and Pittard (2013) is one of the few examples. However, even these simulations include none of the physical mechanisms – magnetic fields, thermal conduction, dust sputtering – that would be required to address any scenario except bulk leakage. Incorporating these mechanisms into future simulations would be a valuable complement to observational studies such as this one, and might lead to the development of new observational diagnostics that could be used to track down the missing energy.

Chapter 6

Conclusions & Future Work

This thesis explored a breadth of topics in massive star formation and early MSC evolution. With the use of analytical and numerical techniques we studied how massive stars form, what physical properties set their initial properties at birth, and how these stars feed back on their environments with their intense radiation fields and fast, radiatively driven winds.

In Chapter 2 we presented an analytical model that described the rotational evolution of accreting massive protostars. Our work showed that, thanks to the speed with which they form, massive stars should all be born rotating at high speeds in agreement with observations (Wolff *et al.*, 2006). This effect makes massive stars more disruptive to their environments since fast rotation leads to higher luminosities and stronger winds.

As discussed, one of the greatest barriers in the formation of massive stars is the radiation pressure associated with their high luminosities. The resulting radia-

tion pressure can oppose gravity and halt accretion. Therefore, detailed simulation of massive star formation requires an accurate treatment of radiation. As we described in Chapter 1, past three-dimensional simulations have provided progress in our understanding of how these stars form. However, these simulations have either used *ad-hoc* prescriptions to model the radiation field from stars (Krumholz *et al.*, 2009); have only been able to simulate a single star fixed in space, thereby suppressing potentially important instabilities (Kuiper *et al.*, 2011, 2012); or did not provide adequate resolution at locations where instabilities may develop (Klassen *et al.*, 2016)

To remedy this we developed a new, highly accurate hybrid radiation scheme that handles both the absorption of energy and momentum from the direct stellar radiation field and its subsequent re-emission and processing by interstellar dust. We added our new method to the ORION astrophysical adaptive mesh refinement code. Our hybrid radiative transfer algorithm was presented in Chapter 3. Our new method, $HARM^2$, uses a long characteristics ray tracer to model the direct stellar radiation field, which traces rays on a cell by cell basis thus providing maximum possible accuracy. Our method is adaptive, in which rays are allowed to split as they travel away from their source, greatly reducing the computational cost (Abel and Wandelt, 2002); and is capable of representing multifrequency stellar irradiation for an arbitrary number of moving stars. The multifrequency treatment is ideal for stars since they have color temperatures much higher than the absorbing medium. In $HARM^2$, the dust-reprocessed radiation pressure is handled by a Flux Limited Diffusion solver (Krumholz *et al.*, 2007b). We showed that our method is highly parallel and can run efficiently on hundreds of pro-

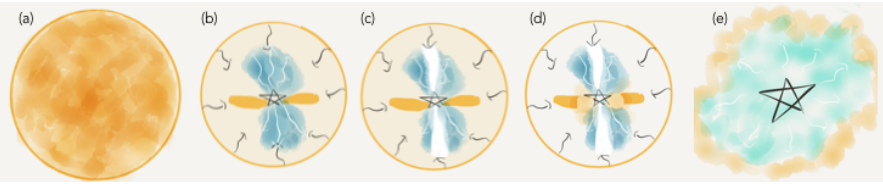

Figure 6.1 Massive star formation schematic. From left to right: (a) Initial magnetized, turbulent pre-stellar core. (b) Collapse of pre-stellar core leads to star surrounded by an accretion disk. Radiation pressure from the star launches radiation pressure dominated bubbles above and below the star. (c) Collimated outflows will punch holes in the ISM along the polar directions of star. (d) Stellar winds will shock-heat infalling material and ablate the accretion disk. (e) The combination of these feedback processes will eject ambient material and may inhibit further accretion onto the star.

cessors, as required for a computational challenge of this magnitude.

With this new tool, we performed a series of massive star formation simulations from the collapse of initially laminar and turbulent pre-stellar cores, presented in Chapter 4. We found that mass is channelled to the massive star via gravitational and Rayleigh-Taylor (RT) instabilities. For laminar pre-stellar cores, we found that proper treatment of the direct radiation pressure produces later onset of RT instability, but does not suppress it entirely. RT instabilities arise immediately for turbulent cores because the initial turbulence seeds the instabilities. Furthermore, we showed that dense infalling filaments supply a significant amount of mass to the massive star. This work represents the most accurate and high-resolution radiation-hydrodynamic simulations of massive star formation performed to date.

The simulations presented in Chapter 4 only focused on how radiative feedback may limit massive star formation. However, the feedback associated with the star's fast, stellar winds and magnetically launched collimated outflows may also limit accretion onto massive stars at late times during their formation. Yet no massive star formation

simulations to date have included feedback from winds and collimated outflows in conjunction with the highly-accurate treatment of the radiation pressure presented in this thesis.

Collimated protostellar outflows impart momentum to the stellar environment, ejecting material along the polar directions of the star. This effect will eventually cut-off accretion as the opening angle of the outflows grow larger with time (Kuiper *et al.*, 2015). Furthermore, outflows may make mass delivery via RT instabilities less significant (Cunningham *et al.*, 2011). Previous theoretical and observational studies find that the typical mass ejection rate from outflows is $\sim 1/3$ of the accretion rate (Beuther *et al.*, 2002; Seifried *et al.*, 2012). In addition, stellar winds collide with infalling material and shock-heat gas to $\sim 10^7$ K that will expand and push on the infalling material, eventually ejecting low density material (Weaver *et al.*, 1977). The interaction of these stellar winds may also lead to disk ablation that will eventually stop disk accretion (Kee *et al.*, 2016). Figure 6.1 illustrates how these different feedback processes can affect the formation of massive stars.

While observations suggest that massive stars with initial masses well in excess of 150 $M_\odot$ may exist (Crowther *et al.*, 2010, 2016), it is unclear how these stars attain such high masses and what role feedback plays on the upper mass limit of the stellar initial mass function. Therefore a complete picture of how the most massive stars form remains incomplete and future work should consider how the combination of radiation pressure, stellar winds, and protostellar outflows can limit accretion onto massive stars, especially at late times in the formation process.

Numerical simulations that include these feedback mechanisms can address several outstanding questions raised by observations of massive star formation: How does feedback determine the star formation efficiency of pre-stellar cores? Is there an upper mass limit to the masses of stars that can form by accretion? If so, how does this upper mass limit compare to observations? If accretion sets a lower limit than observations imply, then are stellar mergers responsible for stars with masses above this limit (de Mink *et al.*, 2014)? If feedback sets an upper mass limit, then which feedback mechanism sets it? Determining which feedback mechanism regulates the formation of massive stars will also provide the foundation to study how the variation of the upper mass limit set by accretion depends on galactic properties. For example, the winds of low-metallicity stars are much weaker due to the lack of iron opacity (Vink *et al.*, 2001). If winds are the dominant feedback mechanism regulating massive star formation then the upper mass limit should be higher in low-metallicity environments. Likewise, radiation pressure will also be weaker in low-metallicity environments because these environments contain less dust. Both of these effects will affect the upper mass limit set by accretion in different galactic environments, while feedback from outflows should have no dependence on metallicity. Thus, while the work presented in this thesis provides an outlet for the radiation pressure barrier in massive star formation there is still much work to be done.

In Chapter 5 we also considered how the kinetic energy from the shocked stellar winds from the numerous massive stars can transfer energy to the surrounding gas in H II regions that host MSCs. As we discussed, previous observational studies

suggest that the hot gas produced by the shock-heating of stellar winds in MSCs is dynamically unimportant because rather than being confined, it tends to "leak" out of the surrounding H II region. The primary piece of evidence for this hypothesis is the surprisingly weak X-ray emission observed in numerous H II regions (Harper-Clark and Murray, 2009; Lopez *et al.*, 2011), which is much weaker than simple theoretical models suggest (Weaver *et al.*, 1977).

By using observations and considering several energy loss mechanisms, we found that laminar conduction and dust heating via collisions could account for a large fraction of the wind energy, assuming the H II region shell is unmagnetized and that the dust is perfectly mixed with the hot gas. Work done on the ISM is usually subdominant, and with the available data it is not possible to estimate loss rates due to physical leakage or turbulent conduction. However, it still remains uncertain if stellar wind feedback is important during the early formation of MSCs.

These results suggest that further progress requires simulations of MSC formation with radiation and stellar wind feedback. Only a couple relevant simulations have been published (Freyer *et al.*, 2003; Rogers and Pittard, 2013), and none thus far have included the physical mechanisms – radiation, magnetic fields, thermal conduction, dust sputtering – that would be required to address any scenario except bulk leakage. Furthermore, the relative role of winds versus other feedback modes (such as photoionization flows, radiation pressure, and SNe) have not been tested. In particular, radiation pressure is the most likely to play an important role in MSCs (Krumholz and Matzner, 2009; Fall *et al.*, 2010; Murray *et al.*, 2010; Yeh and Matzner, 2012), yet no simulations

to date have included it. Luckily, with the use of $HARM^2$ and MHD in AMR codes like ORION, the next generation of simulations can simulate the early phases of MSCs with the relevant feedback mechanisms to improve our understanding of MSC formation and their early evolution. Finally simulations such as these can also shed light on the importance of stellar feedback in galaxy formation and evolution since stellar feedback is likely responsible for the low star formation efficiencies and efficient gas expulsion observed in many galaxies.

To conclude, the work presented in this thesis has paved the way for the next generation of massive star and MSC simulations required to study how stellar feedback from radiation, protostellar outflows, and stellar winds impact their formation. Future work must contain these relevant feedback processes and also magnetic fields since massive star forming regions are magnetized. Such work will lead to a more complete understanding of how the most massive stars and star clusters form. Furthermore, the next generation of simulations can also be used to develop detailed sub-grid stellar feedback models that can be used in future cosmological simulations. Such work will facilitate unprecedented strides in our understanding of how stellar feedback can limit star formation and influence galaxy formation and evolution.

Bibliography

Abel, T. and Wandelt, B. D. Adaptive ray tracing for radiative transfer around point sources. MNRAS **330**, L53 (2002).

Adams, M.; Colella, P.; Graves, D. T.; Johnson, J. N.; Keen, N. D.; Ligocki, T. J.; Martin, D. F.; McCorquodale, P. W.; Modiano, D. andSchwartz, P. O.; Sternberg, T. D. and Van Straalen, B. Chombo software package for amr applications - design document. Tech. Rep. LBNL-6616E, Lawrence Berkeley National Laboratory (2015). Technical Report.

Alecian, E.; Wade, G. A.; Catala, C.; Bagnulo, S.; Boehm, T.; Bohlender, D.; Bouret, J.-C.; Donati, J.-F.; Folsom, C. P.; Grunhut, J. and Landstreet, J. D. Discovery of magnetic fields in the very young, massive stars W601 (NGC 6611) and OI 201 (NGC 2244). A&A **481**, L99 (2008).

Allen, D. A. and Hillier, D. J. The Shape of the Homunchulus Nebula around Eta-Carinae. *Proceedings of the Astronomical Society of Australia* **10**, 338 (1993).

Armitage, P. J. and Clarke, C. J. Magnetic braking of T Tauri stars. MNRAS **280**, 458 (1996).

Arthur, S. J.; Henney, W. J.; Mellema, G.; de Colle, F. and Vázquez-Semadeni, E. Radiation-magnetohydrodynamic simulations of H II regions and their associated PDRs in turbulent molecular clouds. MNRAS **414**, 1747 (2011).

Balick, B.; Boeshaar, G. O. and Gull, T. R. The giant galactic H II region NGC 3603 - Optical studies of its structure and kinematics. ApJ **242**, 584 (1980).

Banerjee, R. and Pudritz, R. E. Massive Star Formation via High Accretion Rates and Early Disk-driven Outflows. ApJ **660**, 479 (2007).

Behrend, R. and Maeder, A. Formation of massive stars by growing accretion rate. A&A **373**, 190 (2001).

Berger, M. J. and Colella, P. Local adaptive mesh refinement for shock hydrodynamics. J. Chem. Phys. **82**, 64 (1989).

Berger, M. J. and Oliger, J. Adaptive mesh refinement for hyperbolic partial differential equations. J. Chem. Phys. **53**, 484 (1984).

Beuther, H.; Leurini, S.; Schilke, P.; Wyrowski, F.; Menten, K. M. and Zhang, Q. Interferometric multi-wavelength (sub)millimeter continuum study of the young high-mass protocluster IRAS 05358+3543. A&A **466**, 1065 (2007).

Beuther, H.; Schilke, P.; Sridharan, T. K.; Menten, K. M.; Walmsley, C. M. and Wyrowski, F. Massive molecular outflows. A&A **383**, 892 (2002).

Bjorkman, J. E. and Cassinelli, J. P. Equatorial disk formation around rotating stars due to Ram pressure confinement by the stellar wind. ApJ **409**, 429 (1993).

Bodenheimer, P. Angular Momentum Evolution of Young Stars and Disks. ARA&A **33**, 199 (1995).

Bolatto, A. D.; Warren, S. R.; Leroy, A. K.; Walter, F.; Veilleux, S.; Ostriker, E. C.; Ott, J.; Zwaan, M.; Fisher, D. B.; Weiss, A.; Rosolowsky, E. and Hodge, J. Suppression of star formation in the galaxy NGC 253 by a starburst-driven molecular wind. Nature **499**, 450 (2013).

Boldyrev, S. Kolmogorov-Burgers Model for Star-forming Turbulence. ApJ **569**, 841 (2002).

Borra, E. F. and Landstreet, J. D. The magnetic field of the helium-strong stars. ApJ **228**, 809 (1979).

Bouvier, J. The rotational evolution of young low mass stars. In Bouvier, J. and Appenzeller, I., eds., *Star-Disk Interaction in Young Stars* (2007), vol. 243 of *IAU Symposium*, pp. 231–240.

Bowen, D. V.; Jenkins, E. B.; Tripp, T. M.; Sembach, K. R.; Savage, B. D.; Moos, H. W.; Oegerle, W. R.; Friedman, S. D.; Gry, C.; Kruk, J. W.; Murphy, E.; Sankrit, R.; Shull, J. M.; Sonneborn, G. and York, D. G. The Far Ultraviolet Spectroscopic Explorer Survey of O VI Absorption in the Disk of the Milky Way. ApJS **176**, 59 (2008).

Breitschwerdt, D. and Kahn, F. D. Stellar winds in H II regions - Unstable waves in ionized shells. MNRAS **235**, 1011 (1988).

Breitschwerdt, D. and Schmutzler, T. The dynamical signature of the ISM in soft X-rays. I. Diffuse soft X-rays from galaxies. A&A **347**, 650 (1999).

Bruhweiler, F. C.; Gull, T. R.; Kafatos, M. and Sofia, S. Stellar winds, supernovae, and the origin of the H I supershells. ApJ **238**, L27 (1980).

Buntemeyer, L.; Banerjee, R.; Peters, T.; Klassen, M. and Pudritz, R. E. Radiation hydrodynamics using characteristics on adaptive decomposed domains for massively parallel star formation simulations. New A **43**, 49 (2016).

Burke, J. R. and Hollenbach, D. J. The gas-grain interaction in the interstellar medium - Thermal accommodation and trapping. ApJ **265**, 223 (1983).

Butler, M. J. and Tan, J. C. Mid-infrared Extinction Mapping of Infrared Dark Clouds. II. The Structure of Massive Starless Cores and Clumps. ApJ **754**, 5 (2012).

Cantó, J.; Raga, A. C. and Rodríguez, L. F. The Hot, Diffuse Gas in a Dense Cluster of Massive Stars. ApJ **536**, 896 (2000).

Caselli, P. and Myers, P. C. The Line Width–Size Relation in Massive Cloud Cores. ApJ **446**, 665 (1995).

Castor, J.; McCray, R. and Weaver, R. Interstellar bubbles. ApJ **200**, L107 (1975).

Cesaroni, R.; Galli, D.; Lodato, G.; Walmsley, C. M. and Zhang, Q. Disks Around Young O-B (Proto)Stars: Observations and Theory. *Protostars and Planets V* pp. 197–212 (2007).

Cesaroni, R.; Galli, D.; Lodato, G.; Walmsley, M. and Zhang, Q. The critical role of disks in the formation of high-mass stars. Nature **444**, 703 (2006).

Chevalier, R. A. and Clegg, A. W. Wind from a starburst galaxy nucleus. Nature **317**, 44 (1985).

Chini, R.; Hoffmeister, V. H.; Nasseri, A.; Stahl, O. and Zinnecker, H. A spectroscopic survey on the multiplicity of high-mass stars. MNRAS **424**, 1925 (2012).

Chini, R.; Hoffmeister, V. H.; Nielbock, M.; Scheyda, C. M.; Steinacker, J.; Siebenmorgen, R. and Nürnberger, D. A Remnant Disk around a Young Massive Star. ApJ **645**, L61 (2006).

Chini, R.; Hoffmeister, V. H. and Nürnberger, D. Evidence for disks around young high-mass stars. *Bulletin de la Societe Royale des Sciences de Liege* **80**, 217 (2011).

Chu, Y.-H. and Kennicutt, Jr., R. C. Kinematic structure of the 30 Doradus giant H II region. ApJ **425**, 720 (1994).

Clayton, C. A.; Ivchenko, V. N.; Meaburn, J. and Walsh, J. R. Echelle observations of the complex H-alpha and N II forbidden line profiles from the galactic H II region M17 (NGC 6618). MNRAS **216**, 761 (1985).

Collier Cameron, A. and Campbell, C. G. Rotational evolution of magnetic T Tauri stars with accretion discs. A&A **274**, 309 (1993).

Commerçon, B.; Teyssier, R.; Audit, E.; Hennebelle, P. and Chabrier, G. Radiation hydrodynamics with adaptive mesh refinement and application to prestellar core collapse. I. Methods. A&A **529**, A35+ (2011).

Cowie, L. L. and McKee, C. F. The evaporation of spherical clouds in a hot gas. I - Classical and saturated mass loss rates. ApJ **211**, 135 (1977).

Crowther, P. A.; Caballero-Nieves, S. M.; Bostroem, K. A.; Maíz Apellániz, J.; Schneider, F. R. N.; Walborn, N. R.; Angus, C. R.; Brott, I.; Bonanos, A.; de Koter, A.; de Mink, S. E.; Evans, C. J.; Gräfener, G.; Herrero, A.; Howarth, I. D.; Langer, N.; Lennon, D. J.; Puls, J.; Sana, H. and Vink, J. S. The R136 star cluster dissected with Hubble Space Telescope/STIS. I. Far-ultraviolet spectroscopic census and the origin of He II λ1640 in young star clusters. MNRAS **458**, 624 (2016).

Crowther, P. A. and Dessart, L. Quantitative spectroscopy of Wolf-Rayet stars in HD97950 and R136a - the cores of giant HII regions. MNRAS **296**, 622 (1998).

Crowther, P. A.; Schnurr, O.; Hirschi, R.; Yusof, N.; Parker, R. J.; Goodwin, S. P. and Kassim, H. A. The R136 star cluster hosts several stars whose individual masses greatly exceed the accepted 150M$_{solar}$ stellar mass limit. MNRAS **408**, 731 (2010).

Crutcher, R. M. Magnetic Fields in Molecular Clouds: Observations Confront Theory. ApJ **520**, 706 (1999).

Crutcher, R. M. Magnetic Fields in Molecular Clouds. ARA&A **50**, 29 (2012).

Crutcher, R. M.; Wandelt, B.; Heiles, C.; Falgarone, E. and Troland, T. H. Magnetic Fields in Interstellar Clouds from Zeeman Observations: Inference of Total Field Strengths by Bayesian Analysis. ApJ **725**, 466 (2010).

Cunningham, A. J.; Klein, R. I.; Krumholz, M. R. and McKee, C. F. Radiation-hydrodynamic Simulations of Massive Star Formation with Protostellar Outflows. ApJ **740**, 107 (2011).

Dale, J. E.; Ercolano, B. and Bonnell, I. A. Ionizing feedback from massive stars in massive clusters - III. Disruption of partially unbound clouds. MNRAS p. 587 (2013).

Davies, B.; Hoare, M. G.; Lumsden, S. L.; Hosokawa, T.; Oudmaijer, R. D.; Urquhart, J. S.; Mottram, J. C. and Stead, J. The Red MSX Source survey: critical tests of accretion models for the formation of massive stars. MNRAS **416**, 972 (2011).

Davis, S. W.; Jiang, Y.-F.; Stone, J. M. and Murray, N. Radiation Feedback in ULIRGs: Are Photons Movers and Shakers? ApJ **796**, 107 (2014).

Davis, S. W.; Stone, J. M. and Jiang, Y.-F. A Radiation Transfer Solver for Athena Using Short Characteristics. ApJS **199**, 9 (2012).

de Mink, S. E.; Sana, H.; Langer, N.; Izzard, R. G. and Schneider, F. R. N. The Incidence of Stellar Mergers and Mass Gainers among Massive Stars. ApJ **782**, 7 (2014).

Dere, K. P.; Landi, E.; Mason, H. E.; Monsignori Fossi, B. C. and Young, P. R. CHIANTI - an atomic database for emission lines. A&AS **125**, 149 (1997).

Donati, J.-F.; Howarth, I. D.; Bouret, J.-C.; Petit, P.; Catala, C. and Landstreet, J. Discovery of a strong magnetic field on the O star HD 191612: new clues to the future of θ^1 Orionis C*. MNRAS **365**, L6 (2006).

Doran, E. I.; Crowther, P. A.; de Koter, A.; Evans, C. J.; McEvoy, C.; Walborn, N. R.; Bastian, N.; Bestenlehner, J. M.; Gräfener, G.; Herrero, A.; Köhler, K.; Maíz Apellániz, J.; Najarro, F.; Puls, J.; Sana, H.; Schneider, F. R. N.; Taylor, W. D.; van Loon, J. T. and Vink, J. S. The VLT-FLAMES Tarantula Survey. XI. A census of the hot luminous stars and their feedback in 30 Doradus. A&A **558**, A134 (2013).

Draine, B. T. *Physics of the Interstellar and Intergalactic Medium*. Princeton University Press (2011).

Dufton, P. L.; Smartt, S. J.; Lee, J. K.; Ryans, R. S. I.; Hunter, I.; Evans, C. J.; Herrero, A.; Trundle, C.; Lennon, D. J.; Irwin, M. J. and Kaufer, A. The VLT-FLAMES survey of massive stars: stellar parameters and rotational velocities in NGC 3293, NGC 4755 and NGC 6611. A&A **457**, 265 (2006).

Dunne, B. C.; Chu, Y.-H.; Chen, C.-H. R.; Lowry, J. D.; Townsley, L.; Gruendl, R. A.; Guerrero, M. A. and Rosado, M. Diffuse X-Ray Emission from the Quiescent Superbubble M17, the Omega Nebula. ApJ **590**, 306 (2003).

Dwek, E. The infrared diagnostic of a dusty plasma with applications to supernova remnants. ApJ **322**, 812 (1987).

Dykema, P. G.; Klein, R. I. and Castor, J. I. A New Scheme for Multidimensional Line Transfer. III. A Two-dimensional Lagrangian Variable Tensor Method with Discontinuous Finite-Element SN Transport. ApJ **457**, 892 (1996).

Ekström, S.; Georgy, C.; Eggenberger, P.; Meynet, G.; Mowlavi, N.; Wyttenbach, A.; Granada, A.; Decressin, T.; Hirschi, R.; Frischknecht, U.; Charbonnel, C. and Maeder, A. Grids of stellar models with rotation. I. Models from 0.8 to 120 M at solar metallicity (Z = 0.014). A&A **537**, A146 (2012).

Fall, S. M.; Krumholz, M. R. and Matzner, C. D. Stellar Feedback in Molecular Clouds and its Influence on the Mass Function of Young Star Clusters. ApJ **710**, L142 (2010).

Federrath, C.; Banerjee, R.; Clark, P. C. and Klessen, R. S. Modeling Collapse and Accretion in Turbulent Gas Clouds: Implementation and Comparison of Sink Particles in AMR and SPH. ApJ **713**, 269 (2010a).

Federrath, C.; Roman-Duval, J.; Klessen, R. S.; Schmidt, W. and Mac Low, M.-M. Comparing the statistics of interstellar turbulence in simulations and observations. Solenoidal versus compressive turbulence forcing. A&A **512**, A81 (2010b).

Fisher, R. T. *Single and Multiple Star Formation in Turbulent Molecular Cloud Cores.* Ph.D. thesis, University of California, Berkeley (2002).

Freyer, T.; Hensler, G. and Yorke, H. W. Massive Stars and the Energy Balance of the Interstellar Medium. I. The Impact of an Isolated 60 M_{solar} Star. ApJ **594**, 888 (2003).

Geach, J. E.; Hickox, R. C.; Diamond-Stanic, A. M.; Krips, M.; Rudnick, G. H.; Tremonti, C. A.; Sell, P. H.; Coil, A. L. and Moustakas, J. Stellar feedback as the origin of an extended molecular outflow in a starburst galaxy. Nature **516**, 68 (2014).

Gendelev, L. and Krumholz, M. R. Evolution of Blister-type H II Regions in a Magnetized Medium. ApJ **745**, 158 (2012).

Ghosh, P. and Lamb, F. K. Disk accretion by magnetic neutron stars. ApJ **223**, L83 (1978).

Gnat, O. and Sternberg, A. Time-dependent Ionization in Radiatively Cooling Gas. ApJS **168**, 213 (2007).

González, M. and Audit, E. Numerical Treatment of Radiative Transfer. Ap&SS **298**, 357 (2005).

Goodman, A. A.; Benson, P. J.; Fuller, G. A. and Myers, P. C. Dense cores in dark clouds. VIII - Velocity gradients. ApJ **406**, 528 (1993).

Górski, K. M.; Hivon, E.; Banday, A. J.; Wandelt, B. D.; Hansen, F. K.; Reinecke, M. and Bartelmann, M. HEALPix: A Framework for High-Resolution Discretization and Fast Analysis of Data Distributed on the Sphere. ApJ **622**, 759 (2005).

Goss, W. M. and Radhakrishnan, V. The Distances of the Galactic H II Regions NGC 3576 and 3603. Astrophys. Lett. **4**, 199 (1969).

Grevesse, N. and Sauval, A. J. Standard Solar Composition. Space Sci. Rev. **85**, 161 (1998).

Grunhut, J. H.; Wade, G. A.; Marcolino, W. L. F.; Petit, V.; Henrichs, H. F.; Cohen, D. H.; Alecian, E.; Bohlender, D.; Bouret, J.-C.; Kochukhov, O.; Neiner, C.; St-Louis, N. and Townsend, R. H. D. Discovery of a magnetic field in the O9 sub-giant star HD 57682 by the MiMeS Collaboration. MNRAS **400**, L94 (2009).

Hanson, M. M.; Howarth, I. D. and Conti, P. S. The Young Massive Stellar Objects of M17. ApJ **489**, 698 (1997).

Harper-Clark, E. and Murray, N. One-Dimensional Dynamical Models of the Carina Nebula Bubble. ApJ **693**, 1696 (2009).

Hartmann, L.; D'Alessio, P.; Calvet, N. and Muzerolle, J. Why Do T Tauri Disks Accrete? ApJ **648**, 484 (2006).

Hartmann, L. and Stauffer, J. R. Additional measurements of pre-main-sequence stellar rotation. AJ **97**, 873 (1989).

Herbst, W.; Eislöffel, J.; Mundt, R. and Scholz, A. The Rotation of Young Low-Mass Stars and Brown Dwarfs. *Protostars and Planets V* pp. 297–311 (2007).

Hills, J. G. The effect of mass loss on the dynamical evolution of a stellar system - Analytic approximations. ApJ **235**, 986 (1980).

Hoffmeister, V. H.; Chini, R.; Scheyda, C. M.; Schulze, D.; Watermann, R.; Nürnberger, D. and Vogt, N. The Stellar Population of M17. ApJ **686**, 310 (2008).

Hofmann, K.-H.; Seggewiss, W. and Weigelt, G. Speckle masking observations of HD 97950 with 75 MAS resolution: evolution of the stellar core of the starburst cluster NGC 3603. A&A **300**, 403 (1995).

Hosokawa, T.; Offner, S. S. R. and Krumholz, M. R. On the Reliability of Stellar Ages and Age Spreads Inferred from Pre-main-sequence Evolutionary Models. ApJ **738**, 140 (2011).

Hosokawa, T. and Omukai, K. Evolution of Massive Protostars with High Accretion Rates. ApJ **691**, 823 (2009).

Howell, L. H. and Greenough, J. A. Radiation diffusion for multi-fluid Eulerian hydrodynamics with adaptive mesh refinement. *Journal of Computational Physics* **184**, 53 (2003).

Huang, W. and Gies, D. R. Stellar Rotation in Young Clusters. II. Evolution of Stellar Rotation and Surface Helium Abundance. ApJ **648**, 591 (2006).

Huang, W.; Gies, D. R. and McSwain, M. V. A Stellar Rotation Census of B Stars: From ZAMS to TAMS. ApJ **722**, 605 (2010).

Hubrig, S.; Schöller, M.; Schnerr, R. S.; González, J. F.; Ignace, R. and Henrichs, H. F. Magnetic field measurements of O stars with FORS 1 at the VLT. A&A **490**, 793 (2008).

Hunter, D. A.; Shaya, E. J.; Holtzman, J. A.; Light, R. M.; O'Neil, Jr., E. J. and Lynds, R. The Intermediate Stellar Mass Population in R136 Determined from Hubble Space Telescope Planetary Camera 2 Images. ApJ **448**, 179 (1995).

Jacquet, E. and Krumholz, M. R. Radiative Rayleigh-Taylor Instabilities. ApJ **730**, 116 (2011).

Jeans, J. H. The Stability of a Spherical Nebula. *Philosophical Transactions of the Royal Society of London Series A* **199**, 1 (1902).

Jiang, Y.-F.; Stone, J. M. and Davis, S. W. A Godunov Method for Multidimensional Radiation Magnetohydrodynamics Based on a Variable Eddington Tensor. ApJS **199**, 14 (2012).

Jijina, J. and Adams, F. C. Infall Collapse Solutions in the Inner Limit: Radiation Pressure and Its Effects on Star Formation. ApJ **462**, 874 (1996).

Johns-Krull, C. M. The Magnetic Fields of Classical T Tauri Stars. ApJ **664**, 975 (2007).

Johnston, K. G.; Robitaille, T. P.; Beuther, H.; Linz, H.; Boley, P.; Kuiper, R.; Keto, E.; Hoare, M. G. and van Boekel, R. A Keplerian-like Disk around the Forming O-type Star AFGL 4176. ApJ **813**, L19 (2015).

Kahn, F. D. Cocoons around early-type stars. A&A **37**, 149 (1974).

Kee, N. D.; Owocki, S. and Sundqvist, J. O. Line-driven ablation of circumstellar discs - I. Optically thin decretion discs of classical Oe/Be stars. MNRAS **458**, 2323 (2016).

Klassen, M.; Kuiper, R.; Pudritz, R. E.; Peters, T.; Banerjee, R. and Buntemeyer, L. A General Hybrid Radiation Transport Scheme for Star Formation Simulations on an Adaptive Grid. ApJ **797**, 4 (2014).

Klassen, M.; Pudritz, R. E.; Kuiper, R.; Peters, T. and Banerjee, R. Simulating the Formation of Massive Protostars. I. Radiative Feedback and Accretion Disks. ApJ **823**, 28 (2016).

Klein, R. I. Star formation with 3-D adaptive mesh refinement: the collapse and fragmentation of molecular clouds. *Journal of Computational and Applied Mathematics* **109**, 123 (1999).

Koenigl, A. Disk accretion onto magnetic T Tauri stars. ApJ **370**, L39 (1991).

Kong, S.; Tan, J. C.; Caselli, P.; Fontani, F.; Liu, M. and Butler, M. J. A Hunt for Massive Starless Cores. ApJ **834**, 193 (2017).

Kroupa, P. On the variation of the initial mass function. MNRAS **322**, 231 (2001).

Krumholz, M. R. Star Formation with Adaptive Mesh Refinement Radiation Hydrodynamics. In Alves, J.; Elmegreen, B. G.; Girart, J. M. and Trimble, V., eds., *Computational Star Formation* (2011), vol. 270 of *IAU Symposium*, pp. 187–194.

Krumholz, M. R. DESPOTIC - a new software library to Derive the Energetics and SPectra of Optically Thick Interstellar Clouds. MNRAS (2013).

Krumholz, M. R. The big problems in star formation: The star formation rate, stellar clustering, and the initial mass function. Phys. Rep. **539**, 49 (2014). In press, arXiv:1402.0867.

Krumholz, M. R.; Bate, M. R.; Arce, H. G.; Dale, J. E.; Gutermuth, R.; Klein, R. I.; Li, Z.-Y.; Nakamura, F. and Zhang, Q. Star Cluster Formation and Feedback. *Protostars and Planets VI* pp. 243–266 (2014).

Krumholz, M. R.; Klein, R. I. and McKee, C. F. Radiation-Hydrodynamic Simulations of Collapse and Fragmentation in Massive Protostellar Cores. ApJ **656**, 959 (2007a).

Krumholz, M. R.; Klein, R. I.; McKee, C. F. and Bolstad, J. Equations and Algorithms for Mixed-frame Flux-limited Diffusion Radiation Hydrodynamics. ApJ **667**, 626 (2007b).

Krumholz, M. R.; Klein, R. I.; McKee, C. F.; Offner, S. S. R. and Cunningham, A. J. The Formation of Massive Star Systems by Accretion. *Science* **323**, 754 (2009).

Krumholz, M. R.; Leroy, A. K. and McKee, C. F. Which Phase of the Interstellar Medium Correlates with the Star Formation Rate? ApJ **731**, 25 (2011).

Krumholz, M. R. and Matzner, C. D. The Dynamics of Radiation-pressure-dominated H II Regions. ApJ **703**, 1352 (2009).

Krumholz, M. R.; McKee, C. F. and Klein, R. I. Embedding Lagrangian Sink Particles in Eulerian Grids. ApJ **611**, 399 (2004).

Krumholz, M. R.; McKee, C. F. and Klein, R. I. How Protostellar Outflows Help Massive Stars Form. ApJ **618**, L33 (2005).

Krumholz, M. R.; Stone, J. M. and Gardiner, T. A. Magnetohydrodynamic Evolution of H II Regions in Molecular Clouds: Simulation Methodology, Tests, and Uniform Media. ApJ **671**, 518 (2007c).

Krumholz, M. R. and Tan, J. C. Slow Star Formation in Dense Gas: Evidence and Implications. ApJ **654**, 304 (2007).

Krumholz, M. R. and Thompson, T. A. Direct Numerical Simulation of Radiation Pressure-driven Turbulence and Winds in Star Clusters and Galactic Disks. ApJ **760**, 155 (2012).

Kudritzki, R. P.; Puls, J.; Lennon, D. J.; Venn, K. A.; Reetz, J.; Najarro, F.; McCarthy, J. K. and Herrero, A. The wind momentum-luminosity relationship of galactic A- and B-supergiants. A&A **350**, 970 (1999).

Kuiper, R.; Klahr, H.; Beuther, H. and Henning, T. Three-dimensional Simulation of Massive Star Formation in the Disk Accretion Scenario. ApJ **732**, 20 (2011).

Kuiper, R.; Klahr, H.; Beuther, H. and Henning, T. On the stability of radiation-pressure-dominated cavities. A&A **537**, A122 (2012).

Kuiper, R.; Klahr, H.; Dullemond, C.; Kley, W. and Henning, T. Fast and accurate frequency-dependent radiation transport for hydrodynamics simulations in massive star formation. A&A **511**, A81 (2010).

Kuiper, R.; Yorke, H. W. and Turner, N. J. Protostellar Outflows and Radiative Feedback from Massive Stars. ApJ **800**, 86 (2015).

Lada, C. J. and Lada, E. A. Embedded Clusters in Molecular Clouds. ARA&A **41**, 57 (2003).

Larson, R. B. Angular momentum and the formation of stars and black holes. *Reports on Progress in Physics* **73**, 014901 (2010).

Larson, R. B. and Starrfield, S. On the formation of massive stars and the upper limit of stellar masses. A&A **13**, 190 (1971).

Leitherer, C.; Robert, C. and Drissen, L. Deposition of mass, momentum, and energy by massive stars into the interstellar medium. ApJ **401**, 596 (1992).

Lejeune, T.; Cuisinier, F. and Buser, R. Standard stellar library for evolutionary synthesis. I. Calibration of theoretical spectra. A&AS **125**, 229 (1997).

Levermore, C. D. and Pomraning, G. C. A flux-limited diffusion theory. ApJ **248**, 321 (1981).

Levesque, E. M. The physical properties of red supergiants. New A Rev. **54**, 1 (2010).

Li, P. S.; Martin, D. F.; Klein, R. I. and McKee, C. F. A Stable, Accurate Methodology for High Mach Number, Strong Magnetic Field MHD Turbulence with Adaptive Mesh Refinement: Resolution and Refinement Studies. ApJ **745**, 139 (2012).

Lin, M.-K.; Krumholz, M. R. and Kratter, K. M. Spin-down of protostars through gravitational torques. MNRAS **416**, 580 (2011).

Longmore, S. N.; Pillai, T.; Keto, E.; Zhang, Q. and Qiu, K. Is Protostellar Heating Sufficient to Halt Fragmentation? A Case Study of the Massive Protocluster G8.68-0.37. ApJ **726**, 97 (2011).

Lopez, L. A.; Krumholz, M. R.; Bolatto, A. D.; Prochaska, J. X. and Ramirez-Ruiz, E. What Drives the Expansion of Giant H II Regions?: A Study of Stellar Feedback in 30 Doradus. ApJ **731**, 91 (2011).

Lopez, L. A.; Krumholz, M. R.; Bolatto, A. D.; Prochaska, J. X.; Ramirez-Ruiz, E. and Castro, D. The Role of Stellar Feedback in the Dynamics of HII Regions. *ArXiv e-prints* (2013a).

Lopez, L. A.; Pearson, S.; Ramirez-Ruiz, E.; Castro, D.; Yamaguchi, H.; Slane, P. O. and Smith, R. K. Unraveling the Origin of Overionized Plasma in the Galactic Supernova Remnant W49B. ApJ **777**, 145 (2013b).

Lovelace, R. V. E.; Romanova, M. M. and Bisnovatyi-Kogan, G. S. Spin-up/spin-down of magnetized stars with accretion discs and outflows. MNRAS **275**, 244 (1995).

Maeder, A. and Meynet, G. Evolution of massive stars with mass loss and rotation. New A Rev. **54**, 32 (2010).

Martins, F.; Donati, J.-F.; Marcolino, W. L. F.; Bouret, J.-C.; Wade, G. A.; Escolano, C.; Howarth, I. D. and Mimes Collaboration. Detection of a magnetic field on HD108:

clues to extreme magnetic braking and the Of?p phenomenon. MNRAS **407**, 1423 (2010).

Masunaga, H. and Inutsuka, S.-i. A Radiation Hydrodynamic Model for Protostellar Collapse. II. The Second Collapse and the Birth of a Protostar. ApJ **531**, 350 (2000).

Masunaga, H.; Miyama, S. M. and Inutsuka, S.-i. A Radiation Hydrodynamic Model for Protostellar Collapse. I. The First Collapse. ApJ **495**, 346 (1998).

Matt, S. and Pudritz, R. E. The spin of accreting stars: dependence on magnetic coupling to the disc. MNRAS **356**, 167 (2005).

Matt, S. P.; Pinzón, G.; de la Reza, R. and Greene, T. P. Spin Evolution of Accreting Young Stars. I. Effect of Magnetic Star-Disk Coupling. ApJ **714**, 989 (2010).

Matzner, C. D. and Jumper, P. H. Star Cluster Formation with Stellar Feedback and Large-scale Inflow. ApJ **815**, 68 (2015).

Matzner, C. D. and McKee, C. F. Efficiencies of Low-Mass Star and Star Cluster Formation. ApJ **545**, 364 (2000).

McKee, C. F. and Ostriker, E. C. Theory of Star Formation. ARA&A **45**, 565 (2007).

McKee, C. F. and Ostriker, J. P. A theory of the interstellar medium - Three components regulated by supernova explosions in an inhomogeneous substrate. ApJ **218**, 148 (1977).

McKee, C. F. and Tan, J. C. The Formation of Massive Stars from Turbulent Cores. ApJ **585**, 850 (2003).

McKee, C. F.; van Buren, D. and Lazareff, B. Photoionized stellar wind bubbles in a cloudy medium. ApJ **278**, L115 (1984).

Mihalas, D. and Auer, L. H. On laboratory-frame radiation hydrodynamics. J. Quant. Spec. Radiat. Transf. **71**, 61 (2001).

Mihalas, D. and Klein, R. I. On the solution of the time-dependent inertial-frame equation of radiative transfer in moving media to O(v/c). *Journal of Computational Physics* **46**, 97 (1982).

Miyoshi, T. and Kusano, K. A multi-state HLL approximate Riemann solver for ideal magnetohydrodynamics. *Journal of Computational Physics* **208**, 315 (2005).

Moffat, A. F. J.; Corcoran, M. F.; Stevens, I. R.; Skalkowski, G.; Marchenko, S. V.; Mücke, A.; Ptak, A.; Koribalski, B. S.; Brenneman, L.; Mushotzky, R.; Pittard, J. M.; Pollock, A. M. T. and Brandner, W. Galactic Starburst NGC 3603 from X-Rays to Radio. ApJ **573**, 191 (2002).

Moss, D. Magnetic Fields in the Ap and Bp Stars: a Theoretical Overview. In Mathys, G.; Solanki, S. K. and Wickramasinghe, D. T., eds., *Magnetic Fields Across the Hertzsprung-Russell Diagram* (2001), vol. 248 of *Astronomical Society of the Pacific Conference Series*, p. 305.

Mueller, K. E.; Shirley, Y. L.; Evans, II, N. J. and Jacobson, H. R. The Physical Conditions for Massive Star Formation: Dust Continuum Maps and Modeling. ApJS **143**, 469 (2002).

Murray, N.; Quataert, E. and Thompson, T. A. The Disruption of Giant Molecular Clouds by Radiation Pressure & the Efficiency of Star Formation in Galaxies. ApJ **709**, 191 (2010).

Murray, S. D.; Castor, J. I.; Klein, R. I. and McKee, C. F. Accretion disk coronae in high-luminosity systems. ApJ **435**, 631 (1994).

Myers, A. T.; McKee, C. F.; Cunningham, A. J.; Klein, R. I. and Krumholz, M. R. The Fragmentation of Magnetized, Massive Star-forming Cores with Radiative Feedback. ApJ **766**, 97 (2013).

Myers, P. C. and Fuller, G. A. Density structure and star formation in dense cores with thermal and nonthermal motions. ApJ **396**, 631 (1992).

Nakamura, F.; McKee, C. F.; Klein, R. I. and Fisher, R. T. On the Hydrodynamic Interaction of Shock Waves with Interstellar Clouds. II. The Effect of Smooth Cloud Boundaries on Cloud Destruction and Cloud Turbulence. ApJS **164**, 477 (2006).

Nakano, T. Conditions for the formation of massive stars through nonspherical accretion. ApJ **345**, 464 (1989).

Nakano, T.; Hasegawa, T.; Morino, J.-I. and Yamashita, T. Evolution of Protostars Accreting Mass at Very High Rates: Is Orion IRc2 a Huge Protostar? ApJ **534**, 976 (2000).

Nieuwenhuijzen, H. and de Jager, C. Parametrization of stellar rates of mass loss as functions of the fundamental stellar parameters M, L, and R. A&A **231**, 134 (1990).

Norman, M. L.; Paschos, P. and Abel, T. Simulating inhomogeneous reionization. Mem. Soc. Astron. Italiana **69**, 455 (1998).

Offner, S. S. R.; Klein, R. I.; McKee, C. F. and Krumholz, M. R. The Effects of Radiative Transfer on Low-Mass Star Formation. ApJ **703**, 131 (2009).

Oksala, M. E.; Wade, G. A.; Marcolino, W. L. F.; Grunhut, J.; Bohlender, D.; Manset, N.; Townsend, R. H. D. and Mimes Collaboration. Discovery of a strong magnetic field in the rapidly rotating B2Vn star HR 7355. MNRAS **405**, L51 (2010).

Ostriker, E. C. and Shu, F. H. Magnetocentrifugally Driven Flows from Young Stars and Disks. IV. The Accretion Funnel and Dead Zone. ApJ **447**, 813 (1995).

Padoan, P. and Nordlund, Å. A Super-Alfvénic Model of Dark Clouds. ApJ **526**, 279 (1999).

Palla, F. and Stahler, S. W. The evolution of intermediate-mass protostars. I - Basic results. ApJ **375**, 288 (1991).

Palla, F. and Stahler, S. W. The evolution of intermediate-mass protostars. II - Influence of the accretion flow. ApJ **392**, 667 (1992).

Pandolfi, M. and D'Ambrosio, D. Numerical instabilities in upwind methods: Analysis and cures for the "carbuncle" phenomenon. *Journal of Computational Physics* **166**, 31 (2001).

Parker, J. W. The OB associations of 30 Doradus in the Large Magellanic Cloud. I - Stellar observations and data reductions. AJ **106**, 560 (1993).

Parravano, A.; Hollenbach, D. J. and McKee, C. F. Time Dependence of the Ultraviolet Radiation Field in the Local Interstellar Medium. ApJ **584**, 797 (2003).

Pellegrini, E. W.; Baldwin, J. A.; Brogan, C. L.; Hanson, M. M.; Abel, N. P.; Ferland, G. J.; Nemala, H. B.; Shaw, G. and Troland, T. H. A Magnetically Supported Photodissociation Region in M17. ApJ **658**, 1119 (2007).

Pellegrini, E. W.; Baldwin, J. A. and Ferland, G. J. Structure and Feedback in 30 Doradus. II. Structure and Chemical Abundances. ApJ **738**, 34 (2011).

Pollack, J. B.; Hollenbach, D.; Beckwith, S.; Simonelli, D. P.; Roush, T. and Fong, W. Composition and radiative properties of grains in molecular clouds and accretion disks. ApJ **421**, 615 (1994).

Press, W. H.; Teukolsky, S. A.; Vetterling, W. T. and Flannery, B. P. *Numerical recipes in C++ : the art of scientific computing*. Cambridge University Press (2002).

Puls, J.; Vink, J. S. and Najarro, F. Mass loss from hot massive stars. A&A Rev. **16**, 209 (2008).

Repolust, T.; Puls, J. and Herrero, A. Stellar and wind parameters of Galactic O-stars. The influence of line-blocking/blanketing. A&A **415**, 349 (2004).

Rijkhorst, E.-J.; Plewa, T.; Dubey, A. and Mellema, G. Hybrid characteristics: 3D radiative transfer for parallel adaptive mesh refinement hydrodynamics. A&A **452**, 907 (2006).

Rogers, H. and Pittard, J. M. Feedback from winds and supernovae in massive stellar clusters - I. Hydrodynamics. MNRAS **431**, 1337 (2013).

Rosdahl, J. and Teyssier, R. A scheme for radiation pressure and photon diffusion with the M1 closure in RAMSES-RT. MNRAS **449**, 4380 (2015).

Rosen, A. L.; Krumholz, M. R.; Oishi, J. S.; Lee, A. T. and Klein, R. I. Hybrid Adaptive Ray-Moment Method (HARM^2): A Highly Parallel Method for Radiation Hydrodynamics on Adaptive Grids. *Journal of Computational Physics* **330**, 924 (2017). Submitted to Journal of Computational Physics, arXiv:1607.01802.

Russell, S. C. and Dopita, M. A. Abundances of the heavy elements in the Magellanic Clouds. III - Interpretation of results. ApJ **384**, 508 (1992).

Sana, H.; Le Bouquin, J.-B.; Lacour, S.; Berger, J.-P.; Duvert, G.; Gauchet, L.; Norris, B.; Olofsson, J.; Pickel, D.; Zins, G.; Absil, O.; de Koter, A.; Kratter, K.; Schnurr, O. and Zinnecker, H. Southern Massive Stars at High Angular Resolution: Observational Campaign and Companion Detection. ApJS **215**, 15 (2014).

Sánchez-Monge, Á.; Palau, A.; Fontani, F.; Busquet, G.; Juárez, C.; Estalella, R.; Tan, J. C.; Sepúlveda, I.; Ho, P. T. P.; Zhang, Q. and Kurtz, S. Properties of dense cores in clustered massive star-forming regions at high angular resolution. MNRAS **432**, 3288 (2013).

Schneider, N.; Csengeri, T.; Bontemps, S.; Motte, F.; Simon, R.; Hennebelle, P.; Federrath, C. and Klessen, R. Dynamic star formation in the massive DR21 filament. A&A **520**, A49 (2010).

Seifried, D.; Pudritz, R. E.; Banerjee, R.; Duffin, D. and Klessen, R. S. Magnetic fields during the early stages of massive star formation - II. A generalized outflow criterion. MNRAS **422**, 347 (2012).

Semenov, D.; Henning, T.; Helling, C.; Ilgner, M. and Sedlmayr, E. Rosseland and Planck mean opacities for protoplanetary discs. A&A **410**, 611 (2003).

Shestakov, A. I. and Offner, S. S. R. A multigroup diffusion solver using pseudo transient continuation for a radiation-hydrodynamic code with patch-based AMR. *Journal of Computational Physics* **227**, 2154 (2008).

Shu, F. H. Self-similar collapse of isothermal spheres and star formation. ApJ **214**, 488 (1977).

Shu, F. H.; Adams, F. C. and Lizano, S. Star formation in molecular clouds - Observation and theory. ARA&A **25**, 23 (1987).

Smith, N. A census of the Carina Nebula - I. Cumulative energy input from massive stars. MNRAS **367**, 763 (2006).

Smith, N. and Brooks, K. J. A census of the Carina Nebula - II. Energy budget and global properties of the nebulosity. MNRAS **379**, 1279 (2007).

Smith, N.; Egan, M. P.; Carey, S.; Price, S. D.; Morse, J. A. and Price, P. A. Large-Scale Structure of the Carina Nebula. ApJ **532**, L145 (2000).

Smith, R. K.; Krzewina, L. G.; Cox, D. P.; Edgar, R. J. and Miller, III, W. W. Time-dependent Cooling and Grain Destruction in Hot Dusty Plasmas: A Simplified Model and Principal Results. ApJ **473**, 864 (1996).

Soker, N. Heat conduction fronts in planetary nebulae. AJ **107**, 276 (1994).

Spitzer, L. *Physics of Fully Ionized Gases*. Interscience Publishers (1962).

Stevens, I. R. and Hartwell, J. M. The cluster wind from local massive star clusters. MNRAS **339**, 280 (2003).

Stone, J. M.; Gardiner, T. A.; Teuben, P.; Hawley, J. F. and Simon, J. B. Athena: A New Code for Astrophysical MHD. ApJS **178**, 137 (2008).

Strickland, D. K. and Stevens, I. R. Predicting X-ray emission from wind-blown bubbles - limitations of FITS to ROSAT spectra. MNRAS **297**, 747 (1998).

Strom, S. E.; Wolff, S. C. and Dror, D. H. A. B Star Rotational Velocities in h and χ Persei: A Probe of Initial Conditions during the Star Formation Epoch? AJ **129**, 809 (2005).

Stutz, A. M. and Gould, A. Slingshot mechanism in Orion: Kinematic evidence for ejection of protostars by filaments. A&A **590**, A2 (2016).

Swift, J. J. Two Massive, Low-Luminosity Cores Toward Infrared Dark Clouds. ApJ **705**, 1456 (2009).

Tan, J. C.; Beltrán, M. T.; Caselli, P.; Fontani, F.; Fuente, A.; Krumholz, M. R.; McKee, C. F. and Stolte, A. Massive Star Formation. *Protostars and Planets VI* pp. 149–172 (2014).

Tan, J. C.; Kong, S.; Butler, M. J.; Caselli, P. and Fontani, F. The Dynamics of Massive Starless Cores with ALMA. ApJ **779**, 96 (2013).

Tan, J. C.; Kong, S.; Zhang, Y.; Fontani, F.; Caselli, P. and Butler, M. J. An Ordered Bipolar Outflow from a Massive Early-stage Core. ApJ **821**, L3 (2016).

Tatematsu, K.; Kandori, R.; Umemoto, T. and Sekimoto, Y. N_2H^+ and HC_3N Observations of the Orion A Cloud. PASJ **60**, 407 (2008).

Teyssier, R. Grid-Based Hydrodynamics in Astrophysical Fluid Flows. ARA&A **53**, 325 (2015).

Thompson, T. A.; Quataert, E. and Murray, N. Radiation Pressure-supported Starburst Disks and Active Galactic Nucleus Fueling. ApJ **630**, 167 (2005).

Tout, C. A.; Pols, O. R.; Eggleton, P. P. and Han, Z. Zero-age main-seqence radii and luminosities as analytic functions of mass and metallicity. MNRAS **281**, 257 (1996).

Townsley, L. K. Diffuse X-ray Structures in Massive Star-forming Regions. In Smith, R. K.; Snowden, S. L. and Kuntz, K. D., eds., *American Institute of Physics Conference Series* (2009), vol. 1156 of *American Institute of Physics Conference Series*, pp. 225–230.

Townsley, L. K.; Broos, P. S.; Chu, Y.-H.; Gruendl, R. A.; Oey, M. S. and Pittard, J. M. The Integrated Diffuse X-ray Emission of the Carina Nebula Compared to Other Massive Star-forming Regions. ApJS **194**, 16 (2011a).

Townsley, L. K.; Broos, P. S.; Corcoran, M. F.; Feigelson, E. D.; Gagné, M.; Montmerle, T.; Oey, M. S.; Smith, N.; Garmire, G. P.; Getman, K. V.; Povich, M. S.; Remage Evans, N.; Nazé, Y.; Parkin, E. R.; Preibisch, T.; Wang, J.; Wolk, S. J.; Chu, Y.-H.; Cohen, D. H.; Gruendl, R. A.; Hamaguchi, K.; King, R. R.; Mac Low, M.-M.; McCaughrean, M. J.; Moffat, A. F. J.; Oskinova, L. M.; Pittard, J. M.; Stassun, K. G.; ud-Doula, A.; Walborn, N. R.; Waldron, W. L.; Churchwell, E.; Nichols, J. S.; Owocki, S. P. and Schulz, N. S. An Introduction to the Chandra Carina Complex Project. ApJS **194**, 1 (2011b).

Townsley, L. K.; Broos, P. S.; Feigelson, E. D.; Brandl, B. R.; Chu, Y.-H.; Garmire, G. P. and Pavlov, G. G. A Chandra ACIS Study of 30 Doradus. I. Superbubbles and Supernova Remnants. AJ **131**, 2140 (2006).

Townsley, L. K.; Feigelson, E. D.; Montmerle, T.; Broos, P. S.; Chu, Y.-H. and Garmire, G. P. 10 MK Gas in M17 and the Rosette Nebula: X-Ray Flows in Galactic H II Regions. ApJ **593**, 874 (2003).

Truelove, J. K.; Klein, R. I.; McKee, C. F.; Holliman, II, J. H.; Howell, L. H. and Greenough, J. A. The Jeans Condition: A New Constraint on Spatial Resolution in Simulations of Isothermal Self-gravitational Hydrodynamics. ApJ **489**, L179 (1997).

Truelove, J. K.; Klein, R. I.; McKee, C. F.; Holliman, II, J. H.; Howell, L. H.; Greenough, J. A. and Woods, D. T. Self-gravitational Hydrodynamics with Three-dimensional Adaptive Mesh Refinement: Methodology and Applications to Molecular Cloud Collapse and Fragmentation. ApJ **495**, 821 (1998).

Tsang, B. T.-H. and Milosavljević, M. Radiation pressure driving of a dusty atmosphere. MNRAS **453**, 1108 (2015).

Turk, M. J.; Smith, B. D.; Oishi, J. S.; Skory, S.; Skillman, S. W.; Abel, T. and Norman, M. L. yt: A Multi-code Analysis Toolkit for Astrophysical Simulation Data. ApJS **192**, 9 (2011).

Uzdensky, D. A.; Königl, A. and Litwin, C. Magnetically Linked Star-Disk Systems. II. Effects of Plasma Inertia and Reconnection in the Magnetosphere. ApJ **565**, 1205 (2002).

van der Tak, F. F. S.; van Dishoeck, E. F.; Evans, II, N. J. and Blake, G. A. Structure and Evolution of the Envelopes of Deeply Embedded Massive Young Stars. ApJ **537**,

283 (2000).

Vink, J. S.; de Koter, A. and Lamers, H. J. G. L. M. Mass-loss predictions for O and B stars as a function of metallicity. A&A **369**, 574 (2001).

Vlemmings, W. H. T.; Surcis, G.; Torstensson, K. J. E. and van Langevelde, H. J. Magnetic field regulated infall on the disc around the massive protostar CepheusAHW2. MNRAS **404**, 134 (2010).

Wade, G. A.; Fullerton, A. W.; Donati, J.-F.; Landstreet, J. D.; Petit, P. and Strasser, S. The magnetic field and confined wind of the O star θ^1 Orionis C. A&A **451**, 195 (2006).

Walder, R.; Folini, D. and Meynet, G. Magnetic Fields in Massive Stars, Their Winds, and Their Nebulae. Space Sci. Rev. **166**, 145 (2012).

Walmsley, M. Dense Cores in Molecular Clouds. In Lizano, S. and Torrelles, J. M., eds., *Revista Mexicana de Astronomia y Astrofisica Conference Series* (1995), vol. 1 of *Revista Mexicana de Astronomia y Astrofisica Conference Series*, p. 137.

Weaver, R.; McCray, R.; Castor, J.; Shapiro, P. and Moore, R. Interstellar bubbles. II - Structure and evolution. ApJ **218**, 377 (1977).

Weber, E. J. and Davis, Jr., L. The Angular Momentum of the Solar Wind. ApJ **148**, 217 (1967).

Weingartner, J. C. and Draine, B. T. Dust Grain-Size Distributions and Extinction in the Milky Way, Large Magellanic Cloud, and Small Magellanic Cloud. ApJ **548**, 296 (2001).

Williams, J. P. and McKee, C. F. The Galactic Distribution of OB Associations in Molecular Clouds. ApJ **476**, 166 (1997).

Wise, J. H. and Abel, T. ENZO+MORAY: radiation hydrodynamics adaptive mesh refinement simulations with adaptive ray tracing. MNRAS **414**, 3458 (2011).

Wolff, S. C.; Strom, S. E.; Cunha, K.; Daflon, S.; Olsen, K. and Dror, D. Rotational Velocities for Early-Type Stars in the Young Large Magellanic Cloud Cluster R136: Further Study of the Relationship Between Rotation Speed and Density in Star-Forming Regions. AJ **136**, 1049 (2008).

Wolff, S. C.; Strom, S. E.; Dror, D.; Lanz, L. and Venn, K. Stellar Rotation: A Clue to the Origin of High-Mass Stars? AJ **132**, 749 (2006).

Wolfire, M. G. and Cassinelli, J. P. The temperature structure in accretion flows onto massive protostars. ApJ **310**, 207 (1986).

Wolfire, M. G. and Cassinelli, J. P. Conditions for the formation of massive stars. ApJ **319**, 850 (1987).

Yeh, S. C. C. and Matzner, C. D. Ionization Parameter as a Diagnostic of Radiation and Wind Pressures in H II Regions and Starburst Galaxies. ApJ **757**, 108 (2012).

Yi, I. Magnetic braking in spin evolution of magnetized T Tauri stars. ApJ **428**, 760 (1994).

Yi, I. Magnetize accretion and spin evolution in classical T Tauri stars. ApJ **442**, 768 (1995).

Yorke, H. W. Calculated infrared spectra of cocoon stars. A&A **58**, 423 (1977).

Yorke, H. W. The evolution of protostellar envelopes of masses 3 and 10 solar masses. I - Structure and hydrodynamic evolution. A&A **80**, 308 (1979).

Yorke, H. W. and Bodenheimer, P. The Formation of Protostellar Disks. III. The Influence of Gravitationally Induced Angular Momentum Transport on Disk Structure and Appearance. ApJ **525**, 330 (1999).

Yorke, H. W.; Bodenheimer, P. and Laughlin, G. The formation of protostellar disks. 2: Disks around intermediate-mass stars. ApJ **443**, 199 (1995).

Yorke, H. W. and Sonnhalter, C. On the Formation of Massive Stars. ApJ **569**, 846 (2002).

Zapata, L. A.; Palau, A.; Ho, P. T. P.; Schilke, P.; Garrod, R. T.; Rodríguez, L. F. and Menten, K. Forming an early O-type star through gas accretion? A&A **479**, L25 (2008).

Zhang, Q.; Wang, Y.; Pillai, T. and Rathborne, J. Fragmentation at the Earliest Phase of Massive Star Formation. ApJ **696**, 268 (2009).

Zinnecker, H. and Yorke, H. W. Toward Understanding Massive Star Formation. ARA&A **45**, 481 (2007).